

2

THE COPY

Modelling Bathymetric Control of Near Coastal Wave Climate: Report 2

AD-A225 131

James T. Kirby and Jeffrey P. Anton
Center for Applied Coastal Research
Department of Civil Engineering
University of Delaware
Newark, Delaware 19716

(with Robert A. Dalrymple and K. D. Suh)

DTIC
JUL 19 1990
S D

Report CACR-90-01

Final Report to the
Office of Naval Research
Contract N00014-89-J-1717

April 1990

DISTRIBUTION STATEMENT A
Approved for public release
Distribution unlimited

125

REPORT DOCUMENTATION PAGE

1. Report No.	2.	3. Recipient's Accession No.	
4. Title and Subtitle MODELLING BATHYMETRIC CONTROL OF NEAR COASTAL WAVE CLIMATE: REPORT 2		5. Report Date APRIL 1990	6.
7. Author(s) James T. Kirby		8. Performing Organization Report No. CACR-90-01	
9. Performing Organization Name and Address University of Delaware Department of Civil Engineering Center for Applied Coastal Research		10. Project/Task/Work Unit No.	
12. Sponsoring Organization Name and Address Office of Naval Research 800 North Quincy Street Arlington, Virginia 22217		11. Contract or Grant No. N00014-89-J-1717	
		13. Type of Report Final Report	
		14.	
15. Supplementary Notes			
16. Abstract This document is the final report for the ONR project N00014-89-J-1717, which was the second phase of a study entitled "Modelling Bathymetric Control of Near Coastal Wave Climate." Most of the effort in this phase of the study was centered around a study of Bragg reflection of waves by nearshore bars. Additional effort has been expended in the development of angular spectrum models for intermediate depth wave propagation. Finally, preparations are being made for an extensive laboratory tests of wave-induced mean flows in the surfzone, and the associated operation of a passive syphon system driven by the pressure head developed by setup in the surfzone. Each area of progress is discussed in this report. The project has been further extended through 1990 by the Office of Naval Research through contract N00014-90-1678.			
17. Originator's Key Words Surface Waves, Wave-current Interaction, Numerical Models		18. Availability Statement	
19. U. S. Security Classif. of the Report Unclassified	20. U. S. Security Classif. of This Page Unclassified	21. No. of Pages 176	22. Price

Modelling Bathymetric Control of Near Coastal Wave Climate: Report 2

James T. Kirby and Jeffrey P. Anton
Center for Applied Coastal Research
Department of Civil Engineering
University of Delaware
Newark, Delaware 19716

(with Robert A. Dalrymple and K. D. Suh)

Report CACR-90-01

Final Report to the
Office of Naval Research
Contract N00014-89-J-1717

April 1990

STATEMENT "A" per R. Peloquin
ONR/Code 1242
TELECON 7/18/90

VG



Approved For	
NTIS	<input checked="" type="checkbox"/>
DTIC TAB	<input type="checkbox"/>
Unannounced	<input type="checkbox"/>
Justification	
By <i>per call</i>	
Distribution	
Availability Codes	
Dist	Availability Codes
A-1	

Contents

1	Summary	2
2	Bragg Reflection from Bars	2
3	Angular Spectrum Modelling	3
4	Mean Flow and Passive Syphon Effects in the Surfzone	3
	References	4

Appendix A: Propagation of surface waves over an undulating bed

Appendix B: Resonant and non-resonant reflection of linear waves over rapidly varying bottom undulations

Appendix C: Nonresonant and resonant reflection of long waves in varying channels

Appendix D: An angular spectrum model for propagation of Stokes waves

Appendix E: Intercomparison of truncated series solutions for shallow water waves

1 Summary

This document is the final report for the ONR project N00014-89-J-1717, which was the second phase of a study entitled "Modelling Bathymetric Control of Near Coastal Wave Climate". Most of the effort in this phase of the study was centered around a study of Bragg reflection of waves by nearshore bars. Additional effort has been expended in the development of angular spectrum models for intermediate depth wave propagation. Finally, preparations are being made for an extensive laboratory of wave-induced mean flows in the surfzone, and the associated operation of a passive syphon system driven by the pressure head developed by setup in the surfzone. Each area of progress is discussed below. The project has been further extended through 1990 by the Office of Naval Research through contract N00014-90-J-1678.

2 Bragg Reflection from Bars

The principle results of progress in this area have been the master's theses of Anton (1989) and McSherry (1989), and a further contribution by Kirby (1989). Kirby (1989) has examined the equations governing the propagation of linear water waves over a small-amplitude bar field (Kirby; 1986), and has shown that the problem may be cast in the form of a Mathieu equation, following Davies et al (1989). The paper by Kirby (1989) is included as Appendix A. Anton (1989) used these formulations to study the effect of discrete bars which were evenly spaced on a flat bottom. Anton demonstrated analytically that a resonant reflection peak arises due to each of the Fourier components describing the shape of the bar field, as conjectured by Mei, Hara and Naciri (1988). He also demonstrated the existence of the second peak (associated with the second harmonic of the bar spacing) experimentally. Agreement between theory and experiment for reflection coefficients is still weak due to finite amplitude bar effects. This effect is being further studied using a boundary element method in order to represent the finite-amplitude bars without approximation. The thesis of Anton is included here as Appendix B.

McSherry (1989) made an attempt to model the wave induced flow over a finite-length bar field, using a grid of radiation stresses derived from the output from a parabolic model for the coupled incident and reflected wave train (Kirby; 1986). This work still contains errors and is being extended and refined during the 1990 budget. The model is also being extended to include nonlinear effects, using coupled parabolic models for the incident and reflected waves (following Liu et al; 1985). An initial example of the Bragg reflection effect in shallow water waves was studied by Kirby and Vengayil (1988), which is included here as Appendix C. (This work was completed under Phase 1 funding, N00014-86-K-0790).

3 Angular Spectrum Modelling

Early work on angular spectrum modelling of intermediate depth waves was described in Kirby (1988) and has been published by Dalrymple and Kirby (1988) and Dalrymple, Suh, Kirby and Chae (1989). This work has been extended to include a correct

representation of Stokes third-order nonlinearity by Suh, Dalrymple and Kirby (1990). This work is included here as Appendix D.

Work along these lines has begun for the case of shallow water waves. A model for the evolution of a directional wave spectrum over laterally-uniform bottom topography is presently being developed and will be completed during the 1990 funding cycle. This model will be followed by a model for waves over bathymetry with weak longshore variations, and for the reflection of waves by on-offshore variations in depth associated with bar fields.

To date, the work mentioned here is represented by a short document (Kirby, 1990) which describes some computational problems associated with the choice of steady wave solutions to use in a model simulation. This work is included as Appendix E.

4 Mean Flow and Passive Syphon Effects in the Surfzone

The 1989 funding cycle has assisted in the development of a two-component laser-doppler flow measurement system and associated analysis software, and in the construction of a wavemaker and precision wave flume in the Ocean Engineering Laboratory of the Center for Applied Coastal Research, Department of Civil Engineering, University of Delaware. This system will be used during the 1990 funding cycle to study various aspects of undertow in periodic and random waves, and to study the operation of a passive syphon system driven by wave setup. In the studies of undertow, we intend to place more emphasis on measurement of Reynolds stress $-\overline{puw}$ than has appeared in previous studies, and we intend to construct a model of the time variation of the Reynolds stress and eddy viscosity with wave phase for the case of periodic waves. We are also going to attempt to directly measure 3 point correlations using the 2-component LDV and two hot-film probes.

References

1. Anton, J. P., 1989, "Resonant and non-resonant reflection of linear waves over rapidly varying bottom undulations", M.S. Thesis, University of Florida, Gainesville (include here as Appendix B).
2. Davies, A. G., Guazzelli, E. and Belzons, M., 1989, "The propagation of long waves over an undulating bed", *Physics of Fluids A1*, 1331-1340.
3. Kirby, J. T., 1986, "A general wave equation for waves over rippled beds", *Journal of Fluid Mechanics*, 162, 171-186.
4. Kirby, J. T., 1988, "Modelling bathymetric control of near coastal wave climate; Report 1". Report UFL/COEL-88/001, Coastal and Oceanographic Engineering Department, University of Florida, Gainesville.
5. Kirby, J. T., 1989, "Propagation of surface waves over an undulating bed", *Physics of Fluids A1*, 1898-1899 (included here as Appendix A).
6. Kirby, J. T., 1990, "Intercomparison of truncated series solutions for shallow water waves", submitted to *Journal of Waterway, Port, Coastal and Ocean Engineering* (included here as Appendix E).
7. Kirby, J. T. and Vengayil, P., 1988, "Nonresonant and resonant reflection of long waves in varying channels", *Journal of Geophysical Research*, 93, 10782-10796. (included here as Appendix C).
8. Liu, P.L-F., Yoon, S. B. and Kirby, J. T., 1985, "Nonlinear refraction-diffraction of waves in shallow water", *Journal of Fluid Mechanics*, 153, 185-201.
9. McSherry, T. R., 1989, "Wave-current interaction over a submerged bar field", M. S. Thesis, University of Florida, Gainesville.
10. Mei, C. C., Hara, T. and Naciri, M., 1988, "Note on Bragg scattering of water waves by parallel bars on the seabed", *Journal of Fluid Mechanics*, 186, 147-162.
11. Suh, K. D., Dalrymple, R. A. and Kirby, J. T., 1990, "An angular spectrum model for propagation of Stokes waves", *Journal of Fluid Mechanics*, in press (included here as Appendix D).

Appendix A: Propagation of surface waves over an undulating bed

Physics of Fluids A1, 1898-1899, 1989.

BRIEF COMMUNICATIONS

The purpose of this Brief Communications section is to present important research results of more limited scope than regular articles appearing in *Physics of Fluids A*. Submission of material of a peripheral or cursory nature is strongly discouraged. Brief Communications cannot exceed three printed pages in length, including space allowed for title, figures, tables, references, and an abstract limited to about 100 words.

Propagation of surface waves over an undulating bed

James T. Kirby

Center for Applied Coastal Research, Department of Civil Engineering, University of Delaware, Newark, Delaware 19716

(Received 5 April 1989; accepted 11 July 1989)

Recent results of Davies *et al.* [Phys. Fluids A 1, 1331 (1989)], which cast the problem of scattering of long surface waves by sinusoidal bed undulations into a Mathieu equation, are extended here to include the case of dispersive, intermediate depth waves. The present formulation is restricted to linear monochromatic wave motions and the bed undulation amplitude is assumed to be small relative to the total water depth.

The problem of reflection of surface water waves by undulating bottom forms has drawn considerable attention in recent years because of its possible importance in the context of coastal geomorphology. In a recent paper, Davies *et al.*¹ have considered the case of a sinusoidal bed undulation of small amplitude superimposed on a region of otherwise constant depth, and have shown that the wave field is governed (to first order in a small parameter based on bar amplitude) by the Mathieu equation. The analysis is restricted to non-dispersive, linear, monochromatic long waves. Davies *et al.* also showed that, in the case of nonresonant reflection, a subsequent expansion assuming a reflected wave of $O(\epsilon = \text{bar amplitude/water depth} \ll 1)$ and transmitted wave of $O(1)$ recovers the long-wave limit of the reflection coefficient found by Davies and Heathershaw.² Close to the Bragg resonance condition, a rescaling is necessary, with both incident and reflected waves taken to be $O(1)$ and the frequency detuning away from resonance to be $O(\epsilon)$. Analysis of this case recovers the long-wave limit of the results of Mei.³

Here, we point out that the analysis given by Davies *et al.* may be extended simply to intermediate depth, dispersive waves, yielding the Mathieu equation formulation with altered coefficients. Thus the limitation to nondispersive long waves is alleviated. We also consider the case of oblique incidence on the bar field.

For the case of waves in intermediate water depth [$kh = O(1)$], we may regard the depth $h(x, y)$ to be composed of a slowly varying mean component $\bar{h}(x, y)$ and a rapid superposed undulation $\delta(x, y)$, according to

$$h = \bar{h}(x, y) - \delta(x, y). \quad (1)$$

We assume the scaling restrictions

$$|\nabla \bar{h} / \bar{h}| = O(\epsilon), \quad |\delta / \bar{h}| = O(\epsilon), \quad \epsilon \ll 1. \quad (2)$$

Under these conditions, Kirby⁴ showed that the surface displacement $\eta(x, y)$ of a time-periodic wave of frequency ω is governed by an extended mild-slope equation, given by

$$\nabla \cdot (\bar{C} \bar{C}_s \nabla \eta) + \bar{k}^2 \bar{C} \bar{C}_s \eta - (g / \cosh^2 \bar{k} \bar{h}) \nabla \cdot (\delta \nabla \eta) = 0, \quad (3)$$

correct to $O(\epsilon)$. Here,

$$\omega^2 = g \bar{k} \tanh \bar{k} \bar{h}, \quad \bar{C} = \frac{\omega}{k}, \quad \bar{C}_s = \frac{\partial \omega}{\partial k}. \quad (4)$$

Since derivatives of $\cosh \bar{k} \bar{h}$ are of $O(\epsilon)$, we may write to the same level of approximation⁵

$$\nabla \cdot (f \nabla \eta) + \bar{k}^2 p \eta = 0, \quad (5)$$

where

$$p = \bar{C} \bar{C}_s, \quad f = p - g \delta / \cosh^2 \bar{k} \bar{h}. \quad (6)$$

Employing the change of variable

$$\eta = f^{-1/2} W \quad (7)$$

changes (5) to the form

$$\nabla^2 W + [\bar{k}^2 + A(\bar{k}^2 \delta + \nabla^2 \delta / 2)] W = 0, \quad (8)$$

where

$$A = g / \bar{C} \bar{C}_s \cosh^2 \bar{k} \bar{h} \quad (9)$$

and where terms proportional to the (slope)² and curvature of \bar{h} have been neglected as being of $O(\epsilon^2)$. (These terms must be retained in the vicinity of shorelines.) Note that as $\bar{k} \bar{h} \rightarrow 0$, $A \rightarrow [1 + O(\bar{k} \bar{h})^2] / \bar{h}$.

We restrict our attention to the case $\bar{h} = \bar{h}(x)$, $\delta = \delta(x)$, and $\partial / \partial y \equiv 0$, where (x, y) is the horizontal plane. Equation (8) reduces to

$$W_{xx} + [\bar{k}^2 + A(\bar{k}^2 \delta + \delta_{xx} / 2)] W = 0. \quad (10)$$

Consider the case $\bar{h} = \text{const}$ and

$$\delta(x) = -\epsilon \bar{h} \cos lx, \quad (11)$$

which corresponds to Davies *et al.* Here, $\epsilon = b / \bar{h}$, b the bar amplitude, and l is the bar wavenumber. Using the change of coordinates $lx = 2z$, we obtain

$$W_{xx} + \lambda^2 \{1 - \epsilon A \bar{h} [(\lambda^2 - 2)/\lambda^2] \cos 2z\} W = 0, \quad (12)$$

where $\lambda^2 = (2\bar{k}/l)^2$. As $\bar{k}\bar{h} \rightarrow 0$, $A\bar{h} \rightarrow 1 + O(\bar{k}\bar{h})^2$ and we recover the model given by Davies *et al.* Equation (12) is the Mathieu equation

$$W_{xx} + (a - 2q \cos 2z) W = 0, \quad (13)$$

with

$$a = \lambda^2, \quad q = \epsilon A \bar{h} (\lambda^2 - 2)/2. \quad (14)$$

The revision of the parameter q in Davies *et al.* by the form given in (14) then allows for the recovery of the general results of Davies and Heathershaw² and Mei,³ rather than just the long-wave limit.

For the case of a bar field of finite extent, matching conditions between the solution over the bar field and the solutions in the uniform domains to either side are required. We take $\delta(z) \neq 0$ in the interval $-\pi/4 < z < (N - \frac{1}{2})\pi$, where N is the number of full bar wavelengths and the shift of 45° causes the undulation to have a value of zero at the bar field edges. Equation (12) may then be solved in the finite domain with the use of appropriate boundary conditions. In $z < -\pi/4$, W may be written as

$$W = W_I + W_R = e^{i\lambda z} + R e^{-i\lambda z}, \quad z < -\pi/4, \quad (15)$$

where R is a complex reflection coefficient. In $z > (N - \frac{1}{2})\pi$, we have

$$W = W_T = T e^{i\lambda z}, \quad z > (N - \frac{1}{2})\pi, \quad (16)$$

where T is the complex transmission coefficient. Noting that the reflected wave W_R and the transmitted wave W_T should satisfy appropriate radiation conditions in their respective domains, we obtain the mixed boundary conditions on W ,

$$W_z = i\lambda(2W_I - W), \quad z = -\pi/4, \quad (17)$$

$$W_z = i\lambda W, \quad z = (N - \frac{1}{2})\pi. \quad (18)$$

Equations (17) and (18), together with (13), may be used as a basis for direct numerical computations. Kirby⁴

has compared a direct solution of (3) with the experimental data of Davies and Heathershaw.² Solutions of (13) are not substantially different and show good agreement with experimental data.

We further show the extension to the case of oblique incidence on the one-dimensional bar field. Returning to the dispersive wave model, we obtain

$$\hat{W}_{xx} + [(\bar{k}^2 - m^2) + A(\bar{k}^2 \delta - \delta_{xx}/2)] \hat{W} = 0, \\ W = \hat{W} e^{imx}, \quad (19)$$

where $\delta = \delta(x)$ only, and

$$m = \bar{k} \sin \theta = \text{const.} \quad (20)$$

The transformations presented above give the Mathieu equation (13) with q given by (14) and

$$a = \lambda^2 - \gamma^2, \quad \gamma = 2m/l = (2\bar{k}/l) \sin \theta. \quad (21)$$

Then

$$a = [(2\bar{k}/l) \cos \theta]^2 > 0 \quad (22)$$

always, and the basic form of the equation is unchanged. Explicit results near resonance for this case have recently been given elsewhere.⁶

ACKNOWLEDGMENTS

This work was supported by the Office of Naval Research through Contract No. N00014-86-K-0790 and No. N00014-89-J-1717.

¹A. G. Davies, E. Guazzelli, and M. Belzons, *Phys. Fluids A* 1, 1331 (1989).

²A. G. Davies and A. D. Heathershaw, *J. Fluid Mech.* 144, 419 (1984).

³C. C. Mei, *J. Fluid Mech.* 152, 315 (1985).

⁴J. T. Kirby, *J. Fluid Mech.* 162, 171 (1986).

⁵P. L.-F. Liu, *J. Fluid Mech.* 179, 371 (1987).

⁶R. A. Dalrymple and J. T. Kirby, *J. Waterway, Port, Coast. Ocean Eng.* 112, 309 (1986); C. C. Mei, T. Hara, and M. Naciri, *J. Fluid Mech.* 186, 147 (1988).

Appendix B: Resonant and non-resonant reflection of linear waves over rapidly varying bottom undulations

M.S. Thesis, University of Florida, Jeffrey P. Anton, August 1989.

RESONANT AND NON-RESONANT REFLECTION OF LINEAR WAVES OVER
RAPIDLY VARYING BOTTOM UNDULATIONS

By

JEFFREY PHILIP ANTON

A THESIS PRESENTED TO THE GRADUATE SCHOOL
OF THE UNIVERSITY OF FLORIDA IN
PARTIAL FULFILLMENT OF THE REQUIREMENTS
FOR THE DEGREE OF MASTER OF SCIENCE

UNIVERSITY OF FLORIDA

1989

TABLE OF CONTENTS

ACKNOWLEDGEMENTS	ii
LIST OF FIGURES	vi
ABSTRACT	viii
CHAPTERS	
1 INTRODUCTION	1
1.1 Review of Weak Reflection Theories	4
1.1.1 Non-Resonant Interaction	4
1.1.2 Formulation of Davies and Heathershaw for Non-Resonant Interaction	5
1.1.3 Miles' Oblique Surface Wave Diffraction	7
1.2 Review of Strong Reflection Theories	8
1.2.1 Mei's Resonant Interaction Solution	9
1.2.2 Depth-Integrated Equation for Small Undulations on Mild Slopes . .	12
1.3 Indirect Solution of Surface Elevation	14
2 EXTENSION OF NON-RESONANT INTERACTION THEORY	16
2.1 Introduction	16
2.2 Governing Equation	16
2.3 Two Dimensional Wave Field	17
2.4 Solution for Periodic Bars	20
2.5 Fourier Decomposition of the Bottom	21
2.5.1 The Resonant Case	23
2.5.2 The Non-Resonant Case	24
2.5.3 Full Solution	24

3	COMPARISON OF SOLUTIONS	27
3.1	Introduction	27
3.2	Derivation of a Complete Governing Equation	27
3.3	Numerical Approximations	29
3.4	Comparison to Existing Theories	32
3.4.1	One-dimensional Wave Field	32
3.4.2	Obliquely Incident Waves	34
3.5	Application of the Solutions	35
4	ANALYSIS TECHNIQUE FOR LABORATORY STUDY	41
4.1	Introduction	41
4.2	Theoretical Background	41
4.3	Inputs to Least Squares	47
4.3.1	Direct Signal Processing	47
4.3.2	Ensemble Averaging of Cross-Correlation Spectra	47
4.4	Results of Least Square Error Fit	49
4.5	Results	53
5	LABORATORY STUDY	55
5.1	Introduction	55
5.2	Equipment	55
5.2.1	Wave Flume	55
5.2.2	Electronic Measurement	58
5.3	Data Analysis	59
5.3.1	Acquisition	59
5.3.2	Data Processing	61
5.3.3	Verification of Analysis Technique	66
5.4	Results and Conclusions	67

6	BARS ON A MILD SLOPE	70
6.1	Introduction	70
6.2	Reformulation of the Mild Slope Equation	70
6.3	Numerical Solution	72
6.4	Model Tests and Examples	75
6.4.1	Response Over a Barfield in Front of a Wall	75
6.4.2	Response Over a Barfield in Front of Beach	78
6.5	Conclusions	84
7	CONCLUSIONS	85
	BIBLIOGRAPHY	86
	BIOGRAPHICAL SKETCH	88

LIST OF FIGURES

1.1	Domain definition sketch	5
2.1	Reflection of single mode bottom	21
2.2	Definition sketch of four cosine bumps on a flat bottom	22
2.3	Contributions to reflection by individual Fourier components	25
2.4	Sum total of the reflection from individual components	26
3.1	Reflection coefficient vs. $2k/\lambda$ for sinusoidal bottom. $h(x) = 0.15m$, four cycles $\delta(x) = 0.05m \sin 2\pi/1.0m$	33
3.2	Reflection coefficient vs. $2k/\lambda$ for four cosine bumps. $h(x) = 0.15m$, $\delta(x) = 0.05m \cos 2\pi/1.0m$, $\lambda = 2\pi/L_0$	34
3.3	Mei's resonant interaction theory reflection coefficient vs. angle of incidence θ and offshore wavenumber k_0	35
3.4	Non-Resonant Extension, reflection coefficient vs. angle of incidence θ and offshore wavenumber k_0	36
3.5	Numerical Solution, reflection coefficient vs. angle of incidence θ and offshore wavenumber k_0	37
3.6	Non-Resonant Extension - Numerical Solution vs. angle of incidence θ and offshore wavenumber k_0	38
3.7	Non-Resonant Extension - Mei's Solution vs. angle of incidence θ and offshore wavenumber k_0	39
3.8	Mei's Solution - Numerical Solution vs. angle of incidence θ and offshore wavenumber k_0	40
4.1	Effect of smoothing on a monochromatic spectrum	51
4.2	Interpolating resolved frequencies in the smoothed monochromatic spectrum to estimate the energy density at the true frequency	52
5.1	Profile of bar field	56
5.2	Typical calibration curve	60

5.3	Improper gage spacing and virtual standing wave	62
5.4	Energy crossing system boundaries	62
5.5	Typical energy density spectrum for incident wave	63
5.6	Typical energy density spectrum for reflected wave	64
5.7	Typical energy density spectrum for transmitted wave	64
5.8	Reflection theory vs. measured, .8 m bar spacing	68
5.9	Reflection theory vs. measured 1.2 m bar spacing	68
5.10	Energy Conserved: Theoretical and Measured .8 m bar spacing	69
6.1	Definition sketch of bar field in front of a wall	76
6.2	Wave envelope in front of a wall for η directly and $\eta = f^{-1/2}W$ numerical schemes, $d = 4$	77
6.3	Wave amplitude at the wall for η directly and $\eta = f^{-1/2}W$ numerical schemes, $d = 4$	77
6.4	Wave envelope in front of a wall for η directly and $\eta = f^{-1/2}W$ numerical schemes, $d = 4.5$	78
6.5	Wave amplitude at the wall for η directly and $\eta = f^{-1/2}W$ numerical schemes, $d = 4.5$	79
6.6	Definition sketch of bar field on a sloping bottom in front of a shoreline	80
6.7	Wave envelope on a sloping beach with 4 sine shaped bumps, $d = 10.0$	80
6.8	Wave envelope on a sloping beach with 4 sine shaped bumps, $d = 10.5$	81
6.9	Wave amplitude at the shoreline vs. $2k/\lambda, d = 10.0$	82
6.10	Wave amplitude at the shoreline vs. $2k/\lambda, d = 10.5$	82
6.11	Wave amplitude at $x = 7$ m vs. $2k/\lambda, d = 10.0$	83
6.12	Wave amplitude at $x = 7$ m vs. $2k/\lambda, d = 10.5$	83

Abstract of Thesis Presented to the Graduate School
of the University of Florida in Partial Fulfillment of the
Requirements for the Degree of Master of Science

RESONANT AND NON-RESONANT REFLECTION OF LINEAR WAVES OVER
RAPIDLY VARYING BOTTOM UNDULATIONS

By

JEFFREY PHILIP ANTON

August 1989

Chairman: Dr. James Thornton Kirby
Major Department: Coastal and Oceanographic Engineering

Recent studies have shown that waves propagating over a bottom with rapid undulations may experience reflection as a result of the wave interacting with the bottom. The strength of reflection is dependent on the ratio of the wavenumber of the surface wave and the wavenumber of the bottom undulations. Specifically, if the wavenumber of the surface wave is close to being one-half of the wavenumber of the undulations, strong resonant reflections are indicated. Weaker non-resonant reflection takes place when this criterion is not met.

This thesis is the culmination of investigations of both resonant and non-resonant interactions of waves propagating over rapid undulations on an otherwise flat bottom. Results are compared numerically and in a laboratory study. A theory for the case of a mildly sloping beach is developed as well. The possibility for large amplitude standing waves between a series of undulations in front of a shoreline and wall is investigated.

CHAPTER 1 INTRODUCTION

Observations of naturally occurring phenomena often give rise to ideas of how man may alter, control or redirect the forces of nature. Observation and explanation are the purpose of science, application of such phenomena that of engineering. Coastal geomorphologists have observed periodic shore parallel bars formed on mild sloping beaches on which plunging breakers occur. There has been speculation that once one such bar existed, others would form, propagating a bar field outward. Also, of interest to coastal scientists and engineers was the possibility that once the bar field formed, resonant and non-resonant reflections of surface waves propagating over the bar field would occur.

Several theories have been put forth as to the evolution of the observed bar fields. Evans (1940) suggested that the first bar is formed when a plunging breaker stirs up sediment on the bottom and the falling crest behind the breaker deposits the sediment behind the wave. It has been suggested by Carter, Liu, and Mei (1974) that this breakpoint bar will initiate reflection of incident wave energy seaward, setting up a standing wave pattern. Due to Lagrangian drift, causing sediment to converge at the nodes and diverge at the anti-nodes, additional bars may form. In addition to seaward growth, it will be pointed out in the present study that due to the possibility of a trapped resonant wave field shoreward of the barfield, the field may also grow shoreward, as observed by McSherry (1989). Hypothetically, the growth of the bar field is a self maintaining process, where, as the bar field grows, stronger reflection occurs causing addition growth. The initial phase of this growth has in fact been observed in laboratory studies by Davies and Heathershaw (1984).

The wave length of the barfield on the bottom has a direct relationship with the relative strength of reflection of a surface wave of a particular frequency. As a scientific problem,

investigators have been interested not only in the evolution of the undulations, but in their effects as well. The evident strength of reflection has captured the attention of coastal scientists. In this study, one of the primary discussions will be the nature of the reflection resulting from the existence of a periodic bottom disturbance. Two domains of reflection, those being resonant and non-resonant reflection, have been identified by workers in the field.

Resonant reflection may be described as a strong backscatter of wave energy due to a tuning mechanism between the surface wave and the bottom undulations. Specifically, for regularly spaced undulations, or bars, resonant reflection will occur when the wavelength of the bottom undulation is half that of the surface wave, or, equivalently when twice the wave number k of the surface wave equals the wave number λ of the bottom undulations,

$$\frac{2k}{\lambda} = 1 \quad (1.1)$$

The similarity to Bragg resonant reflection in crystallography, where strong backscatter of certain frequencies of x-rays has been used to determine the spacing between atoms in a crystal lattice, has brought that name to the resonant backscatter of water waves. Non-resonant reflection, while not as strong but of no less importance, can be described as reflection away from the resonant peak.

Once the science of a phenomenon is well on its way to being worked out, the inevitable progression is the application of the new knowledge - the task of the engineer. The development of wave reflection technology is of interest to coastal engineers as a shore protection measure where it may provide a means to redirect the destructive energies back offshore. It will be shown later that it is possible to choose an artificial bar configuration such that more undesirable frequencies may be more strongly reflected. Naciri and Mei (1988) have been studying the possibility of using the reflective characteristics of a doubly reflective structure on a subsiding bottom to protect the oil rigs in the Ekofisk field of the North Sea. Yoon and Liu (1987) have suggested the use of barfields to replace harbour resonators.

The purpose of this study is not to invent specific applications of the theories introduced

above, but rather to explore the existing solutions to the reflection predictions and offer some deeper insight to potential advantages and problems with employing such a mechanism as an engineering application. The primary goal of this study is to present solutions, through various means, to the problem of predicting the reflective characteristics of shore parallel bars.

The obvious embarkation point of the journey though this thesis will begin with a review of the investigations and discoveries of previous scholars. Non-resonant interaction was studied and quantified by Davies and Heathershaw (1984), while Mei (1985) and Yoon and Liu (1987) neglected non-resonant cases and concentrated on resonant reflection. Kirby (1986) presented a general equation describing the interaction of waves propagating over rapid undulations of small amplitude on an otherwise slowly varying bottom and solved it using a numerical method.

Next, an extension of the non-resonant interaction theory of Davies and Heathershaw (1984) will be developed to accommodate oblique incidence and to solve for the reflection from individual Fourier components of the bottom undulations. Multiple component barfields will be compared to single component bedforms as previously studied in non-resonant interaction investigations. In effect, it will be shown that this method will provide the engineer with a tool to construct a tuned barfield.

Returning to the differences between the forms of the solutions in the literature review, a comprehensive comparison of the existing resonant interaction theory by Mei, the newly developed Fourier extension of the non-resonant interaction, and the numerical solution provided by Kirby will be presented.

Recently, Davies et al. (1989) solved the wave equation in the long wave limit by transforming the water surface variable η to a variable $W = f^{\frac{1}{2}}\eta$ that will be forced to zero at a shoreline. It will be developed in the final chapter how this uniquely allows the solution of the wave field (neglecting energy dissipation) over bars on a mild slope continuing to the shoreline. Also, the indication of shoreward propagating bars will be theoretically

supported.

Lastly, to add physical support to the menagerie of theory, data from a laboratory investigation are presented. While monochromatic waves were used in the wave flume, spectral analysis was employed to ensure the assumption of a single frequency. An exposition on the wonders and idiosyncracies of analysis of monochromatic fields with spectral analysis is also presented. The results of the laboratory experiments are plotted against and compared to theoretical results of the models.

1.1 Review of Weak Reflection Theories

1.1.1 Non-Resonant Interaction

Davies (1982) studied the interaction between surface waves and a finite periodic ripple patch on an otherwise flat bed in a two-dimensional domain. The problem had previously been examined assuming a ripple patch infinite in horizontal extent. However, the solution of the problem is valid only for small reflections of $O(\epsilon) \ll 1$, away from the Bragg resonant condition where $2k/\lambda \rightarrow 1$. k is the wave number of the surface wave and λ is the wave number of the sinusoidal ripple patch. The reflection coefficient is given by

$$R = \frac{2kD}{\sinh 2kh + 2kh} \frac{2k}{\lambda} \left| \frac{\sin(2k/\lambda) N_b \pi}{(2k/\lambda)^2 - 1} \right| \quad (1.2)$$

where N_b is the number of periods in the ripple patch and D is the amplitude of the ripples. This theory breaks down where $2k/\lambda \rightarrow 1$, since R becomes unbounded as N_b increases.

Davies and Heathershaw (1984) re-addressed the problem in an effort to combine the effects of non-resonant reflection and the Bragg resonant condition. The study involved two particular cases, one in which no attenuation of the incident wave occurs as it propagates over the ripple patch, allowing the wave transmitted past the barfield to be equal in amplitude to the incident wave. Thus, if any energy were reflected, the conservation of energy would be violated. To address this problem, another solution was posed in which an ad hoc linear attenuation of the incident wave amplitude was imposed to achieve an energy balance between the incident, reflected and transmitted wave-energy fluxes. It was further assumed

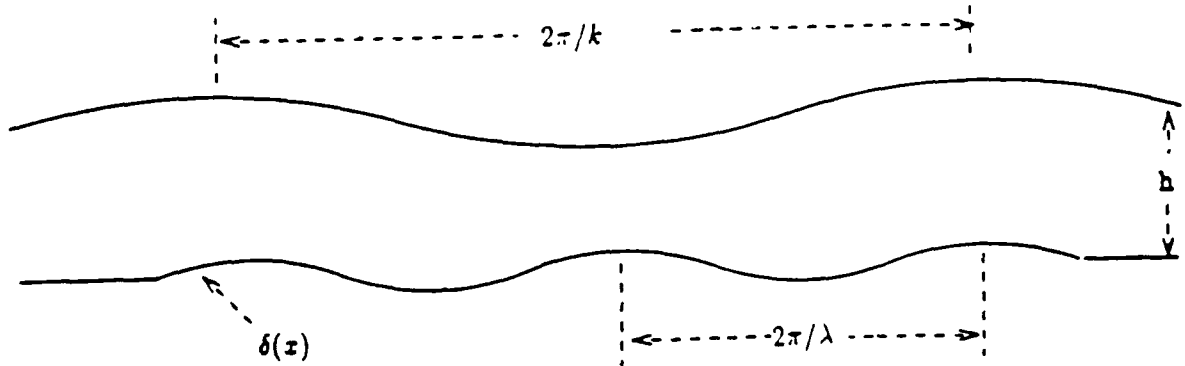


Figure 1.1: Domain definition sketch

that the flow is non-separating from the ripples and it is irrotational, thus no provision is made for the thin boundary layer above the impermeable bed. The ripple patch (Figure 1.1) is the same as used in Davies (1982).

1.1.2 Formulation of Davies and Heathershaw for Non-Resonant Interaction

Constant water depth $-h$ is assumed and the ripples are defined as the departure $\delta(x)$ from this mean. The barfield $\delta(x)$ has characteristic small amplitude D such that

$$\frac{D}{h} \sim O(\epsilon) \ll 1. \quad (1.3)$$

Water surface elevation is defined as $\eta(x, t)$ referenced to the still water level, $z = 0$. Since the flow is assumed to be irrotational in two-dimensions, Laplace's equation is satisfied by the velocity potential $\phi(x, z, t)$.

$$\nabla^2 \phi = 0 \quad (1.4)$$

Proceeding with a perturbation expansion of ϕ , η and δ in powers of a small parameter ϵ

$$\phi = \epsilon \phi_1 + \epsilon^2 \phi_2 + \dots \quad (1.5)$$

$$\eta = \epsilon \eta_1 + \epsilon^2 \eta_2 + \dots \quad (1.6)$$

$$\delta = \epsilon \delta_1 + \epsilon^2 \delta_2 + \dots \quad (1.7)$$

The bottom boundary condition (to first order) which requires that flow normal to the bottom must vanish on the boundary which would be present without the ripple patch, is now treated as new source of fluid motion (in second order) on the plane surface, $z = -h$. The boundary condition on the bottom may be stated

$$\phi_z - \phi_z \delta_z = 0 \quad \text{on} \quad z = -h + \delta \quad (1.8)$$

and the free surface boundary conditions

$$\eta_t + \phi_z - \phi_z \eta_z = 0 \quad \text{on} \quad z = \eta \quad (1.9)$$

$$g\eta + \phi_t + \frac{\phi_z^2 + \phi_z^2}{2} = 0 \quad \text{on} \quad z = \eta \quad (1.10)$$

The boundary conditions are treated by expanding the governing equations 1.8, 1.9 and 1.10 in Taylor series about $y = 0$. This allows the original nonlinear problem to be reduced to sets of linear problems, grouped in terms of powers of ϵ . The first order problem may be stated

$$\nabla^2 \phi_1 = 0 \quad \text{in} \quad -h \leq z \leq 0, -\infty \leq x \leq \infty \quad (1.11)$$

$$\eta_{1t} + \phi_{1z} = 0 \quad \text{on} \quad z = 0 \quad (1.12)$$

$$g\eta_1 - \phi_{1t} = 0 \quad \text{on} \quad z = 0 \quad (1.13)$$

$$\phi_{1z} = 0 \quad \text{on} \quad z = -h \quad (1.14)$$

which describes waves propagating over a flat bottom. The bottom boundary condition to second order contains the effect of the bottom undulations on the water motion. Specifically, the second order problem is solvable in two separable parts, one the Stoke's theory second order approximation, and the other which expresses the interaction between the first order motion and $O(\epsilon)$ bed undulations. Pursuing the second of these, the governing equation and free surface boundary conditions remain in essentially the same form

$$\nabla^2 \phi_2 = 0 \quad \text{in} \quad -h \leq z \leq 0, -\infty \leq x \leq \infty \quad (1.15)$$

$$\eta_{2t} + \phi_{2x} = 0 \quad \text{on } z = 0 \quad (1.16)$$

$$g\eta_2 - \phi_{2z} = 0 \quad \text{on } z = 0 \quad (1.17)$$

while the bottom boundary condition may be expressed

$$\phi_{2x} + \delta_1 \phi_{1xz} - \phi_{1z} \delta_{1x} = 0 \quad (1.18)$$

The bed form required for Davies solution is that depicted in Figure 1.1. The assumption is that the bottom undulations will be sinusoidal in profile and small amplitude. Also, the incident wave is restricted to be normally incident on the ripple patch.

The assumption by Davies and Heathershaw (1984) that all reflection taking place is of second order or $O(\epsilon)$ with respect to the incident wave causes the violation of energy conservation to leading order. To account for this, an artificially imposed energy attenuation correction was added to the solution procedure. The effort was to calculate the energy carried by the wave incident on the ripple patch, calculate the sum of the reflection and transmitted wave energies, which from the assumptions made would be greater than the incident wave energy, and adjust the amplitudes of the transmitted and reflected waves to the point where energy is conserved.

Included in the studies mentioned above were investigations into the possibility of ripple patch growth seaward as a result of Lagrangian drift below the standing wave field in front of the ripple patch. Laboratory studies of the reflection characteristics of a ripple patch on a movable bed on an otherwise flat bottom indicated some propagation of the ripple patch. Shoreward growth downwave of a barfield on a sloping beach has been observed in a three-dimensional laboratory study (McSherry 1989), probably a result of trapping a resonant frequency between the barfield and the shore. This phenomena will be discussed further in a later chapter.

1.1.3 Miles' Oblique Surface Wave Diffraction

Miles (1981) solved the same problem but allowed an arbitrary bottom form and incident waves propagating at oblique angles to the bottom perturbations. A form of the

was assumed, that is, incident and reflected waves are allowed at the offshore boundary and a transmitted wave allowed at the nearshore end. The governing equation was reduced to a solvable form by making the assumption again that the reflection is small. Miles then employed a finite cosine transform, solved the transformed equations, then applied the inverse transform to obtain the solution.

The results of Miles' solution are

$$R = [il(h + K^{-1} \sinh kh)]^{-1} (l^2 - m^2) \int_{-\infty}^{\infty} e^{2ilx} \delta(x) dx \quad (1.19)$$

and

$$T = 1 - [il(h + K^{-1} \sinh kh)]^{-1} (l^2 - m^2) \int_{-\infty}^{\infty} \delta(x) dx \quad (1.20)$$

where

$$k \tanh kh = \omega^2/g \equiv K, \quad (1.21)$$

$$l^2 + m^2 = k^2 \quad (1.22)$$

and R is the reflection coefficient, T is the transmission coefficient and $\delta(x)$ describes the bottom deformation.

It can be seen from the approximations $R = O(\epsilon)$ and $T = 1 + iO(\epsilon)$. Conservation of energy implies $|T|^2 = 1 - |R|^2$, which is not satisfied by the solution to $O(\epsilon)$. Also, where $l = m$ (45° angle of incidence), $R = 0$.

1.2 Review of Strong Reflection Theories

While Miles and Davies and Heathershaw were exploring weak non-resonant reflection, Mei (1985), Yoon and Liu (1987), and Benjamin et al. (1988) explored resonant interaction between the surface waves and rapidly varying bottom undulations. Of these, Mei in particular has performed a number of studies on resonant interaction. The inadequacy of Davies and Heathershaw's theory to handle resonant reflection prompted further study into resonant interaction and obliquely incident waves. Resonant interaction occurs where $2k/\lambda = 1$, and for the purposes of the present discussion, λ will be understood to be the wavenumber of a sinusoidal bottom perturbation.

1.2.1 Mei's Resonant Interaction Solution

Mei (1985) solved Laplace's equation with an undulating bottom as described by Davies and Heathershaw, but solved assuming coupling between the incident and reflected waves, requiring that they be of the same order. The governing equations were linearized with respect to the mean free surface and the mean sea bottom. The velocity potential was given by

$$\nabla_h^2 \phi + \phi_{zz} = 0; \quad -h < z < 0 \quad (1.23)$$

The bottom boundary condition is given by

$$\phi_z = -\nabla_h h \cdot \nabla_h \phi + \epsilon \nabla_h \cdot (\delta \nabla_h \phi) + O(\epsilon^2); \quad z = -h \quad (1.24)$$

where

$$\nabla_h = \left[\frac{\partial}{\partial x}, \frac{\partial}{\partial y} \right] \quad (1.25)$$

and $\delta = \delta(x)$ describes the bottom perturbation. Employing the ray approximation and allowing the wave to be modulated in time and space, the first order potential is taken as

$$\phi^{(1)} = (\psi^+ e^{iS^+} + \dots) + (\psi^- e^{iS^-} + \dots) \quad (1.26)$$

where S is the phase of the $+x$ or $-x$ propagating waves and the velocity profile ψ is given by

$$\psi^\pm = \frac{ig \cosh k(z+h)}{2\omega \cosh kh} A^\pm \quad (1.27)$$

where A^\pm are the complex wave amplitudes.

The assumptions in the solution procedure are that the small order undulations are superimposed on a slowly varying depth (mild slope), the form of incident wave is constructed such that it may be modulated in time and space, and a small parameter ϵ characterizes the slope of the free surface, the mean bottom, the bar amplitude, and C/C_g . Lastly, the bottom contours are shore parallel, although this condition is relaxed in a later paper on a doubly periodic bottom.

Mei introduces a frequency-like term Ω_0 which is defined as the cutoff frequency.

$$\Omega_0 = \frac{\omega k D}{2 \sinh 2kh} \quad (1.28)$$

The reflected wave is formulated such that its amplitude is $O(1)$ in anticipation of strong reflection. The solution is restricted in the sense that reflection must be strong, ie. resonant or close to resonance. Therefore, wave parameters are described in terms of their deviation from the true resonant case. This process is defined as detuning the wave from resonance where k represents the perfectly tuned or resonant wavenumber. The solutions are worked out in form of ratios between the tuned and detuned parameters. The incident wave is slightly detuned from the Bragg resonant condition such that its wave number is $k + \epsilon K$, where K is $O(1)$. The detuning implies a frequency deviation of $\epsilon\Omega$, where

$$\Omega = C_\epsilon K \quad (1.29)$$

The incident wave potential is given by 1.23 and the amplitude by

$$A = A_0 e^{i(Kx - \Omega t)} \quad (1.30)$$

where x and t are slow variables. The governing equation of the wave outside the domain defined by the ends of the bar field is reduced to

$$\left(\frac{\partial}{\partial t} + C_\epsilon \frac{\partial}{\partial x}\right) A = 0 \quad (1.31)$$

Over the bars, the governing equations become nonhomogeneous and coupled

$$\left(\frac{\partial}{\partial t} + C_\epsilon \frac{\partial}{\partial x}\right) A = -i\Omega_0 B \quad (1.32)$$

$$\left(\frac{\partial}{\partial t} - C_\epsilon \frac{\partial}{\partial x}\right) B = -i\Omega_0 A \quad (1.33)$$

where A is the $+x$ propagating amplitude and B is the $-x$ propagating amplitude and

$$\Omega_0 = \frac{gk^2 D}{4\omega \cosh^2 kh} \quad (1.34)$$

Continuity of A and B at the ends of the domain gives four conditions so the solution in all three regions may be easily found, where $B = 0$ if $x > L$, so no $-x$ propagating waves occur in this region.

The solution is split into four regions with respect to the cutoff frequency Ω_0 . The cutoff frequency provides a quantitative point at which the resonant approximation becomes unreliable, that is, where R becomes small. The reflection coefficients as a function of distance into the bar field for the four regions are defined as follows

i) $\Omega > \Omega_0$ Detuning frequency above cutoff

$$R(x) = \frac{-i\Omega_0 \sin P(L-x)}{PC_g \cos PL - i\Omega \sin PL} \quad (1.35)$$

where the envelope wavenumber P is

$$P = \frac{(\Omega^2 - \Omega_0^2)^{1/2}}{C_g} \quad (1.36)$$

and $0 < x < L$ and L is the length of the barfield.

ii) $0 < \Omega < \Omega_0$ Detuning frequency is below the cutoff

Denoting

$$Q = iP, \text{ where } Q = \frac{(\Omega_0^2 - \Omega^2)^{1/2}}{C_g} \quad (1.37)$$

the reflected wave amplitude is

$$R(x) = \frac{\Omega_0 \sinh Q(L-x)}{iQC_g \cosh QL + \Omega \sinh QL} \quad (1.38)$$

iii) $\Omega = 0$ Perfect tuning

Q reduces to K

$$R(x) = \frac{-i \sinh \frac{\Omega_0}{C_g}(L-x)}{\cosh \frac{\Omega_0 L}{C_g}} \quad (1.39)$$

iv) $\Omega = \Omega_0$ At the cutoff frequency

$Q \rightarrow 0$

$$R(x) = \frac{-i\Omega(L-x)/C_g}{1 - i\Omega L/C_g} \quad (1.40)$$

The reflection coefficient measured upwave of the bars is given by $R(0)$.

The above presentation is for normally incident waves over a sinusoidal barfield on an otherwise flat bottom. Mei also provided a solution extending the theory to oblique incidence and a mild slope. The reader is directed to the original work for further details.

It will be shown in a later section that the resonant peak may be somewhat underestimated since the non-resonant interaction of severely detuned modes are neglected, and thus not added to the resonant peak. This is especially apparent when additional Fourier components are added to the bottom profile, in that only the dominant Fourier component of the bottom perturbation is considered in the resonant interaction. As will be pointed out later, second harmonic resonant peaks may become important for arbitrarily shaped bottoms.

Benjamin et al. (1987) provided a similar solution to the resonant case but instead of using a detuning variable, allowed the wavenumber and angular frequency of the incident wave to be defined as physical parameters. The cutoff frequency feature does appear as in Mei's solution. The solution is arrived at using a conformal mapping procedure. The interested reader is encouraged to consult the original work.

1.2.2 Depth-Integrated Equation for Small Undulations on Mild Slopes

Kirby (1986) derived a depth-integrated mild slope equation for waves propagating over an arbitrarily shaped bed restricted to small amplitude. The equation in its homogeneous form is Berkhoff's (1972) equation for waves propagating over a mildly varying slope. The equation is solved in Chapter 3 using a finite difference scheme once the appropriate boundary conditions have been established.

Berkhoff's equation is stated

$$\nabla \cdot (CC_g \nabla \eta) + k^2 CC_g \eta = 0 \quad (1.41)$$

where

$$C = \frac{\omega}{k} \quad (1.42)$$

$$C_g = \frac{\partial \omega}{\partial k} = \frac{\omega}{2k} \left(1 + \frac{2kh}{\sinh 2kh} \right) \quad (1.43)$$

The depth-integrated equation applies to waves propagating over small amplitude bed undulations superimposed on a mild slope. The smallness of the rapid variation allows the bottom boundary conditions to be expanded about the slowly-varying mean depth. Using the Green's formula approach of Smith and Sprinks (1975), let $h'(x, y)$ denote the total still water depth where

$$h'(x, y) = h(x, y) - \delta(x, y) \quad (1.44)$$

and $h(x, y)$ is a slowly varying depth satisfying the mild slope condition

$$\frac{\nabla_h h}{kh} \ll 1, \quad (1.45)$$

where

$$\nabla_h = \left[\frac{\partial}{\partial x}, \frac{\partial}{\partial y} \right] \quad (1.46)$$

and $\delta(x, y)$ satisfies a small amplitude condition. Figure 1.1 illustrates the individual depth components.

The problem is considered linear in wave amplitude but the first-order terms in bed-undulation amplitude are retained, where

$$O\left(\frac{\nabla_h h}{kh}\right) \approx O(k\delta) \ll 1 \quad (1.47)$$

Linearizing the free-surface boundary conditions and expanding the bottom boundary condition about $z = -h$, yields to $O(k\delta)$

$$\nabla_h^2 \phi + \phi_{zz} = 0 \quad \text{on} \quad -h \leq z \leq 0 \quad (1.48)$$

$$\phi_{tt} + g\phi_z = 0 \quad \text{on} \quad z = 0 \quad (1.49)$$

$$\phi_z = -\nabla_h h \cdot \nabla_h \phi + \nabla_h \cdot (\delta \nabla_h \phi) \quad \text{on} \quad z = -h \quad (1.50)$$

Equation 1.50 has been given by Mei(1985) and separately by Davies and Heathershaw (1984). To leading order ($\delta \rightarrow 0$), the solution to 1.48, 1.49 and 1.50 is

$$\phi(x, z, t) = f(x, z)\tilde{\phi}(x, t) + \sum \text{non-propagating modes} + O(k\delta) \quad (1.51)$$

where $f = \cosh k(h + z)/\cosh kh$ is a slowly varying function of x and y , and where

$$\omega^2 = gk \tanh kh \quad (1.52)$$

locally, with ω being the fixed angular frequency and k the wavenumber. Using Green's second identity to extract the propagating component of ϕ

$$\int_{-h}^0 f \phi_{xx} dz - \int_{-h}^0 \phi f_{xx} dz = [f \phi_x - \phi f_x]_{-h}^0 \quad (1.53)$$

Manipulating the integrals and neglecting terms of second order in $k\delta$ yields

$$\tilde{\phi}_{tt} - \nabla_h \cdot (CC_g \nabla_h \tilde{\phi}) + (\omega^2 - k^2 CC_g) \tilde{\phi} + \frac{g}{\cosh^2 kh} \nabla_h \cdot (\delta \nabla_h \tilde{\phi}) = O(k\delta)^2 \quad (1.54)$$

Here $\tilde{\phi}$ is the velocity potential in the plane of the free surface, $C = \omega/k$, and $C_g = \partial\omega/\partial k$. Also note, neglecting the δ terms yields Berkhoff's equation for the slowly varying bottom alone.

In the absence of currents, $\tilde{\phi}$ is simply related to surface displacement η through a constant of proportionality, thus η is substituted in place of $\tilde{\phi}$. In the monochromatic wave case, the spatial surface displacement $\tilde{\eta}$ can be described as

$$\eta(x, y, t) = \tilde{\eta}(x, y) e^{-i\omega t} \quad (1.55)$$

Substituting η for $\tilde{\phi}$ in equation 1.54, in reduced form is given by

$$\nabla \cdot (CC_g \nabla \tilde{\eta}) + k^2 CC_g \tilde{\eta} - \frac{g}{\cosh^2 kh} \nabla \cdot (\delta \nabla \tilde{\eta}) = 0. \quad (1.56)$$

1.3 Indirect Solution of Surface Elevation

Davies et al. (1989) solved the shallow water wave equation by making the substitution

$$\eta = f^{-1/2} W \quad (1.57)$$

where

$$f = g(h - \delta) \quad (1.58)$$

and where f is the shallow water limit of

$$f = CC_g - \frac{g\delta(x)}{\cosh^2 kh} \quad (1.59)$$

and rearranging the equation into a solvable Mathieu equation form. The principal assumption made is that the solution is valid only for long waves over an undulating bed. As pointed out in a discussion by Kirby (1989), when the mild slope equation is restated using the above transform, and is solved for the case of $2k/\lambda \neq 1$ the non-resonant solution of Davies (1982) is recovered. Additionally, solving the case of $2k/\lambda = 1$, Mei's resonant solution is recovered.

The advantage of using the substitution above is that it allows for a solution at the shoreline with no restrictions on η or its derivatives. A more complete formulation of the equation and a numerical solution to it will be presented in a later chapter.

CHAPTER 2 EXTENSION OF NON-RESONANT INTERACTION THEORY

2.1 Introduction

Non-resonant interaction theories are extended to allow waves incident at oblique angles over a one-dimensional topography. Then a bottom with regularly spaced bumps is decomposed into individual Fourier components, the contribution to reflection is calculated and the reflection coefficient calculated as the sum of the contributions.

2.2 Governing Equation

The solution given by Davies and Heathershaw results from a perturbation expansion to second order of the components of the wave field propagating over a sinusoidal bottom of finite length. The major assumption made is that all reflection takes place at $O(\epsilon)$, or the wave is weakly reflected. Thus the leading order component incident on the ripple patch propagates over it unabated. As recognized previously, this assumption violates energy conservation in the domain if any reflection were to take place. To account for this, Davies and Heathershaw artificially impose a linear attenuation on the $+x$ propagating wave, then adjust the solution to match the requirements of energy conservation. Two additional drawbacks to this solution are its inability to adequately handle the Bragg resonant case of strong reflection in the area where $O(1)$ reflection occurs, and in its original form, the inability to solve the problem allowing waves incident at oblique angles.

Miles (1981) solved the same problem for an arbitrary bottom and oblique incidence. The solution method employed involved assuming a form of the incident, reflected and transmitted wave fields and applying them to the problem. The solution method is very similar to the one explained below. It should be noted here, however, that all three solutions,

(Miles, Davies and Heathershaw, and the present work) are in agreement in the final result.

Begin with the governing equation developed in Kirby (1986),

$$\nabla \cdot [CC_g \nabla \phi] + k^2 CC_g \phi = \frac{g}{\cosh^2 kh} \nabla \cdot (\delta \nabla \phi) \quad (2.1)$$

where C and C_g are wave celerity and group velocity, and k is the wavenumber derived from the local value of the slowly varying depth h . The total depth is given by

$$h'(x, y) = h(x, y) - \delta(x, y) \quad (2.2)$$

where $\delta(x, y)$ is the rapid bed undulation. Consider the case of undulations placed on an otherwise constant depth h ; let

$$\alpha = g / \cosh^2 kh = \text{constant}, \quad (2.3)$$

then C, C_g, k are all constants as well. This allows 2.1 to be simplified to the equation

$$\nabla^2 \phi + k^2 \phi = \frac{\alpha}{CC_g} \nabla (\delta \nabla \phi) \quad (2.4)$$

Simplifying further, let

$$\alpha' = \frac{\alpha}{CC_g} = \frac{4k}{2kh + \sinh 2kh} \quad (2.5)$$

Then, equation 2.4 may be rewritten as

$$\nabla^2 \phi + k^2 \phi = \alpha' \nabla (\delta \nabla \phi) \quad (2.6)$$

2.3 Two Dimensional Wave Field

The problem will be extended to solve for wave propagation over a one dimensional topography. Requiring δ to be a function of x only, equation 2.6 becomes

$$\nabla^2 \phi + k^2 \phi = \alpha' \delta_x \phi_x + \alpha' \delta \nabla^2 \phi \quad (2.7)$$

Assume the form of the general solution of ϕ to be

$$\phi(x, y) = \tilde{\phi}(x) e^{im_y y} \quad (2.8)$$

where

$$m = k \sin \theta \quad (2.9)$$

is a constant following Snell's law. Then

$$k^2 - m^2 = k^2(1 - \sin^2 \theta) = k^2 \cos^2 \theta = l^2 \quad (2.10)$$

Equation 2.7 now becomes

$$\tilde{\phi}_{zz} + l^2 \tilde{\phi} = \alpha' \delta_z \tilde{\phi}_z + \alpha' \delta \tilde{\phi}_{zz} - m^2 \alpha' \delta \tilde{\phi} \quad (2.11)$$

Allowing $\delta(x) \rightarrow 0$ for a physically flat bottom, the solution would be given by

$$\tilde{\phi} = A e^{ilz} + B e^{-ilz} \quad (2.12)$$

A and B will be allowed to have complex values to allow for relative phase shifts for the most general solution.

Now, developing the boundary conditions at the ends of the domain for the case of a device causing reflection but still allowing some transmission at the shoreward limit yields

$$\tilde{\phi}(x \rightarrow -\infty) = e^{ilz} + R e^{-ilz} \quad (2.13)$$

where the incident amplitude is taken to be 1 and R is the amplitude of the reflected wave. The reflection coefficient is then given by $|R|$. Likewise, with T being the transmitted amplitude, the boundary condition is

$$\tilde{\phi}(x \rightarrow \infty) = T e^{ilz} \quad (2.14)$$

Strictly, conservation of energy requires

$$|R|^2 + |T|^2 = 1 \quad (2.15)$$

if no energy attenuation occurs in the domain and the mean depth doesn't change.

For an arbitrary but finite bottom undulation in (x) , assuming $\alpha' \delta \sim (D/h)$ is small, or $|\alpha' \delta| \ll 1$, where D is the amplitude of the undulation, let

$$\epsilon(\alpha' \delta)^* = (\alpha' \delta) \quad (2.16)$$

and expand in powers of ϵ

$$\bar{\phi} = \phi_0 + \epsilon\phi_1 + \epsilon^2\phi_2 + \dots \quad (2.17)$$

$$R = R_0 + \epsilon R_1 + \epsilon^2 R_2 + \dots \quad (2.18)$$

$$T = T_0 + \epsilon T_1 + \epsilon^2 T_2 + \dots \quad (2.19)$$

Collecting first order terms gives

$$\phi_{0,zz} + l^2\phi_0 = 0 \quad (2.20)$$

Assuming reflection is of $O(\epsilon)$ at leading order, the solution of 2.20 is given by

$$\phi_0 = e^{ilz}, \quad R_0 = 0, \quad T_0 = 1 \quad (2.21)$$

Collecting $O(\epsilon)$ terms,

$$\phi_{1,zz} + l^2\phi_1 = \alpha'\delta_z\phi_{0,z} + \alpha'\delta\phi_{0,zz} - m^2\alpha'\delta\phi_0 \quad (2.22)$$

Substituting 2.21 into 2.22 and rearranging gives

$$\phi_{1,zz} + l^2\phi_1 = [il\alpha'\delta_z - \alpha'\delta(m^2 + l^2)] e^{ilz} \quad (2.23)$$

where $(m^2 + l^2) = k^2$. The general form of the solution is

$$\phi_1 = c_1 e^{ilz} + c_2 e^{-ilz} + \phi_{1p} \quad (2.24)$$

where ϕ_{1p} is the particular solution.

To solve the non-homogenous part, let

$$q(x) = [il\alpha'\delta_z - \alpha'\delta(m^2 + l^2)] e^{ilz} \quad (2.25)$$

The particular solution is obtained by variation of parameters, and is given by

$$\phi_1 = e^{ilz} \left[c_1 - \frac{i}{2l} \int_{-\infty}^z q(\xi) e^{-il\xi} d\xi \right] + e^{-ilz} \left[c_2 + \frac{i}{2l} \int_{-\infty}^z q(\xi) e^{il\xi} d\xi \right] \quad (2.26)$$

where ξ is a dummy variable of integration. From the expansion at the offshore limit,

$x \rightarrow -\infty$

$$\phi_0 + \epsilon\phi_1 + \dots = e^{ilz} + R_0 e^{-ilz} + \epsilon R_1 e^{-ilz} + O(\epsilon^2) \quad (2.27)$$

the homogeneous solution of the second order terms gives

$$c_1 = 0 \quad c_2 = R_1 \quad (2.28)$$

At the nearshore limit, $x \rightarrow \infty$,

$$\phi_0 + \epsilon \phi_1 + \dots = T_0 e^{ilx} + \epsilon T_1 e^{ilx} \quad (2.29)$$

so

$$\phi_1 = T_1 e^{ilx}; \quad x = \infty \quad (2.30)$$

From equation 2.25 and the two solutions for ϕ_1 above, the reflection and transmission at $O(\epsilon)$ are given by

$$R_1 = \frac{-i}{2l} \int_{-\infty}^{\infty} q(x) e^{ilx} dx \quad (2.31)$$

$$T_1 = -\frac{i}{2l} \int_{-\infty}^{\infty} q(x) e^{-ilx} dx \quad (2.32)$$

Evaluating the expression 2.30 for R_1 yields

$$R_1 = \frac{-i\alpha'}{2l} (l^2 - m^2) \int_{-\infty}^{\infty} \delta(x) e^{2ilx} dx \quad (2.33)$$

Equation 2.32 is an expression for the weak, or non-resonant, reflection of a wave of wavenumber k over an arbitrary bottom at any angle of incidence. In its current form, it provides the same results as determined by Miles (1981), and restricted to normal incidence and a sinusoidal bottom would be identical to the result of Davies and Heathershaw (1984).

2.4 Solution for Periodic Bars

For the case of a sinusoidal perturbation (as assumed by Davies and Heathershaw)

$$\delta(x) = D \sin 2\pi x/L \quad (2.34)$$

where L is the spacing between crests and $\lambda = 2\pi/L$, it can be seen that the solution of the non-resonant case by Davies and Heathershaw will be recovered in the case of normal incidence.

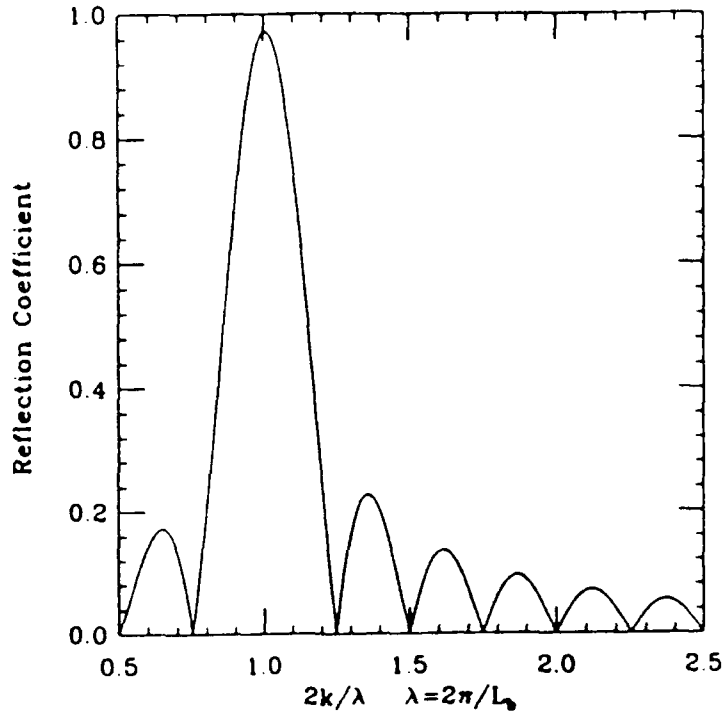


Figure 2.1: Reflection of single mode bottom

$$|R| = \frac{2kD}{\sinh 2kh + 2kh} \left(1 - \frac{m^2}{l^2}\right) \frac{2l}{\lambda} \left| \frac{\sin \frac{2l}{\lambda} N_b \pi}{\left(\frac{2l}{\lambda}\right)^2 - 1} \right| \quad (2.35)$$

where $l = k$. The result for this case is plotted in Figure 2.1. The solution at resonance $2l = \lambda$ is given by

$$|R| = \frac{-i\alpha'}{2l} (l^2 - m^2) \cdot \frac{N_b \pi}{2} \quad (2.36)$$

For the plotted case, the bottom configuration is

$$\delta(x) = 0.05m \sin 2\pi x / 1.0m \quad (2.37)$$

2.5 Fourier Decomposition of the Bottom

Exploring now the case where $\delta(x)$ is a field of discrete cosine shaped bumps with arbitrary, but even spacing, such that

$$h(x) = \begin{cases} D \sin(2\pi(x - b_L/2)/b_L) & ; (nL/2 - b_L/2) \leq x \leq nL/2 + b_L/2 \\ 0.0 & ; \text{otherwise} \end{cases} \quad (2.38)$$

$$n = 0, 1, 2, 3$$

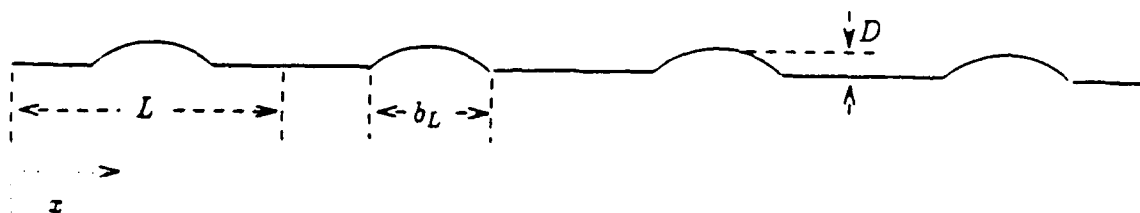


Figure 2.2: Definition sketch of four cosine bumps on a flat bottom

where L is the spacing between crests and b_L is the length of a single undulation, it can be seen that the field may be described by a Fourier series expansion,

$$\delta(x) = \sum_{n=0}^{\infty} D_n \cos \frac{2n\pi x}{L} \quad (2.39)$$

The Fourier coefficients for the case of four cosine bumps shown in Figure 2.2 on a flat bottom are given by

$$D_0 = \frac{D}{\pi} \quad (2.40)$$

$$D_1 = \frac{-D}{2} \quad (2.41)$$

$$D_n = D \frac{\cos \frac{n\pi}{2}}{\pi(1-n^2)} (1 + \cos n\pi) \quad (2.42)$$

The cosine transform is used in this case since it is even about the starting point of the domain.

R_1 becomes

$$R_1 = \frac{-i\alpha'}{2l} (l^2 - m^2) \int_0^{N_b L} \left[\sum_{n=0}^{\infty} D_n \cos \frac{2n\pi x}{L} \right] e^{2ilx} dx \quad (2.43)$$

where N_b is the number of bars in the field. For purposes of creating the most effective design, it would be helpful to determine the relative contribution of each Fourier component

to the reflection assuming a constant wave field, that is

$$\frac{-i}{2l} \alpha' (l^2 - m^2) = \text{constant} \quad (2.44)$$

Combining this constant with D_n , let

$$a_n = D_n \frac{-i}{2l} \alpha' (l^2 - m^2) \quad (2.45)$$

2.39 reduces to

$$R_1 = \sum_{n=0}^{\infty} a_n \int_0^{N_b L} \cos \frac{2n\pi x}{L} e^{2ilz} dx \quad (2.46)$$

Letting

$$\frac{2\pi}{L} = \lambda \quad (2.47)$$

the integral part of the solution may be expressed by

$$I = \int_0^{N_b L} (\cos n\lambda x) e^{2ilz} dx \quad (2.48)$$

Expressing the cosine term in its exponential form, I becomes

$$I = \frac{1}{2} \int_0^{N_b L} (e^{i(2l+n\lambda)x} + e^{i(2l-n\lambda)x}) dx \quad (2.49)$$

2.5.1 The Resonant Case

In the special case of

$$2l = n\lambda \quad (2.50)$$

it can be seen

$$e^{i(2l-n\lambda)x} = 1 \quad (2.51)$$

so I becomes

$$I = \frac{-i}{2l + n\lambda} [e^{i(2l+n\lambda)N_b L} - 1] + \frac{N_b L}{2} \quad (2.52)$$

Since

$$\frac{2l}{\lambda} = n \quad (2.53)$$

I can be simplified to

$$I = \frac{-i}{4l} [e^{i4n\lambda N_b \frac{2x}{\lambda}} - 1] + \frac{N_b L}{2} \quad (2.54)$$

By factoring $e^{i2\pi n N_b}$ out of the bracketed term, thereby forcing it into a sine form with an argument of $2\pi n N_b$, where $n N_b$ are integer, it can easily be shown that the final form for the case of $2l = n\lambda$ is

$$I = \frac{N_b L}{2} = \frac{N_b \pi}{\lambda} \quad (2.55)$$

2.5.2 The Non-Resonant Case

In the case where the z component of the wave is away from resonance or

$$2l - n\lambda \neq 0 \quad (2.56)$$

I will change considerably. The integral portion is stated

$$I = \frac{1}{2i\lambda} \left[\frac{e^{inN_b 2\pi} e^{i(\frac{2l}{\lambda})2\pi N_b} - 1}{2l + n\lambda} - \frac{e^{-inN_b 2\pi} e^{i(\frac{2l}{\lambda})2\pi N_b} - 1}{2l - n\lambda} \right] \quad (2.57)$$

Letting

$$\gamma = \frac{2l}{\lambda} \quad (2.58)$$

2.58 becomes

$$I = \frac{-2\gamma}{\lambda(n^2 - \gamma^2)} e^{i\pi\gamma N_b} \left[\frac{(e^{i\pi\gamma N_b} - e^{-i\pi\gamma N_b})}{2i} \right] \quad (2.59)$$

Applying trigonometric identities and rearranging, gives

$$I = \frac{\gamma^2}{l(\gamma^2 - n^2)} e^{i\pi N_b L} \sin l N_b L \quad (2.60)$$

2.5.3 Full Solution

For a bottom with the positive branch of a cosine curve imposed on a flat bottom, the reflection coefficient for a given wavenumber component of the wave field, R , would be calculated by summing the effect of all non-resonant Fourier components of the bottom plus the effect of the resonant component. The full solution is given by

$$R = \sum_{n \neq \frac{2l}{\lambda}}^{\infty} a_n \frac{1}{l(\gamma^2 - n^2)} e^{i\pi N_b L} \sin l N_b L + a_n \frac{N_b \pi}{\lambda} \Big|_{n=\frac{2l}{\lambda}} \quad (2.61)$$

where n is the n^{th} Fourier component of the bottom perturbation, λ is $2\pi/L$ with L being the bar spacing, N_b is the number of bars in the field, and $l = k \cos \theta$.

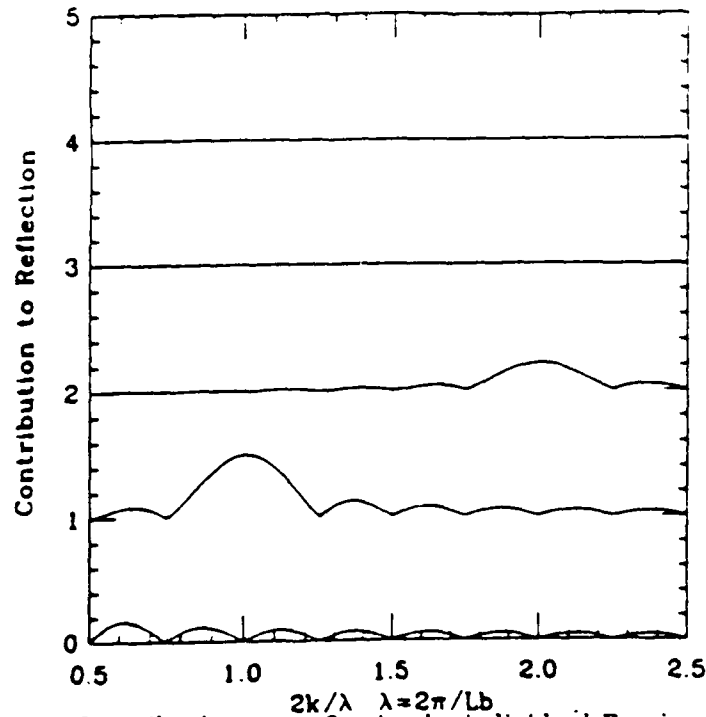


Figure 2.3: Contributions to reflection by individual Fourier components

Plots of the contributions to the reflection of the first five modes of the barfield are shown in Figure 2.3. The abscissa is marked for the mode, with the space between them allowed for the reflection coefficient plot. The ordinate is referenced to the surface wavenumber over the wavenumber of the fundamental mode of the barfield. Additionally, the total reflection coefficient for a normally incident wave, $\theta = 0$, is shown in Figure 2.4. The ordinate units again are $2k/\lambda$, where k is the surface wavenumber, and λ is the wavenumber of the bar spacing, or $\lambda = 2\pi/L$. This unit designation will be irrelevant for mixed spaced bars, thus the ordinate units would be changed to period, T , or some equally pertinent parameter.

The calculation of the reflective characteristics of a given bottom perturbation in this manner allows the prediction of which components of the bottom may be most strongly reflective for a particular wave frequency. However, the true power of this technique is that it would easily lend itself to customizing a barfield to be more strongly reflective of certain frequencies, simply by building the Fourier series of the bottom that would best reflect the more undesirable frequencies. While the maximum reflection for a particular frequency occurs when one of the primary components in the bottom has wavelength twice that of the

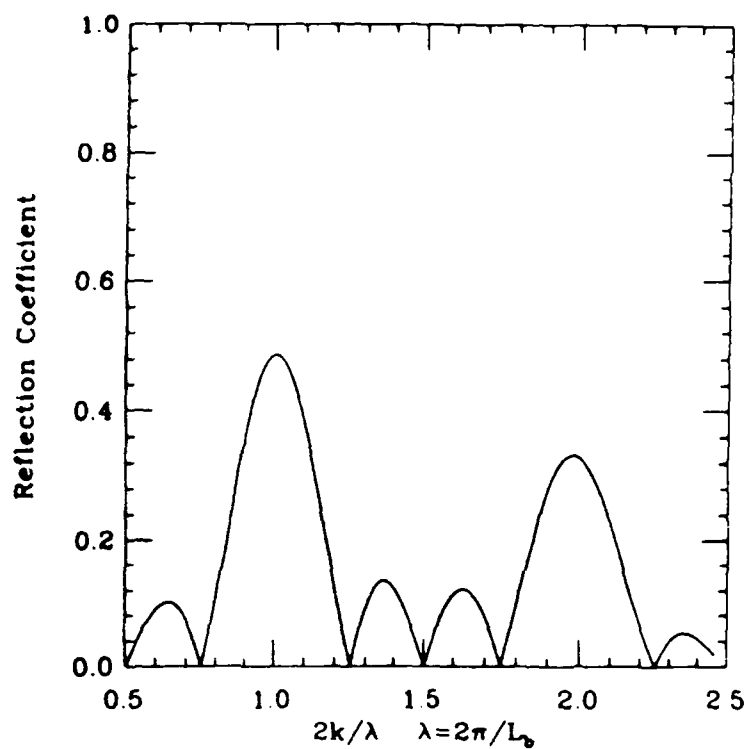


Figure 2.4: Sum total of the reflection from individual components

surface wavelength, it should be noted as additional components are emphasized the peak reflection of other de-emphasised components are reduced.

CHAPTER 3 COMPARISON OF SOLUTIONS

3.1 Introduction

The development of a finite difference scheme to solve the mild slope equation (Kirby 1986) will be presented. The numerical results will then be compared to the analytic solutions of Mei (1985) and the extension to the non-resonant interaction solution.

3.2 Derivation of a Complete Governing Equation

Kirby (1986) developed an extension to the mild slope equation of Berkhoff (1972) for shoaling waves to allow rapid, small-amplitude variations in depth. This equation was presented in Chapter 1. This equation is again stated

$$\nabla \cdot (CC_g \nabla \bar{\eta}) + k^2 CC_g \bar{\eta} - \frac{g}{\cosh kh^2} \nabla \cdot (\delta \nabla \bar{\eta}) = 0. \quad (3.1)$$

The undulating bottom on a mild slope is described by

$$h'(x, y) = h(x, y) - \delta(x, y) \quad (3.2)$$

where $h(x, y)$ is the slowly varying component, and $\delta(x, y)$ describes the undulations. Restricting the model topography of equation 3.2 to one dimension in the x direction, equation 3.1 is reduced to

$$CC_g(\nabla^2 \bar{\eta} + k^2 \bar{\eta}) + (CC_g)_x \bar{\eta}_x - \frac{g\delta}{\cosh^2 kh} \nabla^2 \bar{\eta} - \frac{g}{\cosh^2 kh} \delta_x \bar{\eta}_x = 0 \quad (3.3)$$

Allow the two dimensional surface $\bar{\eta}$ to represent a wave of arbitrary amplitude and frequency which will refract over the slowly varying topography $h(x)$ according to Snell's law of refraction. For a given wave of frequency ω incident at angle θ_0 in deep water, Snell's law is

$$k \sin \theta = k_0 \sin \theta_0 \quad (3.4)$$

where

$$k_0 = \frac{\omega^2}{g} \quad (3.5)$$

Split the local wavenumber into x and y components

$$l = k \cos \theta \quad (3.6)$$

$$m = k \sin \theta = k_0 \sin \theta_0 \quad (3.7)$$

and

$$k^2 = l^2 + m^2 \quad (3.8)$$

Since $m \leq k_0$ from equation 3.7, $\bar{\eta}$ may be expressed as

$$\bar{\eta} = \int_{-k_0}^{k_0} \hat{\eta}(x, m) e^{im y} dm \quad (3.9)$$

Substituting 3.9 into 3.3 then yields a second-order ODE for $\hat{\eta}(m)$

$$(CC_g \hat{\eta}_x)_x - \frac{g}{\cosh^2 kh} (\delta \hat{\eta}_x)_x + [l^2 CC_g + \frac{gm^2 \delta}{\cosh^2 kh}] \hat{\eta} = 0 \quad (3.10)$$

Equation 3.10 is a well posed problem for the reflection of waves incident at any angle after specifying boundary conditions. Formally, the problem is posed on the interval $-\infty \leq x \leq 0$, where $x = 0$ is the shoreline and $x = -\infty$ is deep water. The solution over this interval is, however, unwieldy. A simplification at the limits of integration is attained assuming the incident wave condition at some finite distance offshore, x_1 , is known, and neglecting the region of the surfzone, establish a second station, x_2 , between the topography in question and the surfzone. The energy propagating past x_2 is assumed to be fully dissipated in breaking. Equation 3.10 is solved only in the domain $x_1 \leq x \leq x_2$ with boundary conditions known at x_1 and x_2 ; thus the reflection from shoreline conditions will not be included.

The boundary condition at the shoreward station, x_2 , is assumed to be a wave propagating out of the solution domain in the $+x$ direction

$$\hat{\eta}_x = il(x) \hat{\eta} \quad ; \quad x = x_2 \quad (3.11)$$

At the seaward station, x_1 , the boundary condition $\hat{\eta}_z$ is assumed to be a superposition of an incident wave $\hat{\eta}_i$ propagating in the $+x$ direction from deep water, and a reflected wave $\hat{\eta}_r$ propagating in the $-x$ direction out of the solution domain. The incident wave $\hat{\eta}_i$ is assumed to be known, and the reflected wave $\hat{\eta}_r$ must satisfy a radiation condition for propagation out of the domain

$$\hat{\eta}_{rz} = -il(x)\hat{\eta}_r \quad ; \quad x = x_1 \quad (3.12)$$

Noting that

$$\hat{\eta}_r = \hat{\eta} - \hat{\eta}_i \quad (3.13)$$

and substituting into 3.12, the condition at x_1 is thus described.

$$\hat{\eta}_z = il(2\hat{\eta}_i - \hat{\eta}) \quad ; \quad x = x_1 \quad (3.14)$$

The problem to be solved is fully specified by equation 3.10 and the boundary conditions 3.11 and 3.14.

3.3 Numerical Approximations

Proceeding further from Kirby (1987), the problem specified in the previous section may be solved using a finite-difference scheme. The superscript will be dropped here and the notations

$$p = CC_g \quad (3.15)$$

$$\gamma = \frac{g}{\cosh^2 kh} \quad (3.16)$$

are defined. The domain $x_1 \leq x \leq x_2$ is discretized according to

$$x^i = x_1 + (i+1)\Delta x \quad ; \quad 1 \leq i \leq n \quad (3.17)$$

where

$$\Delta x = \frac{x_2 - x_1}{n-1} \quad (3.18)$$

All other coefficients and the variable η are affected by local conditions in the grid and are defined in discrete form at the grid locations x^i . From this, a centered finite-difference

scheme is developed and is given by

$$\begin{aligned} & \frac{(p^{i+1} + p^i)(\eta^{i+1} - \eta^i) - (p^i + p^{i-1})(\eta^i - \eta^{i-1})}{2\Delta x^2} - \\ & \gamma^i \frac{(\delta^{i+1} + \delta^i)(\eta^{i+1} - \eta^i) - (\delta^i + \delta^{i-1})(\eta^i - \eta^{i-1})}{2\Delta x^2} + \\ & \left[(l^i)^2 p^i + m^2 \gamma^i \delta^i \right] \eta^i = 0 \end{aligned} \quad (3.19)$$

Equation 3.19 may be simplified to the form

$$A^i \eta^{i-1} + B^i \eta^i + C^i \eta^{i+1} = 0 \quad ; \quad i = 2, 3, \dots, n-1 \quad (3.20)$$

where

$$A^i = p^i + p^{i-1} - \gamma^i (\delta^i + \delta^{i-1}) \quad (3.21)$$

$$\begin{aligned} B^i = & -(p^{i+1} + 2p^i + p^{i-1}) + \gamma^i (\delta^{i+1} + 2\delta^i + \delta^{i-1}) \\ & + 2\Delta x^2 [(l^i)^2 p^i + m^2 \gamma^i \delta^i] \end{aligned} \quad (3.22)$$

$$C^i = p^{i+1} + p^i - \gamma^i (\delta^{i+1} + \delta^i) \quad (3.23)$$

In order to simplify the application of the boundary conditions, the input topography is restricted to a flat bottom at the edges of the domain;

$$h^1 = h^2 \quad (3.24)$$

$$h^{n-1} = h^n \quad (3.25)$$

The bed undulations are also subject to this restriction in order that the waves radiating at the boundary are not interacting with the rapid variations. Thus it is also required that

$$\delta^1 = \delta^2 = \delta^{n-1} = \delta^n = 0 \quad (3.26)$$

Now to express the boundary conditions in finite difference form, equation 3.11 is

$$\eta^n (1 - \alpha^n) = \eta^{n-1} (1 + \alpha^n) \quad (3.27)$$

where

$$\alpha^n = \frac{i\Delta x}{2} l^n \quad (3.28)$$

Defining 3.11 in the finite difference form,

$$B^n = 1 - \alpha^n \quad (3.29)$$

$$A^n = -(1 + \alpha^n) \quad (3.30)$$

Likewise, at station x_1 the boundary condition may be restated as

$$(1 + \alpha^1)\eta^2 - (1 - \alpha^1)\eta^1 = 2a(m)\alpha^1[e^{2\alpha^1} + 1] \quad (3.31)$$

where

$$\alpha^1 = \frac{i\Delta x}{2} l^1 \quad (3.32)$$

and it is assumed the incident wave is described by

$$\eta_i(x) = a(m)e^{i l^1(x-x_1)} \quad (3.33)$$

Again, putting 3.14 into the finite difference form gives

$$B^1 = -(1 - \alpha^1) \quad (3.34)$$

$$C^1 = 1 + \alpha^1 \quad (3.35)$$

$$D^1 = 2a(m)\alpha^1[e^{2\alpha^1} + 1] \quad (3.36)$$

The problem may be written in the form of a linear matrix equation

$$\mathbf{A}\eta = \mathbf{D} \quad (3.37)$$

where \mathbf{D} is a column vector with $D^2 - Dn = 0$, η is a column vector with elements $\eta^1 - \eta^n$, and \mathbf{A} is a tridiagonal matrix with diagonal vectors A^i , B^i and C^i . The solution is obtained using the double sweep algorithm as given by Carnahan, Luther and Wilkes (1969).

Reflection and transmission coefficients may be determined once the solution for η has been calculated. Two estimates for the reflection coefficient R are obtained at x_1 . From equation 3.31 η_r at x_1 may be written

$$\eta_r^1 = \eta^1 - a(m) \quad (3.38)$$

$$\eta_r^2 = \eta^2 - a(m)e^{2\alpha^1} \quad (3.39)$$

Define the two estimates for reflection coefficients as

$$R_1 = \frac{|\eta_r^1|}{a(m)} \quad (3.40)$$

$$R_2 = \frac{|\eta_r^2|}{a(m)} \quad (3.41)$$

and R as the average of R_1 and R_2 . Transmission coefficients at x_2 are estimated by

$$T_1 = \frac{|\eta^{n-1}|}{a(m)} \quad (3.42)$$

$$T_2 = \frac{|\eta^n|}{a(m)} \quad (3.43)$$

which are likewise averaged to obtain T . A test of the accuracy of the solution is obtained by checking the conservation of energy requirement

$$R^2 + T^2 \left(\frac{C_g^n / n k^1}{C_g^1 / l^1 k^n} \right) = 1 \quad (3.44)$$

By applying this model at a number of discrete frequencies and angles of incidence, prediction of the reflection characteristics for a frequency and dimensional spectrum may be built. The results of this full numerical solution will be used to compare against the oblique and arbitrary bottom extension of non-resonant solution, and the resonant detuning solution.

3.4 Comparison to Existing Theories

The numerical solution to the mild slope equation offers a method to calculate the reflection coefficient valid for all values of $2k/\lambda$. In this section, the numerical solution will be used to compare the existing resonant and non-resonant interaction theories.

3.4.1 One-dimensional Wave Field

The initial investigations of this topic concentrated on bottoms of sinusoidal form. Figure 3.1 is a plot of the three methods described previously, Mei's resonant interaction (Mei) presented in Chapter 1, the extension of the non-resonant interaction (Non-Res Extension), and the numerical solution of the mild-slope equation (Numeric). It can be

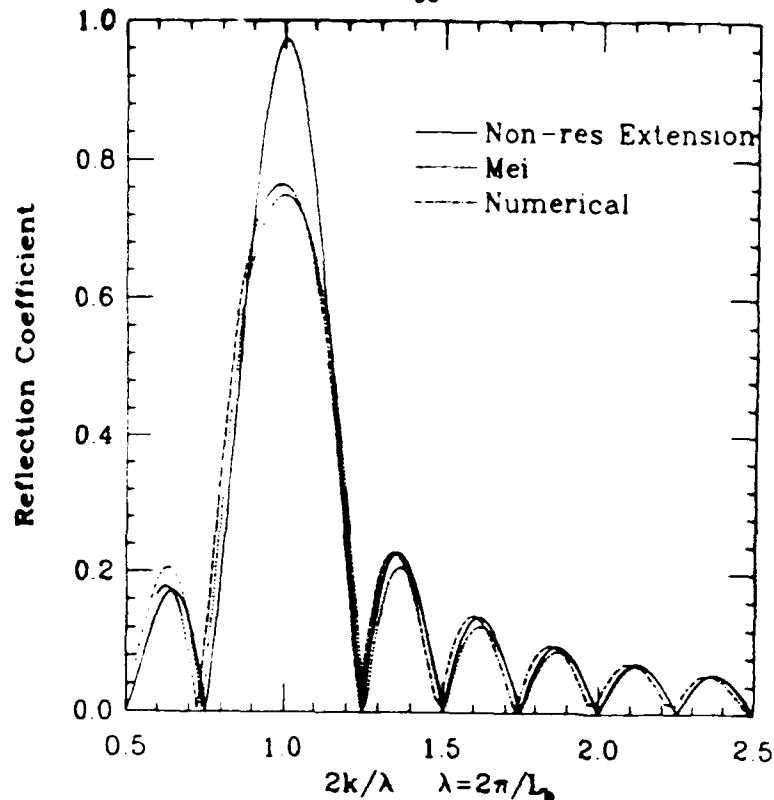


Figure 3.1: Reflection coefficient vs. $2k/\lambda$ for sinusoidal bottom. $h(x) = 0.15m$, four cycles $\delta(x) = 0.05m \sin 2\pi/1.0m$

seen from figure 3.1 that the resonant interaction agrees well with the numerical solution near the resonant peak. Conversely, the non-resonant extension solution agrees well in areas of small reflection, except for a slight shift in phase with respect to $2k/\lambda$. It is also very obvious that the non-resonant solution severely overpredicts the reflection at the resonant peak.

Now a case of discrete but evenly spaced bumps will be investigated. The bedform used in these calculations are identical to that described in chapter 2. It should be noted that while the numerical solution will calculate the reflection coefficient using a discretized bottom, the non-resonant extension and Mei's solution is a summation of the reflection coefficients from the Fourier components of the bottom. From the plot of the numerical solution and non-resonant extension in figure 3.2, it can be seen that a second peak of substantial reflection occurs due to the interaction with the second Fourier component of the bar field. The resonant peaks for the first two Fourier components were calculated inde-

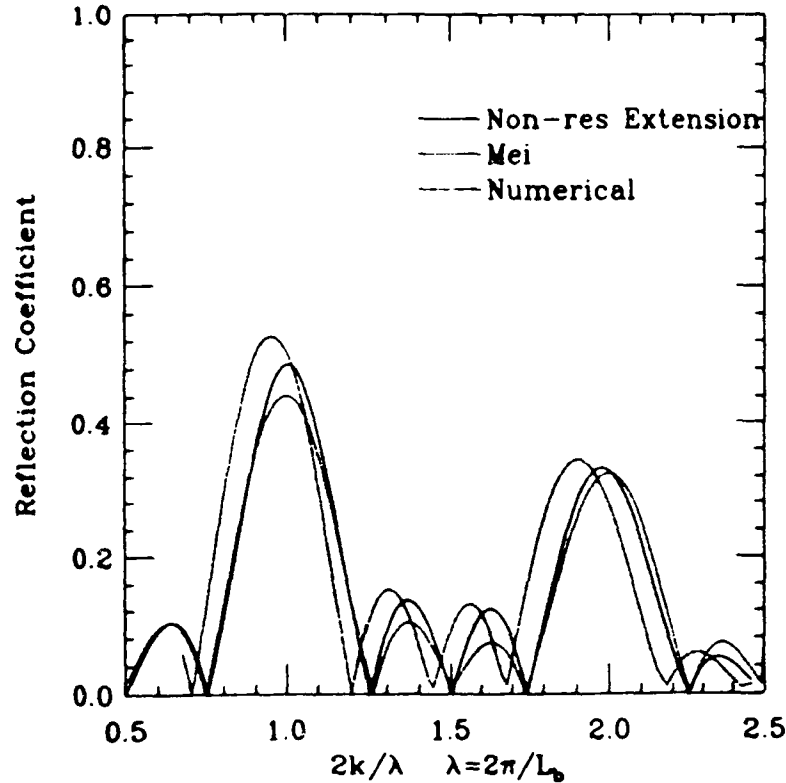


Figure 3.2: Reflection coefficient vs. $2k/\lambda$ for four cosine bumps. $h(x) = 0.15m$, $\delta(x) = 0.05m \cos 2\pi/1.0m$, $\lambda = 2\pi/L_b$

pendently assuming the theory to be valid near resonance. Agreement between all theories is poor. Surprisingly, the non-resonant theory resonant peaks show smaller reflection than the numerical solution. It is possible that first order solutions may not adequately predict the reflective characteristics of such a field.

3.4.2 Obliquely Incident Waves

Bars placed in the environment will have waves incident at all angles. The contour plots to follow are reflection coefficient solutions for various wave numbers k propagating at angles θ from normal incidence. The bottom form assumed for these plots is a shore parallel ($\delta = \delta(x)$) sinusoidal bar field. The solution for the extension of non-resonant theory for obliquely incident waves is presented in Chapter 2 and the mild slope solution is presented in previous sections of this chapter. The extension of Mei's resonant interaction theory is achieved by allowing

$$\omega^3 = \frac{g\lambda}{2 \cos \theta} \left(\tanh \frac{\lambda h}{2 \cos \theta} \right) \quad (3.45)$$

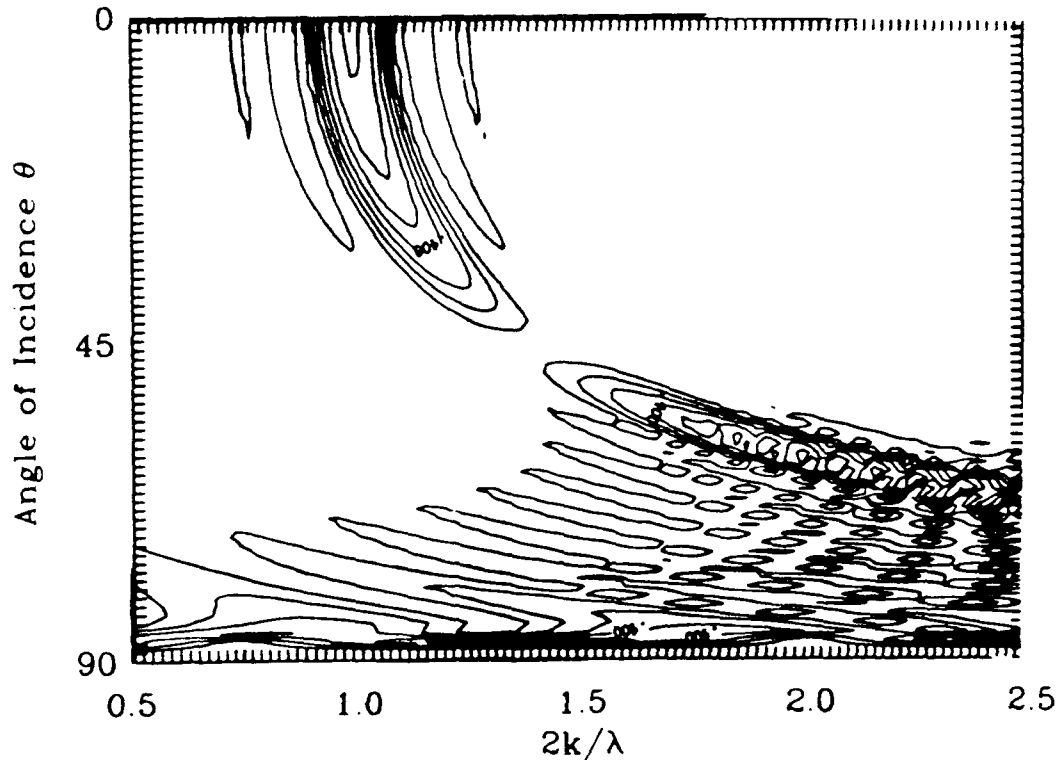


Figure 3.3: Mei's resonant interaction theory reflection coefficient vs. angle of incidence θ and offshore wavenumber k_o .

and the cutoff frequency to be defined by

$$\Omega_0 = \Omega_0 \frac{\cos 2\theta}{\cos^2 \theta} \quad (3.46)$$

It can easily be seen from these plots, as the theories indicate, that the bar field is invisible to waves incident at 45 degrees.

Figures 3.6, 3.7 and 3.8 are plots of the differences of the predicted reflection between theories. Angles of incidence range from 0° to 45° since the large values of reflection and slight phase shifts at higher angles may cause the differences to be as large as the peaks, thus the additional information would be irrelevant.

3.5 Application of the Solutions

Kirby (1987) presented model test examples for directional and frequency spectra with various bottom configurations. Of principal interest from a practical engineering standpoint,

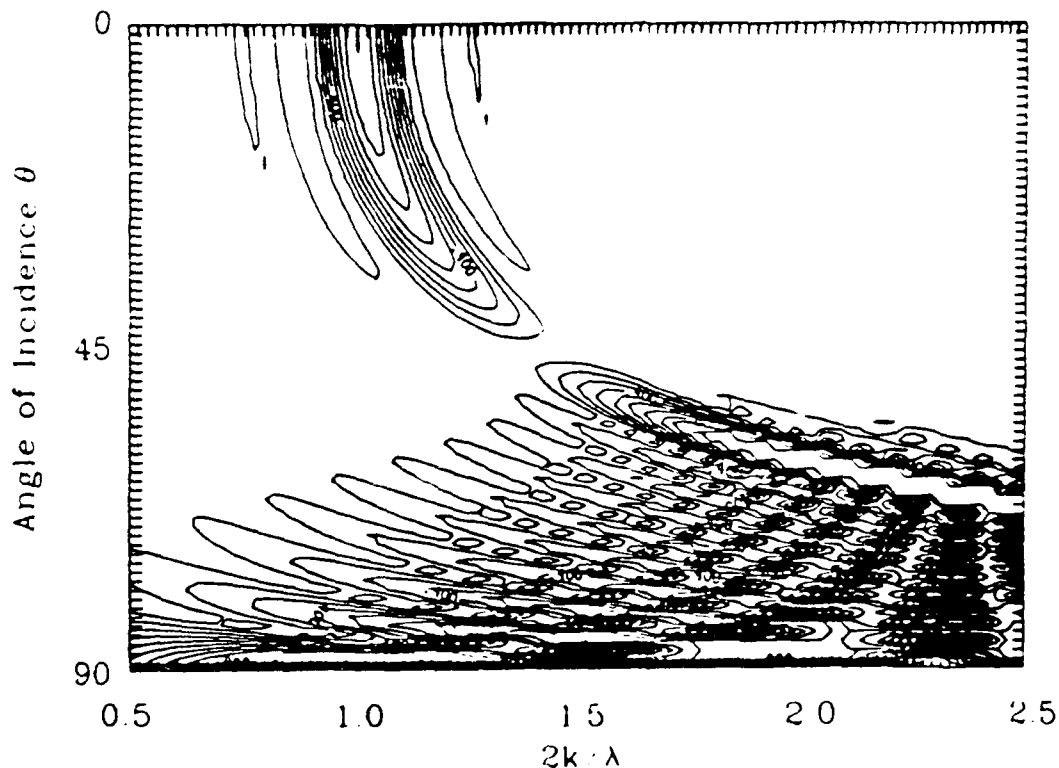


Figure 3.4: Non-Resonant Extension, reflection coefficient vs. angle of incidence θ and offshore wavenumber k_o .

are the cases of discrete artificial bars. The probable prototype design is a series of artificial bars consisting of specifically shaped bumps whose longitudinal axes are shore parallel and are laid on the bottom at predetermined spacings in the offshore direction. The process of determining the optimum spacing is defined by Kirby as tuning the barfield. The study assumes that the bed is non-movable, thus the seaward propagation of additional bars in the form of sand waves as proposed by Davies and Heathershaw (1984) and scour between the bars will not affect the reflection characteristics of the topography. In addition to the directional spectrum comparison with previous solutions to the problem, the numerical model was used to predict the reflection characteristics of a bar patch to be verified in a laboratory study using normally incident waves. The laboratory study is presented in Chapter 5.

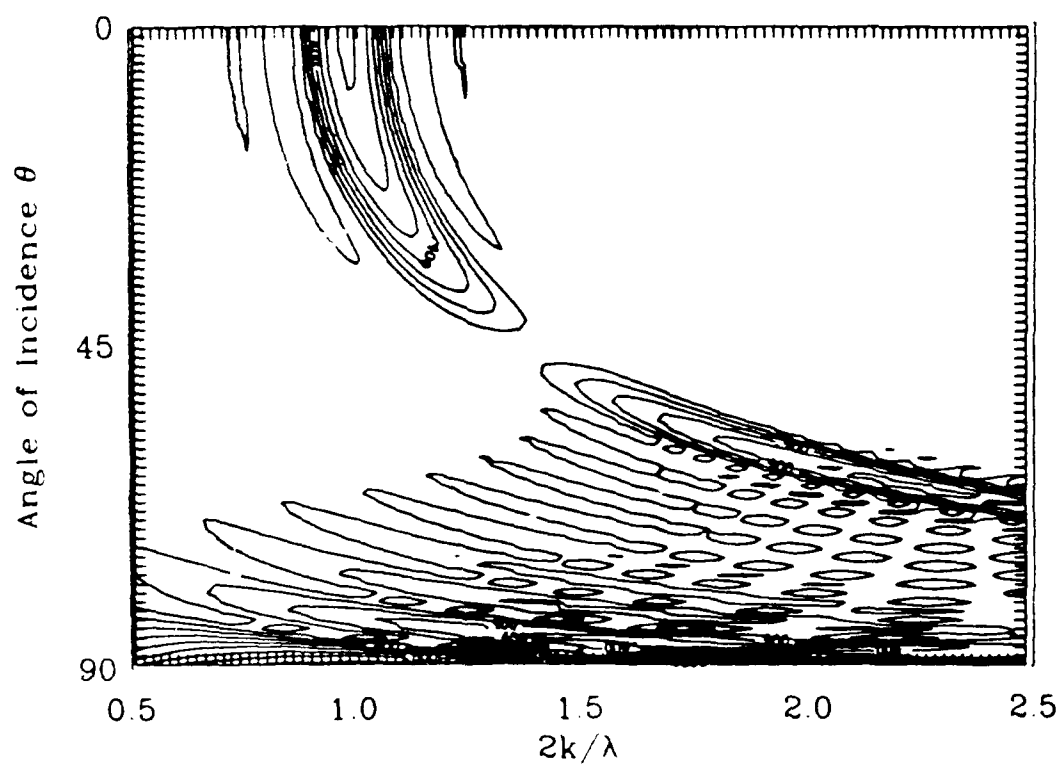


Figure 3.5: Numerical Solution, reflection coefficient vs. angle of incidence θ and offshore wavenumber k_0 .

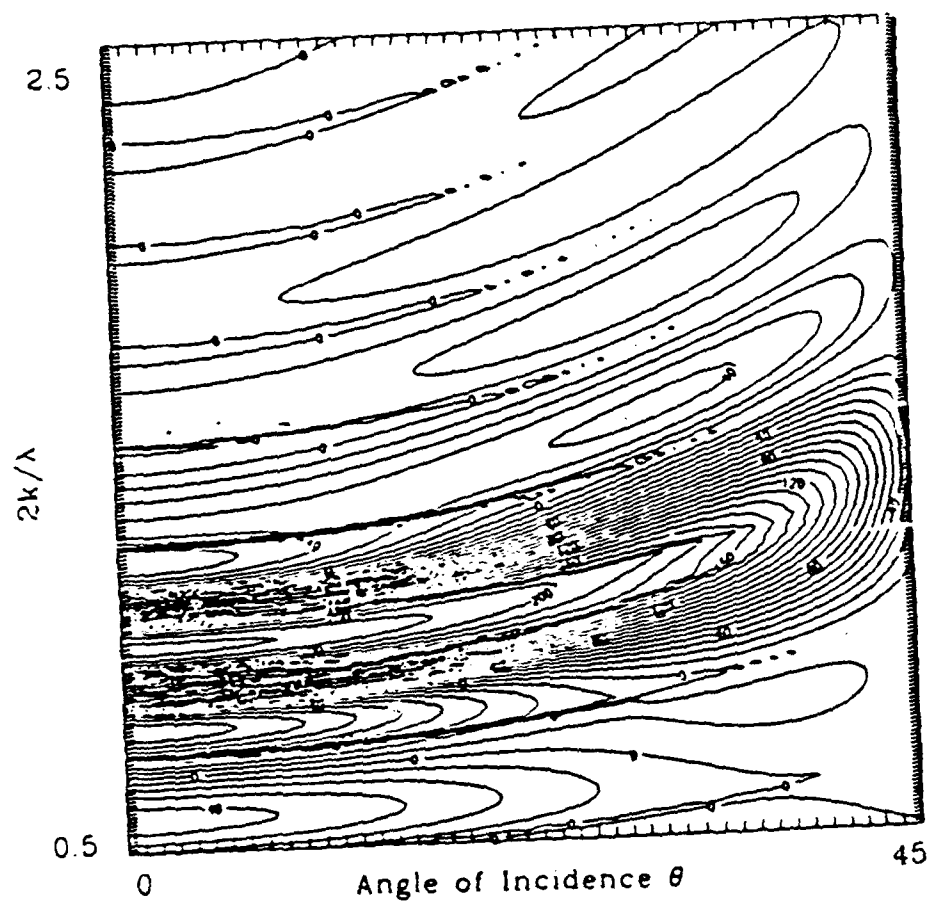


Figure 3.6: Non-Resonant Extension - Numerical Solution vs. angle of incidence θ and offshore wavenumber k_o

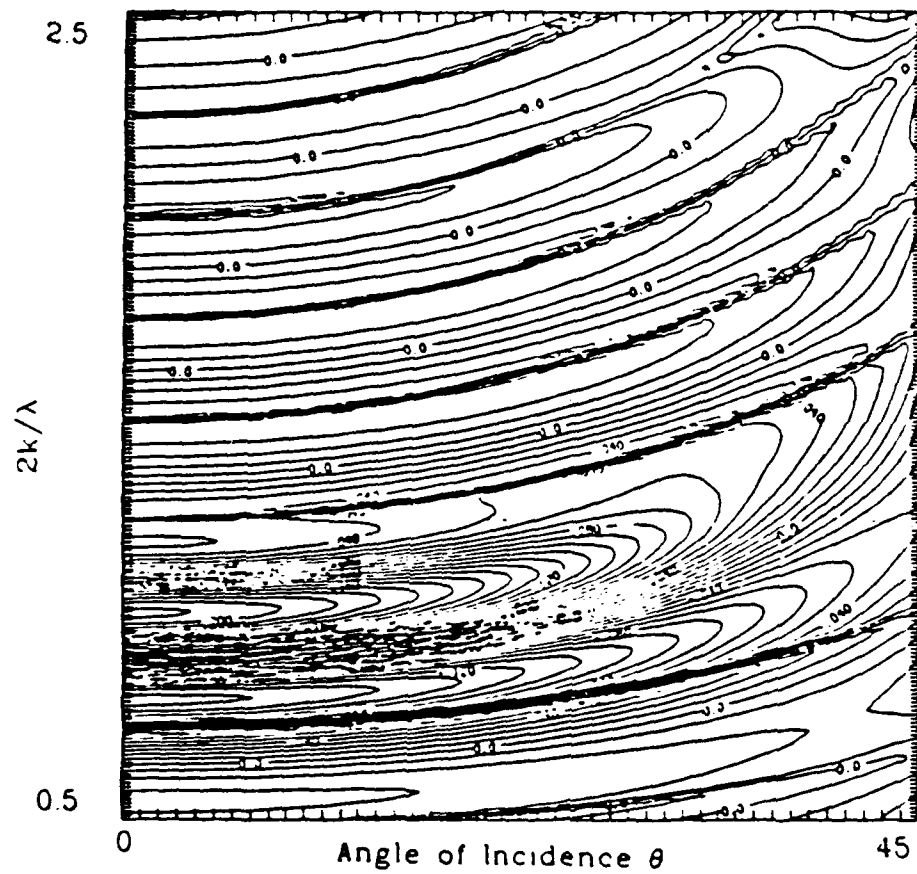


Figure 3.7: Non-Resonant Extension - Mei's Solution vs. angle of incidence θ and offshore wavenumber k_0 .

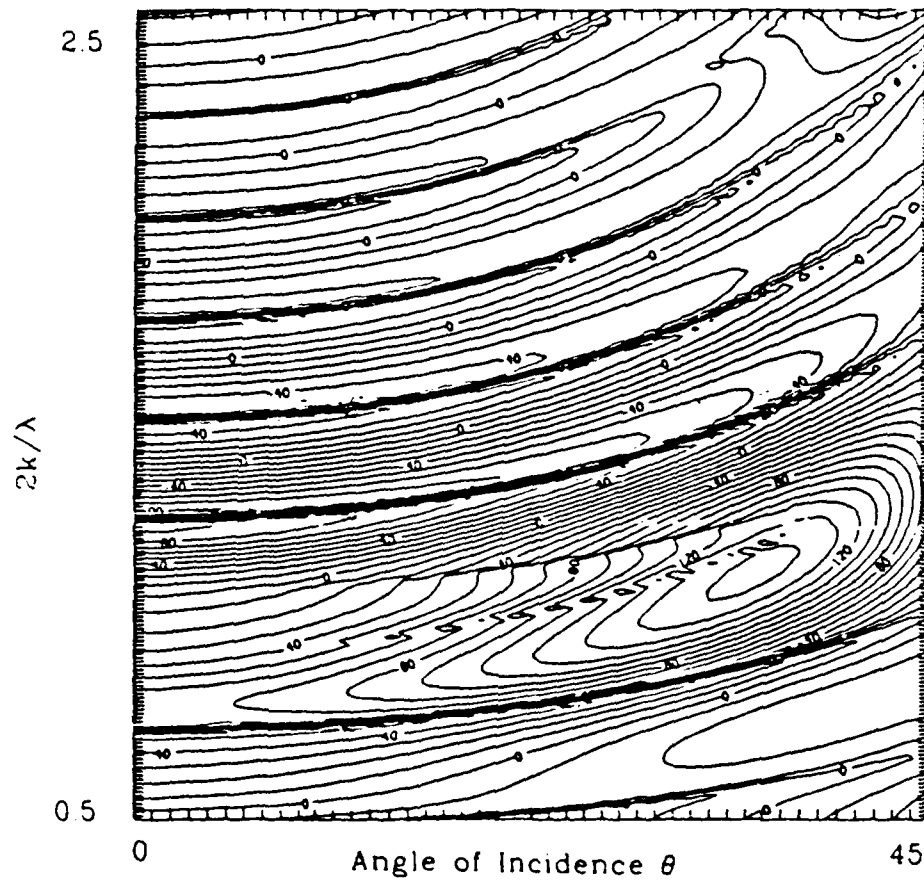


Figure 3.8: Mei's Solution - Numerical Solution vs. angle of incidence θ and offshore wavenumber k_0

CHAPTER 4 ANALYSIS TECHNIQUE FOR LABORATORY STUDY

4.1 Introduction

A formulation for the calculation of two wave field spectra travelling in opposite directions to be used in analyzing the laboratory data from the experiments described in Chapter 5 is developed. The method used is a three point method using a least squares analysis for decomposing the measured spectra into incident and reflected spectra (Funke and Mansard, 1980). This method requires a simultaneous measurement of the wave field at three positions which are in reasonable proximity to each other and in a line parallel to the direction of wave propagation.

4.2 Theoretical Background

Although these calculations may be made by measuring the wave field with two gages of known distance apart and solving two linear equations directly, Funke and Mansard (1980) put forth a method for resolving the wave train spectra using multiple gages to measure the wave field and a least squares fit to resolve the incident and reflected wave spectra, in an effort to improve accuracy and reduce sensitivity to signal noise and non-linearities of the waves. The theory makes use of the axiom that an irregular sea state may be described as the superposition of an infinite number of discrete components

$$\eta = \sum_{n=0}^{\infty} \eta_n \quad (4.1)$$

where

$$\eta_n = A_n e^{i(k_n x - \omega_n t)}, \quad (4.2)$$

and the assumption that each component will travel at a unique speed in a given water depth. The superposition will result in a time series $\eta_1(t)$, $\eta_2(t)$, and $\eta_3(t)$ of the water

elevation at each gage position. The spacing between the gages is known, and wave celerity may be determined by

$$C = \frac{\omega}{k} \quad (4.3)$$

where

$$\omega = \frac{2\pi}{T} \quad (4.4)$$

where T is the wave period. Solving the implicit equation

$$\omega^2 = gk \tanh kh \quad (4.5)$$

for k iteratively, where g is the acceleration of gravity, k is the wave number, and h is the water depth, it is possible to calculate the phase relationships between the wave trains as they pass the probes.

Beginning by executing a Fourier transform on each signal,

$$B(\omega) = \int_{-\infty}^{\infty} \eta(t) e^{-i\omega t} dt \quad (4.6)$$

the discrete Fourier components may be resolved and written in polar form as

$$B_{p,n} = A_{p,n} e^{i\alpha_{p,n}} \quad (4.7)$$

or in rectangular form as

$$B_{p,n} = A_{p,n} \cos \alpha_{p,n} + i A_{p,n} \sin \alpha_{p,n} \quad (4.8)$$

where $A_{p,n}$ is the amplitude of the n^{th} component at gage p , and α is the phase relative to the time origin of the record. The Fourier transform will enable the calculation of half as many frequency components as data points, N .

These coexisting amplitude-phase spectra determined at the gage positions are a result, as stated above, of the superposition of the discrete frequency components, and are in fact, each a measurement of the same wave fields. The goal is now to separate out the two interacting fields, those being the incident and reflected wave fields. Making use of the

dispersion relationship, it can be seen that it is possible to calculate the phase relationships of each component as they are measured at each gage. By assuming superposition of two wave fields travelling in opposite directions, the time series will be

$$\eta_1(t) = \sum_{n=1}^N A_{I,n} e^{-i(k_n z - \omega_n t)} + \sum_{n=1}^N A_{R,n} e^{-i(k_n(z+2x_{r1}) + \omega_n t)} \quad (4.9)$$

where A_I and A_R are the component amplitudes of the incident and reflected spectra, and x_{r1} is the distance from gage 1 to the point of reflection, arbitrarily set at the center of the bar field. The record at the second gage will be identical in form, except that the phases will be

$$PH_{I,12} = k_n(x + x_{12}) - \omega_n t \quad (4.10)$$

for the incident wave train, and

$$PH_{R,12} = k(x + 2(x_{r1} - x_{12})) - \omega_n t \quad (4.11)$$

for the reflected wave train, where x_{12} is the distance between gages 1 and 2. The phases will be likewise for the third gage record, with the obvious replacement of a 3 where 2 appears.

The phase lag between probes is preserved in the Fourier transform, and since it is only these that are required to complete the calculation, the initial phase, or the phase at the first gage can be factored out of each component at each gage. Thus, with phases referenced to the phase at the first gage, the spectrum at a given gage may also be described by

$$B_{p,n} = Z_{I,n} e^{ik_n x_{1p}} + Z_{R,n} e^{-ik_n x_{1p}} + Z_{N,p,n} \quad (4.12)$$

where Z is the n^{th} Fourier component of the wave field, k is the wave number of the n^{th} component, and X_{1p} is the distance between the first gage and the gage in question.

It can be seen that, given only two gage spectra of known distance apart, the simultaneous equations may be solved for Z_I and Z_R . However, to improve accuracy, additional gages may be added, and Z_I and Z_R solved for using a least square error approach, where

Z_N is the error spectrum for a particular gage. Following directly from Funke and Mansard (1980), define

$$\beta_n = \frac{k_n}{x_{12}} \quad (4.13)$$

$$\gamma_n = \frac{k_n}{x_{13}} \quad (4.14)$$

Equation 4.12 may be restated for all three gages as

$$\epsilon_{1,n} = Z_{I,n} + Z_{R,n} - B_{1,n} \quad (4.15)$$

$$\epsilon_{2,n} = Z_{I,n}e^{i\beta_n} + Z_{R,n}e^{-i\beta_n} - B_{2,n} \quad (4.16)$$

$$\epsilon_{3,n} = Z_{I,n}e^{i\gamma_n} + Z_{R,n}e^{-i\gamma_n} - B_{3,n} \quad (4.17)$$

where

$$\epsilon_{p,k} = -Z_{N,p,n} + f_e(Z_{I,n}, Z_{R,n}) \quad (4.18)$$

where f_e is an expression for the error associated with the entire domain, thus common to all three gages.

Now a least squares fit may be used to find those values of Z_R and Z_I for which the sum of the squares of $\epsilon_{p,n}$, for all values of p is a minimum. This will occur at

$$f_e(Z_{I,n}, Z_{R,n}) = 0. \quad (4.19)$$

Therefore, it is required that the sum of the squared error over each gage

$$\sum_{p=1}^3 (\epsilon_{p,n})^2 = \sum_{p=1}^3 (Z_{I,n}e^{i\psi_{p,n}} + Z_{R,n}e^{-i\psi_{p,n}} - B_{p,n})^2 \quad (4.20)$$

be minimized, where $\psi_{p,n}$ is either β or γ .

It is assumed that a minimum will be reached when both partial derivatives are zero.

Differentiating 4.20 with respect to Z_I and Z_R results in,

$$\sum_{p=1}^3 (Z_{I,n}e^{i\psi_{p,n}} + Z_{R,n}e^{-i\psi_{p,n}} - B_{p,n})e^{i\psi_{p,n}} = 0 \quad (4.21)$$

and

$$\sum_{p=1}^3 (Z_{I,n}e^{i\psi_{p,n}} + Z_{R,n}e^{-i\psi_{p,n}} - B_{p,n})e^{-i\psi_{p,n}} = 0 \quad (4.22)$$

Expanding the terms in the sum and rearranging terms results in two equations

$$Z_{I,n}(1 + e^{i2\beta_n} + e^{i2\gamma_n}) + 3Z_{R,n} = B_{1,n} + B_{2,n}e^{i\beta_n} + B_{3,n}e^{i\gamma_n} \quad (4.23)$$

$$Z_{R,n}(1 + e^{-i2\beta_n} + e^{-i2\gamma_n}) + 3Z_{I,n} = B_{1,n} + B_{2,n}e^{-i\beta_n} + B_{3,n}e^{-i\gamma_n} \quad (4.24)$$

which may be solved simultaneously in terms of β, γ , and $B_{p,n}$. Let

$$Z_{R,n} = \frac{-3Z_{I,n} + B_{1,n} + B_{2,n}e^{-i\beta_n} + B_{3,n}e^{-i\gamma_n}}{(1 + e^{-i2\beta_n} + e^{-i2\gamma_n})} \quad (4.25)$$

substitute 4.25 into 4.23

$$Z_{I,n}(1 + e^{i2\beta_n} + e^{i2\gamma_n}) + \frac{3(-3Z_{I,n} + B_{1,n} + B_{2,n}e^{-i\beta_n} + B_{3,n}e^{-i\gamma_n})}{(1 + e^{-i2\beta_n} + e^{-i2\gamma_n})} = B_{1,n} + B_{2,n}e^{i\beta_n} + B_{3,n}e^{i\gamma_n} \quad (4.26)$$

The n subscript will be dropped here to ease the derivation, although it is understood to be attached to all terms. Multiply both sides by $(1 + e^{-i2\beta} + e^{-i2\gamma})$ and subtract the gage spectra on the left hand side to get

$$Z_I((1 + e^{i2\beta} + e^{i2\gamma})(1 + e^{-i2\beta} + e^{-i2\gamma}) - 9) = (B_1 + B_2e^{i\beta} + B_3e^{i\gamma})(1 + e^{-i2\beta} + e^{-i2\gamma}) - 3(B_1 + B_2e^{-i\beta} + B_3e^{-i\gamma}) \quad (4.27)$$

and finally,

$$Z_I = \frac{(B_1 + B_2e^{i\beta} + B_3e^{i\gamma})(1 + e^{-i2\beta} + e^{-i2\gamma}) - 3(B_1 + B_2e^{-i\beta} + B_3e^{-i\gamma})}{((1 + e^{i2\beta} + e^{i2\gamma})(1 + e^{-i2\beta} + e^{-i2\gamma}) - 9)} \quad (4.28)$$

By rearranging terms, and applying the proper trigonometric identities, it can be shown that the coefficients for the gage spectra that will solve this equation are as follows: The divisor for the right hand side D is

$$(1 + e^{i2\beta} + e^{i2\gamma})(1 + e^{-i2\beta} + e^{-i2\gamma}) - 9 = 2(\sin^2 \beta + \sin^2 \gamma + \sin^2 (\gamma - \beta)) \quad (4.29)$$

The B_1 coefficient, $R_1 + iQ_1$

$$(e^{-i2\beta} + e^{-i2\gamma} - 2) = \sin^2 \beta + \sin^2 \gamma + i(\sin \beta \cos \beta + \sin \gamma \cos \gamma) \quad (4.30)$$

the B_2 coefficient, $R_2 + iQ_2$

$$(-2e^{-i\beta} + e^{i\beta} + e^{(-i2\gamma+i\beta)}) = \sin \gamma \sin \gamma - \beta + i(\sin \gamma \cos(\gamma - \beta) - 2 \sin \beta) \quad (4.31)$$

and the B_3 coefficient, $R_3 + iQ_3$

$$(-2e^{-i\gamma} + e^{i\gamma} + e^{(-i2\beta+i\gamma)}) = -\sin \beta \sin \gamma - \beta + i(\sin \beta \cos(\gamma - \beta) - 2 \sin \gamma) \quad (4.32)$$

The incident spectrum may then be expressed

$$Z_I = \frac{1}{D}(B_1(R_1 + iQ_1)) + (B_2(R_2 + iQ_2)) + (B_3(R_3 + iQ_3)) \quad (4.33)$$

and the reflected spectrum

$$Z_R = \frac{1}{D}(B_1(R_1 - iQ_1)) + (B_2(R_2 - iQ_2)) + (B_3(R_3 - iQ_3)) \quad (4.34)$$

The coefficients are all in terms of γ and β which are found by the geometry of the gage array and the wavenumber k .

As Z_I and Z_R represent amplitude spectra, the energy density spectra may easily be determined by squaring the amplitude and dividing by the increment in angular frequency, or

$$E_I = \frac{Z_I^2}{2\Delta\omega} \quad (4.35)$$

where

$$\Delta\omega = \frac{2\pi}{N\Delta t} \quad (4.36)$$

where Δt is the sampling rate.

In an effort to assure that the experiment was running correctly, and that the data were being collected and analyzed properly, the energies of the reflected and transmitted wave fields were compared by conservation of energy to the wave field incident from the paddle. (see Chapter 5)

$$E_I = E_R + E_T \quad (4.37)$$

4.3 Inputs to Least Squares

Two methods of calculating the amplitude spectra for each gage were used and their results compared.

4.3.1 Direct Signal Processing

The first method used the full record of 2048 points. The Fourier Transform was performed on each of the gage records, after the mean was taken out, using an FFT algorithm. The resulting amplitude and phase spectra were used directly in the least square calculation of the incident and reflected wave field spectra. Note that there was no smoothing performed on the data in this method. Demeaning the data

$$\bar{\eta}^p = \frac{1}{2048} \sum_{i=1}^{2048} \eta_i^p \quad (4.38)$$

$$S_n^p = \eta_n^p - \bar{\eta}^p \quad (4.39)$$

$$S^p \xrightarrow{\text{FFT}} B^p = a^p - ib^p \quad (4.40)$$

where η^p is the elevation time record at gage p , $\bar{\eta}^p$ is the mean over all elements in the record at gage p , S is the demeaned signal, and B is the complex amplitude spectrum.

4.3.2 Ensemble Averaging of Cross-Correlation Spectra

The second method is the same as the one proposed in Funke and Mansard (1980). This method applies an ensemble averaging to the data by separating the time series into, in this case, four separate realizations, in an effort to reduce noise effects. Of course, in applying any type of averaging window, one sacrifices resolution in the resultant spectrum. The second difference in this method, is that after each Fourier component is determined, its amplitude is joined with the phase lag of that component relative to the first gage in the series, the first gage having phase lag of zero. The computations of the gage spectra are as follows:

The time series of 2048 points is split into four realizations of 512 points each. The

mean is computed by

$$\overline{\eta^{p,m}} = \frac{1}{512} \sum_{t=1}^{512} \eta_t^{p,m} \quad (4.41)$$

where p is the gage number 1,2 or 3, and m is the realization number, and η_t is the water elevation read in the time series η at time t . This value is then subtracted from each data point

$$S_n^{p,m} = \eta_n^{p,m} - \overline{\eta^{p,m}} \quad (4.42)$$

to yield the demeaned record S . The Fourier Transform is obtained for each realization in an FFT algorithm resulting in

$$S^{p,m} \xrightarrow{\text{FFT}} B^{p,m} = a^{p,m} - ib^{p,m} \quad (4.43)$$

or in polar form

$$B^{p,m} = A^{p,m} e^{i\phi^{p,m}} \quad (4.44)$$

Next, the absolute amplitude spectrum is extracted from the Fourier series,

$$A_n^{p,m} = \sqrt{\frac{2B_n^{p,m} B_n^{*p,m}}{\Delta t}} \quad (4.45)$$

where B^* is the complex conjugate of B , and averaged by component n over the number of realizations.

$$\overline{A_n^p} = \frac{1}{4} \sum_{m=1}^4 A_n^{p,m} \quad (4.46)$$

The phase of the cross correlation between the first gage and subsequent gages is attached to the respective amplitudes at each frequency component. The cospectrum is calculated by;

$$C_{12} = B^1 B^{2*} \quad (4.47)$$

where B^* is the conjugate of the transform. Note that the m and n notations have been dropped merely for convenience at this point, and will reappear later. Thus,

$$C_{12} = (a_1 - ib_1)(a_2 + ib_2) \quad (4.48)$$

$$= a_1 a_2 + b_1 b_2 + i(a_1 b_2 - a_2 b_1) \quad (4.49)$$

$$= A_{12} e^{i\phi_{12}} \quad (4.50)$$

So,

$$\tan \phi_{12} = \frac{a_1 b_2 - a_2 b_1}{a_1 a_2 + b_1 b_2} \quad (4.51)$$

Averaging by frequency over the four realizations,

$$\overline{\tan \phi_{12}} = \frac{\frac{1}{4} \sum_{m=1}^4 a_1^m b_2^m - a_2^m b_1^m}{\frac{1}{4} \sum_{m=1}^4 a_1^m a_2^m + b_1^m b_2^m} \quad (4.52)$$

or

$$\overline{\tan \phi_{12}} = \frac{\sum_{m=1}^4 (a_1 b_2 - a_2 b_1)^m}{\sum_{m=1}^4 (a_1 a_2 + b_1 b_2)^m} \quad (4.53)$$

Thus the gage spectra used in the analysis are given by

$$B_n^1 = A_n^1 \quad (4.54)$$

$$B_n^2 = A_n^2 e^{i\phi_{12,n}} \quad (4.55)$$

$$B_n^3 = A_n^3 e^{i\phi_{13,n}} \quad (4.56)$$

4.4 Results of Least Square Error Fit

As stated above, the ensemble averaging was performed to reduce noise interactions at the cost of resolution. Assuming the resolution of the full record analysis looks like

$$\Delta\omega, 2\Delta\omega, 3\Delta\omega, 4\Delta\omega, 5\Delta\omega \dots \quad (4.57)$$

where

$$\Delta\omega = \frac{2\pi}{N\Delta t}, \quad (4.58)$$

the resolution of the smoothed spectrum is

$$4\Delta\omega, 8\Delta\omega, 12\Delta\omega, \dots \quad (4.59)$$

and the number of spectral components will be one quarter the number in the full record analysis. The range of frequencies covered will be the same for both spectrum lengths.

The resulting incident and reflected spectra from the full record transform behaved very nicely and predictably. However, for the output from the smoothed spectrum scheme, this was not the case. After a few trial runs of the program with artificial data at a discrete

frequency, it became apparent that the reflection coefficient (as would the energy densities) would be significantly over or underestimated, unless the frequency picked was resolvable in both the full record and the quarter length cross correlation method, ie.

$$\omega_{peak} = m\Delta\omega \quad (4.60)$$

if $m = 4, 8, 12, \dots$ in which case the reflection coefficient was identical using both resolutions. No particular pattern in over- or underestimation was readily apparent, except that the reflection coefficient spectrum in the vicinity of the chosen frequency would follow a general upward or downward trend rather smoothly. It is probable that this phenomena is due to leakage from the dominant frequency to adjacent frequencies. The mechanism by which this is working is not yet understood, but would involve the interaction of the leaked spectral data in the two Fourier spectra combined in estimating the cross-spectrum. See Figure 4.1.

The above explanation does not resolve the problem of obtaining a resultant reflection coefficient spectrum (as well as the incident and reflected spectral energy densities) that is smoothed or has the system noise and nonlinear effects filtered out, but rather compounds the problem. However, the potential for extracting a reasonable result did present itself when it was noticed that the reflection coefficient at the dominant frequency, as calculated by the full record analysis was between those at the frequencies directly on either side of the dominant frequency as calculated from the smoothed spectrum. See Figure 4.3. By performing a linear interpolation between the values at these two frequencies, it was found, for synthetic data, to yield a value very close to that calculated by the unsmoothed data. More precisely stated, for values of $\omega = m\Delta\omega$ where m is equal to an integer multiple of 4, the reflection coefficients would be equal. But if m were other than a multiple of 4, a reasonable estimate of the reflection may be calculated by linearly interpolating between the nearest resolved frequencies.

Assuming a monochromatic wave field, a dominant frequency may be picked out by finding the frequency with the greatest value of the power spectrum from a particular gage spectrum in the full record analysis. Then finding the frequencies between which it lies

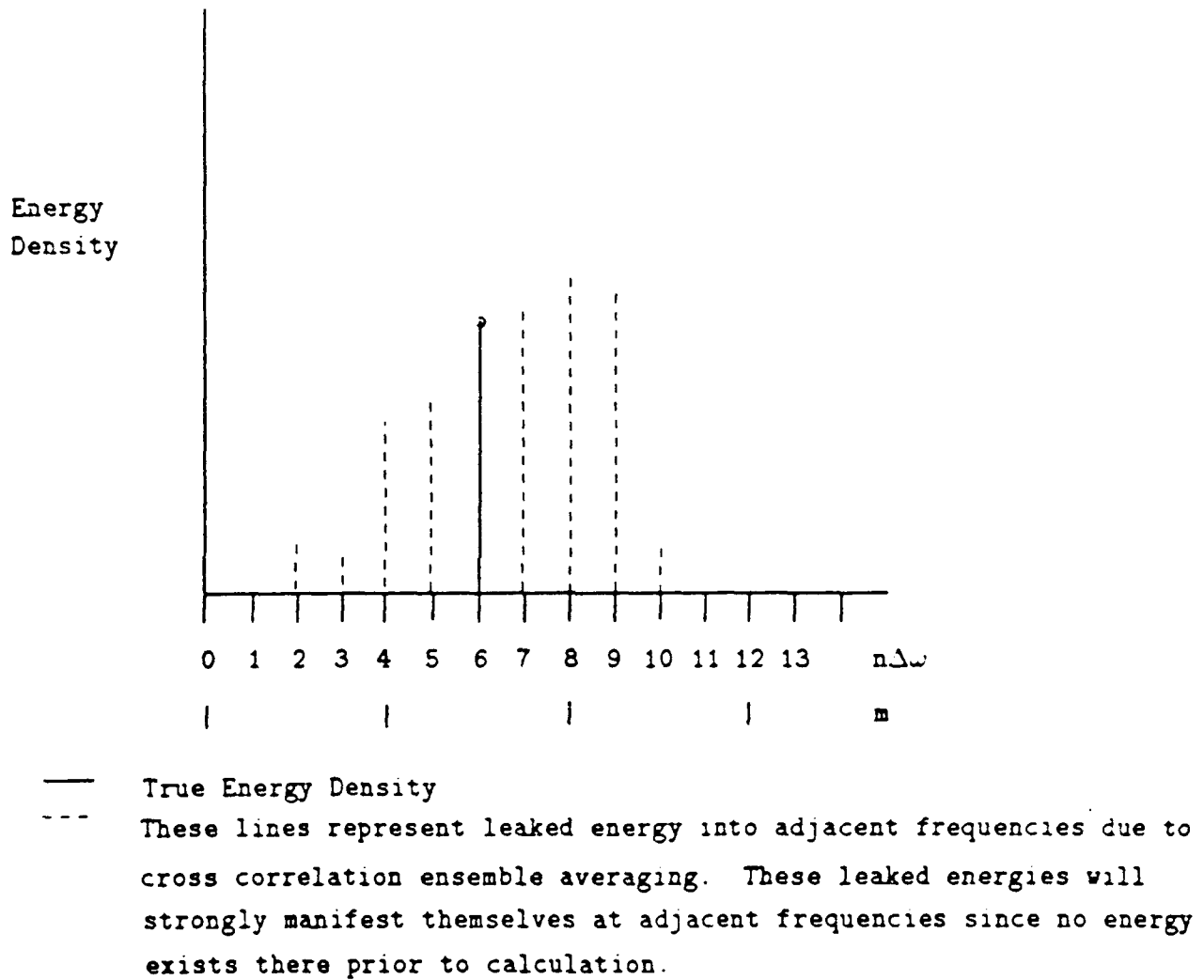


Figure 4.1: Effect of smoothing on a monochromatic spectrum

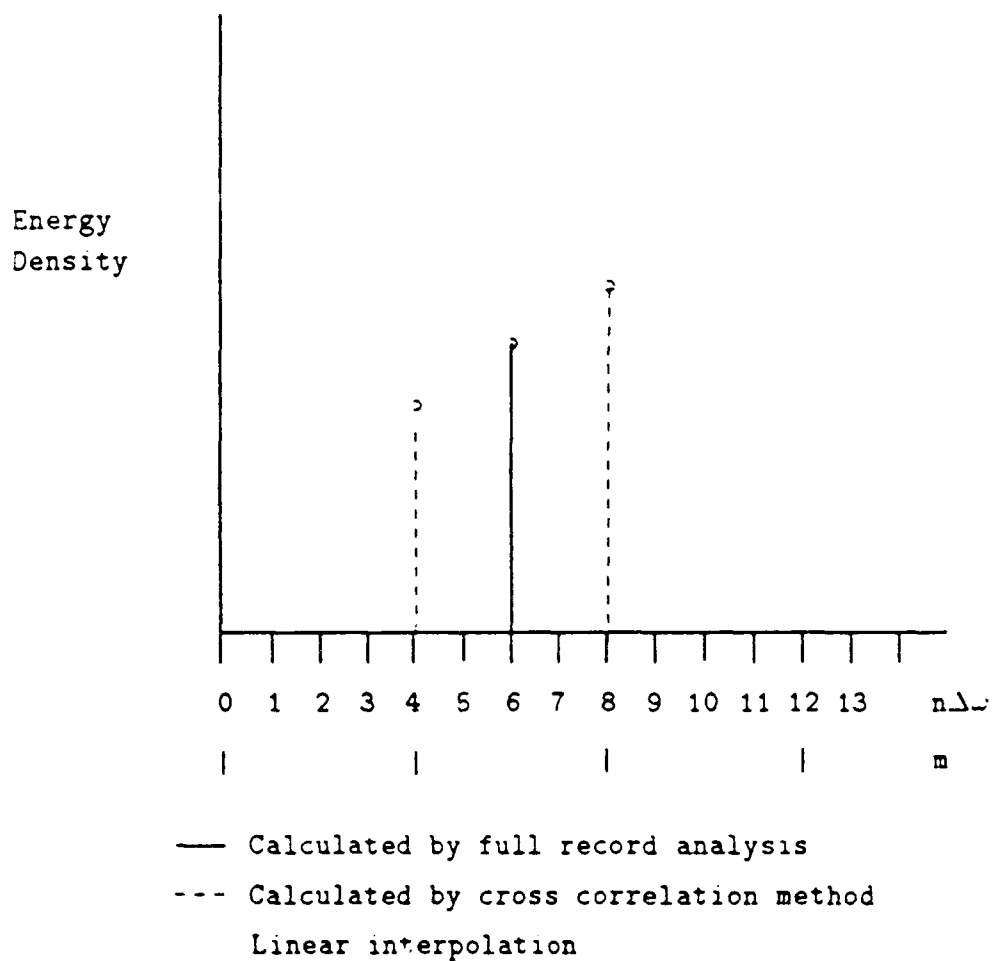


Figure 4.2: Interpolating resolved frequencies in the smoothed monochromatic spectrum to estimate the energy density at the true frequency

in the smoothed spectrum, a reasonable estimate for the true reflection coefficient may be established by linear interpolation. For instance, assume the dominant frequency as resolved by the full record is

$$\omega_{\text{dominant}} = 10\Delta\omega. \quad (4.61)$$

This frequency is bounded by the frequencies

$$\omega = 8\Delta\omega \quad (4.62)$$

and

$$\omega = 12\Delta\omega \quad (4.63)$$

which are resolvable by the smoothed spectra. The reflection coefficient at one of these bounding frequencies will be higher than the reflection coefficient at the dominant frequency calculated using the full record, while the other will be lower. The linear interpolation is simply

$$\kappa_{r10} = \frac{(\kappa_{r12} - \kappa_{r8})}{(12 - 8)}(12 - 10) + \kappa_{r8} \quad (4.64)$$

where κ_{rm} is the reflection coefficient of the m^{th} component of the full record spectrum. By assuming a local linear relationship between frequency and energy density, this interpolation can be easily be adapted for energy density calculation.

This method was developed by observing the interaction of a synthetically generated monochromatic spectrum, which by its nature is very clean, ie. no energy at frequencies other than the one defined. Therefore, it is justifiable to use this technique to analyze the data collected in the laboratory experiments explained in Chapter 5, since that data itself is very clean. Viewing a typical energy density spectrum shown in figure 5.8, it is apparent that all of the significant energy is contained at one frequency.

4.4.1 Results

The result of performing the smoothing and interpolation scheme presented above on the data collected in the laboratory experiments proved to be minimal. The change in the resulting reflection coefficients was generally on the order of 10^{-3} . It is therefore suggested

that the full record of a monochromatic wave field, transformed to the resolution allowed by the recording apparatus, be used in determining incident and reflected energies, and reflection coefficients in a monochromatic wave field.

CHAPTER 5 LABORATORY STUDY

5.1 Introduction

A laboratory experiment was performed to verify the predictions of the numerical solution for monochromatic waves of normal incidence. The laboratory set up used was very similar to that of Davies and Heathershaw (1984) except that, where Davies and Heathershaw used a sinusoidal ripple patch, a set of four discrete bars with positive amplitude only on an otherwise flat bottom were installed in the wave flume. In the present study two bar fields were tested, both with the same shaped bars but with different spacing between them.

5.2 Equipment

5.2.1 Wave Flume

The tests were done in a 26m x 0.6m x 1.1m wave flume at the Coastal and Oceanographic Engineering Laboratory (COEL) at the University of Florida. The water depth was 15 cm in the flume. The bar patch began 14m down wave of the wave generator and ended 7.8m up wave of an energy absorbing beach at the end of the flume. Waves were generated by a Seasim piston wave maker .4 m high. Although the Seasim system is capable of generating a 16 band spectral wave field, only monochromatic waves were used in order to achieve better resolution and accuracy. The paddle was driven by a servo-controlled system with pneumatic hydrostatic balance. The signal generator was capable of accurately controlling the period of the paddle stroke to one hundredth of a second. This provided good resolution for the comparison curve at low frequencies and thus small values of $2k/\lambda$, but resolution decreased at higher frequencies. The range of periods was from 0.6667 s to

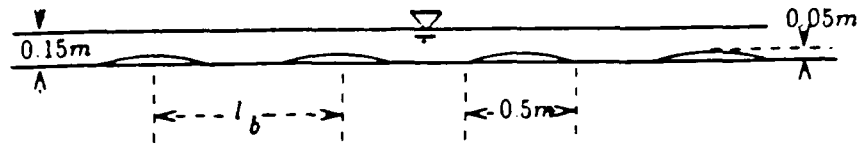


Figure 5.1: Profile of bar field

the system maximum of 2.5 s. The range of $2k/\lambda$ was from 0.45 to 2.5.

The bar patch can be described by

$$h = \begin{cases} 0.05 \sin(2\pi x); & 0 + nl_b \leq x \leq 0.5 + nl_b \\ 0.0; & 0.5 + nl_b \leq x \leq nl_b \end{cases} \quad n = 0, 1, 2, 3 \quad (5.1)$$

$l_b = \text{bar spacing}$

Two bar spacings were used, 0.8 m and 1.2 m on center. For purposes of comparison,

$$\lambda = \frac{2\pi}{l_b} \quad (5.2)$$

assuming l_b is wavelength of the dominant Fourier component of the barfield. The bars were constructed of fiberglass resin and mat in a female mold constructed of sheet metal on a wood frame. They were trimmed to a tolerance of .005 m in length and .002 m in height. Any holes that remained after curing were filled to yield a smooth surface, and edges meeting the bottom of the flume were sanded to a sharp edge to allow a smooth transition from bottom to bar. Pin holes were drilled into the tops of the bars to allow trapped air to escape while the flume was filling to avoid buoyant forces on the bars during the experiment. The bars were installed using a small amount of silicone caulk on each edge of the bar where it met the flume side or bottom.

At the down wave end of the flume, a wave absorbing beach was constructed of rubberized horsehair and bagged stone. The horsehair was held in place with wire mesh in a

convex up shape in order to dissipate wave energy in the most effective manner. This beach extended 1.5 m up wave of the bagged stone. It was important to minimize reflection off of this beach so as not to pollute the reflection of the bar patch.

Measurements prior to bar installation showed reflections from the beach of less than 15 percent, and generally less than 10 percent. During these measurements, the array that was to be up wave of the bar field, the stationary array, was installed 12 m up wave of the beach. The array on the cart was placed 2 m up wave of the beach in an effort to determine the change in reflection coefficient due to position and examine energy decay of the reflected wave. However, during this portion of the experiment, one of the gages in the cart array malfunctioned and only a few runs were made with both arrays in operation. For verification of each coefficient, two runs were made at each frequency and the results averaged. An attempt to test the algorithm described in the the previous chapter was performed using a hand held vertical wall in an attempt to achieve near total reflection. The results of these tests are presented in Table 5.1.

Table 5.1: Percent Reflection from Flume End w/o Bars

Frequency Hz.	Stationary	Cart
0.4	10.6	na
0.5	8.4	na
0.6	6.9	na
0.7	4.7	na
0.8	4.6	na
0.9	5.8	na
1.0	6.6	6.6
1.2	6.4	13.7
1.3	11.4	10.4
1.4	6.7	8.2
1.5	4.0	8.4
1.6	20.2	41.9
vert board 1.3	78.5	79.1

The very high reflection at 1.6 Hz remains a mystery. However, the highest frequency used in tests once the bars were installed was 1.5 Hz so no further investigation of this phenomenon was deemed necessary.

5.2.2 Electronic Measurement

Two arrays of three gages each were employed, one 1.8 m up wave of the bar patch and the other 1.2 m down wave. The gages were a standard in house design with minor alterations to improve sensitivity. The gages operate by comparing the frequencies of two inductive-capacitive (LC) circuits where:

$$f = \frac{1}{2\pi\sqrt{LC}} \quad (5.3)$$

Inductance and capacitance were adjusted in a reference circuit to run at a constant frequency around 1 MHz. The sampling circuit was identical to the reference circuit except that an additional 'capacitor' was added, that being the capacitance contained between the probes, that is to say the probes act as capacitance plates with water being a variable dielectric. Since the wave amplitudes were to be less than 1.5 cm to maintain linear theory, the probes were only 6 cm long. Normally these gages are used with probe lengths 0.5 m or longer and the capacitance contained between them is of the order of 100 microfarads, while the 6 cm probes contained less than 10 microfarads. This made tuning the sample and reference circuits to be of greater importance than normal for these gages. The sampling circuit was tuned to run at a slightly lower frequency than the reference circuit for the full range of capacitance change in the probes. The two frequencies were subtracted in a chip and the difference frequency sent in the form of an RF signal to the signal conditioner. Therefore, as water level increased, the capacitance between the probes increased resulting in a drop in the frequency in the sampling circuit thus increasing the difference between the two frequencies, which, when processed in the signal conditioner, showed an increase in voltage.

The signal conditioner worked somewhat like a radio receiver, converting a RF signal to a voltage. The signal conditioner had adjustable gain and zero offset controls. The zero offset control allowed for the positioning of the mean voltage output, and was set, such that at still water the output was close to zero, (usually ± 0.2 volts). The gain was adjusted so

that immersing the length of the probe corresponded to a 10 volt change in output from the signal conditioner. Thus, full immersion of the probe resulted in an output of +5 volts and an output of -5 volts if just the tip of the probe was immersed.

The output voltage was then fed through an analog to digital conversion board mounted on the back of a Digital Equipment Corporation Micro PDP-11 (PDP- 11). This board read the voltage and converted it to an integer value corresponding to the voltage. A voltage in the range of -5 to +5 volts corresponded to an integer between 0 and 4096. Thus, the resolution achieved between discrete voltages was

$$\frac{10\text{volts}}{4096\text{points}} = 0.00244\text{volts/division} \quad (5.4)$$

translating into a resolution of the probes of

$$\frac{6\text{cm}}{10\text{volts}} 0.00244\text{volts/division} = .00122\text{cm/division} \quad (5.5)$$

The PDP-11 would sample 2048 points at each gage location at a rate of 0.1 s or frequency of 10Hz for one complete data set.

5.3 Data Analysis

5.3.1 Acquisition

The gages were set in two arrays of three each with 19 cm. between the first and second gages and 31 cm. between the second and third. The choice of this spacing will be expanded upon in the next section. Each gage in the array was attached to a rigid bar connected to a rack and pinion vernier marked in millimeters. The rigid bar was stabilized by two vertical parallel bearing tracks which in turn were connected to an aluminum frame. The array up wave of the bar patch (reflected end or R-array) was mounted directly to the sides of the flume, while the down wave array (transmitted end or T-array) was attached to a cart that is capable of moving along the length of the flume.

The vernier allowed for precise static calibration of the gages. Calibration data was taken at water elevation values of 2.60 cm, 1.50 cm, 0.00 cm, -1.00 cm, and -2.00 cm. The

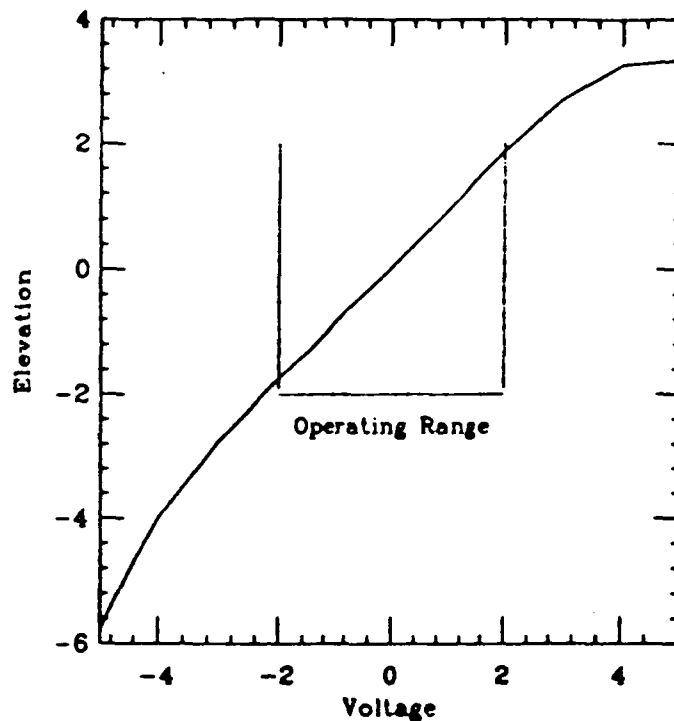


Figure 5.2: Typical calibration curve

voltages for each gage at each elevation were stored in the PDP-11. The raw elevation vs. voltage data was used to calculate the coefficients of a fourth order curve to account for any subtle nonlinearities in the gage response. A typical calibration curve with the calibration data points is shown in Figure 5.2.

Gages were calibrated at the beginning of a laboratory session. They were recalibrated when the difference in voltage between two gages in the same array, at still water, drifted 0.1 volt, translating to a mean water shift of approximately 0.05 cm, from the reading at the previous calibration. This would keep gage error to less than 5 percent for a 1 cm (typical) wave, which is less than the amplitude of the measured electronic system noise.

The PDP-11 was programmed to simultaneously sample the voltage output of each gage circuit for 2048 points at a frequency of 10 Hz. (Simultaneous sampling is suggested although the computer can sample only one circuit at a time, the time difference between the samples of adjacent gages being considered negligible.) A frequency of 10 Hz was adequate since the range of wave frequencies was between 0.4 and 1.6 Hz allowing measurement of at

least the fifth harmonic of the base frequency of the wave in question. The time series of integer values was stored in a data file in the PDP-11.

5.3.2 Data Processing

The first step in processing the data received from the PDP-11 was to convert the voltages into real water elevations using the calibration constants. The data was then run through the algorithm developed by Funke and Mansard (1980) described in chapter 4. Briefly, this algorithm employs the use of the Fourier transformed data of three gages, of known spacing, to calculate the incident and reflected spectra of a wave field passing through the array. Any arbitrary choice of spacings will work well for this algorithm except those spacings where the distance between the second and third gages are integer multiples of the spacing between the first and second gages, especially in ratios of 1:2, 1:3, and 2:3. If the gages are spaced at such a ratio, the algorithm will 'see' a virtual standing wave that will fit inside the gages with nodal points at the gages. Thus it will calculate a fully reflected wave, at a wave length equal to twice the distance of the spacing between the first two gages. (See Figure 5.3.)

For each data set, four energy density spectra were calculated, viz., incident (flux to the right) and reflected (flux to the left) spectra at the reflection end (R-array) of the barfield, and the incident (right) and reflected (left) spectra at the transmission end (T-array). Since the model was one dimensional, this has the effect of measuring the wave field energy passing the boundaries established by the arrays at either end of the bar field into or out of the control volume. Thus the incident and reflected spectra at the T-array represent the energy transmitted over the bar field and the reflected energy off of the beach at the end of the flume. (See Figure 5.4) During the laboratory trials, the dominant frequency, or that with the highest energy, in each spectrum was picked out and displayed for ease in calculation of the reflected energy ratio and reflection coefficient. A listing of the processing program is presented in the appendix.

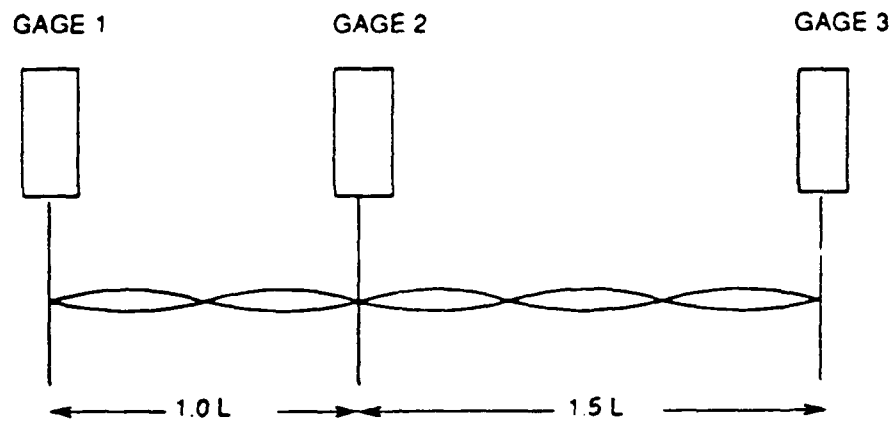


Figure 5.3: Improper gage spacing and virtual standing wave

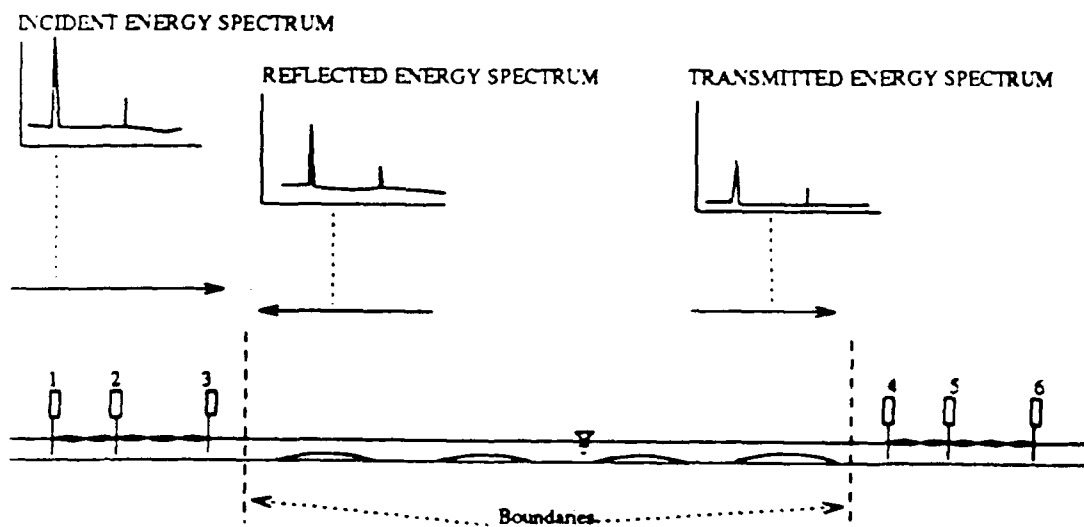


Figure 5.4: Energy crossing system boundaries

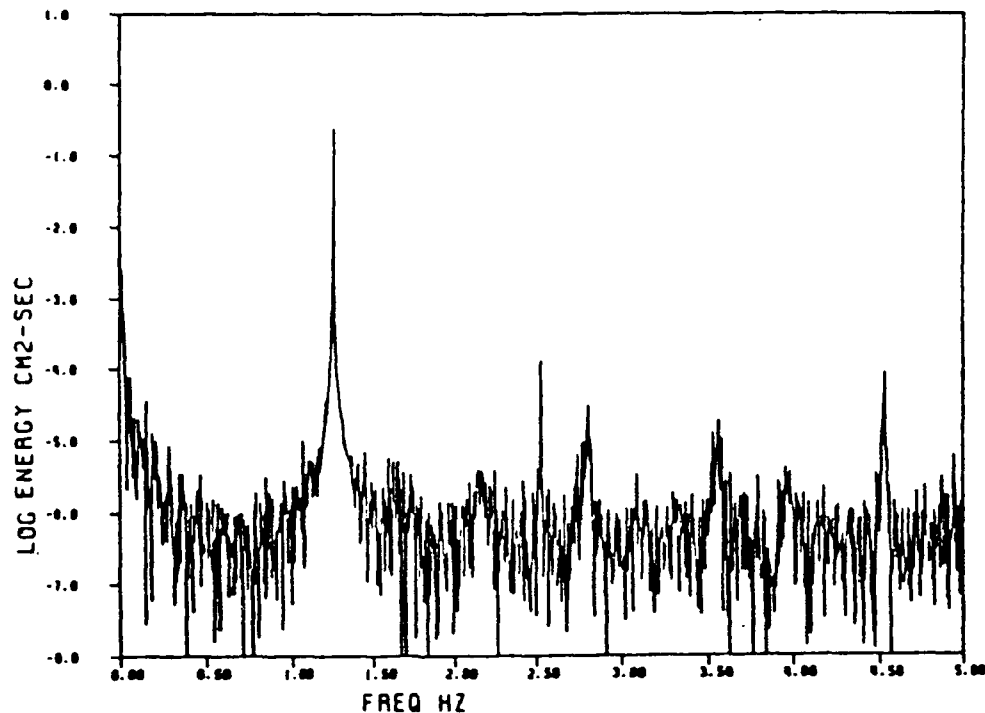


Figure 5.5: Typical energy density spectrum for incident wave

Since the spectra passing each array were referenced to a physical scale, that is water elevation, one could assume by the law of conservation of energy, that the energy measured going into the system (incident energy at the R-array only, assuming the energy re-entering the system from the reflection of the beach at the T-array is negligible) should equal the energy leaving the system in either direction (reflected and transmitted energy). Again, the reader is reminded that although the energy density spectrum is used in these calculations, the assumption that all of the energy is contained in a single frequency band and that all spectra used in the calculation are of the same frequency resolution, this description is valid.

After the spectra had been calculated, the peak value of each spectrum was found and displayed along with its corresponding frequency. This frequency was usually in very good agreement with the expected peak frequency as established by the output of the signal generator control of the wave paddle. The spectra were plotted (Figures 5.5, 5.6, 5.7) and higher harmonics of the base frequency are evident in these plots. However, only the characteristics of the base frequencies were investigated. With the incident, reflected, and

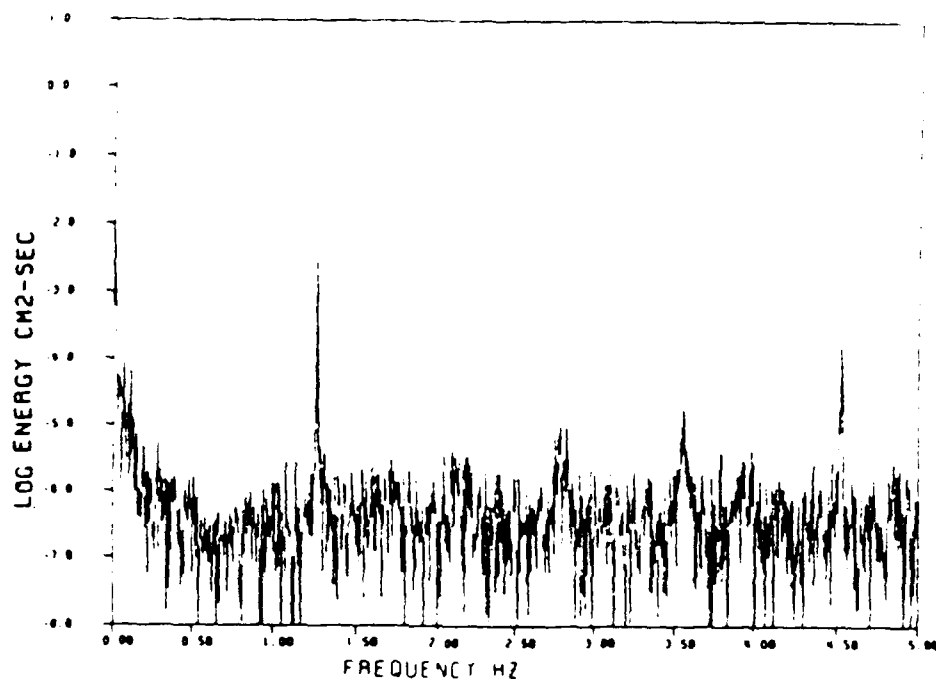


Figure 5.6: Typical energy density spectrum for reflected wave

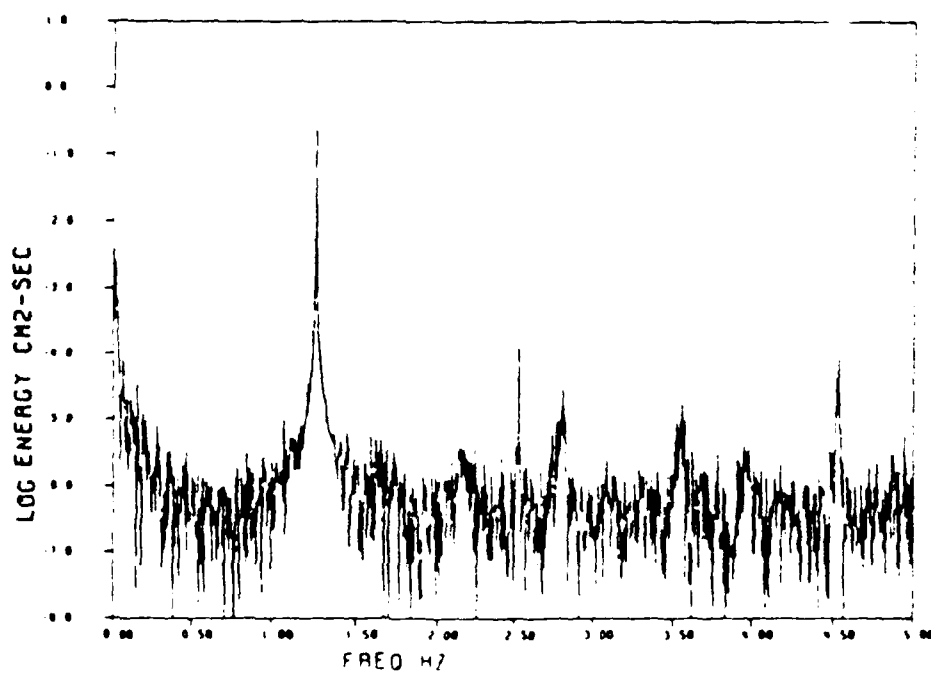


Figure 5.7: Typical energy density spectrum for transmitted wave

transmitted energies established, the transmitted and reflected energy ratios and reflection coefficient could be determined. Also, total energy of the system could be tested against the incident energy by adding reflected and transmitted energy and dividing by incident energy. Since by linear theory

$$E = \frac{1}{8} \rho g H^2 \quad (5.6)$$

and reflected and transmitted energy ratios

$$R_r = \frac{E_r}{E_i} \quad (5.7)$$

$$T_t = \frac{E_t}{E_i} \quad (5.8)$$

r = Reflected at R-array

t = Incident at T-array

i = Incident at R-array

(5.9)

Then the reflection coefficient is,

$$\kappa_r = \sqrt{\frac{E_r}{E_i}} \quad (5.10)$$

By conservation of energy

$$E_i = E_r + E_t \quad (5.11)$$

Or, since $h(x1) = h(x2)$,

$$1 = R_r^2 + T_t^2 \quad (5.12)$$

As will be seen in section 5.4, for most runs only about 75 percent of the energy measured entering the system was measured exiting the system through reflection and transmission. Again using linear theory, estimates of the energy attenuation due to bottom and side boundary friction were calculated. In a channel of uniform width b and depth h , the damping of a linear wave propagating over a distance l may be estimated to be

$$a = a_0 e^{-\Delta/l} \quad (5.13)$$

where

$$\Delta f = \frac{2k}{b} \sqrt{\frac{\nu}{2\omega}} \frac{kb + \sinh 2kh}{2kh + \sinh 2kh} \quad (5.14)$$

a_0 is the wave amplitude incident on the barfield, a is the attenuated wave amplitude (Hunt 1957) and ν is the kinematic viscosity at $1.005E-6 \text{ m}^2/\text{s}$. For shallow water where $kh \rightarrow 0$ this reduces to

$$\Delta f = \frac{k}{4h} \sqrt{\frac{2\nu}{\omega}} \frac{(b + 2h)}{b} \quad (5.15)$$

Length of travel of the waves was assumed to be the distance between the arrays for both the transmitted and reflected waves. The approximation that the distance the reflected wave travel equals to the total distance between the arrays is chosen by assuming that all of the reflection would take place exactly in the middle of the bar field. Over the range of frequencies used in the experiment, theoretical predictions showed a 10 percent attenuation to total energy due to friction.

5.3.3 Verification of Analysis Technique

The analysis technique, being relatively new, was verified using established technique of measuring wave envelopes using a moving wave gage. Actually, three gages were used simultaneously on the same cart since they were already mounted on the cart for the technique described above. Data were collected in the same manner as with the six stationary gages. However, since measurement of envelopes is a relative maximum amplitude measurement of with respect to position in the wave field, and is dependent only on what the individual gage measures, the data were not converted into true elevation but left in the form of a voltage reading. The data were then processed in a routine that picked out the local maxima (crests) and minima (troughs) which were subtracted from each other and stored as a wave height. (This data was smoothed since, often, small peaks in the raw data due to tank and system noise resulted in gaps in the resulting envelope.) The maxima and minima of the resulting envelope wave were then picked out in the same manner, representing maximum (H_{max}) and minimum (H_{min}) wave heights. A reflection coefficient was then calculated

using the theory described in Dean and Dalrymple (1984).

$$\kappa_r = \frac{H_{max} - H_{min}}{H_{max} + H_{min}} \quad (5.16)$$

While envelope measurement is considered to be more exact, due to its simplicity and directness of calculation (i.e., no resolution or aliasing problems resulting from Fourier transforming of data) it did not lend itself well to this experiment because 1) the rails supporting the cart were trued to $\pm .3$ cm which would have added a random mean shift in the data, 2) vibrations caused by the motor transmitted to the gages would have added substantial noise, 3) it provided no means of measuring the transmitted wave, and 4) provided no means to calculate the energy of the incident, reflected, and transmitted wave fields.

In only one out of the four tests did the moving gage and Funke and Mansard measurement techniques provide inconsistent results. Although no cause for this discrepancy was established, it was assumed that it was just a bad data set, most likely due to the stationary gages being out of calibration.

5.4 Results and Conclusions

The final result desired from the data after reduction was a reflection coefficient for each spectral band. Although the reduction of data in the lab was referenced to frequency, the final spectral output was in the form of the ratio of twice the water wavenumber to wavenumber of the bar field, or $2k/\lambda$. The plot of the lab reflection coefficients along with the numerical prediction for each bar spacing is shown in Figures 5.8 and 5.9. It is possible that the disagreement in phase with respect to $2k/\lambda$ may be due to the numerical solution being a first order solution. Further investigation into the effects of higher order terms may be required.

The total energy in the system was measured as one of the steps to determining the reflection coefficient and was used to check the effectiveness of the measuring technique using conservation of energy. The sum of energy leaving the system should equal that coming into

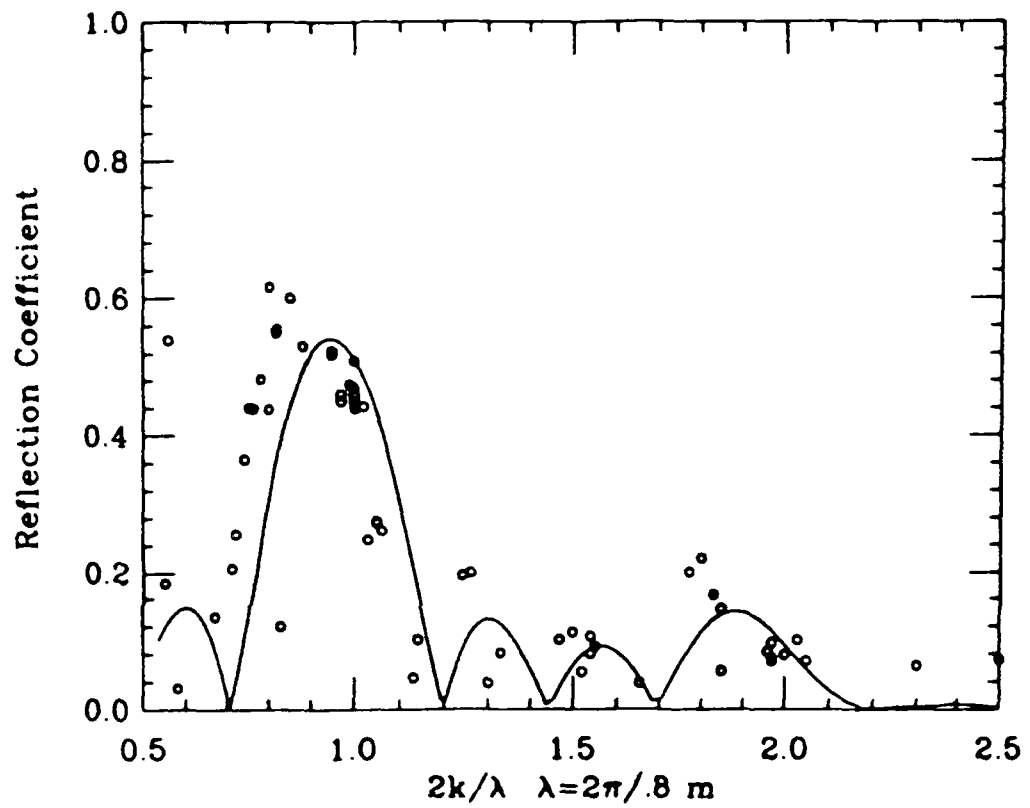


Figure 5.8: Reflection theory vs. measured, .8 m bar spacing

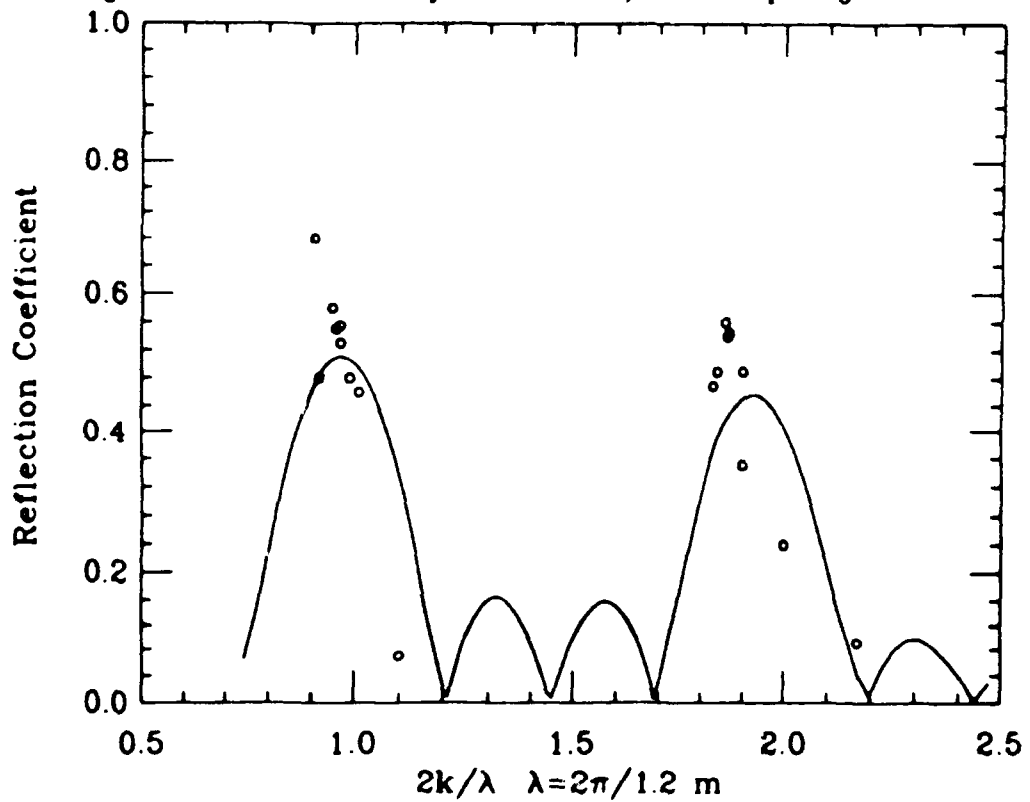


Figure 5.9: Reflection theory vs. measured 1.2 m bar spacing

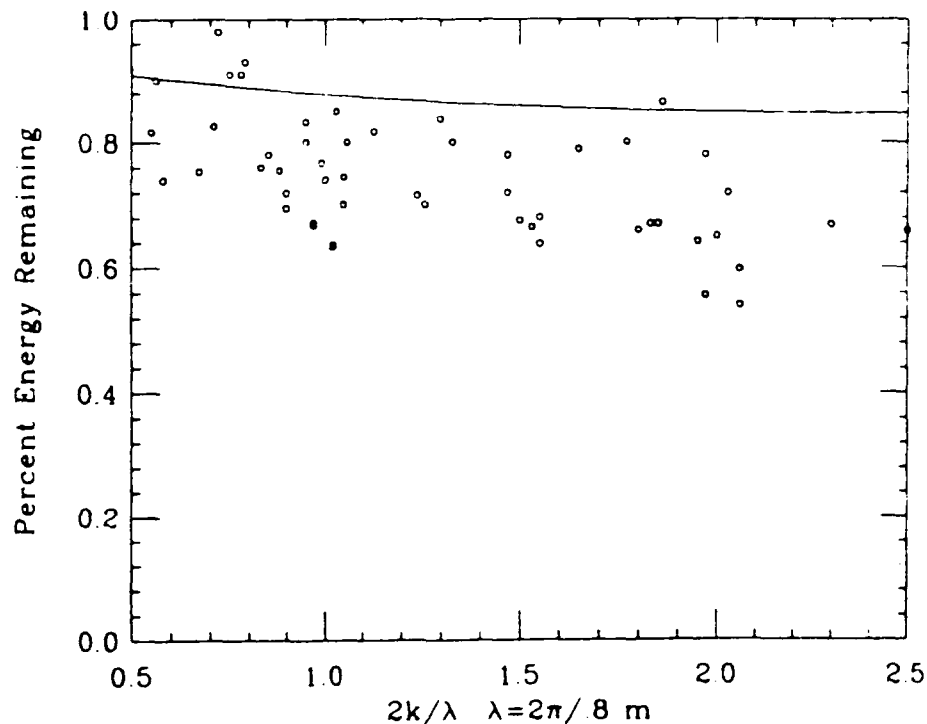


Figure 5.10: Energy Conserved: Theoretical and Measured .8 m bar spacing

the system, less the energy dissipated inside the system. Theoretical predictions show this value of dissipation to be around 10 percent, or rather 90 percent of the energy should be leaving. However, the sum total of energies usually measured less than the 90th percentile (See Figure 5.10). Significant scatter is apparent in this measurement. No relationship between the deviation in total conserved energy, and deviation in the reflection coefficient is apparent. Scatter of the energy attenuation seems to be independent of frequency as well. Looking at the energy levels did aid in quickly determining if a given sample was giving unreasonable results. The energy plotted in Figure 5.10 is the sum of the ratios of the transmitted and reflected energy of the single band being tested.

The ratios of energy contained in the full spectra were also determined and viewed. These were slightly higher than the single band but were usually very close to the single band ratios.

CHAPTER 6 BARS ON A MILD SLOPE

6.1 Introduction

In this chapter, the effects of a series of undulations placed on a mildly sloping beach are investigated. The equations presented remain in linear theory, thus no energy is dissipated in breaking. Also no damping due to bottom friction is applied. It will be shown that for this case, reflection in steady state will be complete for the whole system. The interest, then, lies in the displacement response at the shoreward boundary and between the shoreline and barfield.

6.2 Reformulation of the Mild Slope Equation

Davies et al. (1989) developed a linearized equation for non-dispersive long waves propagating over sinusoidal undulations on an otherwise flat bottom. The analytic solution was obtained by transforming the surface displacement variable and solving the resulting Mathieu equation form. The form of the solution is restricted to two forms, or cases, those being where $2k/\lambda = 1$ and where $2k/\lambda \neq 1$. The governing equation presented in Chapter 2 is restated as the well known Mathieu equation

$$\frac{\partial^2 W}{\partial z^2} + \kappa^2 W \left[1 - \frac{\epsilon(\kappa^2 - 2)}{\kappa^2} \cos 2z \right] = 0 \quad (6.1)$$

where $\kappa^2 = 4\omega^2/gH_o\lambda^2$, ϵH_o is the amplitude of the bed undulations and $\epsilon \ll 1$. The transform variable is

$$W = H^{1/2} \xi(z) \quad (6.2)$$

where $H(z)$ is the total depth according to

$$H(z) = H_o(1 + \epsilon \cos \lambda z) \quad \text{and} \quad \eta(z, t) = \xi(z)e^{-i\omega t} \quad (6.3)$$

This form of the governing equation was then solved analytically. Kirby (1989) develops essentially the same form but for intermediate depth, dispersive waves. Also, the form of the governing equation is extended to accomodate obliquely incident waves. Since the derivatives of $\cosh kh$ in the extended mild slope equation (Kirby, 1986) given in Chapter 2 are of $O(\epsilon)$ and using the same variable definitions, it may be rewritten as

$$\nabla \cdot (f \nabla \eta) + k^2 p \eta = 0 \quad (6.4)$$

where

$$p = CC_g, \quad f = p - \frac{g\delta}{\cosh^2 kh} \quad (6.5)$$

Introducing the variable transformation

$$\eta = f^{-1/2} W, \quad (6.6)$$

6.4 becomes

$$\nabla^2 W + [k^2 + A(k^2 \delta + \frac{\nabla^2 \delta}{2})] W = 0 \quad (6.7)$$

where

$$A = \frac{g}{CC_g \cosh^2 kh} = \frac{4k}{2kh + \sinh 2kh} = \alpha' \quad (6.8)$$

as in Chapter 2.

If (x, y) is the horizontal plane and $h = h(x)$, $\delta = \delta(x)$, $\partial/\partial y \equiv 0$, equation 6.7 becomes

$$W_{xx} + [k^2 + A(k^2 \delta + \frac{\delta_{xx}}{2})] W = 0 \quad (6.9)$$

Allowing oblique incidence, let

$$m = k \sin \theta = \text{constant} \quad (6.10)$$

equation 6.9 becomes

$$\hat{W}_{xx} + [(k^2 - m^2) + A(k^2 \delta + \frac{\delta_{xx}}{2})] \hat{W} = 0 \quad W = \hat{W} e^{im y} \quad (6.11)$$

It becomes apparent, however, that as $h \rightarrow 0$, $1/f^{1/2} = 1/\sqrt{gh} \rightarrow \infty$ explicitly violating the restriction that η remain bounded at the shoreline. The only recourse to remedy this situation is to require the boundary condition at the shore to be

$$W(x_2) = 0 \quad (6.12)$$

The seaward boundary conditions are again specified in the form of radiation conditions with an incident wave propagating in the $+x$ direction and a reflected wave propagating in the $-x$ direction. The incident wave η_i is assumed to be known, and the reflected wave η_r must satisfy a radiation condition for propagation out of the domain

$$\dot{W}_r(x) = -il(x)\dot{W}_i \quad ; \quad x = x_1 \quad (6.13)$$

Similar to the boundary condition as in chapter 4,

$$\dot{W}_r = \dot{W} - \dot{W}_i \quad (6.14)$$

and substituting, the boundary condition at x_1 is thus described.

$$\dot{W}(x) = il(2\dot{W}_i - \dot{W}) \quad ; \quad x = x_1 \quad (6.15)$$

6.3 Numerical Solution

The problem specified in the previous section may be solved using a finite-difference scheme very similar to the one used in the previous chapter. The full form of the transformed mild slope equation will be used in the scheme, which when expanded, becomes

$$W_{xx} + \left[\frac{(k^2 - m^2)p}{f} + \frac{f_z^2}{4f^2} - \frac{f_{xz}}{2f} \right] W = 0 \quad (6.16)$$

The domain $x_1 \leq x \leq x_2$ is discretized according to

$$x^i = x_1 + (i+1)\Delta x \quad ; \quad 1 \leq i \leq n \quad (6.17)$$

where

$$\Delta x = \frac{x_2 - x_1}{n - 1} \quad (6.18)$$

All other coefficients and the variable W are affected by local conditions in the grid and are defined in discrete form at the grid locations x^i . From this, a centered finite-difference scheme is developed and given by

$$\frac{W^{i-1} - 2W^i + W^{i+1}}{\Delta x^2} + \left[\frac{(k^2 - m^2)p}{f^i} + \frac{f_z^2}{4f^{i^2}} - \frac{f_{zz}}{2f} \right] W^i = 0 \quad (6.19)$$

where

$$f_z = \frac{f^{i+1} - f^{i-1}}{2\Delta x} \quad f_{zz} = \frac{f^{i+1} - 2f^i + f^{i-1}}{\Delta x^2} \quad (6.20)$$

The scheme may be simplified by

$$A^i W^{i-1} + B^i W^i + C^i W^{i+1} = 0 \quad ; \quad i = 2, 3, \dots, n-1 \quad (6.21)$$

where

$$A^i = 1 \quad (6.22)$$

$$B^i = -2 + \Delta x^2 \left[\frac{(k^2 - m^2)p}{f^i} + \frac{f_z^2}{4f^{i^2}} - \frac{f_{zz}}{2f} \right] \quad (6.23)$$

$$C^i = 1 \quad (6.24)$$

The bed undulations are subject to the restriction that they do not affect the wave in the locale of either boundary in order that the waves radiating at the boundary are not interacting with the rapid variations. Thus it is required that

$$\delta^1 = \delta^2 = \delta^{n-1} = \delta^n = 0 \quad (6.25)$$

Expressing the boundary conditions in finite difference form, equation 6.15 is

$$W^n = 0 \quad (6.26)$$

Defining 6.29 in the finite difference form

$$B^n = 1 \quad (6.27)$$

$$A^n = 0 \quad \text{and} \quad C^n = 0 \quad (6.28)$$

At station x_1 the boundary condition may be restated as

$$(1 + \alpha^1)W^2 - (1 - \alpha^1)W^1 = 2f^{1/2}a(m)\alpha^1[e^{2\alpha^1} + 1] \quad (6.29)$$

where

$$\alpha^1 = \frac{i\Delta x}{2}i^1 \quad (6.30)$$

and it is assumed the incident wave is described by

$$\eta_i(x) = a(m)e^{i1(x-x_1)} \quad (6.31)$$

Again, putting 6.34 into the finite difference form, gives

$$B^1 = -(1 - \alpha^1) \quad (6.32)$$

$$C^1 = 1 + \alpha^1 \quad (6.33)$$

$$D^1 = 2f^{1/2}a(m)\alpha^1[e^{2\alpha^1} + 1] \quad (6.34)$$

The problem may be written in the form of a linear matrix equation

$$AW = D \quad (6.35)$$

where D is a column vector with $D^2 - DW = 0$, η is a column vector with elements $W^1 - W^n$, and A is a tridiagonal matrix with diagonal vectors A^i , B^i and C^i . The solution is again obtained using the double sweep algorithm as given by Carnahan, Luther and Wilkes (1969).

The reflection coefficient may be determined once the solution for W is obtained. The reflection coefficient may be extracted directly since W is a propagating term and f will be the same for the $+x$ and $-x$ propagating components at any particular point. Two estimates for the reflection coefficient R are obtained at x_1 . From equation 6.34 W_r at x_1 may be written

$$W_r^1 = W^1 - a(m) \quad (6.36)$$

$$W_r^2 = W^2 - a(m)e^{2\alpha^1} \quad (6.37)$$

Define the two estimates for reflection coefficients as

$$R_1 = \frac{|W_r^1|}{a(m)} \quad (6.38)$$

$$R_2 = \frac{|W_r^2|}{a(m)} \quad (6.39)$$

and R as the average of R_1 and R_2 . This calculation, however, is trivial for this solution, since no damping due to bottom friction exists in the present solution, no energy is dissipated in breaking in linear theory, and no energy is transmitted past the shoreline. Therefore, in order that energy be conserved, the energy carried by the reflected wave must be equal and in opposite direction to the energy carried by the incident wave in steady state.

Since the boundary condition at the shoreward end of the domain is restricted to keep η bounded, the response at the shoreline may be estimated by extrapolating the surface displacement directly seaward of the shoreline by

$$\eta^n = \eta^{n-1} + \frac{\eta^{n-1} - \eta^{n-2}}{\Delta x} \Delta x \quad (6.40)$$

which can easily be seen reduces to

$$\eta^n = 2\eta^{n-1} - \eta^{n-2} \quad (6.41)$$

where

$$|\eta^i| = \left| \frac{W^i}{\sqrt{f^i}} \right| \quad (6.42)$$

Additionally, from 6.45 the magnitude of the surface displacement in the domain may be calculated.

6.4 Model Tests and Examples

6.4.1 Response Over a Barfield in Front of a Wall

In order to verify the validity of the model formulated above, it will first be compared to a case that the model in the form of equation 6.4 can easily handle. This would be the case where the restriction

$$\frac{\partial \eta}{\partial x} = 0 \quad (6.43)$$

is valid. This boundary condition is required for a wave field at a vertical wall. In the finite difference scheme, the boundary condition is applied by

$$\eta^n - \eta^{n-1} = 0 \quad (6.44)$$

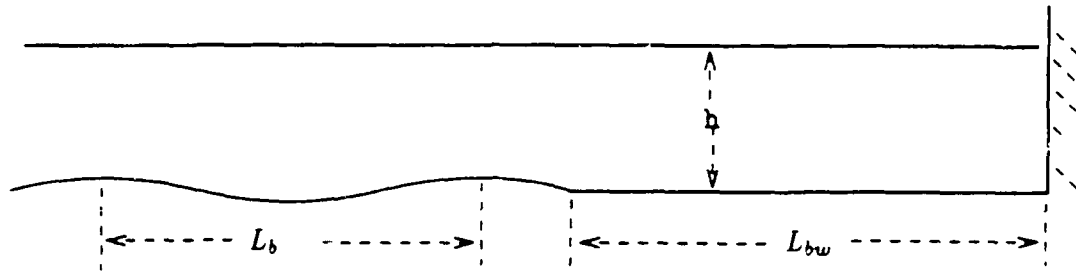


Figure 6.1: Definition sketch of bar field in front of a wall

so

$$A^n = -1 \quad \text{and} \quad B^n = 1 \quad (6.45)$$

The results for a wave at normal incidence where $2k/\lambda = 1$ with λ being the fundamental mode ($\lambda = 2\pi/L_b$) of the barfield described by

$$h = \begin{cases} 0.05 \sin(2\pi x); & 0 + nl_b \leq x \leq 0.5 + nl_b \\ 0.0; & 0.5 + nl_b \leq x \leq nl_b \end{cases} \quad n = 0, 1, 2, 3 \quad (6.46)$$

l_b = bar spacing

The bottom otherwise is assumed flat.

Also, the length L_{bw} between the barfield and wall is defined as a function of L_b

$$L_{bw} = L_b d \quad (6.47)$$

where d is any real value. The domain is depicted in Figure 6.1.

Let $d = 4$, an integer value, such that the wall rises 2 surface wavelengths (for the resonant case) past the barfield. The incident wave is arbitrarily set at 1 since linear theory is being used. Also, the absolute value of the wave field is being plotted below, thus no phase shifting or time dependence is evident. The results plotted in Figure 6.2 show the wave envelope as calculated by both schemes for the resonant condition. The amplitude of the wave at the wall boundary is plotted in Figure 6.3 as a function of $2k/\lambda$.

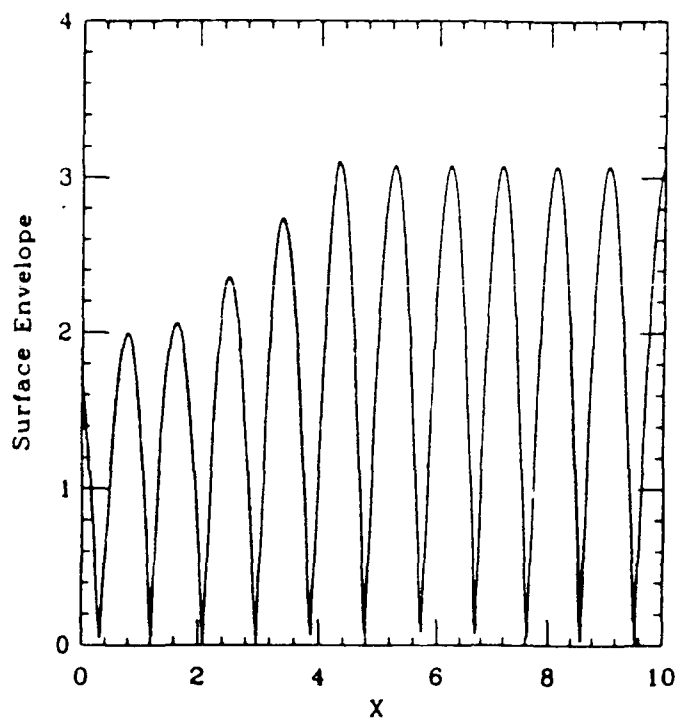


Figure 6.2: Wave envelope in front of a wall for η directly and $\eta = f^{-1/2}W$ numerical schemes, $d = 4$

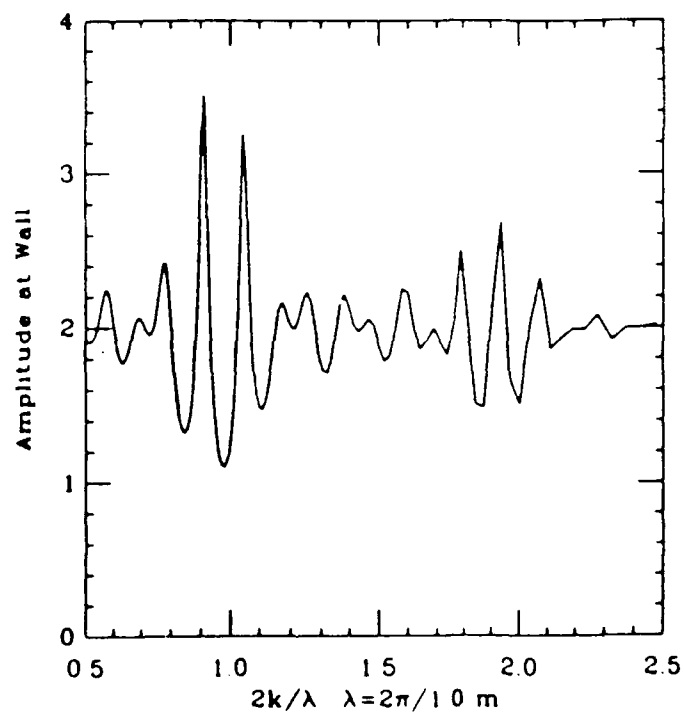


Figure 6.3: Wave amplitude at the wall for η directly and $\eta = f^{-1/2}W$ numerical schemes, $d = 4$

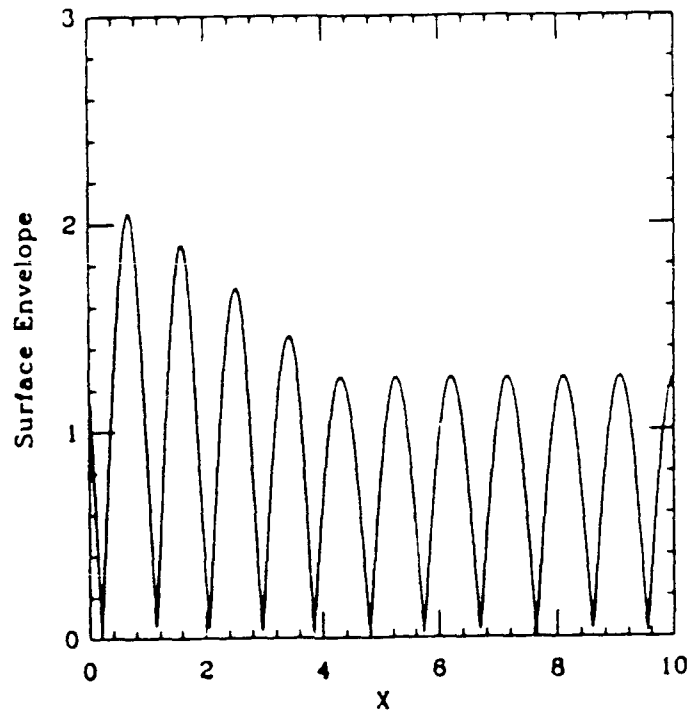


Figure 6.4: Wave envelope in front of a wall for η directly and $\eta = f^{-1/2}W$ numerical schemes, $d = 4.5$

Now let $d = 4.5$, such that barfield lies 2.25 surface wavelengths in front of the wall. The wave envelope for this case is plotted in Figure 6.4 and the maximum displacement at the wall in Figure 6.5.

It can clearly be seen that the choice of L_{bw} can have drastic effects on the wave field between the barfield and the wall. What seems to be happening is if the spacing is an integer multiple of half of a surface wave length, the wave field becomes trapped between the bars and the wall. This would be due to tertiary reflection of the wave field, primary being offshore reflection, secondary being reflection off the wall and tertiary being the reflection by the barfield of the wave reflected off the wall. The final effect is the standing wave in front of the wall is resonated, and potentially quite violent oscillations may occur.

6.4.2 Response Over a Barfield in Front of Beach

From the above section, it is seen that the new form of the mild slope equation is valid. Now, attention is restricted to the case where a barfield is placed on a mild slope and waves

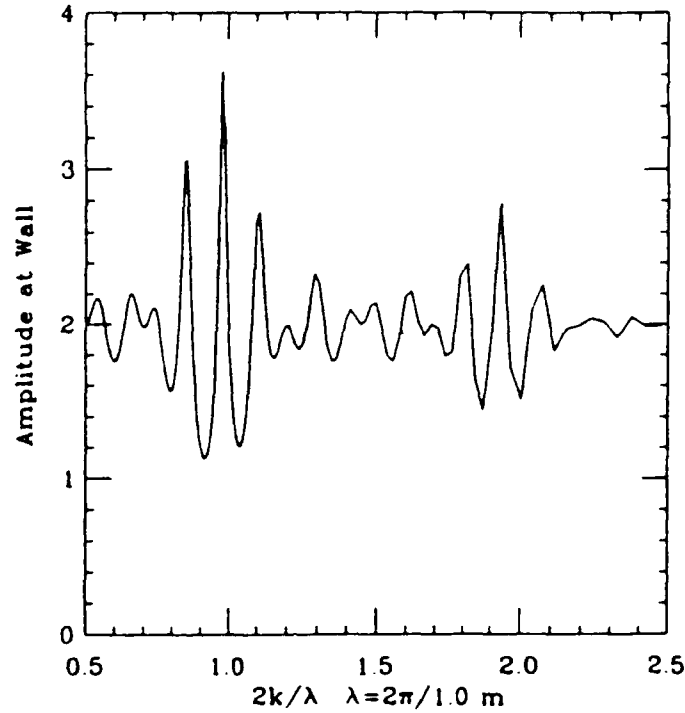


Figure 6.5: Wave amplitude at the wall for η directly and $\eta = f^{-1/2}W$ numerical schemes, $d = 4.5$

are allowed to propagate to the shoreline. It is assumed that no breaking occurs as the wave shoals and no attenuation due to bottom friction is present. The solution of the equation in the form of 6.4 cannot be used since unrealistic restrictions on η_x at the shoreline are required. The finite difference scheme developed in section 6.3 is now employed with its pertinent boundary condition at the shoreline. The adjusted domain can be seen in Figure 6.6.

Since the bottom is sloping, and the wavelength changes as the wave shoals, the exact value of L_{bw} that would result in strong tertiary reflection is not as easily determined. However, wave envelopes are plotted for the same frequency near resonance for two choices of d . The bottom is plotted below the envelopes. The bottom parameters, except d , are identical for both cases where, $h = .15m$, the bumps, shaped $\delta(x) = 0.05m \sin 2\pi/0.5m$ for the positive branch only, are spaced $1.0m$ apart. For Figure 6.7 $d = 10.0$, and $d = 10.5$ for figure 6.8.

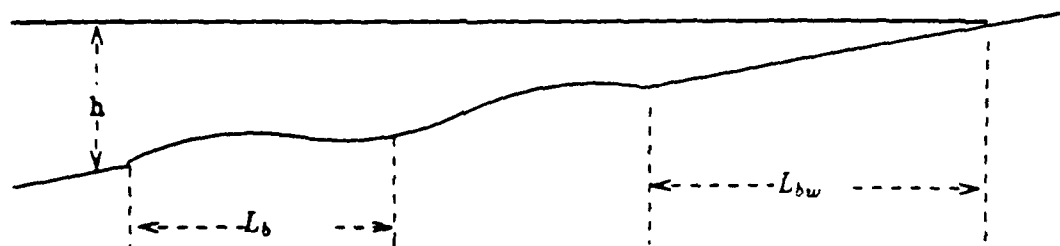


Figure 6.6: Definition sketch of bar field on a sloping bottom in front of a shoreline

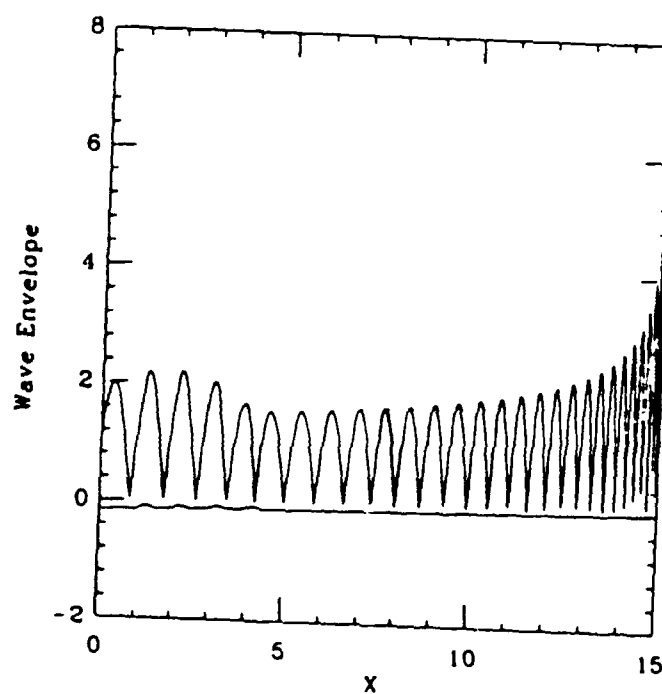


Figure 6.7: Wave envelope on a sloping beach with 4 sine shaped bumps, $d = 10.0$

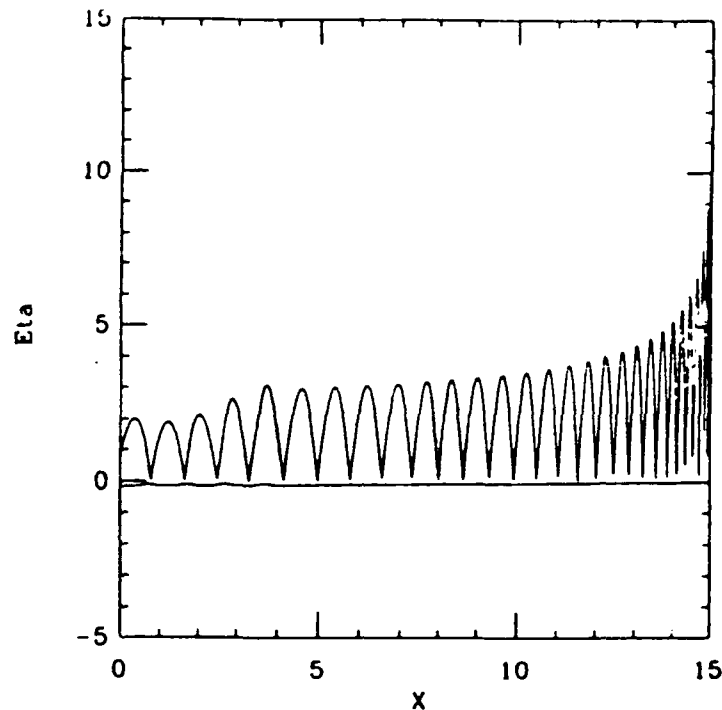


Figure 6.8: Wave envelope on a sloping beach with 4 sine shaped bumps, $d = 10.5$

Lastly, for the two cases above, the amplitude at the shoreline is plotted against $2k/\lambda$ in Figures 6.9 and 6.10.

Looking at the last two plots, it can be seen that very small changes in frequency will change the resonant response between the barfield and shoreline drastically. Since the response at the shoreline is unreasonably large, the envelope amplitude at a point ($x=7$ m) midway between the barfield and shoreline will be plotted in Figures 6.11 and 6.12.

The wave envelope again is sensitive to small changes in frequency, yet the trapped wave amplitudes are a bit more believable at this point in the wave field. However, it is also clearly evident that the presence of the barfield can cause large standing waves in the nearshore zone. Interpreting the plots, any surface displacement above 2 (the incident wave amplitude of 1 superimposed on the reflected wave amplitude) would be identified as a trapped mode.

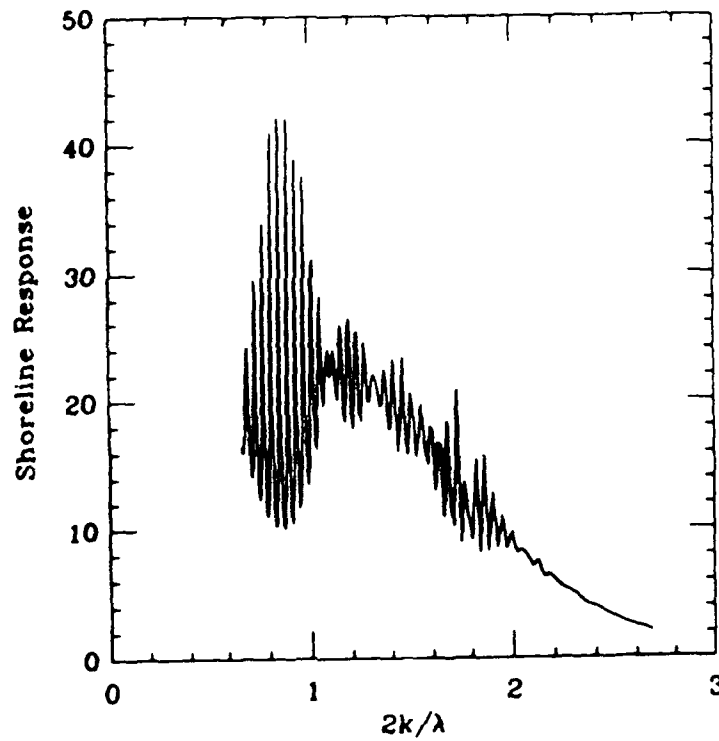


Figure 6.9: Wave amplitude at the shoreline vs. $2k/\lambda$, $d = 10.0$

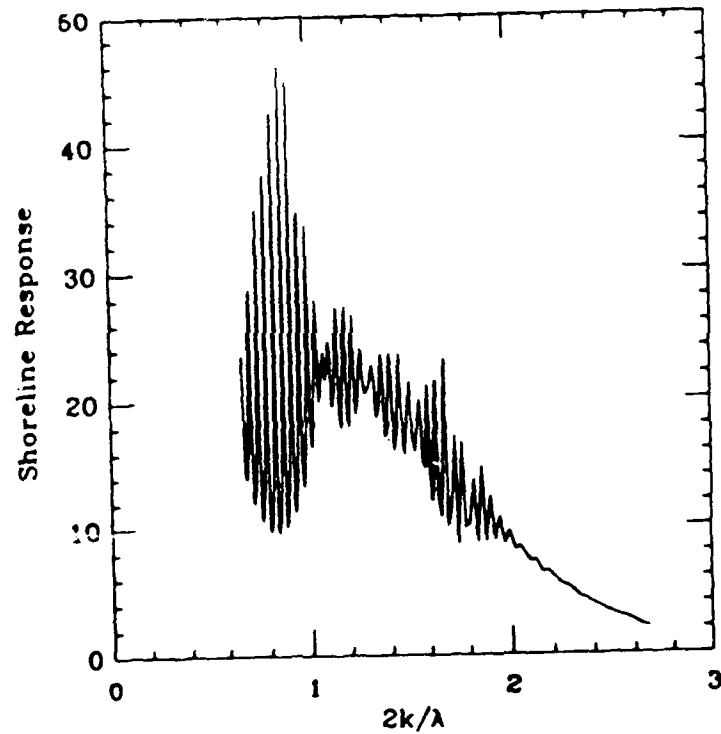


Figure 6.10: Wave amplitude at the shoreline vs. $2k/\lambda$, $d = 10.5$

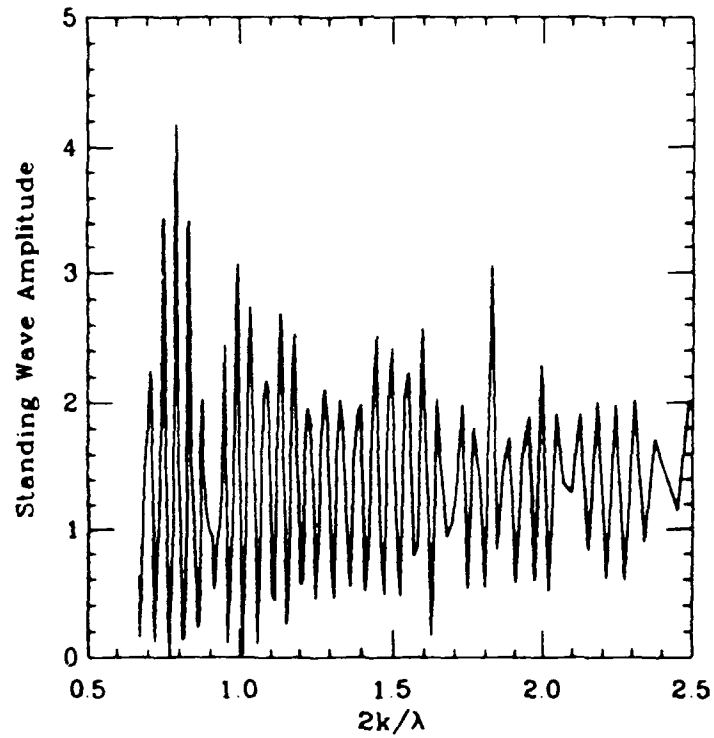


Figure 6.11: Wave amplitude at $x = 7$ m vs. $2k/\lambda$, $d = 10.0$

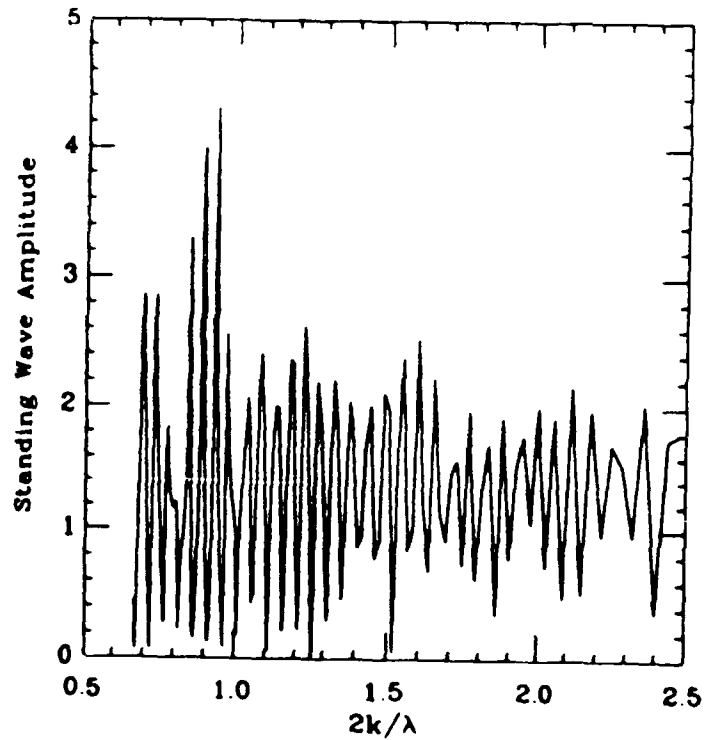


Figure 6.12: Wave amplitude at $x = 7$ m vs. $2k/\lambda$, $d = 10.5$

6.5 Conclusions

In the previous section, it was pointed out that the installation of a bar field described may cause the trapping of waves in the nearshore zone. The calculations made were done assuming no energy dissipation due to breaking or bottom friction, which may reduce the resulting large amplitudes considerably. It may be surmised from the results that the standing wave between the bars and shoreline may cause shoreward growth of the barfield, just as it has been hypothesised that the standing wave seaward of the bars may cause seaward growth of the barfield. This phenomena has been observed in the laboratory using a barfield placed on a sand bottom by McSherry (1989).

CHAPTER 7 CONCLUSIONS

In this thesis, an extension to non-resonant interaction theories was developed to accommodate oblique incidence and seabeds of other than sinusoidal shape, specifically, a series of cosine bumps on a flat bottom. The new theory was compared to existing theories for normal and oblique incidence. Agreement between all theories for arbitrary bottoms was fair.

Additionally, the numerical solution of a complete governing equation for undulations on a mild slope was compared to laboratory data. The comparison shows a slight shift in frequency at resonant peaks. This may be due to inadequate description of the bottom boundary condition used in the solution. Included in the laboratory study was an application of using spectral analysis to determine the incident and reflected wave energies for a monochromatic wave field.

Finally, an investigation of wave fields between a barfield and beach was performed. The numerical predictions, although neglecting wave damping and nonlinearities, show the potential for large amplitude trapped modes between the barfield and shoreline. It is apparent additional work in this application is necessary before implementing prototypes in the environment.

BIBLIOGRAPHY

- Berkhoff, J.C. (1972), "Computation of Combined Refraction- Diffraction," In Proc. 13th Intl. Conf. Coastal Engineering, V. 2: 471-490
- Benjamin, T.B., Karakiewicz, B., and Pritchard, W.G. (1987) "Reflection of Water Waves in a Channel with a Corrugated Bed," *Journal of Fluid Mech.* V. 85: 249-274
- Carnahan, B., Luther, H.A., and Wilkes, J.O. (1969) Applied Numerical Methods Wiley, New York
- Carter, T., Liu, P., and Mei, C.C. (1972) "Mass Transport by Water Waves," *Water Resources and Hydrodynamics Report No. 146*, Cambridge, MA
- Davies, A.G. (1982) "On the Interaction Between Surface Waves and Undulations on the Seabed," *Journal of Marine Research*, V. 20:2 331-368
- Davies, A.G., Guazzelli, E., and Belzons, M. (in press), "Propagation of Long Waves Over an Undulating Bed," *Physics of Fluids*
- Davies, A.G., and Heathershaw, A.D. (1984), "Surface-wave Propagation Over Sinu- soidally Varying Topography," *Journal of Fluid Mechanics*, V. 144: 419-443
- Dean, R.G., and Dalrymple, R.A. (1984), Water Wave Mechanics for Engineers and Scientists, Prentice-Hall, Englewood Cliffs, N.J.
- Evans, O.F. (1940), "Classification of Wave Formed Ripple Marks," *Journal of Sedimen- tary Petrology*, V. 11 No. 1 37-41
- Funke, E.R., and Mansard, E.R.D. (1980) "Measurement of Incident and Reflected Spec- tra Using a Least Squares Approach," *Proc. of 17th Coastal Conference*, V. 1 154-172
- Heathershaw, A.D. (1982), "Seabed-Wave Resonance and Sand Bar Growth," *Nature*, V. 296: 343-345
- Heathershaw A.D., and Davies, A.G. (1985), "Resonant Wave Reflection by Transverse Bedforms and its Relation to Beaches and Offshore Bars," *Marine Geology*, V. 62: 321-338
- Kirby, J.T. (1986), "A General Wave Equation For Waves Over Rippled Beds," *Journal of Fluid Mechanics*, V. 162: 171-186
- Kirby, J.T. (1987), "A Program For Calculating the Reflectivity of Beach Profiles," Uni- versity of Florida UFL/COEL-87/004

- Kirby, J.T. (1989), "Propagation Of Surface Waves Over an Undulating Bed," submitted to Physics of Fluids
- Liu, P.L.-F., Yoon, S.B., and Kirby, J.T. (1985), "Non-linear Refraction-Diffraction of Waves in Shallow Water," Journal of Fluid Mech., V. 153: 185-201
- McSherry, T.R. (1989) "Wave Current Interactin Over a Submerged Bed," Thesis, University of Florida
- Mei, C.C. (1985), "Resonant Reflection of Surface Water Waves by Periodic Sandbars," Journal of Fluid Mech., V. 152: 315-335
- Mei, C.C., Hara, T., Naciri, M. (1988), "Note on Bragg Scattering of Water Waves by Parallel Bars on the Seabed," Journal of Fluid Mech., V. 186: 147-162
- Miles, J.W. (1981), "Oblique Surface-Wave Diffraction by a Cylindrical Obstacle," Dynamics of Atmospheres and Oceans, V. 6: 121-123
- Naciri, M., and Mei, C.C. (1988), "Bragg Scattering of Water Waves by a Doubly Periodic Seabed," Journal of Fluid Mech., V. 192: 51-74
- Smith, R., and Sprinks, T. (1975) "Scattering of Surface Waves by a Conical Island," Journal of Fluid Mech., V. 72: 373-384
- Yoon, S.B., and Liu, P. (1987) "Resonant Reflection of Shallow Water Waves Due to Corrugated Boundaries," Journal of Fluid Mech. V. 180: 451-469

Appendix C: Nonresonant and resonant reflection of long waves in varying channels

Journal of Geophysical Research, 93, 10782-10796, 1988.

NONRESONANT AND RESONANT REFLECTION OF LONG WAVES IN VARYING CHANNELS

James T. Kirby and Padmaraj Vengayil¹

Coastal and Oceanographic Engineering Department, University of Florida, Gainesville

Abstract. One of the principal drawbacks associated with the use of equations of Korteweg-deVries (KdV) or Kadomtsev-Petviashvili (K-P) form to model wave propagation in a varying channel is the implicit neglect of reflection in those equations. This study formulates pairs of KdV or K-P equations which are coupled through inhomogeneity in bottom slope or channel width, and applies these equations to several propagation problems involving aperiodic and periodic wave motion. The formulation eliminates the neglect of reflection effects in the single KdV or K-P equation approach. Forms of the KdV equations are given which totally account for mass flux balance between the incident and reflected wave. We then examine several cases involving waves propagating in variable channels and compare model results to previously available data.

1. Introduction

Evolution equations for weakly dispersive waves in the form of the Korteweg-deVries (KdV) or Boussinesq equations have long been known to be reasonably good predictors of wave form and propagation in channels of uniform and shallow depth, with the Boussinesq equations being able to describe general two-dimensional (in plan) motions but the KdV equation or its variants being limited to strictly one-dimensional, one-way propagation. Recently, the weakly two-dimensional equation of Kadomtsev and Petviashvili [1970] (K-P), which describes nearly one-dimensional propagation with weak transverse modulation, has been added to the arsenal of equations describing uniform depth motion.

Recently, interest in shallow water wave motion has been extended to the consideration of shoaling and other effects due to propagation in an inhomogeneous domain. This interest has led to a number of variable depth extensions to the evolution equations listed above. Peregrine [1967] has provided a variable depth extension to the Boussinesq equations which allows for the shoaling and reflection of waves incident on a bottom slope. Peregrine's and other equations of similar form may be regarded as general models for two-dimensional propagation in regions of gradually varying depth. Variable depth forms of the KdV equation have also been developed which similarly allow for shoaling effects in one-dimensional propagation; a relevant form of equation of this type is chosen for this study from the work of

Svendsen and Buhr Hansen [1978]. Liu et al. [1985] have similarly provided a variable depth form of the K-P equation and have applied that equation to the study of wave focusing and refraction by variable topography; a derivation of the variable-depth K-P equation appearing in that study is given here.

Despite their usefulness in describing the evolution of the dominant incident wave over topography, the KdV and K-P equations are considered by a number of investigators to be flawed, since the reflected wave is implicitly neglected and hence may be constructed only after identification of a mass sink in the incident wave, which then serves as a source for the reflected wave calculation [Miles, 1979; Knickerbocker and Newell, 1985]. The purpose of this study is to derive a set of coupled evolution equations for incident and reflected waves which account for mass exchange directly, and thus restore the direct applicability of the KdV and K-P equations in regions where strong reflection may significantly affect wave evolution.

In section 2 we outline a scheme for constructing coupled equations of KdV or K-P form using a heuristic approach based on the method of operator correspondence. Domain inhomogeneity is limited to variations in still water depth. In section 3 we turn our attention to propagation in channels and extend the KdV form of the equation to include variations in channel width as well as depth. Development of the model equations in mass-conserving form is considered in section 4. In section 5 the ability of the model to predict reflection is tested by comparison with the previous results of Goring [1978], who studied transmission and reflection of solitary waves at a sloping step. In section 6, examples of the scattering of a solitary wave in a channel with gradually varied width are given, and the influence of mass balance effects on wave evolution in the study of Chang et al. [1979] are investigated. Finally, in section 7 we turn to the problem of scattering of periodic waves by periodic bottom disturbances, and extend the study of the gradual reflection of a cnoidal wave by a sinusoidal bed started recently by Yoon and Liu [1987]. Two-dimensional calculations based on the K-P forms of the model equations will be reported separately.

2. Reflection From Varying Bottom Topography

The goal of this section is to derive a set of coupled equations of KdV or K-P type to model the forward-scattered and backscattered wave trains in a variable domain and to describe the exchange of energy between the waves due to interaction with bottom topography. The derivation is based on heuristic arguments and is aided by several key points. First, we neglect nonlinear interactions between incident and reflected waves to the order of terms considered. In particular, consideration

¹ Now at Civil Engineering Department, Massachusetts Institute of Technology, Cambridge.

of the three-wave resonance conditions for opposite going periodic waves shows that no resonant interaction takes place between the waves at the order of quadratic nonlinearity. For the different case of aperiodic waves such as solitary waves, previous results (Maxworthy [1976] and Sol and Mirie [1980], among others) have documented a phase-shifting, nonlinear interaction between colliding solitary waves. The present formulation neglects this possibility, which should not be of importance in the present study of reflection because of the expected smallness of the reflected wave, $O(\epsilon\alpha)$, relative to the incident wave at $O(\epsilon)$, where α characterizes a bottom slope or channel width variation. (The case of resonant reflection of periodic waves represents reflection $\sim O(\epsilon)$; however, the conclusion on three-wave interactions covers this case.)

The scaling for weakly nonlinear, weakly dispersive shallow water waves in a varying domain is

$$O(\epsilon) = O(u^2) = O(\alpha) \ll 1$$

where ϵ denotes nonlinear effects and is characterized by $\max(|\eta|/h)$, u^2 denotes dispersive effects and is proportional to $\omega^2 h/g$, and α characterizes maximum bottom slope. Further, η is the surface displacement, h is water depth, g is gravitational acceleration, and ω is a characteristic frequency. It is clear that under the scaling used here, nonlinear, dispersive, and wave-bottom coupling effects need only appear at leading order in equations involving all three effects. As a consequence, the coupling due to bottom slope effects may be derived directly from the nondispersive linear wave equation for variable depth, after which the terms describing nonlinearity and dispersion may be added in a consistent manner.

The method of operator correspondence is used to derive the set of coupled linear equations describing wave-bottom coupling effects. The general wave equation describing the propagation of linear, nondispersive waves over a variable topography is given by

$$\eta_{tt} - g \nabla_h \cdot (h \nabla_h \eta) = 0 \quad (1)$$

where here η represents a general two-dimensional surface displacement. Substituting frequencies for time derivatives in (1) according to

$$\eta_t = -i\omega\eta; \quad \omega = (gh)^{1/2} k = ck \quad (2)$$

equation (1) is rewritten as

$$\eta_{xx} + \frac{h_x}{h} \eta_x + \gamma^2 \eta = 0 \quad (3)$$

where

$$\gamma^2 \eta = \frac{\omega^2}{gh} \eta + \frac{1}{h} (h \eta_y)_y \quad (4)$$

The surface displacement η is written as the sum of the displacements of the forward-scattered wave

traveling in $+x$ direction, η^+ , and the backscattered wave traveling in $-x$ direction, η^- . Coupled equations of the form

$$\eta_x^+ = i\gamma\eta^+ + F(\eta^+, \eta^-) \quad (5a)$$

$$\eta_x^- = -i\gamma\eta^- - F(\eta^+, \eta^-) \quad (5b)$$

are sought, where F is the desired unknown coupling function. Repeated substitution of (5) in (3) gives

$$F = -\frac{1}{2} \frac{(\gamma h)_x}{\gamma h} (\eta^+ - \eta^-) \quad (6)$$

From (4), γ is a pseudo differential operator which may be approximated by binomial expansion if the following assumption holds:

$$\frac{1}{h} \frac{\partial}{\partial y} \left(h \frac{\partial}{\partial y} \right) \ll \frac{\omega^2}{gh} \quad (7)$$

This indicates a restriction to small propagation angles with respect to the x direction. This restriction is analyzed (and the connection to the parabolic approximation is discussed) in Appendix A.

Using a binomial expansion, the general expression for γ is

$$\gamma = \frac{\omega}{c} + \frac{c}{2\omega h} \frac{\partial}{\partial y} \left(h \frac{\partial}{\partial y} \right) \quad (8)$$

To leading order, γ is given by (from Appendix A)

$$\gamma = \frac{\omega}{c} + O(\theta^2) \quad (9)$$

where θ denotes a necessarily small propagation direction with respect to the x axis, (we assume $\theta^2 = O(\epsilon)$) and hence

$$\gamma_x = -\frac{\omega}{c^2} c_x = -\frac{\omega}{2c} \frac{h_x}{h} \quad (10)$$

Using (9) and (10), equation (6) is rewritten as

$$F = -\frac{h_x}{4h} (\eta^+ - \eta^-) = -\frac{c_x}{2c} (\eta^+ - \eta^-) \quad (11)$$

The coupled equations are obtained from (5) using the expressions for F and γ and are written together as

$$\eta_x^\pm = \pm \frac{i\omega}{c} \eta^\pm \mp \frac{c_x}{2c} (\eta^+ - \eta^-) \pm \frac{ic}{2\omega h} (h \eta_y^\pm)_y \quad (12)$$

Inverting the operator form of the $i\omega\eta^\pm$ terms and further using $\omega = kc$ in the y derivative terms, (12) is written as

$$\pm ik \left\{ n_t^{\pm} \pm cn_x^{\pm} + \frac{c}{2} (n^{+} - n^{-}) \right\} = \mp \frac{1}{2c} (c^2 n_y^{\pm})_y \quad (113)$$

Allowing ik to correspond to an integral over x ,

$$\frac{1}{ik} n^{+} = \int_x n^{+} dx \quad \frac{1}{-ik} n^{-} = \int_x n^{-} dx \quad (114)$$

(113) may be rewritten as

$$- \frac{1}{ik} \pm cn_x^{\pm} + \frac{c}{2} (n^{+} - n^{-}) \mp \int_x \frac{1}{2c} (c^2 n_y^{\pm})_y dx = 0 \quad (115)$$

This corresponds to the integro-differential form of the K-P equation, which has proven to be more convenient for numerical computations (see, for example, Katsis and Akylas [1987]). The set of coupled equations (15) represents linearized, nondispersive K-P equations describing incident and reflected wave fields which are linearly coupled through the bottom slope h_x .

It may be shown by back substitution that the set of linear nondispersive equations neglecting y derivatives are completely equivalent to the one-dimensional form of (1). Similar correspondence between (15) and the original model (1) does not exist, of course, because of the binomial approximation used. For the case of localized disturbances vanishing at $x \rightarrow \pm \infty$ together with their derivatives, summing the two components of (15) (neglecting y derivatives) and integrating from $-\infty$ to $+\infty$ gives

$$\frac{d}{dt} \int_{-\infty}^{+\infty} n dx = 0 \quad (116)$$

The linear nondispersive reflection process thus conserves the total mass of displacement in the two wave trains.

The equations (15) may be extended to include weakly nonlinear, weakly dispersive effects. The variable depth KdV equation in stationary coordinates, given by Svendsen and Buhr Hansen [1978], may be written as

$$n_t + cn_x + \frac{c}{2} n + \frac{3cn}{2h} + \frac{h^2 c}{6} n_{xxx} = 0 \quad (117)$$

Equation (17) is valid for the scaling assumed here. The appropriate forms of the nonlinear term and linear dispersive term of (17) can be added directly to (15) to give the coupled equations for weakly nonlinear, weakly dispersive shallow water waves. Adding the appropriate terms in equations (115) gives the K-P type coupled evolution equations for nonlinear shallow water waves

$$n_t^{\pm} \pm cn_x^{\pm} + \frac{c}{2} (n^{+} - n^{-}) \pm \frac{3cn^{\pm}}{2h} \pm \frac{h^2 c}{6} n_{xxx}^{\pm}$$

$$\mp \int_x \frac{1}{2c} (c^2 n_y^{\pm})_y dx = 0 \quad (118)$$

The variable depth K-P equation given by Liu et al. [1985] is obtained by neglecting the coupling in (18) and differentiating with respect to x . Further, neglecting y dependence yields the desired coupled KdV equations, while further neglecting coupling recovers (17) for the incident wave alone.

To the order of approximation assumed, spatial derivatives may be replaced by time derivatives in the linear dispersive terms to improve estimates of linear dispersion. We adopt a form of the equations incorporating one time derivative in the dispersive term, leading to equations analogous to the regularized long wave (RLW) equation of Peregrine [1966] and Benjamin et al. [1972]. The resulting model for one-dimensional propagation is then taken to be

$$n_t^{\pm} \pm cn_x^{\pm} + \frac{c}{2} (n^{+} - n^{-}) \pm \frac{3cn^{\pm}}{2h} - \frac{h^2}{6} n_{xxt}^{\pm} = 0 \quad (119)$$

We further note here that the form

$$n_x = \frac{i\omega}{c} n - \frac{c}{2c} n + \frac{1c}{2wh} (hn_y)_y \quad (120)$$

from (12) may be inverted twice in time to obtain

$$n_{tt} + cn_{xt} + \frac{c}{2} n_t = \frac{1}{2} (c^2 n_y)_y \quad (121)$$

This is equivalent to the second approximation to a radiating boundary condition obtained by Engquist and Majda [1977], further extended to the case of variable depth.

3. Equations for a Gradually Varied Channel

Shuto [1974], among others, has considered an extension to the one-dimensional KdV equation for the case of waves propagating in a long channel of depth $h(x)$ and half width $b(x)$. Shuto's equation may be written in dimensional form and stationary coordinates as

$$bn_t + bcn_x + \frac{(bc)_x}{2} n + \frac{3bc}{2h} nn_x + \frac{bch^2}{6} n_{xxx} = 0 \quad (122)$$

The extension to Svendsen and Buhr Hansen's [1978] equation to account for varying channel width is readily apparent. In this section, we extend (22) to account for reflections from changes in channel width as well as depth.

Starting with the linear wave equation (7), we impose lateral boundary conditions

$$n_y - b_x n_x = 0 \quad y = \pm b(x) \quad (123)$$

Integrating (1) from $y=-b$ to b , applying Leibnitz rule, and assuming cross-channel variations of n

to be weak enough to ignore, we obtain an integrated wave equation given by

$$\eta_{tt} - \frac{1}{b} (ghb\eta_x)_x = 0 \quad (24)$$

Following the procedure of section 2, we expand (24) and employ operator correspondence in the time domain to obtain

$$-\eta_{xx} + \frac{(bh)_x}{bh} \eta_x + \gamma^2 \eta = 0 \quad (25)$$

where now γ^2 is given simply by

$$\gamma^2 \eta = \frac{u^2}{gh} \eta \quad (26)$$

Employing the procedure of section 2 leads to coupled equations of the form (5) with $F(\eta^+, \eta^-)$ given by

$$F = -\frac{(bc)_x}{2bc} (\eta^+ - \eta^-) \quad (27)$$

Use of (27) in the coupled equations along with

$$\eta = \frac{u}{c(x)} \eta \quad (28)$$

then leads directly to the coupled linear equations

$$\frac{1}{c} \eta_t^\pm = \pm \eta_x^\pm + \frac{(bc)_x}{2bc} (\eta^+ - \eta^-) = 0 \quad (29)$$

Assuming bottom slope and width changes to be small, we consistently add dispersive and nonlinear effects to obtain

$$b\eta_t^\pm \pm bc\eta_x^\pm \pm \frac{(bc)_x}{2} (\eta^+ - \eta^-) \pm \frac{3bc}{2h} \eta^\pm \eta_x^\pm \pm \frac{bch^2}{6} \eta_{xxx}^\pm = 0 \quad (30)$$

Neglecting coupling in each component equation of (30) leads to two separate equations of Shuto's type describing waves propagating in each direction in the unchannel. The coupling term implies that any varying channel whose variations maintain the constancy of bc is completely transparent to the passage of a wave, even though the wave itself undergoes evolution due to variations in $h(x)$. As was the case with the results of section 2, the model equations (30) may be arbitrarily altered to RLW form.

4. Mass-Conserving Forms of the KdV Equations

The sets of coupled KdV equations (21) and (30) may be written in forms which lead to exact conservation of mass in the total wave system, to

the level of the approximation used here, following the arguments of Miles [1979]. Rearranging the nonlinear and dispersive terms in (30) gives

$$(b\eta^\pm)_t \pm bc\eta_x^\pm + \frac{(bc)_x}{2} (\eta^+ - \eta^-) \pm \left\{ \frac{3bc\eta^\pm}{4h} + \frac{bch^2}{6} \eta_{xxx}^\pm \right\}_x = 0(c\alpha, u^2\alpha) \quad (31)$$

Terms appearing on the right-hand sides of (31) are formally small with respect to the present approximation and may be dropped, leaving the proposed mass-conserving form of the equation. Corresponding results for a channel of constant width follow by setting $b = 1$.

For the case of disturbances η^\pm which vanish as $|x| \rightarrow \infty$, mass conservation in the total system follows simply by adding the component equations of (31) and then integrating over x , to obtain

$$\frac{d}{dt} \int_{-\infty}^{\infty} b(\eta^+ + \eta^-) dx = \frac{d}{dt} \int_{-\infty}^{\infty} bndx = 0 \quad (32)$$

An alternate arrangement of equations (31) and integration from some fixed position x_0 to ∞ yields the relations

$$\frac{d}{dt} \int_{x_0}^{\infty} (b\eta^\pm) dx = \pm \tilde{Q}^\pm \pm \frac{1}{2} \int_{x_0}^{\infty} (bc)_x \eta^\pm dx \quad (33)$$

where

$$\tilde{Q}^\pm(x_0) = \left\{ bc\eta^\pm + \frac{3bc\eta^{\pm 2}}{4h} + \frac{bch^2}{6} \eta_{xxx}^\pm \right\}_{x_0} \quad (34)$$

represents flux of mass across station x_0 into $x > x_0$. The integral term on the right-hand side of (33) represents the sink or source of mass flux into or out of each wave system, which is seen to be equal and opposite in sign for each equation, indicating equivalence of interchanged mass in each subsection of the x interval. For the case of weak reflection, $0|\eta^-| \ll 0|\eta^+|$, the integral on the right hand sides of (33) reduces to the approximate form

$$\int_x^\infty (bc)_x \eta^\pm dx = \int_x^\infty (bc)_x \eta^\pm dx + O(\epsilon^2\alpha) \quad (35)$$

We note that Miles [1979], who analyzed Shuto's one-way equation, gave the mass flux $Q^+(x)$ as

$$Q^+(x) = \tilde{Q}^+(x) + \frac{1}{2} \int_x^\infty (bc)_x \eta^+ dx \quad (36)$$

and then identified the approximation in (35) as the principal source of mass to the reflected wave because of its dominance of the term $Q^+(x)$ as $x \rightarrow -\infty$. This interpretation arises naturally here through the analysis of the corresponding equation for the reflected wave motion, with the addition that the integral may be immediately identified as a source-sink mechanism without the intermediate analysis of residual fluxes. In

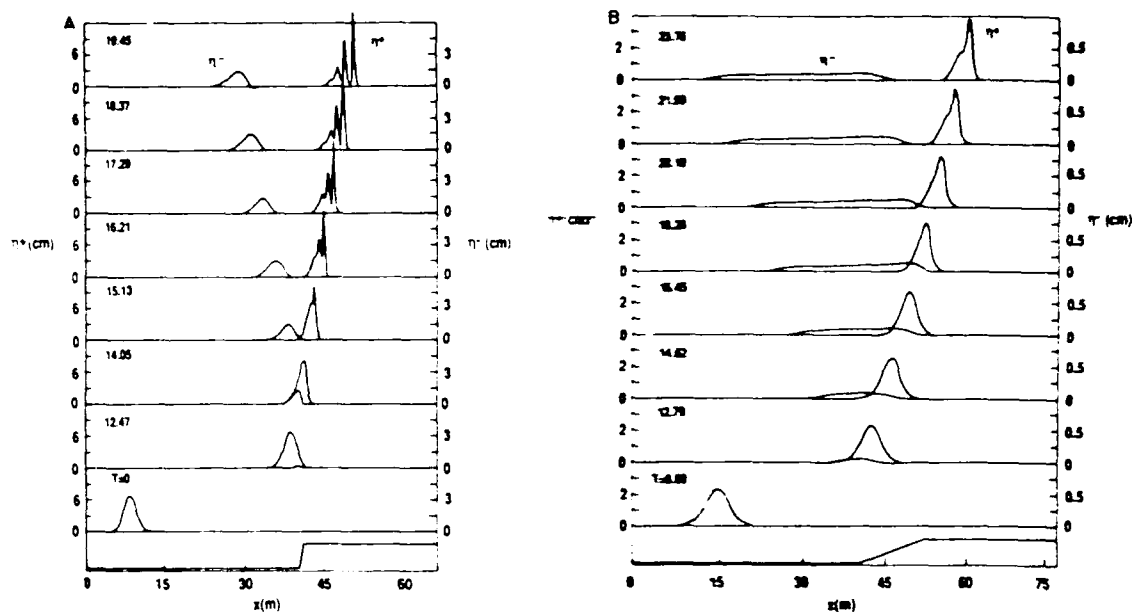


Fig. 1. Reflection and transmission of a solitary wave propagating onto a shelf. (a) $H_1/h_1 = 0.15$, $L/l = 0.5$, $h_1/h_2 = 3.0$. (b) $H_1/h_1 = 0.05$, $L/l = 4.0$, $h_1/h_2 = 3.0$.

addition, we obtain the complete feedback between the reflected and incident wave through the unapproximated form of (35).

In the following, we use the mass-conserving equations (31) written in RLW form, which gives

$$bn_{\pm}^{\pm} \pm bcn_{\pm}^{\pm} + \frac{(bc)x}{2} (n^{+} - n^{-}) \pm \left(\frac{3bcn_{\pm}^{\pm 2}}{4h} \mp \frac{bh^2}{6} n_{\pm}^{\pm} \right)_{\pm} = 0 \quad (37)$$

The corresponding nonconservative forms are obtained from (30) after multiplying by bc . The numerical scheme used in the following two sections is a simple extension of the three-level, implicit scheme developed by Eilbeck and McGuire [1975], extended to account for variable coefficients. Details are omitted and may be found in the work of Vengayil and Kirby [1986] for the nonconservative forms of the RLW equations.

5. Solitary Waves Propagating Onto a Shelf

We first test the ability of the linear coupling mechanism to calculate reflection. An accurate set of measurements of reflections from a solitary wave propagating over a slope is available from the study of Goring [1978]. We consider waves of initial height H_1 , in water of depth h_1 , which propagate into water of depth h_2 over a linear transition of length L and slope $(h_1 - h_2)/L$. The depth transitions considered here are fairly short ($L/l = O(1)$, where l is a characteristic wave length) and the mass balance corrections discussed in the preceding section are not significant, with results of conservative and non-conservative calculations agreeing to within 1-2%.

5.1. Reflected Waves

The independent length scales involved in the reflection problem are the incident wave height H_1 , upstream water depth h_1 , downstream water depth h_2 , and slope length L . The reflected wave height is given by H_R . A characteristic horizontal length l of a solitary wave is completely defined by the incident wave height H_1 and upstream depth h_1 , and is defined by Goring [1978] as

$$l = 1.5 (H_1/h_1)^{-1/2} h_1 \quad (38)$$

The reflection process is characterized by three nondimensional parameters; the relative incident wave height, H_1/h_1 , the length ratio L/l , and the depth ratio, h_1/h_2 . Choosing specific values for the nondimensional parameters L/l and h_1/h_2 characterizes the slope as mild or steep.

In Figure 1a, an example of the propagation of an incident wave of $H_1/h_1 = 0.15$ over a fairly steep slope of $L/l = 0.5$ and $h_1/h_2 = 3$ is presented. As the wave propagates up the slope, a reflected wave similar in shape to the incident wave and nearly a fifth of the incident wave amplitude emerges. As it propagates on the shelf, the transmitted wave disintegrates into a series of solitary waves with the leading wave being the largest. The mildly sloping shelf shown in Figure 1b produces a reflected wave which is less peaked than the incident wave. The rear end of the wave shows a higher amplitude, indicating an increase in reflection as the incident wave moves up the slope. For this case, $L/l = 4.0$, $h_1/h_2 = 3$, and $H_1/h_1 = 0.05$. Goring [1978] presented an extensive study of the effect of the length ratio L/l on the shape of the reflected wave. Results obtained in the present study are in excellent

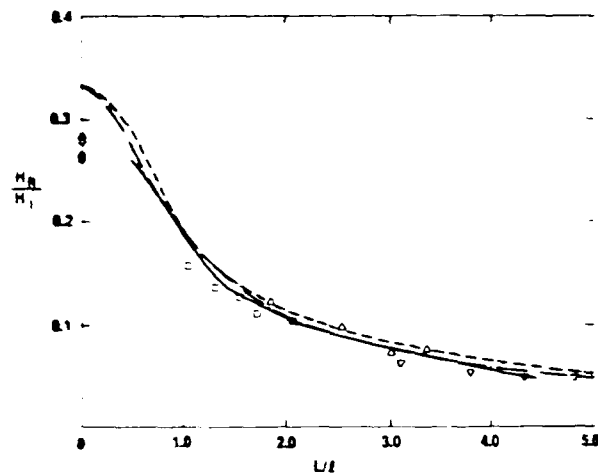


Fig. 2. Variation of reflection coefficient H_R/H_I with length ratio L/l , for a depth ratio $h_1/h_2 = 4.0$. The solid line shows the present results, the dashed line shows Goring's [1978] nonlinear dispersive results, and the dashed-dotted line shows Goring's [1978] linear nondispersive results. Data from Goring [1978].

agreement with the results obtained by Goring [1978] using linear nondispersive theory.

In Figure 2, the reflection coefficient H_R/H_I is plotted as a function of the length ratio L/l , for a solitary wave of $H_I/h_1 = 0.1$ and a depth ratio $h_1/h_2 = 4$. The reflection coefficients are compared with Goring's nonlinear dispersive and linear nondispersive theories and with his experimental results for various slopes and relative incident wave heights. The numbers next to the points indicate the values of the relative incident wave height H_I/h_1 . Since the coupled evolution equations are valid only for mildly varying topographies, slopes with length ratio L/l

0.25 are not considered. In all cases the present theory underpredicts the reflection coefficient when compared with Goring's nonlinear dispersive theory, but it is in reasonable agreement with results of Goring's linear nondispersive theory. The effect of the relative incident wave height on wave reflection is seen to be almost negligible from the results presented in Table 1, where reflections computed by the present method are compared with Goring's results obtained using linear nondispersive theory.

TABLE 1. Reflection Coefficients H_R/H_I for Various Length Ratios L/l and Relative Incident Wave Heights H_I/h_1 for the Depth Ratio $h_1/h_2 = 3.0$

L/l	H_I/h_1		
	0.05	0.10	0.15
0.53	0.214 (0.218)	0.212	0.212
1.03	0.151 (0.152)	0.155	0.155
1.56	0.108 (0.110)	0.106	0.111
2.00	0.088 (0.089)	0.087	0.0995

Goring's [1978] linear results are given in parentheses.

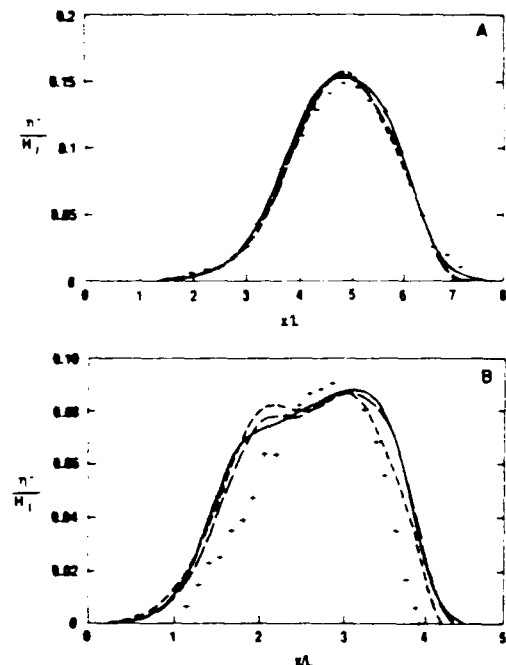


Fig. 3. Comparison of numerical reflected wave profiles with experimental results of Goring [1978] for (a) $L/l = 1$, and (b) $L/l = 2$. Numerical results are shown for $H_I/h_1 = 0.05$ (solid line), $H_I/h_1 = 0.10$ (long-dashed line), and $H_I/h_1 = 0.15$ (short-dashed line), and experimental results are shown for $H_I/h_1 = 0.0522$ (pluses).

In Figure 3 the predicted wave profile of the reflected wave is compared with experimental results of Goring. The amplitude of the reflected wave is normalized with respect to the incident wave height so that reflected waves corresponding to different incident wave heights can be compared directly. The experimental results are for a wave of $H_I/h_1 = 0.0522$ and numerical results are presented for three cases of $H_I/h_1 = 0.05$, 0.10, and 0.15. In Figure 3a the reflected waves from a slope ($L/l = 1.0$ and $h_1/h_2 = 3.0$) are compared with the experimental data and the agreement is fairly good, except at the crest. This discrepancy may be due to the neglect of friction in the numerical model. The results for a slope $L/l = 2.0$ and $h_1/h_2 = 3.0$, presented in Figure 3b, are not in agreement with the data, but the overall shape of the predicted wave is similar to the experimental data. Accuracy of measurement of the reflected waves, which are very small compared with the incident wave, may influence the shape of the wave considerably. In view of the close agreement in the profiles of waves of different relative wave amplitudes, it may be postulated that reflection may be considered to be a linear process dependent on the parameters L/l and h_1/h_2 characterizing the slope, a view which was also put forward by Goring. These results support the use of the simple coupling mechanism assumed here.

5.2. Transmitted Waves

Results for evolution of the transmitted wave in the constant depth region beyond the slope

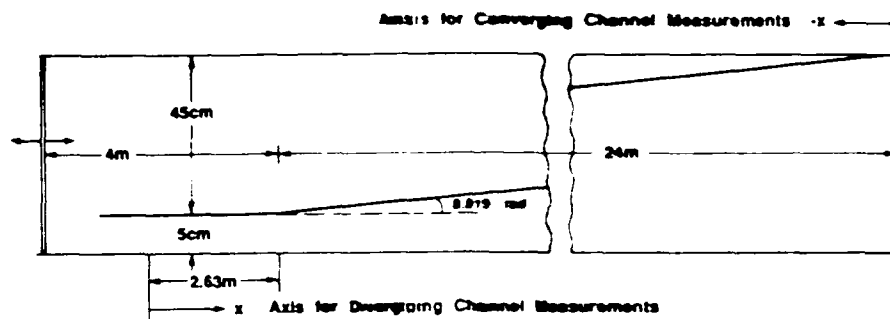


Fig. 4. Plan view of wave channel in experiments of Chang et al. [1979].

exhibit the usual features of disintegration into a train of several solitary waves and are not reproduced here. Numerical results for surface displacement were found to agree well with the experimental results presented by Goring. We remark here that the integrable property of the KdV equation in the transmitted-wave region would allow for a prediction of the number of solitons which evolve out of the wave computed at the top of the slope. No data are available to confirm or deny these predictions, so we have not pursued this question further.

6. Solitary Waves in Diverging and Converging Channels

We now consider a case of waves in a much more gradual transition, consisting of a linear variation in channel width. A comprehensive set of data is provided by Chang et al. [1979] (hereinafter referred to as CMM). Because of the slow variation of the channel width used here, reflection is of only minor importance in determining the height of the transmitted wave; however, the mass balance correction discussed in section 4 becomes quite important.

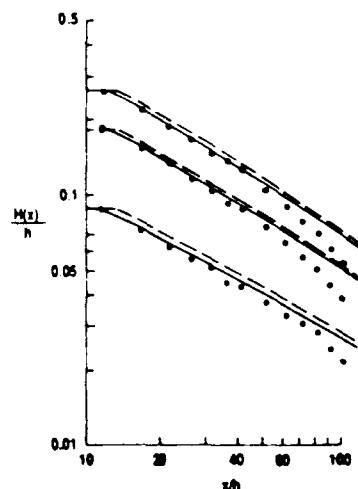


Fig. 5. Normalized amplitude of solitary waves in diverging channel with $h = 20$ cm and initial amplitudes $H_0/h = 0.088, 0.185,$ and 0.259 . Circles show data from CMM, solid lines show the total wave train, and dashed lines show the incident wave alone.

6.1. CMM Experiments

CMM measured the evolution of wave height of an initial solitary wave in both a diverging and a converging laboratory flume. A schematic of the channel geometries is given in Figure 4, which is adapted from Figure 1 of CMM. CMM measured waves for a range of initial wave heights and still water depths. The most detailed sets of results are for the cases of 20 cm depth in a diverging channel (three initial amplitudes [CMM, Figure 2]) and 30 cm depth in a converging channel (four initial amplitudes [CMM Figure 4]). Data consist of measured maximum $\eta(t)/h$ versus position along the channel. Reflections were not reliably measured. The data given by CMM are reproduced in Figures 5 and 6. CMM provided numerical computations based on the nonconservative form (equation (22)) further transformed to a coordinate system moving at the linear long-wave speed. For the case of the diverging channel, numerical results indicated asymptotic agreement with results for the adiabatic evolution of a solitary wave, which gives [Miles, 1979]

$$H(x) = H_0 \left(\frac{b(x)}{b_0} \right)^{-2/3} \quad (39)$$

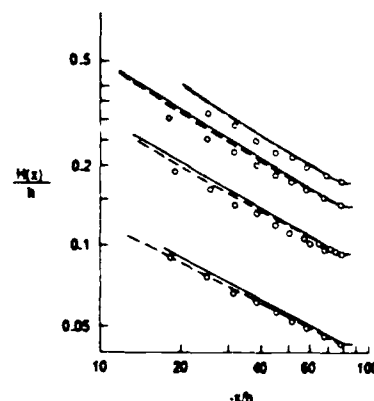


Fig. 6. Normalized amplitude of solitary waves in converging channel with $h = 30$ cm and initial amplitudes $H_0/h = 0.043, 0.093, 0.140,$ and 0.174 . Circles show data from CMM, solid curves show the total wave train, and dashed curves show the incident wave alone.

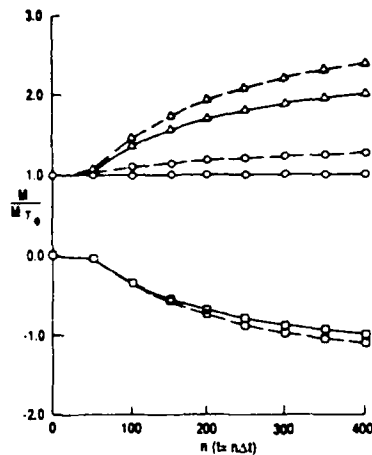


Fig. 7. Total mass in wave train components. Diverging channel. Circles, triangles, and squares show total, incident wave, and reflected wave mass, respectively; solid and dashed curves show mass-conserving and nonconserving equations, respectively.

where b_0 is the initial channel width and H_0 and $H(x)$ are the initial and evolved maximum wave heights. The numerical results reproduce the data well up to 40 water depths beyond the initial measurement station, beyond which the data drop progressively further below the asymptotic $-2/3$ slope. This drop in experimental wave height is presumably due to frictional damping.

For the case of a converging channel, the experimental wave height evolves according to a much flatter, $-1/2$ slope which mimics a Green's law evolution. The numerical results of CMM reproduce this behavior. CMM offered, as explanation of the $-2/3$ and $-1/2$ slope discrepancies, an argument based on nonlinear distortion of the linear characteristics in the converging channel case. CMM's results are questioned below, however. It is noted that the numerical results of CMM for the converging channel actually tend to underpredict wave height at large distances from the initial measuring station and thus do not show any accumulating effect of frictional damping. (CMM provide a discussion of the asymptotic wave height resulting from additional damping in the diverging channel case, but do not apply the results to converging channels or provide any explicit computations).

The results of the following two sections indicate that the agreement between data and computations found by CMM in the converging channel case may have been fortuitous, and we thus will concentrate on this point where appropriate.

6.2. Numerical Computations

The mass-conserving RLW equations (37) were used first to compute wave evolution in the converging and diverging channels. Results are shown in Figures 5 and 6. The numerical channels were taken to correspond to the experimental channels as closely as possible; the small tails of constant amplitude on each curve correspond to the constant width entrance channels. In each figure, solid curves correspond to maximum wave height in

the combined transmitted-reflected wave system ($n = n^+ + n^-$), while the dashed curves correspond to a transmitted wave alone ($n = n^+$) when reflection is neglected.

In both the cases of channel divergence and convergence, the wave heights computed from mass-conserving equations evolve largely according to the $-2/3$ slope, adiabatic relation. For the diverging channel (Figure 5), these results are in close agreement with CMM's results, with the only deviation between experiment and numerical results being presumably due to the slow accumulation of frictional effects. For the converging channel case, the results here differ markedly from CMM's numerical results and from data, which essentially evolves at a different ($-1/2$) slope right from the initial measurement point. These results are initially discouraging, since it is not apparent that the deviation is due to a similar slow accumulation of frictional damping (however, see section 6.3).

Corresponding results were computed using non-conservative RLW equations obtained from (30). The evolution obtained from the nonconservative equations differs markedly from the conservative evolution, with wave heights evolving approximately along a $(-1/2)$ slope. This leads to (again fortuitous) agreement between data and computations for the converging channel (again with slight underprediction of data at large distances), but significant overprediction of data for the diverging channel case.

The fact that CMM obtained agreement, in the diverging channel, with the $-2/3$ slope evolution in the data rather than with the present, non-conservative estimate of a $-1/2$ slope, is due in part to their idealization of the channel geometry as a uniform wedge with no uniform entrance channel. Wave height in the idealized channel was initialized according to data from the first measurement point in the model channel, which is located approximately 38 cm back in the uniform 5-cm channel before the junction with the expanding channel, or 225 cm from the virtual origin of the idealized wedge (judging from Figure 2 of CMM). The measured wave is thus placed in a numerical channel $\sim 15\%$ narrower than the physical channel and consequently has 15% less total mass than the experimental wave. Using the present nonconservative model with the idealized geometry and the initial measured wave heights at the first measurement point, we obtained numerical results which are in agreement with those presented by CMM. We believe these to be in error because of the idealization of the channel geometry.

We finish here with a discussion of mass balance in the conserving and nonconserving equations. Since the differences between conserving and nonconserving equations lie in terms which are small compared to the orders of magnitude considered in obtaining the original KdV equations, it would be expected that local errors in the nonconserving equations should be small over several wavelengths. This argument does not hold up for the propagation distances considered in the experiments.

In Figures 7 and 8, we show the evolution of total, incident wave, and reflected wave mass with time in the computations described above. Results are for the largest-amplitude cases in each of Figures 5 and 6; since the reflection mechanism is

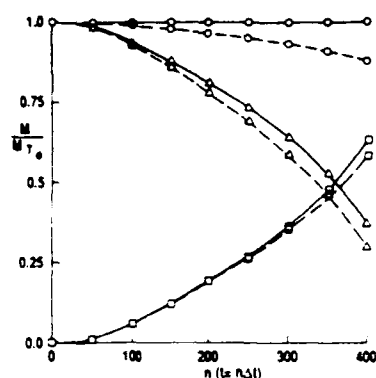


Fig. 8. Total mass in wave train components. (converging channel). Symbols are as in Figure 7.

linear, little variation occurs for different initial amplitudes in each case. For all the computations above, the implicit schemes were run at a Courant number of 1, as suggested by Eilbeck and McGuire [1975]. No attempt was made to optimize accuracy of results by varying grid spacing and Courant number. For the mass-conserving results (indicated by solid lines), total mass was maintained to an accuracy of three significant figures in double precision computations, which is sufficient for the comparisons given here. Deviations in transmitted, reflected, and total mass for the nonconserving results (indicated by dashed lines) are significant for the propagation distances considered. In each case, the majority of deviation from the mass-conserving results is contained in the transmitted wave. These results indicate that the modifications to the basic forms of the equations employed by Miles [1979] to construct mass balance arguments should be incorporated in the governing equations themselves in any practical calculation involving waves in a slowly varying channel.

6.3. Linear Damping Effects

We now consider the effect of a simple linear damping as a possible explanation of the discrepancy between data and numerical results in the previous section. Rather than attempting to obtain a damping coefficient analytically, we posit a simple coefficient β with initially unknown value, and modify the KdV-RLW model equations into the revised forms

$$bn_t^{\pm} \pm bc n_x^{\pm} + \dots + \beta(b + 2h)n^{\pm} = 0 \quad (40)$$

The factor $(b + 2h)$ is retained to include the varying effect of channel width and depth (i.e., the relative importance of sidewall and bottom friction) as channel geometry changes. The quantity $(b + 2h)$ is the wetted perimeter of the channel in the linear approximation. The inclusion of the damping term modifies the conclusions on total mass balance. Adding the component equations of (40) and integrating out to $\pm \infty$ yields the expression

$$\frac{d}{dt} \int_{-\infty}^{\infty} bndx = -\beta \int_{-\infty}^{\infty} (b + 2h)ndx \quad (41)$$

The sink term then represents a loss of mass from organized wave motion due to frictional damping of the fluid velocity. This loss of mass would necessarily be absorbed by the stationary (non-wave) water column, leading (at $t \rightarrow \infty$) to a distributed increase in depth commensurate with the total initial mass of the organized wave form.

We proceed by examining the largest-amplitude diverging channel case. The value of β is adjusted to obtain reasonable agreement between data and numerical wave height over the entire range of evolution. (This agreement is evaluated purely qualitatively; small changes in β do not significantly alter the results.) On the basis of this procedure, a value of $\beta = 0.004$ is chosen and then is held fixed for the remainder of the computations. Calculations for the three initial amplitudes of the diverging channel case are shown in Figure 9. The linear damping mechanism is successful in representing the gradual accumulation of damping in the diverging channel case.

Turning to the converging channel case, we keep $\beta = 0.004$ and compute the results presented in Figure 10. In this case, linear damping effects accumulate immediately and are seen to account for the general lower slope evolution of the wave height. It is thus apparent that the discrepancy between data and the preferred mass-conserving computations is explainable by simple laminar damping in both the diverging and converging channels, even though the discrepancies accumulate differently. We feel that these results support the validity of the present computations over those given by CPM. There is some indication from the low-amplitude converging channel case that the tuned value of β is somewhat too high. This would be expected, since the converging channel water depth is 50% greater than the diverging channel depth, and thus laminar damping effects would be somewhat reduced.

We remark that a somewhat more standard means of adding a damping term would be to add Burgher's type (second derivative) terms to the equations.

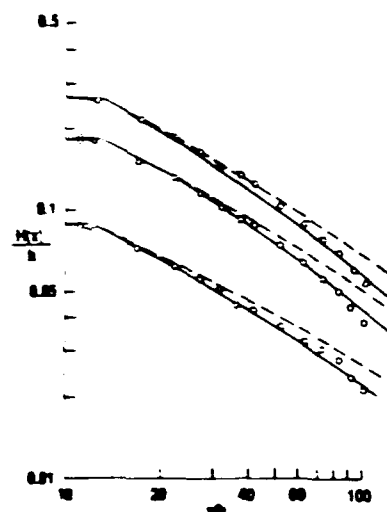


Fig. 9. Linear damping of solitary wave in diverging channel. Conditions are as in Figure 5. Circles show data from CPM, dashed curves show the undamped wave, and solid curves show the damped wave.

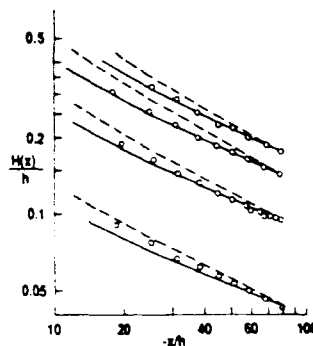


Fig. 10. Linear damping of solitary wave in converging channel. Conditions as in Figure 6. Circles show data from CMM, dashed curves show the undamped wave, and solid curves shown the damped wave.

However, the factors which make this type of damping term appropriate in studying shock dynamics are inappropriate for the application here. In the case of a dissipative shock forming in a nondispersive environment, numerical results become contaminated by high-frequency noise which is essentially a parasitic addition to a low-frequency (infinitely long wavelength) process. The second-derivative damping term concentrates damping in the high-frequency components. In the present case, where well-organized wave motions are present at a range of frequencies in evolved wave fields, experience would indicate that bottom boundary layer damping of high-frequency components should be lower than for low-frequency components, because of increasing relative water depth. The present model distributes damping uniformly over all frequencies; this is not a completely desirable result but is certainly more appropriate than the Burgher's form.

7. Reflection of Time-Periodic Wave Trains by Undular Beds

We now turn to a case where strong reflections arise due to a resonant reflection mechanism. In particular, we study the reflection of a cnoidal wave by a field of sinusoidal bars placed on the bottom of an otherwise uniform channel. This problem has been studied in the linear wave limit by Davies and Heathershaw [1984] and Mei [1985]. Recently, Yoon and Liu [1987] have considered the problem studied here from the point of view of resonant interaction theory, where attention is restricted solely to the interaction of the fundamental Fourier component of the cnoidal wave and the bottom undulation, and all simple shoaling effects are neglected. A more complete set of calculations is provided here which exhibit several physical features which do not arise in the results of Yoon and Liu.

7.1. Evolution Equations for Time-Periodic Waves

Neglecting transverse (y direction) variations, the surface displacements of time-periodic incident and reflected waves governed by (19) may be expressed as a sum of Fourier modes with variable amplitudes:

$$\eta = \sum_{n=1}^N \left[\frac{A_n(x)}{2} e^{in(\int k dx - \omega t)} + c.c. \right] \quad (42a)$$

$$\zeta = \sum_{n=1}^N \left[\frac{B_n(x)}{2} e^{in(-\int k dx - \omega t)} + c.c. \right] \quad (42b)$$

where $n = n^+$ and $\zeta = n^-$ for convenience and c.c. denotes the complex conjugate. Substituting the forms of η and ζ in the coupled KdV equations (19) yields the lowest order coupled evolution equations for the incident wave amplitude

$$A_n \frac{dx}{x} + \frac{h}{4h} [A_n - B_n e^{-2in\int k dx}] - \frac{in^3 k^3 h^2}{6} A_n + \frac{3ink}{8h} \left[\sum_{l=1}^{n-1} A_l A_{n-l} + 2 \sum_{l=1}^{N-n} A_l^* A_{n+l} \right] = 0 \quad (43)$$

and a corresponding equation for the reflected wave amplitude. These equations represent a more complete model of the wave propagation problem than the final equations employed by Yoon and Liu [1987] to study resonant reflection. Equations similar to theirs are derived in Appendix B, and the effect of using the more complete form (43) is discussed below.

Energy conservation in the reflection process may be analyzed using the coupled evolution equations and is used below as a test of accuracy for the numerical scheme. The conservation law derived from (43) and its counterpart is given by

$$\left[c \sum_{n=1}^N |A_n|^2 \right]_x - \left[c \sum_{n=1}^N |B_n|^2 \right]_x = 0$$

or

$$c \left\{ \sum_{n=1}^N (|A_n|^2 - |B_n|^2) \right\} = \text{constant} \quad (44)$$

In the case of a rippled bed in constant mean depth (Figure 11), the conservation equation (44) becomes

$$\sum_{n=1}^N (I_n^2 - R_n^2 - T_n^2) = 0 \quad (45)$$

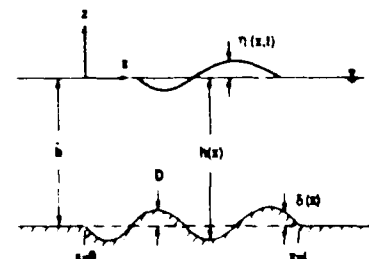


Fig. 11. Geometry of the sinusoidal bed form.

where

$$T_n = \frac{|A_n(L)|}{|A_1(0)|} \quad R_n = \frac{|B_n(0)|}{|A_1(0)|}$$

$$I_n = \frac{|A_n(0)|}{|A_1(0)|} \quad (46)$$

Here, I_n represents a measure of each harmonic amplitude to the fundamental amplitude in the steady incident wave, and R_n and T_n are reflection and transmission coefficients for each mode, normalized by the fundamental incident amplitude.

7.2. Numerical Scheme

Reflections from a rippled bed with periodic sinusoidal depth variations are studied using the evolution equations (43) developed in numerical form. A finite difference scheme centered on $x = (m + 1/2)\Delta x$ is used for the equations, giving

$$\frac{A_n^{m+1} - A_n^m}{\Delta x} + \frac{(h^{m+1} - h^m)}{4\Delta x} \frac{(A_n^{m+1} + A_n^m)}{(h^{m+1} + h^m)}$$

$$- \frac{\ln^3(k^3 h^2 A_n^m)^{m+1}}{12} - \frac{\ln^3(k^3 h^2 A_n^m)^m}{12}$$

$$+ \frac{3\ln}{16} \left[\left(\frac{k}{h} \sum_{l=1}^{n-1} A_l A_{n-l} \right)^{m+1} + \left(\frac{k}{h} \sum_{l=1}^{n-1} A_l A_{n-l} \right)^m \right]$$

$$+ \left(\frac{k}{h} \sum_{l=1}^{N-n} A_l^* A_{n+l} \right)^{m+1} + \left(\frac{2k}{h} \sum_{l=1}^{N-n} A_l^* A_{n+l} \right)^m$$

$$= \frac{(h^{m+1} - h^m)}{4\Delta x} \frac{(B_n^{m+1} e^{-2in\psi^{m+1}} + B_n^m e^{-2in\psi^m})}{(h^{m+1} + h^m)} \quad (47)$$

and a similar form for the reflected wave component.

The reflected and transmitted waves are obtained by an iterative procedure. First for $k=0$, using initial values for $A_n(m=0)$ as specified by the permanent cnoidal wave solution, the incident wave (obtained using equation (47)) is marched in x (without considering the reflected wave) using an iterative scheme to linearize the quadratic terms. Then using the present value of the incident wave field along the disturbance, the equations for the B_n are solved by starting at a point downstream of the disturbance where reflection is absent and marching backwards to solve for the reflected wave field. The incident wave and reflected wave are then successively updated until the relative error between two successive solutions (k and $k+1$) of the reflected and incident wave field is less than a predetermined value ρ , i.e.,

$$\frac{|A_n^{m+1}|^k - |A_n^m|^k}{|A_n^m|^k} < \rho \quad \frac{|B_n^{m+1}|^k - |B_n^m|^k}{|B_n^m|^k} < \rho \quad (48)$$

where $k+1$ and k represent the current and the previous iterations. For $\rho=10^{-4}$, only three iterations are required to obtain solutions of A_n and B_n . The phase $\psi = \int k dx$ is calculated using the trapezoidal rule.

7.3. Reflection From a Rippled Bed

For the present numerical calculations, a rippled bed is defined by

$$h = \bar{h} - \delta(x) \quad 0 < x < L \quad (49)$$

where L is length of the ripple patch, \bar{h} is the constant depth and δ is a small but rapid variation to the depth. Choosing sinusoidal bed variations as in previous works, δ is given by

$$\delta = D \sin \lambda x \quad 0 < x < L \quad (50)$$

where D is the ripple amplitude and λ is the ripple wave number.

We first consider the propagation of linear waves over the ripple patch. Linear wave reflection from the ripple patch is a function of the number of ripples in the patch, the ripple amplitude and the ripple length. To examine the effects of the ripple length on reflection, calculations are carried out for a wide range of values of the parameter $2K_1/\lambda$, where K_1 is the wave number of the fundamental component of the incident wave, correct to $O(kh)^2$. The parameter $2K_1/\lambda$ is varied by changing the ripple length for a fixed wave number. This approach is preferred to varying wave period for a fixed rippled length because in the latter approach the waves in the short-wave regime (K_1 large) may not satisfy the shallow water scaling. In all the cases analyzed here, waves of period $T = 1.8$ s in water depth $h = 0.1$ m are used, corresponding to a value of $\mu^2 = \omega^2 h/g = 0.124$. To study the effect of the number of ripples in the patch, two patches, one consisting of two ripples and another of four ripples, are modeled.

In Figure 12, results for propagation of a linear wave over rippled beds are presented for a ripple amplitude $D/h = 0.4$. All calculations were carried out using a $\Delta x = \pi/20\lambda$ to obtain accurate results at large $2K_1/\lambda$. Resonant Bragg scattering is observed at $2K_1/\lambda = 1$. The conservation law (equation (45)) reduces to

$$R^2 + T^2 = 1 \quad (51)$$

for linear waves. For small ripple amplitudes, the conservation law is satisfied for the entire range of $2K_1/\lambda$ values with errors less than 10^{-3} . For $D/h = 0.4$ in the region $0.95 < 2K_1/\lambda < 1.05$ the scheme is not convergent owing to overprediction of the reflection on the first pass. To rectify this problem, the numerical scheme is

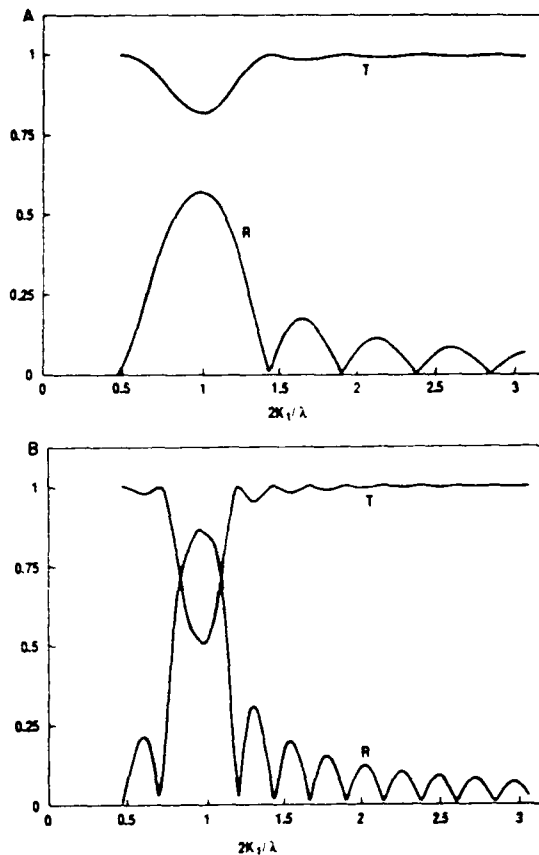


Fig. 12. Variation of reflection and transmission coefficients with $2K_1/\lambda$ for linear waves normally incident on a sinusoidal patch, for (a) $n = 2$, $D/h = 0.4$ and (b) $n = 4$, $D/h = 0.4$.

solved by an iterative procedure. First, the incident and reflected wave field for ripple amplitude $D/h = 0.2$ is calculated. Using the calculated wave field as the initial value for the incident and reflected wave fields, the numerical scheme is solved for increasing ripple amplitude with an increment $\Delta D/h = 0.05$, until $D/h = 0.4$ is reached. This approach reduced the errors in the conservation law to less than 10^{-2} for the range $0.95 < 2K_1/\lambda < 1.05$.

Reflection and transmission coefficients R , T are presented as a function of $2K_1/\lambda$ in Figure 12. Figures 12a and b show results for ripple patches containing two and four ripples, respectively. The major effect of increasing the number of ripples, while holding ripple amplitude and water depth constant, is to tune the resonant response of the ripple bed and increase the magnitude of the resonant reflection. These effects are similar to the general trend of results in intermediate depth, as studied by Davies and Heathershaw [1984] and Kirby [1986].

Reflection of nonlinear waves from a rippled bed is next studied. The propagation of a cnoidal wave of period 1.8 s and wave height 0.02 m is considered. In Figure 13a, the reflection and transmission coefficients of the fundamental component (R_1 , T_1) as defined in (46) are presented. The ripple amplitude $D/h = 0.4$ and the number of ripples is 2 for this case. There is no appreciable change in the values of reflection

coefficient from the linear case, but there is a small shift in the peaks and zeros of R_1 which is presumably due to nonlinear distortion of the incident wave length. In the near-resonance region there is no appreciable change in the transmission coefficient T_1 with respect to the linear result. The total energy transmitted (E_T) and reflected (E_R), normalized with respect to initial energy, are shown as dotted lines. Energy conservation defined by (45) is satisfied with an error $< 10^{-3}$.

We note that in this region of $2K_1/\lambda > 1$, the transmission coefficient of the fundamental component, T_1 , experiences a significant drop even though the value E_T indicates that no significant reflection is occurring. In this region the sinusoidal ripples are becoming comparable in length to or longer than the surface wave length, and the surface waves are able to evolve by nontrivial amounts as they shoal over the ripple crests. The reduction of T_1 represents a destabilization of the incident wave, after which energy is transferred to higher harmonics. This effect would not appear in the results of the model developed by Zhao and Liu [1987] where nonresonant shoaling effects are neglected.

We also note a rise in E_R and a drop in E_T as $2K_1/\lambda \rightarrow 0.5$. This represents the resonant inter-

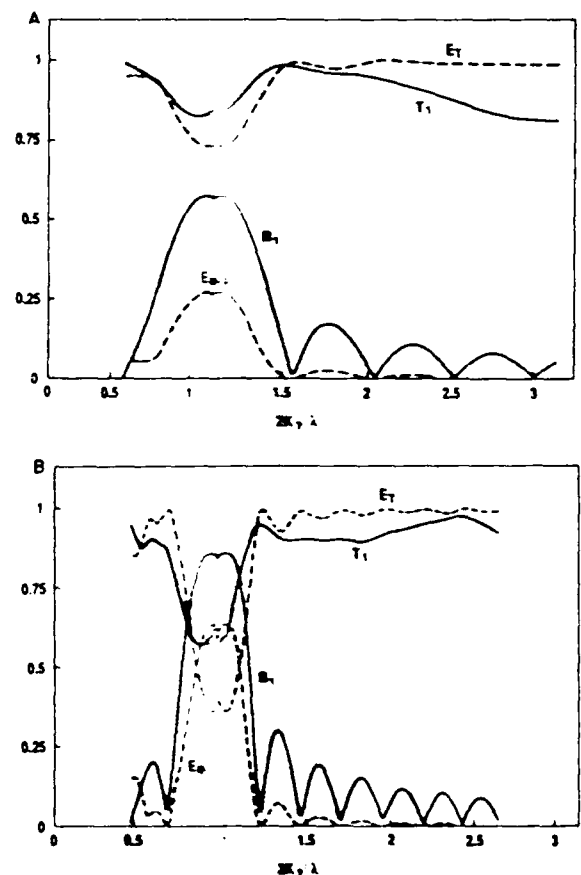


Fig. 13. Variation of reflection and transmission coefficients of fundamental harmonic with $2K_1/\lambda$ for nonlinear wave propagation over a sinusoidal patch for (a) $n = 2$, $D/h = 0.4$ and (b) $n = 4$, $D/h = 0.4$. The normalized reflected and transmitted energy E_R and E_T are shown.

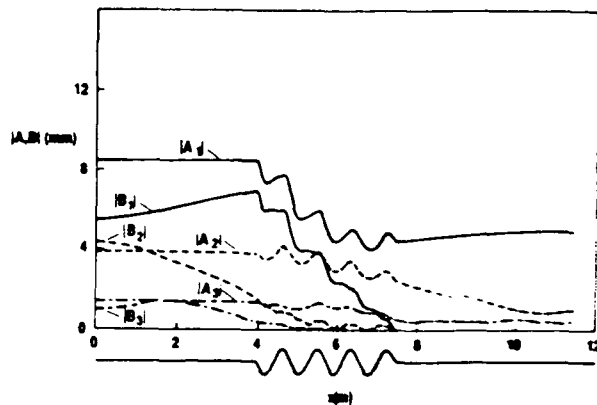


Fig. 14. Variation of component amplitudes of transmitted and reflected waves with x , at Bragg resonance for nonlinear wave propagation over a sinusoidal patch of 4 ripples and $D/h = 0.4$ (first three harmonics).

action between the first superharmonic of the wave field and the ripple patch. The modification to the total transmitted energy is then due to the decreasing energy content in the harmonic amplitude.

Figure 13b presents nonlinear results for the patch with four ripples. Differences between linear and nonlinear results are more accentuated than in the two bar case. In the region of resonant reflection, T_1 is greater in the nonlinear case than in the linear case. This result is due to the fact that the transmitted component continually gains energy from its harmonics as it is lost to reflection over the bar field, and thus ends up with a surplus in comparison to the linear case. In contrast, the reflection coefficient R_1 is again little changed from the linear case. The maintenance of a higher value of the incident amplitude $A_1(x)$ over the bar field should lead to greater energy transfer to the reflected wave component $B_1(x)$. This effect is balanced by the fact that the B_1 component loses energy through harmonic generation as the reflected wave height increases, and in the present case, the two effects nearly cancel each other.

After the incident and reflected waves move into the region of constant depth, these waves evolve as they propagate owing to nonequilibrium between the Fourier components of the surface displacement. To illustrate this evolution, the transformation of the component amplitudes of the incident and reflected wave are analyzed for the case of resonant Bragg scattering. In Figure 14, the evolution of the component amplitudes of the incident and reflected wave is presented, for waves propagating over a patch of four ripples, with ripple amplitude $D/h = 0.4$. Results were calculated for an initial permanent form wave consisting of 20 harmonics, although only the evolution of the first three harmonics are presented. The loss of energy in harmonics of the incident wave and the gain of energy in the reflected wave harmonics are both apparent. Also apparent is the disequilibrium of the transmitted waves and reflected waves as they leave the area of the ripple patch. This disequilibrium leads to a continuous evolution of the reflected wave and

transmitted wave away from the ripple patch. This effect presents serious difficulties in the practical measurement of reflection and transmission, since these quantities are essentially functions of space. (The only spatially uniform quantity would be the energy flux of the reflected and transmitted wave trains.)

8. Conclusions

The present study has developed a scheme for obtaining the linear coupling between opposite going, weakly dispersive long waves due to channel variations in the direction of propagation. The model is shown to predict the generation of a reflected wave quite well in some case where comprehensive data are available.

Computational results have indicated that errors in mass conservation embedded in standard forms of the KdV-RLW evolution equations, which are locally of smaller order than the approximation employed in the equations, nevertheless interfere in numerical integrations over length scales appropriate to existing physical experiments. By extension, these effects would be expected to have serious impacts in field applications. Appropriate mass-conserving forms of the equations have been provided which are accurate to the same degree of approximation as the original equations.

It is noted that the neglect of nonlinear interaction between opposite going waves in this study renders the model inapplicable to the study of details of the head-on collision of solitary waves of comparable amplitude. Derivation of the appropriate coupling terms would represent a valuable addition to the present model. Further, application of the weakly two-dimensional model obtained in sections 2 and 3 would be of value; cases employing only the forward-propagating component will be reported on shortly.

Appendix A: Approximate Angular Relations in K-P Dispersion

The restriction to small angles of propagation implied in the K-P equation may be analyzed by looking at the propagation of a plane wave given by

$$\eta = ae^{i(k\cos\theta x + k\sin\theta y - \omega t)} \quad (A1)$$

The expression $\gamma^2 \eta$ in (4) is then given by

$$\gamma^2 \eta = \left(\frac{u^2}{gh} - k^2 \sin^2 \theta \right) \eta = k^2 (1 - \sin^2 \theta) \eta \quad (A2)$$

An expression for $\gamma \eta$ based on the binomial expansion employed in section 2 is then

$$\gamma \eta = k(1 - \sin^2 \theta)^{1/2} \eta = k \left(1 - \frac{1}{2} \sin^2 \theta \right) \eta \quad (A3)$$

which is only valid if $\sin \theta = \theta \ll 1$. The direction of wave propagation is thus only allowed to deviate slightly from the preferred x direction.

This scaling distinction may be further understood by comparing the model K-P equations obtained here with the usual parabolic approximation for time-harmonic linear waves. The set of

coupled equations (15) in differential form may be compared with the coupled parabolic equations given by Liu and Tsay [1983] by making the substitution

$$\begin{aligned} \eta^+ &= A(x, y) e^{i(k_0 x - \omega t)} \\ \eta^- &= B(x, y) e^{i(-k_0 x - \omega t)} \end{aligned} \quad (A4)$$

to yield

$$\begin{aligned} 2ikhA_x + 2kh(k-k_0)A + i(kh)_x A + (hA_y)_y \\ = i(kh)_x B e^{-2ikx} \end{aligned} \quad (A5a)$$

$$\begin{aligned} 2ikhB_x - 2kh(k-k_0)B + i(kh)_x B - (hB_y)_y \\ = i(kh)_x A e^{2ikx} \end{aligned} \quad (A5b)$$

which are essentially similar to the shallow water limits of the coupled parabolic equations of Liu and Tsay [1983, equations (2.12-2.13)].

Appendix B: Simplified Equations for Near-Resonant Reflection

The set of equations (43) represents a general model for reflection of periodic waves from bottom topography $h(x)$ and covers the special case of reflection of waves from a bed of sinusoidal ripples of small amplitude. Yoon and Liu [1986] have provided a more restricted theory for near-resonant interaction (small detuning with respect to the Bragg condition) which neglects contributions to reflection which are far from resonance and which also neglects shoaling effects in each wave component alone. Here, we obtain an analogous dimensional form of the governing equations as a reduction of the general theory (equation (43)).

We consider the depth $h(x)$ to be split into a slowly varying portion $\bar{h}(x)$ and a rapidly varying, small-amplitude portion $\delta(x)$, with $\delta/\bar{h} = O(\alpha)$. The coupling coefficient $h_x/4h$ is then given by (to $O(\alpha)$)

$$\frac{h_x}{4h} = \frac{\bar{h}_x}{4\bar{h}} - \frac{\delta_x}{4\bar{h}} \quad (B1)$$

Since simple shoaling effects do not lead to resonant reflection, (43) may be rewritten as

$$\begin{aligned} A_{n,x} - \frac{in^3 k^3 \bar{h}^2}{6} A_n + \frac{3in\bar{k}}{8\bar{h}} \left\{ \sum_{l=1}^{n-1} A_l A_{n-l} \right. \\ \left. + 2 \sum_{l=1}^{N-n} A_l^* A_{n+l} \right\} = -\frac{\delta_x}{4\bar{h}} B_n e^{-2in\int \bar{k} dx} + O(\alpha^2) \end{aligned} \quad (B2a)$$

$$\begin{aligned} B_{n,x} + \frac{in^3 k^3 \bar{h}^2}{6} B_n - \frac{3in\bar{k}}{8\bar{h}} \left\{ \sum_{l=1}^{n-1} B_l B_{n-l} \right. \\ \left. + 2 \sum_{l=1}^{N-n} B_l^* B_{n-l} \right\} = -\frac{\delta_x}{4\bar{h}} A_n e^{2in\int \bar{k} dx} + O(\alpha^2) \end{aligned} \quad (B2b)$$

We note here that the wave phase may be written with respect to \bar{k} to $O(1)$. The dispersion term may be eliminated by the transformation

$$\begin{aligned} A_n e^{in\int \bar{k} dx} &= A'_n e^{i\int K_n dx}; \\ B_n e^{-in\int \bar{k} dx} &= B'_n e^{-i\int K_n dx} \end{aligned} \quad (B3)$$

where

$$K_n = n\bar{k} \left(1 + \frac{n^2 k^2 \bar{h}^2}{6} \right) \quad (B4)$$

to give

$$\begin{aligned} A'_{n,x} + \frac{3in\bar{k}}{8\bar{h}} \left\{ \sum_{l=1}^{n-1} A'_l A'_{n-l} e^{i\Delta\alpha_{nl}^+ x} \right. \\ \left. + 2 \sum_{l=1}^{N-n} A'_l A'_{n+l} e^{i\Delta\alpha_{nl}^+ x} \right\} \\ = -\frac{\delta_x}{4\bar{h}} B'_n e^{-2i\int K_n dx} \end{aligned} \quad (B5a)$$

$$\begin{aligned} B'_{n,x} - \frac{3in\bar{k}}{8\bar{h}} \left\{ \sum_{l=1}^{n-1} B'_l B'_{n-l} e^{-i\Delta\alpha_{nl}^+ x} \right. \\ \left. + 2 \sum_{l=1}^{N-n} A'_l A'_{n+l} e^{i\Delta\alpha_{nl}^+ x} \right\} \\ = -\frac{\delta_x}{4\bar{h}} A'_n e^{2i\int K_n dx} \end{aligned} \quad (B5b)$$

where the $\Delta\alpha_{nl}^\pm$ are detuning parameters given by

$$\Delta\alpha_{nl}^\pm = \frac{1}{2x} n l (l \pm n) \int \bar{k}^3 \bar{h}^2 dx \quad (B6)$$

Finally, we take the bottom displacement to be given by

$$\delta = \sum_{p=1}^{\infty} \left(\frac{D_p}{2} e^{ip\int \lambda dx} + c.c. \right) \quad (B7)$$

where λ is the characteristic wave number of the bottom undulation. We assume that λ adjusts according to the shoaling effect of the mean slope, i.e., $\lambda/k = \text{constant}$. Differentiating (B7) and substituting in (B5) then gives

$$\begin{aligned} A'_n + \frac{3\lambda k}{8h} \left\{ \sum_{l=1}^{n-1} A'_l A'_{n-l} e^{i\Delta\alpha_{nl}^- x} \right. \\ \left. + \sum_{l=1}^{N-n} A'_l A'_{n+l} e^{i\Delta\alpha_{nl}^+ x} \right\} = \\ = -\frac{i\lambda D}{8h} B'_n e^{i\int(p\lambda - 2K_n)dx} \end{aligned} \quad (B8a)$$

$$\begin{aligned} B'_n - \frac{3\lambda k}{8h} \left\{ \sum_{l=1}^{n-1} B'_l B'_{n-l} e^{-i\Delta\alpha_{nl}^- x} \right. \\ \left. + 2 \sum_{l=1}^{N-n} B'_l B'_{n+l} e^{-i\Delta\alpha_{nl}^+ x} \right\} = \\ = \frac{i\lambda D}{8h} A'_n e^{-i\int(p\lambda - 2K_n)dx} \end{aligned} \quad (B8b)$$

where the near-resonant component p is chosen as being that one which minimizes the quantity $(p\lambda - 2K_n)$ and thus minimizes the rate of oscillation of the coupling coefficient. Identifying the factor

$$\Delta\delta_n = \frac{1}{p} \int (2K_n - p\lambda) dx \quad (B9)$$

completes the comparisons to Yoon and Liu's model, which is essentially similar to (B8). We further note that the coefficient $\lambda D/8h$ is the appropriate shallow water limit of the coefficient derived from Kirby's [1986] intermediate depth theory.

Acknowledgments. This work was supported in its later stages by the Office of Naval Research through contract N00014-86-K-0790.

References

- Benjamin, T. B., J. L. Bona, and J. J. Mahony, Model equations for long waves in nonlinear dispersive systems, *Philos. Trans. R. Soc. London, Ser. A* **A272**, 47-78, 1972.
- Chang, P., W. K. Melville, and J. W. Miles, On the evolution of a solitary wave in a gradually varying channel, *J. Fluid Mech.*, **95**, 401-414, 1979.
- Davies, A. G., and A. D. Heathershaw, Surface-wave propagation over sinusoidally varying topography, *J. Fluid Mech.*, **144**, 419-443, 1984.
- Eilbeck, J. C., and G. R. McGuire, Numerical study of the regularized long-wave equation, I, numerical methods, *J. Comput. Phys.*, **19**, 43-57, 1975.
- Engquist, B. and A. Majda, Absorbing boundary conditions for the numerical simulation of waves, *Math. Comput.*, **31**, 629-651, 1977.
- Goring, D. G., Tsunamis - the propagation of long waves onto a shelf, Rep. KH-R-38, W. M. Keck Lab. of Hydraul. and Water Resour., Calif. Inst. of Technol., Pasadena, 1978.
- Kadomtsev, B. B., and V. I. Petviashvili, On the stability of solitary waves in weakly dispersive media, *Sov. Phys. Dokl.*, **Engrl. Transl.**, **15**, 539-541, 1970.
- Katsis, C., and T. R. Akylas, On the excitation of long nonlinear water waves by a moving pressure distribution, 2, Three-dimensional effects, *J. Fluid Mech.*, **177**, 49-65, 1987.
- Kirby, J. T., A general wave equation for waves over rippled beds, *J. Fluid Mech.*, **162**, 171-186, 1986.
- Knickerbocker, C. J., and A. C. Newell, Reflections from solitary waves in channels of decreasing depth, *J. Fluid Mech.*, **153**, 1-16, 1985.
- Liu, P. L.-F., and T.-K. Tsay, On weak reflection of water waves, *J. Fluid Mech.*, **131**, 59-71, 1983.
- Liu, P. L.-F., S. B. Yoon, and J. T. Kirby, Nonlinear refraction-diffraction of waves in shallow water, *J. Fluid Mech.*, **153**, 185-201, 1985.
- Maxworthy, T., Experiments on collisions between solitary waves, *J. Fluid Mech.*, **76**, 177-185, 1976.
- Mei, C. C., Resonant reflection of surface water waves by periodic sand bars, *J. Fluid Mech.*, **152**, 315-335, 1985.
- Miles, J. W., On the Korteweg-deVries equation for a gradually varying channel, *J. Fluid Mech.*, **91**, 181-190, 1979.
- Peregrine, D. R., Calculations of the development of an undular bore, *J. Fluid Mech.*, **25**, 321-331, 1966.
- Peregrine, D. R., Long waves on a beach, *J. Fluid Mech.*, **27**, 815-827, 1967.
- Shuto, N., Nonlinear long waves in a channel of variable section, *Coastal Eng. in Jpn.*, **17**, 1-12, 1974.
- Su, C. H., and R. M. Mirie, On head-on collisions between two solitary waves, *J. Fluid Mech.*, **98**, 509-525, 1980.
- Svendsen, I. A., and J. Buhr Hansen, On the deformation of periodic long waves over a gently sloping bottom, *J. Fluid Mech.*, **87**, 433-448, 1978.
- Vengayil, P., and J. T. Kirby, Shoaling and reflection of nonlinear shallow water waves, Tech. Rep. UFL/COEL-TR/062, Coastal and Oceanogr. Eng. Dep., Univ. of Fla., Gainesville, 1986.
- Yoon, S. B., and P. L.-F. Liu, Resonant reflection of shallow-water waves due to corrugated boundaries, *J. Fluid Mech.*, **180**, 451-469, 1987.
- J. T. Kirby, Coastal and Oceanographic Engineering Department, College of Engineering, 336 Weil Hall, University of Florida, Gainesville, FL 32611.
- P. Vengayil, Civil Engineering Department, Massachusetts Institute of Technology, Cambridge, MA 02139.

(Received September 10, 1987;
accepted October 23, 1987.)

Appendix D: An angular spectrum model for propagation of Stokes waves

Journal of Fluid Mechanics, in press, 1990.

An angular spectrum model for propagation of Stokes waves

By Kyung Duck Suh¹, Robert A. Dalrymple and James T. Kirby

Center for Applied Coastal Research, Department of Civil Engineering

University of Delaware, Newark, DE 19716, USA

Abstract

An angular spectrum model for predicting the transformation of Stokes waves on a mildly-varying topography is developed, including refraction, diffraction, shoaling and nonlinear wave interactions. The equations governing the water wave motion are perturbed using the method of multiple scales and Stokes expansions for the velocity potential and free surface displacement. The first-order solution is expressed as an angular spectrum, or directional modes, of the wave field propagating on a beach with straight iso-baths whose depth is given by laterally-averaged depths. The equations for the evolution of the angular spectrum due to the effects of bottom variation and cubic resonant interaction are obtained from the higher-order problems. Comparison of the present model with existing models is made for some simple cases. Numerical examples of the time-independent version of the model are presented for laboratory experiments for wave diffraction behind a breakwater gap and wave focusing over submerged shoals: an elliptic shoal on a sloping beach and a circular shoal on a flat bottom.

1 Introduction

Since Booker & Clemmow (1950) clarified the concept of the angular spectrum of plane waves, it has been applied in various branches of physics and engineering that deal with wave propagation, see Ratcliffe (1956), Gabor (1961), and Clemmow (1966). In water wave propagation problems, Stamnes *et al.* (1983) have used an angular spectrum model to study wave focusing by a lens in water of constant depth. Recently Dalrymple & Kirby (1988) developed an angular spectrum model for propagation of linear water waves on a beach with straight and parallel bottom contours. This model was extended to the case of irregular bathymetry by Dalrymple *et al.* (1989). These models are solved by a marching method starting from given wave data offshore and give accurate results for waves propagating at large angles from the assumed propagation direction (positive x direction in this paper) if the bottom variation in the y direction is not severe.

The governing equation in the models of Dalrymple & Kirby (1988) and Dalrymple *et al.* (1989) is the linear mild-slope equation developed by Berkhoff (1972). Dalrymple *et al.* incorporated nonlinearity in the model by correcting the wave parameters iteratively using an empirical nonlinear dispersion relationship proposed by Kirby & Dalrymple (1986). In the present study, we develop an angular spectrum model for the propagation of Stokes waves over a mildly-varying topography, including nonlinearity in a more rigorous fashion. In §2, a simple angular spectrum model for water of constant depth is derived, illustrating the angular spectrum and its physical significance. In §3, the equations governing the water wave motion are perturbed using the method of multiple scales

¹Present address: Virginia Institute of Marine Science, Gloucester Point, VA 23062, USA

and Stokes expansions for the velocity potential and free surface displacement, yielding a set of perturbation equations at each order in wave steepness. In §4, the first- and second-order problems are solved completely and a set of equations governing the slow evolution of the angular spectrum is obtained. In §5, we explore some subsets of the equations derived in §4 and they are compared with some existing models. Numerical examples to show the ability of the model are presented in §6, and finally a summary of the main results of the paper is given in §7.

2 The angular spectrum and its physical interpretation

In order to illustrate the concept of the angular spectrum and its physical significance, we consider the Helmholtz equation in $\Phi(x, y)$ in water of constant depth:

$$\frac{\partial^2 \Phi}{\partial x^2} + \frac{\partial^2 \Phi}{\partial y^2} + k^2 \Phi = 0, \quad (2.1)$$

where k is the constant wavenumber and the complex wave potential $\Phi(x, y)$ is related to the total velocity potential for the wave motion, $\phi(x, y, z, t)$, by

$$\phi = \Phi(x, y) \cosh k(h + z) e^{-i\omega t}, \quad (2.2)$$

where $i = \sqrt{-1}$, ω is the angular frequency of the wave, h is the constant water depth, and the vertical coordinate z is measured vertically upwards from the still water line.

Suppose that a wave field represented by $\Phi(0, y)$ is incident on the line $x = 0$, propagating into the half-plane $y > 0$. The Fourier transform of $\Phi(0, y)$ in the y direction is

$$\hat{\Phi}(0, \lambda) = \int_{-\infty}^{\infty} \Phi(0, y) e^{-i\lambda y} dy, \quad (2.3)$$

where the caret denotes a transformed variable and λ is the continuous Fourier parameter. The inverse Fourier transform is

$$\Phi(0, y) = \frac{1}{2\pi} \int_{-\infty}^{\infty} \hat{\Phi}(0, \lambda) e^{i\lambda y} d\lambda. \quad (2.4)$$

Noting that the unit-amplitude plane wave propagating in the direction of $\vec{k} \equiv (\sqrt{k^2 - \lambda^2}, \lambda)$ is $\exp[i(\sqrt{k^2 - \lambda^2} x + \lambda y)]$, $\exp(i\lambda y)$ may be regarded as a unit-amplitude plane wave propagating in that direction at $x = 0$. The complex amplitude of that plane wave component is simply $(1/2\pi)\hat{\Phi}(0, \lambda) d\lambda$ as can be seen in (2.4). For this reason, $\hat{\Phi}(0, \lambda)$ is called the *angular spectrum* of the wave field $\Phi(0, y)$. The angular spectrum is merely the Fourier transform of a wave field along a straight line, each component of which represents the complex amplitude of the plane wave propagating in a certain direction.

The Fourier transform of (2.1) in the y direction provides an equation for the evolution of the angular spectrum $\hat{\Phi}(x, \lambda)$:

$$\hat{\Phi}_{xx} + (k^2 - \lambda^2) \hat{\Phi} = 0, \quad (2.5)$$

where subscripts denote partial differentiation. An elementary solution to this equation for constant k is

$$\hat{\Phi}(x, \lambda) = \hat{\Phi}(0, \lambda) e^{i\sqrt{k^2 - \lambda^2} x}. \quad (2.6)$$

This result will be interpreted differently depending on the magnitude of $(k^2 - \lambda^2)$. If $(k^2 - \lambda^2) > 0$, then the effect of propagation over a distance x is simply a change in the relative phases of the various components of the angular spectrum. Since each plane wave component propagates at a different angle, each travels a different distance to reach a given observation point and relative phase delays are thus introduced. If $(k^2 - \lambda^2) < 0$, these wave components decay exponentially as they propagate in the x direction. Such components of the angular spectrum are called *evanescent modes*. The limiting case, $(k^2 - \lambda^2) = 0$, corresponds to the plane wave propagating in the y direction, contributing no net energy flow in the x direction.

Finally, the inverse Fourier transform of (2.6) gives the solution to (2.1) in terms of the initial angular spectrum $\hat{\Phi}(0, \lambda)$:

$$\Phi(x, y) = \frac{1}{2\pi} \int_{-\infty}^{\infty} \hat{\Phi}(0, \lambda) e^{i\sqrt{k^2 - \lambda^2} x} e^{i\lambda y} d\lambda. \quad (2.7)$$

In the actual computation using discrete data values on a computational grid, a discrete Fourier transform is used under the assumption that the model domain is periodic in the y direction. By discretizing the domain of width ℓ by $N + 1$ equidistant points of spacing $\Delta y = \ell/N$, the velocity potential $\Phi(x, y)$ defined on these points can be transformed into discrete Fourier modes by

$$\hat{\Phi}(x, p) = \frac{1}{N} \sum_{j=0}^{N-1} \Phi(x, j\Delta y) e^{-ip\lambda_j \Delta y}, \quad p = 0, \pm 1, \pm 2, \dots, \pm(\frac{N}{2} - 1), -\frac{N}{2}, \quad (2.8)$$

which describe the wave components propagating in different directions as indicated in figure 1. The inversion formula is

$$\Phi(x, j\Delta y) = \sum_p \hat{\Phi}(x, p) e^{ip\lambda_j \Delta y}, \quad j = 0, 1, 2, \dots, (N - 1), \quad (2.9)$$

where

$$\lambda = \frac{2\pi}{N\Delta y}, \quad (2.10)$$

which is different from the continuous Fourier parameter λ used previously. These transforms can be performed efficiently by using a fast Fourier transform.

3 Governing equations and multiple-scale perturbation expansions

The exact equations governing the velocity potential $\phi(x, y, z, t)$ and the free surface $\eta(x, y, t)$ of the waves propagating in water of finite depth, assuming incompressible fluid and irrotational flow motion, are given by

$$\nabla^2 \phi = 0 \quad (-h < z < \eta), \quad (3.1)$$

$$g\phi_z + \phi_{tt} + |\nabla\phi|_t^2 + \frac{1}{2}(\nabla\phi \cdot \nabla)|\nabla\phi|^2 = 0 \quad (z = \eta), \quad (3.2)$$

$$\phi_t + \frac{1}{2}|\nabla\phi|^2 + g\eta = 0 \quad (z = \eta), \quad (3.3)$$

$$\phi_z = -\nabla_h \phi \cdot \nabla_h h \quad (z = -h), \quad (3.4)$$

where ∇ and ∇_h are the three-dimensional and horizontal gradient operators, respectively, g is the gravitational acceleration, and $h(x, y)$ is the water depth measured from the still water line.

The method of multiple scales has been proven to be a powerful tool for problems of weakly-nonlinear waves by Benney & Roskes (1969), Yue & Mei (1980), and Kirby & Dalrymple (1983), among others. In the present multiple-scale analysis we introduce the following slow variables:

$$x_1 = \epsilon x, \quad x_2 = \epsilon^2 x, \quad \dots; \quad t_1 = \epsilon t, \quad t_2 = \epsilon^2 t, \quad \dots, \quad (3.5)$$

where ϵ is the Stokes-wave steepness parameter, so that the derivatives with respect to x and t are replaced by

$$\frac{\partial}{\partial x} \sim \frac{\partial}{\partial x} + \epsilon \frac{\partial}{\partial x_1} + \epsilon^2 \frac{\partial}{\partial x_2} + \dots; \quad \frac{\partial}{\partial t} \sim \frac{\partial}{\partial t} + \epsilon \frac{\partial}{\partial t_1} + \epsilon^2 \frac{\partial}{\partial t_2} + \dots, \quad (3.6)$$

where x and t relate to the fast wave-like characteristics while x_1, x_2, \dots , and t_1, t_2, \dots , cover the slower modulation of the wave field.

No assumption is made yet for scales for y since the lateral variation of the wave field will be taken care of later by its angular spectrum representation, which therefore makes it possible to model the large-angle components and the small-angle components of the wave field equally well (cf. figure 1). This differs from previously derived models in which appropriate scaling for y was also made depending on the problem to be considered. In the parabolic models of Yue & Mei (1980) and Kirby & Dalrymple (1983), for example, they chose two scales x and x_2 in the x direction, while in the y direction only one variable, $y_1 = \epsilon y$, was chosen under the assumption that no fast wave-like variation occurs in the y direction, consistent with the parabolic approximation, but the effect of finite angles of propagation with respect to the x axis allows the amplitude to vary in the y direction $O(\epsilon^{-1})$ times faster than in the x direction.

The bottom boundary condition (3.4) is defined for different water depths at different locations in the y direction. For its angular spectrum representation, however, we need to express it for a reference depth which is constant in the y direction. This is chosen, in this study, as the laterally averaged depth, \bar{h} , given by

$$\bar{h}(x) = \frac{1}{\ell} \int_0^\ell h(x, y) dy, \quad (3.7)$$

so that

$$h(x, y) = \bar{h}(1 - \nu), \quad (3.8)$$

where

$$\nu(x, y) = \frac{\delta(x, y)}{\bar{h}(x)}. \quad (3.9)$$

Here $\delta(x, y)$ is the deviation of the actual bottom from the laterally averaged depth, as indicated in figure 2. Note that \bar{h} is a function of x only and the variability of depth in the y direction is contained in $\nu(x, y)$, whose magnitude is usually much smaller than unity if the topography does not deviate greatly from straight and parallel contours.

In order to determine the point at which the effect of bottom slope and bottom irregularity (in the y direction) enters the bottom boundary condition, we need to choose the scales for $\nabla_h h$ and $\nu(x, y)$. Assuming mildly-varying topography, we restrict $\nabla_h h$ to be $O(\epsilon^2)$, that is,

$$h_x \sim \epsilon^2 h_{x_2}, \quad h_y \sim \epsilon^2 h_{y_2}, \quad (3.10)$$

where an additional scale, $y_2 \sim \epsilon^2 y$, was defined. Accordingly, we assume

$$\bar{h}_x \sim \epsilon^2 \bar{h}_{x_2}, \quad \delta_x \sim \epsilon^2 \delta_{x_2}, \quad \delta_y \sim \epsilon^2 \delta_{y_2}. \quad (3.11)$$

The bottom is then effectively locally flat up to the third order in ϵ . These scales for bottom slopes were chosen by Djordjević & Redekopp (1978) and Kirby & Dalrymple (1983). With this choice the effect of bottom slope becomes as important as the nonlinearities; that is, both the bottom slope terms and the cubic nonlinear terms appear first in the equations at third order.

For the magnitude of the lateral bottom irregularities, we assume $\nu \sim O(\epsilon)$ so that

$$\delta(x, y) = \epsilon \bar{h} \mu(x, y), \quad (3.12)$$

where $\mu(x, y) \sim O(1)$ is introduced for later convenience. The effect of lateral bottom irregularities then appears at the second order in ϵ . This scale necessitates the choice of the slow variables x_1 and t_1 which are omitted in Yue & Mei (1980) and Kirby & Dalrymple (1983) based on the argument that for Stokes waves the modulation scales in horizontal space and time are $O(\epsilon^{-2})$ times greater than the wavelength and wave period, respectively. Without these slow variables, the ϕ_{21} problem in §4.2 becomes unsolvable since it is then identical to the homogeneous first-order problem except for the inhomogeneous bottom boundary condition. The bottom forcing term in the second-order problem is introduced by the process of modifying the actual bottom boundary

condition (3.4) to one on the laterally averaged depth. In the models of Yue & Mei and Kirby & Dalrymple, this process is not necessary and the ϕ_{21} problem is identical to the first-order problem, so they neglected the solution for ϕ_{21} . If we assumed $\nu \sim O(\epsilon^2)$, this difficulty could be avoided; the bottom topography, however, then could be assumed as straight and parallel contours.

We proceed by expanding the free surface conditions (3.2) and (3.3) about $z = 0$ and the bottom boundary condition (3.4) about $z = -\bar{h}(x)$ in Taylor series. Substitution of Stokes expansions for ϕ and η :

$$\phi = \sum_{n=1}^{\infty} \epsilon^n \phi_n; \quad \eta = \sum_{n=1}^{\infty} \epsilon^n \eta_n \quad (3.13)$$

into these equations, with the scales (3.6), (3.10) – (3.12), then gives a boundary value problem in z for each order of n :

$$\nabla^2 \phi_n = F_n \quad (-\bar{h} < z < 0), \quad (3.14)$$

$$g\phi_{n,z} + \phi_{n,zz} = G_n \quad (z = 0), \quad (3.15)$$

$$\phi_{n,t} + g\eta_n = H_n \quad (z = 0), \quad (3.16)$$

$$\phi_{n,z} = B_n \quad (z = -\bar{h}), \quad (3.17)$$

where F_n , G_n , H_n , B_n are the forcing terms determined by lower-order solutions and are given in the appendix.

4 Evolution of the angular spectrum

The boundary value problems (3.14) – (3.17) need to be solved up to the second order in order to obtain the third-order forcing terms which describe the cubic nonlinear interaction. The first-order solution is expressed in terms of the angular spectrum. Since the higher-order problems are linear in ϕ_n , the method of superposition allows the solution in the form, $\phi_n = \phi_{n1} + \phi_{n2} + \dots + \phi_{nn}$, where ϕ_{n1} is the waves proportional to the first harmonics, ϕ_{n2} is the sum and difference waves, and so forth. Then since the problem of ϕ_{n1} is inhomogeneous and its homogeneous version (i.e., the first-order problem) has ϕ_1 as a nontrivial solution, they must satisfy a solvability condition, which follows by applying Green's second identity to ϕ_1 and ϕ_{n1} and leads to the so-called *evolution equations* governing the slow modulation of the angular spectrum.

4.1 First-order solution

For $n = 1$, the problem (3.14) – (3.17) is homogeneous. This problem describes waves propagating on a beach with straight and parallel bottom contours whose depth is given by $\bar{h}(x)$. The solutions for ϕ_1 and η_1 can be readily obtained in the form of discrete Fourier transform (cf. equation 2.9) as

$$\phi_1 = \sum_p \left(-\frac{ig}{2\omega} \int A_p e^{i\psi_p} + \text{c.c.} \right); \quad \eta_1 = \sum_p \left(\frac{A_p}{2} e^{i\psi_p} + \text{c.c.} \right), \quad (4.1)$$

where c.c. is the complex conjugate, ψ_p is the phase function:

$$\psi_p = \int^x \sqrt{\bar{k}^2 - (p\lambda)^2} dx + p\lambda y - \omega t, \quad (4.2)$$

in which λ is given by (2.10), and the angular frequency ω is related to the laterally averaged depth, $\bar{h}(x)$, and the corresponding wavenumber $\bar{k}(x)$ (hereafter we use $k \equiv \bar{k}$ for simplicity) by

$$\omega^2 = gk \tanh k\bar{h}. \quad (4.3)$$

$A_p(x_1, x_2, t_1, t_2)$ is the slowly varying complex amplitude of the wave component propagating in the direction $\bar{k} = (\sqrt{k^2 - (p\lambda)^2}, p\lambda)$, and

$$f = \frac{\cosh k(\bar{h} + z)}{\cosh k\bar{h}}. \quad (4.4)$$

The index p varying from $-\frac{N}{2}$ to $(\frac{N}{2} - 1)$ (cf. equation 2.8) describes the plane wave components propagating in different directions as indicated in figure 1. The wave components for which $(p\lambda)^2 > k^2$ represent the evanescent modes which decay exponentially in the x direction. Since in general k has the minimum value at the offshore boundary, some evanescent modes become progressive modes as they propagate into shallower region. In this study, these evanescent modes are neglected and only the progressive modes at the offshore boundary are carried into the domain, assuming the energy of the evanescent modes is negligibly small compared with that of the progressive modes. We close this section by mentioning that $k_x \sim \epsilon^2 k_{x_2}$ and $f_x = \epsilon^2 f_{x_2}$ since we assumed \bar{h}_x to be $O(\epsilon^2)$.

4.2 Second-order solution

Since the second-order problem is linear in ϕ_2 and η_2 , it can be advantageously solved by assuming

$$\phi_2 = \phi_{21} + \phi_{22}; \quad \eta_2 = \eta_{21} + \eta_{22}, \quad (4.5)$$

in which ϕ_{21} and η_{21} are taken to satisfy the problem with the forcing terms proportional to the first harmonics (i.e., $\exp(\pm i\psi_p)$), while ϕ_{22} and η_{22} should satisfy the problem with the remaining forcing terms proportional to $\exp[\pm i(\psi_q \pm \psi_r)]$.

Assuming ϕ_{21} and η_{21} to have the forms

$$\phi_{21} = \sum_p [(\phi_{21})_p e^{i\Omega_p} e^{ip\lambda y} + \text{c.c.}]; \quad \eta_{21} = \sum_p [(\eta_{21})_p e^{i\Omega_p} e^{ip\lambda y} + \text{c.c.}], \quad (4.6)$$

where

$$\Omega_p = \int^x \sqrt{k^2 - (p\lambda)^2} dx - \omega t, \quad (4.7)$$

and recalling the formula for inverse discrete Fourier transform (2.9), we observe that $(\phi_{21})_p \exp(i\Omega_p)$, $p = 0, \pm 1, \dots$, represent the discrete Fourier components of ϕ_{21} neglecting its conjugate part. Expressing the forcing terms in the same form as equation (4.6), for example,

$$F_{21} = \sum_p \left[(F_{21})_p e^{i\Omega_p} e^{ip\lambda y} + \text{c.c.} \right], \quad (4.8)$$

the discrete Fourier transform of the ϕ_{21} problem, neglecting the conjugate part and dividing through by $\exp(i\Omega_p)$, is given by

$$\left(\frac{\partial^2}{\partial z^2} - k^2 \right) (\phi_{21})_p = (F_{21})_p \quad (-\bar{h} < z < 0), \quad (4.9)$$

$$g \frac{\partial}{\partial z} (\phi_{21})_p - \omega^2 (\phi_{21})_p = (G_{21})_p \quad (z = 0), \quad (4.10)$$

$$-i\omega (\phi_{21})_p + g (\eta_{21})_p = (H_{21})_p \quad (z = 0), \quad (4.11)$$

$$\frac{\partial}{\partial z} (\phi_{21})_p = (B_{21})_p \quad (z = -\bar{h}). \quad (4.12)$$

Before proceeding to solve this problem, we need the evolution equation for A_p at the second order. By letting

$$\phi_1 = \sum_p \left[(\phi_{11})_p e^{i\Omega_p} e^{ip\lambda y} + \text{c.c.} \right], \quad (4.13)$$

the boundary value problem for $(\phi_{11})_p$ is the homogeneous form of the equations (4.9) - (4.12). Applying Green's second identity to $(\phi_{11})_p$ and $(\phi_{21})_p$, we obtain the solvability condition

$$\int_{-\bar{h}}^0 (F_{21})_p f dz = \frac{1}{g} (G_{21})_p - \frac{(B_{21})_p}{\cosh k\bar{h}}. \quad (4.14)$$

Performing the integration over depth and noting that

$$\int_{-\bar{h}}^0 f^2 dz = \frac{CC_g}{g}, \quad (4.15)$$

where $C = \omega/k$, $C_g = \partial\omega/\partial k$, leads to the evolution equation for A_p

$$A_{p,1} = - \frac{\sqrt{k^2 - (p\lambda)^2}}{k} C_g A_{p,1} + \frac{i\omega k \bar{h}}{\sinh 2k\bar{h}} e^{-i\Theta_p} I_p^1, \quad (4.16)$$

where

$$\Theta_p = \int^x \sqrt{k^2 - (p\lambda)^2} dx, \quad (4.17)$$

and

$$I_p^1 = F_p \left[\mu(x, y) F^{-1} (A_m e^{i\Theta_m}) \right] \quad (4.18)$$

represents the forcing due to the interaction between surface wave modes and lateral bottom variation. F^{-1} and F_p on the right side denote the inverse Fourier transform and the p th component of the discrete Fourier transform, respectively. The superscript 1 in I_p^1 is used because other wave-bottom interaction terms of the similar form will appear later. Each mode of the angular spectrum, A_p , thus can be modified at the second order through the interaction of surface waves with the lateral bottom variation. On straight and parallel contours, the wave-bottom interaction term I_p^1 vanishes since $\mu(x, y) = 0$ everywhere. The effect of bottom slope has not entered yet at the second order. Without the wave-bottom interaction term, thus equation (4.16) describes the wave envelope A_p propagating without change of form on a locally flat bottom at the speed $(\sqrt{k^2 - (p\lambda)^2}/k)C_g$ in the x direction which is the x component of the group velocity C_g .

The solution for $(\phi_{21})_p$ is obtained by using the method of variation of parameters as

$$(\phi_{21})_p = -\frac{g}{2\omega} \frac{\sqrt{k^2 - (p\lambda)^2}}{k} (\bar{h} + z) \frac{\sinh k(\bar{h} + z)}{\cosh k\bar{h}} A_{p_{z_1}} + \frac{i}{2} \omega \bar{h} \frac{\sinh k(\bar{h} + z)}{\sinh k\bar{h}} e^{-i\Theta_p} I_p^1. \quad (4.19)$$

The corresponding free surface displacement $(\eta_{21})_p$ is

$$(\eta_{21})_p = -\frac{i}{2\omega} \frac{\sqrt{k^2 - (p\lambda)^2}}{k} (C_g + \omega \bar{h} \tanh k\bar{h}) A_{p_{z_1}} + \frac{k\bar{h}(2 \sinh^2 k\bar{h} - 1)}{2 \sinh 2k\bar{h}} e^{-i\Theta_p} I_p^1. \quad (4.20)$$

The solution for the sum and difference waves is given, as in Sharma & Dean (1979), by

$$\phi_{22} = \sum_q \sum_r \left[C_{qr}^+ f_{qr}^+ A_q A_r e^{i(\psi_q + \psi_r)} + C_{qr}^- f_{qr}^- A_q A_r^* e^{i(\psi_q - \psi_r)} \right] + \text{c.c.}, \quad (4.21)$$

$$\eta_{22} = \sum_q \sum_r \left[D_{qr}^+ A_q A_r e^{i(\psi_q + \psi_r)} + D_{qr}^- A_q A_r^* e^{i(\psi_q - \psi_r)} \right] + \text{c.c.}, \quad (4.22)$$

where * also denotes the complex conjugate and

$$C_{qr}^\pm = \frac{\Gamma_{qr}^\pm}{g k_{qr}^\pm \tanh k_{qr}^\pm \bar{h} - (\omega \pm \omega)^2}, \quad (4.23)$$

$$D_{qr}^\pm = \frac{1}{g} \left[\Delta_{qr}^\pm + i(\omega \pm \omega) C_{qr}^\pm \right], \quad (4.24)$$

$$\Gamma_{qr}^\pm = \pm \frac{ig^2}{2\omega} \left(\sqrt{k^2 - (q\lambda)^2} \sqrt{k^2 - (r\lambda)^2} + (q\lambda)(r\lambda) \mp \frac{3}{2} R^2 \pm \frac{k^2}{2} \right), \quad (4.25)$$

$$\Delta_{qr}^{\pm} = -\frac{g^2}{8\omega^2} \left(\sqrt{k^2 - (q\lambda)^2} \sqrt{k^2 - (r\lambda)^2} + (q\lambda)(r\lambda) \mp R^2 - 2R^2 \right), \quad (4.26)$$

$$R = k \tanh k\bar{h} = \frac{\omega^2}{g}, \quad (4.27)$$

$$f_{qr}^{\pm} = \frac{\cosh k_{qr}^{\pm}(\bar{h} + z)}{\cosh k_{qr}^{\pm}\bar{h}}, \quad (4.28)$$

$$k_{qr}^{\pm} = |\bar{k}_q \pm \bar{k}_r|, \quad (4.29)$$

$$\bar{k}_q = \sqrt{k^2 - (q\lambda)^2} \bar{i} + (q\lambda) \bar{j}, \quad (4.30)$$

where \bar{i} and \bar{j} are the unit vectors in the x and y directions, respectively. It can be shown for the case of a single wave train that this solution reduces to that of Stokes second-order theory, i.e.,

$$\phi_{22}(q = r) = -\frac{3}{16} i\omega \frac{\cosh 2k(\bar{h} + z)}{\sinh^4 k\bar{h}} A_q e^{2i\psi_q} + \text{c.c.} \quad (4.31)$$

4.3 Evolution equations for the angular spectrum A ,

For $n = 3$, again the problem is linear in ϕ_3 so that we can assume the solution as $\phi_3 = \phi_{31} + \phi_{32} + \phi_{33}$ as in the second-order problem. Neglecting the forcing terms, F_{32} , G_{32} and B_{32} , representing quadratic resonances which can occur only in shallow water, and expressing ϕ_{31} as

$$\phi_{31} = \sum_s \left[(\phi_{31})_s e^{i\Omega_s} e^{i s \lambda y} + \text{c.c.} \right], \quad (4.32)$$

the discrete Fourier transform of the ϕ_{31} problem, neglecting its conjugate part, is given by

$$\left(\frac{\partial^2}{\partial z^2} - k^2 \right) (\phi_{31})_s e^{i\Omega_s} = (F_{31})_s e^{i\Omega_s} \quad (-\bar{h} < z < 0), \quad (4.33)$$

$$g \frac{\partial}{\partial z} (\phi_{31})_s e^{i\Omega_s} - \omega^2 (\phi_{31})_s e^{i\Omega_s} = (G_{31})_s e^{i\Omega_s} + (G_{33})_s \quad (z = 0), \quad (4.34)$$

$$\frac{\partial}{\partial z} (\phi_{31})_s e^{i\Omega_s} = (B_{31})_s e^{i\Omega_s} \quad (z = -\bar{h}). \quad (4.35)$$

The forcing terms, $(F_{31})_s$, $(G_{31})_s$, and $(B_{31})_s$, are obtained from the third-order forcing terms directly proportional to the first harmonics, and the cubic resonant interaction term $(G_{33})_s$, due to the interactions between the primary waves and the sum and difference waves or among the primary waves themselves is

$$(G_{33})_s = \sum_p \sum_q \sum_r Q A_p A_q A_r^* \exp[i(\Omega_p + \Omega_q - \Omega_r)] \delta_{s=p+q-r}, \quad (4.36)$$

where the interaction coefficient Q is given by

$$\begin{aligned}
Q = & -g \left[\sqrt{k^2 - (r\lambda)^2} \left(\sqrt{k^2 - (q\lambda)^2} - \sqrt{k^2 - (p\lambda)^2} \right) (r\lambda)(q\lambda + p\lambda) \right. \\
& - Rk_{qp}^+ \tanh(k_{qp}^+ \bar{h}) + \frac{1}{2} k_{qp}^{+2} \left. \right] C_{qp}^+ - \frac{ig^2}{2\omega} (k^2 - R^2) (D_{qp}^+ - D_{qr}^- - D_{rq}^-) \\
& - \frac{i}{8} \frac{g^3}{\omega^3} \left[\sqrt{k^2 - (p\lambda)^2} \sqrt{k^2 - (q\lambda)^2} \sqrt{k^2 - (r\lambda)^2} \left(2\sqrt{k^2 - (p\lambda)^2} - \sqrt{k^2 - (r\lambda)^2} \right) \right. \\
& + (p\lambda)(q\lambda)(r\lambda)(2(p\lambda) - (r\lambda)) + k^2 R^2 + 2\sqrt{k^2 - (p\lambda)^2} \sqrt{k^2 - (r\lambda)^2} (q\lambda)(p\lambda - r\lambda) \\
& + 2\sqrt{k^2 - (p\lambda)^2} \sqrt{k^2 - (q\lambda)^2} (q\lambda)(r\lambda) - 4R^2 \left(\sqrt{k^2 - (p\lambda)^2} \sqrt{k^2 - (r\lambda)^2} + (p\lambda)(r\lambda) \right) \\
& \left. \left. - 2R^2 \left(\sqrt{k^2 - (p\lambda)^2} \sqrt{k^2 - (q\lambda)^2} + (p\lambda)(q\lambda) \right) \right] \right], \quad (4.37)
\end{aligned}$$

and the Kronecker delta, $\delta_{s=p+q-r}$, describing the resonant condition has the value 1 if $s = p + q - r$ is satisfied and is 0 otherwise. For the self-interaction of a single wave train ($p = q = r = s$), this reduces to

$$Q = \frac{i}{2} g \omega k^2 \frac{\cosh 4k\bar{h} + 2 \tanh^2 k\bar{h}}{8 \sinh^4 k\bar{h}}, \quad (4.38)$$

which is the coefficient of the cubic nonlinear term in the nonlinear Schrödinger equations of Yue & Mei (1980) and Kirby & Dalrymple (1983).

Again applying Green's second identity to $(\phi_{31})_s e^{i\Omega_s}$ and $(\phi_{11})_s e^{i\Omega_s}$, we obtain the solvability condition

$$\int_{-\bar{h}}^0 (F_{31})_s f dz = \frac{1}{g} \left[(G_{31})_s + (G_{33})_s e^{-i\Omega_s} \right] - \frac{(B_{31})_s}{\cosh k\bar{h}}, \quad (4.39)$$

which leads to the evolution equation for A_s at the third order:

$$\begin{aligned}
& A_{s,12} + \frac{\sqrt{k^2 - (s\lambda)^2}}{k} C_g A_{s,2} + \frac{[\sqrt{k^2 - (s\lambda)^2} C C_g]_{x_2}}{2\omega} A_s + i D_s A_{s,1,1} \\
& + \frac{\bar{h} \sqrt{k^2 - (s\lambda)^2}}{\sinh 2k\bar{h}} \left(\frac{C_g}{2} + \omega \bar{h} \tanh k\bar{h} \right) e^{-i\Theta_s} I_s^5 \\
& + \frac{\bar{h}}{\sinh 2k\bar{h}} \left(\frac{C_g}{2} + (2C_g - C) \sinh^2 k\bar{h} - 2C \right) e^{-i\Theta_s} I_s^2 \\
& - \frac{i\omega k^2 \bar{h}}{2 \sinh^2 2k\bar{h}} (1 + 4\bar{h} \sinh^2 k\bar{h}) e^{-i\Theta_s} I_s^6 \\
& - \frac{g}{2\omega \cosh^2 k\bar{h}} e^{-i\Theta_s} (I_s^3 + I_s^4) + \frac{1}{g} (G_{33})_s e^{-i\Omega_s} = 0, \quad (4.40)
\end{aligned}$$

where

$$D_s = \frac{k^2 - (s\lambda)^2}{k^2} \left(\frac{C_g^2}{2\omega} + C_g \bar{h} \tanh k\bar{h} \right) - \frac{C_g}{2k} - \frac{g(k^2 - (s\lambda)^2)}{4\omega k^2} \left(\bar{h} + \bar{h} \tanh^2 k\bar{h} - \frac{\tanh k\bar{h}}{k} \right), \quad (4.41)$$

and the new wave-bottom interaction terms are

$$I_s^2 = F_s \left[\mu(x, y) F^{-1} \left(\sqrt{k^2 - (m\lambda)^2} A_{m, x_1} e^{i\Theta_m} \right) \right], \quad (4.42)$$

$$I_s^3 = F_s \left[\delta_{x_2} F^{-1} \left(\sqrt{k^2 - (m\lambda)^2} A_m e^{i\Theta_m} \right) \right], \quad (4.43)$$

$$I_s^4 = F_s \left[\delta_{y_2} F^{-1} \left((m\lambda) A_m e^{i\Theta_m} \right) \right], \quad (4.44)$$

$$I_s^5 = F_s \left[\mu(x, y) F^{-1} \left(A_{m, x_1} e^{i\Theta_m} \right) \right], \quad (4.45)$$

$$I_s^6 = F_s \left[\mu^2 F^{-1} \left(A_m e^{i\Theta_m} \right) \right]. \quad (4.46)$$

Adding the equation (4.16) with s instead of p and ϵ times the equation (4.40), considering A_s as functions of x_1 and t_1 only, that is,

$$\frac{\partial}{\partial t_1} + \epsilon \frac{\partial}{\partial t_2} \longrightarrow \frac{\partial}{\partial t_1}, \quad \frac{\partial}{\partial x_1} + \epsilon \frac{\partial}{\partial x_2} \longrightarrow \frac{\partial}{\partial x_1}, \quad (4.47)$$

yield

$$\begin{aligned} A_{s, t_1} + \frac{\sqrt{k^2 - (s\lambda)^2}}{k} C_g A_{s, x_1} + \epsilon \frac{[\sqrt{k^2 - (s\lambda)^2} C C_g]_{x_2}}{2\omega} A_s + i\epsilon D_s A_{s, x_1 x_1} \\ - \frac{i\omega k \bar{h}}{\sinh 2k\bar{h}} e^{-i\Theta_s} I_s^1 + \epsilon \frac{\bar{h} \sqrt{k^2 - (s\lambda)^2}}{\sinh 2k\bar{h}} \left(\frac{C_g}{2} + \omega \bar{h} \tanh k\bar{h} \right) e^{-i\Theta_s} I_s^5 \\ + \epsilon \frac{\bar{h}}{\sinh 2k\bar{h}} \left(\frac{C_g}{2} + (2C_g - C) \sinh^2 k\bar{h} - 2C \right) e^{-i\Theta_s} I_s^2 \\ - \epsilon \frac{i\omega k^2 \bar{h}}{2 \sinh^2 2k\bar{h}} (1 + 4\bar{h} \sinh^2 k\bar{h}) e^{-i\Theta_s} I_s^6 \\ - \epsilon \frac{g}{2\omega \cosh^2 k\bar{h}} e^{-i\Theta_s} (I_s^3 + I_s^4) + \frac{\epsilon}{g} (G_{33})_s e^{-i\Theta_s} = 0. \end{aligned} \quad (4.48)$$

Using the scales, $\partial/\partial t_1 \sim \epsilon^{-1}(\partial/\partial t)$, $\partial/\partial x_1 \sim \epsilon^{-1}(\partial/\partial x)$, $\partial/\partial x_2 \sim \epsilon^{-2}(\partial/\partial x)$, $\mu \sim \epsilon^{-1}\nu$, $\delta_{x_2} \sim \epsilon^{-2}\delta_x$, $\delta_{y_2} \sim \epsilon^{-2}\delta_y$, finally we obtain the evolution equation for A_s in the physical coordinates (x, y, t) :

$$\begin{aligned} A_{s, t} + \frac{\sqrt{k^2 - (s\lambda)^2}}{k} C_g A_{s, x} + \frac{[\sqrt{k^2 - (s\lambda)^2} C C_g]_x}{2\omega} A_s + iD_s A_{s, xx} \\ - \frac{i\omega k \bar{h}}{\sinh 2k\bar{h}} e^{-i\Theta_s} F_s \left[\nu F^{-1} (A_m e^{i\Theta_m}) \right] \\ + \frac{\bar{h} \sqrt{k^2 - (s\lambda)^2}}{\sinh 2k\bar{h}} \left(\frac{C_g}{2} + \omega \bar{h} \tanh k\bar{h} \right) e^{-i\Theta_s} F_s \left[\nu F^{-1} (A_{m, x} e^{i\Theta_m}) \right] \\ + \frac{\bar{h}}{\sinh 2k\bar{h}} \left(\frac{C_g}{2} + (2C_g - C) \sinh^2 k\bar{h} - 2C \right) e^{-i\Theta_s} F_s \left[\nu F^{-1} \left(\sqrt{k^2 - (m\lambda)^2} A_{m, x} e^{i\Theta_m} \right) \right] \\ - \frac{i\omega k^2 \bar{h}}{2 \sinh^2 2k\bar{h}} (1 + 4\bar{h} \sinh^2 k\bar{h}) e^{-i\Theta_s} F_s \left[\nu^2 F^{-1} (A_m e^{i\Theta_m}) \right] \\ - \frac{g e^{-i\Theta_s}}{2\omega \cosh^2 k\bar{h}} F_s \left[\delta_x F^{-1} \left(\sqrt{k^2 - (m\lambda)^2} A_m e^{i\Theta_m} \right) + \delta_y F^{-1} \left((m\lambda) A_m e^{i\Theta_m} \right) \right] \\ + \frac{1}{g} (G_{33})_s e^{-i\Theta_s} = 0. \end{aligned} \quad (4.49)$$

The ordering parameter ϵ was removed from the last term since it has served its purpose. This equation governs the slow evolution of the wave component A_s due to refraction, diffraction, shoaling, and nonlinear wave interactions. The third term represents the shoaling/refraction of each wave component on laterally averaged depth. The complicated periodic convolution terms represent wave diffraction due to the interaction between surface wave and the lateral bottom variation, which disappear on straight and parallel contours, and the last term is the cubic nonlinear terms.

The time-dependent equation (4.49) is of parabolic type. This equation represents a very general approach to the solution of wave propagation in a domain with properly posed initial condition (at $t = 0$) and boundary conditions (at $x = 0$ and $x = b$ where b is the length of the domain in the x direction). In many practical applications, however, the assumption of steadiness of the wave field may be appropriately utilized. The time-independent equation for A_s cannot be obtained simply by dropping the first term in (4.49) since the time dependency of A_s was extensively involved in deriving other terms. One may obtain it by setting the derivatives with respect to the slow times t_1 and t_2 to be zero from the outset and repeating the derivation. The resulting expression for the time-independent evolution equations for A_s is

$$\begin{aligned} & \frac{\sqrt{k^2 - (s\lambda)^2}}{k} C_g A_{s,x} + \frac{[\sqrt{k^2 - (s\lambda)^2} C C_g]}{2\omega} A_s - i \frac{\omega k \bar{h}}{\sinh 2k\bar{h}} e^{-i\Theta_s} F_s \left[\nu F^{-1} (A_m e^{i\Theta_m}) \right] \\ & + i \frac{\omega^2 k^4 \bar{h}^2}{C_g^2 \sqrt{k^2 - (s\lambda)^2} \sinh^2 2k\bar{h}} E_s e^{-i\Theta_s} F_s \left[\nu F^{-1} \left\{ \frac{1}{\sqrt{k^2 - (m\lambda)^2}} F_m \left[\nu F^{-1} (A_n e^{i\Theta_n}) \right] \right\} \right] \\ & - i \frac{\omega k^2 \bar{h}^2}{C_g \sinh 2k\bar{h}} \left(\frac{C}{2} \tanh k\bar{h} + \frac{g}{\omega \cosh^2 k\bar{h}} \right) e^{-i\Theta_s} F_s \left[\nu^2 F^{-1} (A_m e^{i\Theta_m}) \right] \\ & - \frac{g e^{-i\Theta_s}}{2\omega \cosh^2 k\bar{h}} F_s \left[\delta_x F^{-1} \left(\sqrt{k^2 - (m\lambda)^2} A_m e^{i\Theta_m} \right) + \delta_y F^{-1} \left((m\lambda) A_m e^{i\Theta_m} \right) \right] \\ & + \frac{1}{g} (G_{33})_s e^{-i\Theta_s} = 0, \end{aligned} \quad (4.50)$$

where

$$E_s = \frac{1}{2} \left[\frac{C_g}{k} + \frac{g(k^2 - (s\lambda)^2)}{2\omega k^2} \left(\bar{h} + \bar{h} \tanh^2 k\bar{h} - \frac{\tanh k\bar{h}}{k} \right) \right]. \quad (4.51)$$

The angular spectrum A_s is now phase-shifted by the substitution

$$A_s = A'_s e^{i(\sqrt{k_0^2 - (s\lambda)^2} x - \int^x \sqrt{k^2 - (s\lambda)^2} dx)}, \quad (4.52)$$

where k_0 is a fixed reference wavenumber at $x = 0$ (the offshore boundary). A'_s is then the angular spectrum of the velocity potential ϕ_1 given by

$$\phi_1 = \sum_s \left(-\frac{ig}{2\omega} \int A'_s e^{i(\sqrt{k_0^2 - (s\lambda)^2} x + s\lambda y - \omega t)} + \text{c.c.} \right). \quad (4.53)$$

By this procedure, we can eliminate the integral of the wavenumber component in the x direction, $\int^x \sqrt{k^2 - (s\lambda)^2} dx$, which introduces errors when it is computed numerically. Substituting (4.52)

into (4.50) and multiplying through by $k/(\sqrt{k^2 - (s\lambda)^2}C_g)$ give

$$\begin{aligned}
A'_{s,x} = & i \left(\sqrt{k^2 - (s\lambda)^2} - \sqrt{k_o^2 - (s\lambda)^2} \right) A'_s - \frac{[\sqrt{k^2 - (s\lambda)^2} C C_g]_x}{2\sqrt{k^2 - (s\lambda)^2} C C_g} A'_s \\
& + i \frac{\omega k^2 \bar{h}}{C_g \sqrt{k^2 - (s\lambda)^2} \sinh 2k\bar{h}} e^{-i\Theta'_s F_s} \left[\nu F^{-1} \left(A'_m e^{i\Theta'_m} \right) \right] \\
& - i \frac{\omega^2 k^5 \bar{h}^2}{C_g^3 (k^2 - (s\lambda)^2) \sinh^2 2k\bar{h}} E_s e^{-i\Theta'_s F_s} \left[\nu F^{-1} \left\{ \frac{1}{\sqrt{k^2 - (m\lambda)^2}} F_m \left[\nu F^{-1} \left(A'_n e^{i\Theta'_n} \right) \right] \right\} \right] \\
& + i \frac{\omega k^3 \bar{h}^2}{C_g \sqrt{k^2 - (s\lambda)^2} \sinh 2k\bar{h}} \left(\frac{C}{2} \tanh k\bar{h} + \frac{g}{\omega \cosh^2 k\bar{h}} \right) e^{-i\Theta'_s F_s} \left[\nu^2 F^{-1} \left(A'_m e^{i\Theta'_m} \right) \right] \\
& + \frac{g e^{-i\Theta'_s}}{2 C C_g \sqrt{k^2 - (s\lambda)^2} \cosh^2 k\bar{h}} F_s \left[\delta_x F^{-1} \left(\sqrt{k^2 - (m\lambda)^2} A'_m e^{i\Theta'_m} \right) \right. \\
& \quad \left. + \delta_y F^{-1} \left((m\lambda) A'_m e^{i\Theta'_m} \right) \right] \\
& - \frac{k}{g C_g \sqrt{k^2 - (s\lambda)^2}} (G_{33})'_s e^{-i\Omega'_s}, \quad s = 0, \pm 1, \pm 2, \dots,
\end{aligned} \tag{4.54}$$

where

$$\Theta'_s = \sqrt{k_o^2 - (s\lambda)^2} x, \tag{4.55}$$

$$(G_{33})'_s = \sum_p \sum_q \sum_r Q A'_p A'_q A'^*_r \exp \left[i \left(\Omega'_p + \Omega'_q - \Omega'_r \right) \right] \delta_{s=p+q-r}, \tag{4.56}$$

$$\Omega'_s = \Theta'_s - \omega t. \tag{4.57}$$

Equation (4.54) is coupled nonlinear first-order ordinary differential equations for A'_s , $s = 0, \pm 1, \dots$, which can be solved by standard numerical methods provided initial conditions for A'_s at $x = 0$ (offshore boundary) are specified. In this study, we use the fourth-order Runge-Kutta method. The details of finite-differencing and stability analysis of the numerical method are referred to Suh (1989).

5 Comparison with previously derived models for some simple cases

In this section, we explore the correspondences of our evolution equations to previously derived models.

5.1 Time-dependent models

5.1.1 Evolution of wave envelopes propagating normal to shore on a beach with straight and parallel contours

Djordjević & Redekopp (1978) derived an evolution equation for wave envelopes propagating normal to shore (positive x direction in this study) on a beach with straight iso-baths. Simplification of the evolution equation (4.48) to this case can be made by setting $s = 0$ ($A = A_0$), dropping all the wave-bottom interaction terms, and using the scales $\partial/\partial t_1 \sim \epsilon(\partial/\partial t_2)$ and $\partial/\partial x_1 \sim \epsilon(\partial/\partial x_2)$, to yield

$$A_{t_2} + C_g A_{x_2} + \frac{[kCC_g]_{x_2}}{2\omega} A - \frac{i}{2} \epsilon^2 \frac{\partial^2 \omega}{\partial k^2} A_{x_2 x_2} + iK|A|^2 A = 0, \quad (5.1)$$

where

$$D_s(s=0) = \frac{C_g^2}{2\omega} + C_g h \tanh kh - \frac{\omega h \cosh^2 kh}{k \sinh 2kh} = -\frac{1}{2} \frac{\partial^2 \omega}{\partial k^2} \quad (5.2)$$

was used and

$$K = \omega k^2 \frac{\cosh 4kh + 8 - 2 \tanh^2 kh}{16 \sinh^4 kh}. \quad (5.3)$$

On a constant depth, the third term in (5.1) disappears and the equation reduces to the two-dimensional version of Davey & Stewartson (1974) equation without the term representing the effect of first-order long waves, which were omitted in the present study.

By introducing the following variables:

$$\tau = \epsilon \left[\int^x \frac{dx}{C_g(\xi)} - t \right] = \epsilon^{-1} \int^\xi \frac{d\xi}{C_g(\xi)} - \epsilon^{-1} t_2, \quad (5.4)$$

$$\xi = \epsilon^2 x = x_2, \quad (5.5)$$

into (5.1) as in Djordjević & Redekopp (1978), we obtain, after neglecting the terms of $O(\epsilon)$ or smaller, the evolution equation for $A(\xi, \tau)$ as

$$2i\omega C_g A_\xi + i[kCC_g]_\xi A + \frac{\omega}{C_g^2} \frac{\partial^2 \omega}{\partial k^2} A_{\tau\tau} - 2\omega K|A|^2 A = 0. \quad (5.6)$$

In the notation of Djordjević & Redekopp, this equation can be written as

$$\begin{aligned} 2i\omega C_g A_\xi &= ig\sigma \frac{k_\xi}{k} (1 - kh\sigma) A - \left\{ 1 - \frac{gh}{C_g^2} (1 - kh\sigma)(1 - \sigma^2) \right\} A_{\tau\tau} \\ &- \frac{gk^3}{8\sigma} \left(\frac{9}{\sigma^2} - 12 + 13\sigma^2 - 2\sigma^4 \right) |A|^2 A = 0, \end{aligned} \quad (5.7)$$

where $\sigma = \tanh kh$. Except for some algebraic differences in the last term, this equation is identical to Djordjević & Redekopp equation without the term involving long waves. The fourth term in their equation is dimensionally incorrect.

5.1.2 Resonant interactions between two trains of deep-water gravity waves

Following the analysis of Phillips (1960) for the growth of a tertiary wave by the resonant interaction among three primary waves, Longuet-Higgins (1962) studied the resonant interaction between two trains of deep-water gravity waves which is a simpler case of the three-wave interaction when two of the three primary waves are identical. Studies for the nonlinear evolution of wave envelopes due to cubic resonances were also made in parallel. Based on the work of Benney & Newell (1967), Roskes (1976a) presented a nonlinear Schrödinger equation system of the following form to describe the slowly varying amplitudes of two deep-water waves:

$$A_{1T} + \bar{C}_{g1} \cdot \nabla_h A_1 - i\epsilon \sum_{i,j} \gamma_{1,ij} \frac{\partial^2 A_1}{\partial X_i \partial X_j} - i\epsilon A_1 [\beta_{11}|A_1|^2 + \beta_{12}|A_2|^2] = 0, \quad (5.8)$$

$$A_{2T} + \bar{C}_{g2} \cdot \nabla_h A_2 - i\epsilon \sum_{i,j} \gamma_{2,ij} \frac{\partial^2 A_2}{\partial X_i \partial X_j} - i\epsilon A_2 [\beta_{21}|A_1|^2 + \beta_{22}|A_2|^2] = 0, \quad (5.9)$$

where $T = \epsilon t$, $\bar{X} = \epsilon \bar{x}$, β_{ij} is the interaction coefficients, and the dispersion tensors γ_{li} , $l = 1, 2$, are defined by

$$\gamma_{li} = \frac{1}{2} \frac{\partial^2}{\partial k_i \partial k_j} \omega(\bar{k}_l). \quad (5.10)$$

For an angular spectrum which varies only in the x direction, (5.8) and (5.9) can be simplified by dropping the terms involving the derivative of the amplitude with respect to X_2 which corresponds to the y direction in our notation. If we consider two components of an angular spectrum, each propagating in directions $\bar{k}_m = \sqrt{k^2 - (m\lambda)^2} \bar{i} + (m\lambda) \bar{j}$ and $\bar{k}_n = \sqrt{k^2 - (n\lambda)^2} \bar{i} + (n\lambda) \bar{j}$ with the same frequency ω , (5.8) and (5.9) can be written in the present notation as

$$A_{m,1} + \frac{\sqrt{k^2 - (m\lambda)^2}}{k} C_g A_{m,x_1} + i\epsilon D_m A_{m,x_1,x_1} - i\epsilon A_m [\beta_{11}|A_m|^2 + \beta_{12}|A_n|^2] = 0, \quad (5.11)$$

$$A_{n,1} + \frac{\sqrt{k^2 - (n\lambda)^2}}{k} C_g A_{n,x_1} + i\epsilon D_n A_{n,x_1,x_1} - i\epsilon A_n [\beta_{21}|A_m|^2 + \beta_{22}|A_n|^2] = 0, \quad (5.12)$$

which are equivalent to (4.48) in deep water. For this case, Roskes (1976b) gave the interaction coefficients β_{ij} as

$$\beta_{11} = \beta_{22} = -\omega k^2/2, \quad (5.13)$$

$$\begin{aligned} \beta_{12} = \beta_{21} = & -\omega k |\bar{k}_m + \bar{k}_n| \sin^2 \frac{\theta}{2} - 4\omega k^2 |\bar{k}_m + \bar{k}_n| \sin^2 \frac{\theta}{2} \sin^2 \frac{\phi}{2} / (|\bar{k}_m + \bar{k}_n| - 4k) \\ & + 2\omega k^2 \sin^2 \frac{\theta}{2} - \omega k^2 \left(\sin^2 \frac{\theta}{2} \cos^2 \frac{\theta}{2} + 1 \right), \end{aligned} \quad (5.14)$$

where θ is the angle between \vec{k}_m and \vec{k}_n , and ϕ is the angle between $-\vec{k}_m$ and $(\vec{k}_m + \vec{k}_n)$ as indicated in figure 3. Comparing the cubic nonlinear terms in equations (4.48) and (5.11), it can be shown (see Suh, 1989) that

$$Q(p = q = r = m) = -ig\beta_{11}, \quad (5.15)$$

$$Q(p = m, q = r = n) + Q(p = n, q = m, r = n) = -ig\beta_{12}. \quad (5.16)$$

5.2 Time-independent angular spectrum models

The simplest case to be considered of the time-independent model (4.50) may be waves propagating on a constant depth. Neglecting nonlinearity, it becomes

$$A_{s,x} = 0 \quad (5.17)$$

whose solution is

$$A_s(x) = \text{constant} = A_s(0), \quad (5.18)$$

implying the angular spectrum does not change as it propagates on a constant depth.

Another simple case is when waves propagate on a beach with straight and parallel depth contours. For this case, taking the Fourier transform of the mild-slope equation of Berkhoff (1972) in the y direction, splitting the velocity potential into forward-propagating and backscattered potentials, and neglecting the assumed small backscattered potential, Dalrymple & Kirby (1988) constructed an angular spectrum model given by

$$2\sqrt{k^2 - (s\lambda)^2} CC_g \Phi_s^+ - 2i(k^2 - (s\lambda)^2) CC_g \Phi_s^+ + \left[\sqrt{k^2 - (s\lambda)^2} CC_g \right]_x \Phi_s^+ = 0, \quad (5.19)$$

where the superscript $+$ denotes the forward-propagating component of the wave potential Φ in the mild-slope equation. After substituting for Φ_s^+ by

$$\Phi_s^+ = A_s e^{i \int^x \sqrt{k^2 - (s\lambda)^2} dx}, \quad (5.20)$$

equation (5.19) becomes

$$\frac{\sqrt{k^2 - (s\lambda)^2}}{k} C_g A_{s,x} + \frac{\left[\sqrt{k^2 - (s\lambda)^2} CC_g \right]_x}{2\omega} A_s = 0, \quad (5.21)$$

which can be obtained by linearizing (4.50) on straight and parallel contours. Thus, (4.50) on straight and parallel contours is the nonlinear extension of Dalrymple & Kirby's wide-angle wave propagation model.

Dalrymple & Kirby's model was extended to the case of irregular bathymetry by Dalrymple *et al.* (1989) in the following form:

$$2\sqrt{\bar{k}^2 - (s\lambda)^2} \bar{\Phi}_{s,x}^+ - 2i(\bar{k}^2 - (s\lambda)^2) \bar{\Phi}_s^+ + \left[\sqrt{\bar{k}^2 - (s\lambda)^2} \right]_x \bar{\Phi}_s^+ + i\bar{k}^2 F_s \left[\nu^2 F^{-1}(\bar{\Phi}_m^+) \right] = 0, \quad (5.22)$$

where $\bar{\Phi} = \sqrt{CC_g} \Phi$ and again the superscript + denotes the forward-propagating wave. Instead of using a laterally averaged depth they used an averaged wavenumber

$$\bar{k}^2 = \frac{1}{\ell} \int_0^\ell k_c^2 dy, \quad (5.23)$$

where

$$k_c^2 = k^2 - \frac{\nabla^2 \sqrt{CC_g}}{\sqrt{CC_g}}, \quad (5.24)$$

so ν in (5.22) defined by

$$\nu^2(x, y) = 1 - \frac{k_c^2}{\bar{k}^2} \quad (5.25)$$

is different from ν in the present study (cf. equation 3.9) even though both of them represent lateral depth variation. The last term in (5.22) representing wave diffraction due to the interaction between surface wave and lateral bottom variation is replaced by more complicated wave-bottom interaction terms in (4.50).

6 Numerical examples

In order to test the capability of the model for various physical phenomena such as combined refraction-diffraction and nonlinearity, we apply the time-independent model (4.54) to several different water wave problems for which experimental data are available. These include wave diffraction through a breakwater gap and wave focusing behind submerged shoals.

6.1 Wave diffraction behind a breakwater gap

The problem of breakwater gap wave diffraction is important for studying calmness in a breakwater harbor. The experiments of Pos & Kilner (1987) show that linear theory overpredicts wave heights in the open region behind the gap, but underpredicts them in the shadow zones. We apply our nonlinear model to this problem to examine the effect of nonlinearity.

The wave basin used in Pos & Kilner experiment consists of two impermeable shore-attached breakwaters lying on the y axis seaward ends of which are extended offshore by jetties separated by a distance B , as shown in figure 4. The wave propagating in the positive x direction between the jetties is diffracted into the basin. In order to investigate the pure diffraction without distortion

of the diffracted wave field by reflection from the circumferential beaches, they used a photogrammetric wave height measurement technique. Some uncertainties associated with this technique are discussed later.

Six tests of various gap widths and wave characteristics were carried out in the experiments of Pos & Kilner. Here we test our model for only one case for which detailed measurement data along a cross-section are provided in their paper. The constant water depth is 0.125 m. The period and amplitude of the incident wave are 0.67 sec and 2.775 cm, respectively. The wavelength, L , computed by linear theory is 0.604 m and the gap width, B , is 0.99 m, so that $B/L = 1.64$.

Since laterally periodic boundary condition is assumed in the present model, in order to assure negligible effects of the side gaps on the gap being modelled the width of the model domain should be taken large enough compared with the gap width. The model width is taken as sixteen wavelengths so that the ratio of the gap width to the breakwater length is 0.1025. The initial condition is given by the Kirchhoff condition on Φ_x^+ along the breakwater, i.e.,

$$\Phi_x^+(0, y) = \begin{cases} ikA_0, & |y| < B/2, \\ 0, & |y| > B/2, \end{cases} \quad (6.1)$$

where Φ^+ is the velocity potential in Dalrymple & Kirby equation (5.19) and A_0 is the initial amplitude assumed to be constant at the gap. $\Phi_{sx}^+(0)$ is obtained by an FFT of (6.1), and then $\Phi_s^+(0)$ is computed by

$$\Phi_{sx}^+(0) = i\sqrt{k^2 - (s\lambda)^2} \Phi_s^+(0), \quad (6.2)$$

which is the reduced form of (5.19) on a constant depth. Finally $A_s'(0) = A_s(0) = \Phi_s^+(0)$ by the equations (4.52) and (5.20).

Angular spectrum models using the Fourier transform technique have, in principle, infinite order of accuracy, if the solution is smooth (see Osher 1984). However, the situation changes drastically when discontinuities are present as in equation (6.1). Gibbs phenomenon occurs near the discontinuities and high-frequency oscillations pollute the solution globally since we use a finite Fourier transform in practice. Several smoothing techniques have been used to eliminate this deterioration. The simplest way is to merely set to zero all of the wavenumber spectrum beyond a prescribed magnitude. A slightly more elegant technique is to utilize a low-pass filter which consists of an exponential cut-off of high wavenumbers (e.g., Majda *et al.* 1978). However, by using this kind of smoothing technique, we lose the most advantageous feature of our model in which the waves propagating at large angles from the predominant wave direction are carried by the high wavenumber components.

Another way to resolve the high-frequency oscillation is to weight-average the solution in the physical domain rather than in the Fourier domain, see, for example, Gottlieb *et al.* (1981). In this numerical example, we apply a 5-point averaging in the y direction to the final solution $A(x, y)$. A 5-point averaging in general has the following form:

$$\bar{A}_j = \alpha A_{j-2} + \beta A_{j-1} + \gamma A_j + \beta A_{j+1} + \alpha A_{j+2}, \quad (6.3)$$

in which the subscripts denote the location in the y direction (e.g., $A_j = A(x, j\Delta y)$), $2(\alpha + \beta) + \gamma = 1$ and usually $\gamma > \beta > \alpha > 0$. Applying this averaging to the complex solution $A(x, y)$ smooths not only its magnitude but also its phase. However, we want to smooth the magnitude of the solution in a row with its phase unchanged. For this purpose, we propose the following smoothing procedure. First, the averaged magnitude of the solution at the j th point is calculated by

$$\overline{|A_j|} = \alpha|A_{j-2}| + \beta|A_{j-1}| + \gamma|A_j| + \beta|A_{j+1}| + \alpha|A_{j+2}|. \quad (6.4)$$

The actual smoothed solution is then calculated by

$$\overline{A_j} = \frac{\overline{|A_j|}}{|A_j|} A_j. \quad (6.5)$$

Note that this smoothing is applied to the final solution so that the smoothing effect does not enter the model during the computation of the angular spectrum. In this computation, $\alpha = 0.1$, $\beta = 0.2$, and $\gamma = 0.4$ were used.

The computational results of the present model (both linear and nonlinear) are presented in figure 5 along with the experimental data in terms of diffraction coefficient across the cross-section at $x/L = 3$. The solution of Penney & Price (1952) is also presented for comparison with the linear model result. Since the problem is symmetric about the x axis, only the right half is presented. As expected, the nonlinear model predicts smaller wave height in the open region and larger wave height in the shadow zone compared with the linear model results, giving better agreement with the experimental data than the linear model.

The nonlinear model underpredicts the measurements throughout the cross-section, and the linear model also provides severe underprediction except at the centerline where it slightly overpredicts the measurement. In the experiments of Pos & Kilner, the photographs of the wave field were taken when the first wave front arrived at the toe of the back wall beach to avoid the contamination of the diffractive wave field by waves reflected from the beaches. By this time, however, the area near the gap would most likely have been contaminated by wave reflection from the side wall beaches since the distances from the gap to the side wall beaches are only about half of that from the gap to the back wall beach. Another question in their experiments is whether the wave field in the basin had reached a steady state at the instant when the photograph was taken, as it is known that there are modulations in wave amplitude at the leading edge of transient wave trains. Upwave reflection in the entrance channel due to the abrupt channel transition may also contribute to the discrepancy between the measurement and model prediction. Assuming perfectly-reflecting side walls, Dalrymple (1989) estimated the reflection at 6 %. This upwave reflection and its re-reflection from the wavemaker will produce partial standing waves in the entrance channel. It is not clear if this was taken into consideration in their experiment.

6.2 Wave focusing behind an elliptic shoal on a sloping beach

For the purpose of testing the model for the prediction of wave deformation on an irregular bathymetry, we have chosen the experiment reported in Berkhoff *et al.* (1982). The experimental

Section no.	N	Linear		Nonlinear	
		DSKC	Present	DSKC	Present
1	28	0.852	0.897	0.913	0.897
2	28	0.847	0.953	0.945	0.952
3	28	0.946	0.995	0.986	0.988
4	27	0.898	0.976	0.991	0.993
5	28	0.706	0.944	0.982	0.988
6	23	0.472	0.883	0.970	0.969
7	23	0.699	0.972	0.954	0.981
8	23	0.844	0.930	0.796	0.901
Total	208	0.867	0.973	0.982	0.987

Table 1: Indices of agreement for comparing the numerical model results against the measurements for the experiment of Berkhoff *et al.* (1982).

bathymetry consists of an elliptic shoal situating on a sloping beach with a slope 1:50. The slope rises from a region of constant depth $h = 0.45$ m, and the entire slope is rotated at an angle of 20° from the y axis as shown in figure 6, where the solid lines indicate bottom contours and the dashed lines are the transects along which data from the experiment of Berkhoff *et al.* are available. The details of the geometry of the shoal in the present coordinate system are referred to Dalrymple *et al.* (1989). The wave propagating in the positive x direction at $x = 0$ has 2.32 cm amplitude and 1 sec period.

The graphical comparison between the model results and the measurements along the transects 1-8 is given in Suh (1989), showing that the nonlinearity is important at the transects 4 and 5 where the wave has passed through the caustic cusp. Here we present a more quantitative comparison using a statistical parameter proposed by Willmott (1981). As a measure of the degree to which a model's predictions are error-free, he introduced a dimensionless quantity, d , as an index of agreement

$$d = 1 - \frac{\sum_{i=1}^N (P_i - O_i)^2}{\sum_{i=1}^N (|P_i - \bar{O}| + |O_i - \bar{O}|)^2}, \quad (6.6)$$

where \bar{O} is the mean of the observed variates O_i , and P_i , $i = 1$ to N , are the predicted variates. The values for d vary between 0 and 1.0, where 1.0 indicates perfect agreement between observation and prediction, and 0 connotes complete disagreement.

The indices of agreement computed for each transect in figure 6 and for total measurement points are given in table 1, in which the results of Dalrymple *et al.* model (5.22) (abbreviated to DSKC in the table) are also presented for comparison. For all the transects, the present linear model gives better agreement with the measurements than the DSKC linear model, probably because the wave-

bottom interaction is represented in a more elaborate manner in the present model. On transects 2, 3 and 8, the present linear model gives even better agreement than the nonlinear models. The indices of agreement do not show big difference between the two nonlinear models and are close to 1.0, indicating that the DSKC nonlinear model is as good as the present nonlinear model.

6.3 Wave focusing behind a circular shoal resting on a flat bottom

The most advantageous feature of the angular spectrum model is that it permits solution by a marching method like the parabolic model but is valid for waves propagating at large angles from the assumed propagation direction. For the purpose of testing the model for waves propagating over an irregular bathymetry at large angles of incidence, we have chosen the experiment reported by Ito & Tanimoto (1972). Their experimental bathymetry consists of a circular shoal resting on a flat bottom. A monochromatic wave train propagates over the shoal and wave focusing occurs behind the shoal. Due to the axisymmetry of the circular shoal, the wave focusing pattern behind the shoal should be independent of the angle of incidence, if the model predicts it 'correctly'.

The geometry of Ito & Tanimoto experiment is shown in figure 7. The water depth on the flat bottom $h_1 = 0.15$ m, and the water depth in the shoal region is described by

$$h = h_2 + 0.15625 [(x - 1.2)^2 + (y - 1.2)^2] \quad (6.7)$$

where $h_2 = 0.05$ m is the depth at the shoal crest. A monochromatic wave train with 1.04 cm wave height and 0.511 sec period enters the domain at $\theta_o = 0^\circ$. For the three different sections indicated in figure 7, data from the experiment of Ito & Tanimoto are available. Comparison with the model results along these sections are shown in figure 8 (a-c) in terms of normalized wave amplitude with respect to the incident amplitude. In each figure, nonlinear results of the present model are given by solid lines, while triangles indicate measured data points. The results of the large-angle parabolic model of Kirby (1986) are also given by dashed lines. This model uses the minimax approximation to obtain better accuracy for waves propagating at large angles. Both models predict the measurement reasonably well.

In order to test the model for a large angle of incidence, the flat bottom in figure 7 is extended to $y \simeq 4.8$ m and the wave focusing is modelled for two different incident angles: $\theta_o = 45^\circ$ and $\theta_o = 60^\circ$. For satisfying the lateral periodicity of the wave field, the model width is taken to be an integer times the lateral wavelength of the incident wave field but close to 4.8 m. Otherwise the discontinuity of the initial wave field at the side boundaries propagates into the domain, polluting the solution. A qualitative comparison with the results of normal incidence can be made by comparing the contour maps of wave amplitude or instantaneous surface elevation for each incident angle. For a more quantitative comparison, the variation of the normalized amplitude along the section 3 (in figure 7) for different angles of incidence is plotted in figure 9. The values of normal incidence are indicated by a solid line, and the solid and open circles indicate the values at $\theta_o = 45^\circ$ and 60° , respectively, which were obtained by digitization from the contour maps of normalized amplitude. A similar figure for the parabolic model of Kirby (1986) is also presented.

The results of the present model for $\theta_o = 45^\circ$ closely follow those of normal incidence except near the right depression, whereas for $\theta_o = 60^\circ$ the disagreement is more pronounced, especially

on the right side of the caustic cusp. The overall shapes of the results of the parabolic model for $\theta_o = 45^\circ$ and 60° are very similar to that for normal incidence, but they are shifted to the left, indicating that the focused wave fields for $\theta_o = 45^\circ$ and 60° rotate towards the positive x direction. The shift becomes severe with increasing angle of incidence, and it is more prominent on the right side of the caustic cusp.

Dalrymple *et al.* (1989) have presented a simple theoretical analysis regarding the accuracy of their angular spectrum model in terms of lateral depth variation and wave propagation angle, concluding that in order for their model to be accurate for a large angle of incidence, the lateral depth variation should be small. A similar analysis can be applied to the wave-bottom interaction terms involving ν in the present model (4.54). The height of the shoal in the above example is $2/3$ of the water depth on the flat bottom (unusually high considering the normal situation in real cases). In order to examine the effects of the magnitude of the lateral bottom variation, we have tested the model for a shoal having one half of the height of the shoal shown in figure 7 (i.e., $h_2 = 0.1$ m in equation 6.7). Figure 10 presents results similar to those presented in figure 9 for smaller shoal height. The results for $\theta_o = 45^\circ$ almost exactly match those of normal incidence in both models and those for $\theta_o = 60^\circ$ also give good agreement with the normal incidence.

There are some other problems associated with the large-angle propagation in this example. Firstly, the constant-depth region before the shoal ($x < 0.4$ m in figure 7) should be affected by the presence of the shoal if a large angle of incidence is modelled, but this is not detected by the model since it does not include backscattering waves. Secondly, the assumption of lateral periodicity makes the effect of the upwave shoal appear in the domain to be modelled when wave is incident at a large angle. The latter problem can be resolved by taking a wider domain.

7 Conclusions

The present study has developed an angular spectrum model for predicting the transformation of Stokes waves due to refraction, diffraction, shoaling and nonlinear wave interactions in water of varying depth but free of ambient currents. The bottom slope is assumed to be $O(\epsilon^2)$ and the deviation of the actual depth from the laterally-averaged depth is assumed to be $O(\epsilon)$ of the laterally-averaged depth. In order for the model to be valid for the case in which waves propagate at large angles from the x direction, the second assumption should not be violated.

Through the example for wave focusing behind an elliptic shoal on a sloping beach, the present linear model has proven to predict the wave transformation on an irregular bathymetry much better than the linear model of Dalrymple *et al.* (1989), probably due to the more elaborate expressions for the wave-bottom interaction in the present model. The nonlinear models, however, did not show big difference between each other and both predicted the measurement reasonably well. The advantages of Dalrymple *et al.* nonlinear model are that it can be applied over entire range of water depths and that the effects of ambient current can be included easily by modifying the dispersion relationship. The advantage of the present model is that it can be extended to a random directional wave field including the nonlinear interaction among the waves with different frequencies as in Suh (1989).

This work is partly a result of research sponsored by NOAA Office of Sea Grant, Department

of Commerce, under Grant No. NA86AADSG040. J.T. Kirby received support from the Office of Naval Research, contracts N00014-86-K-0790 and N00014-89-J-1717. The U.S. Government is authorized to produce and distribute reprints for governmental purposes, notwithstanding any copyright notation that may appear herein.

References

1. Benney, D.J. & Newell, A.C. 1967. The propagation of nonlinear wave envelopes. *J. Math. Phys.* **46**, 133-139.
2. Benney, D.J. & Roskes, G.J. 1969. Wave instabilities. *Stud. Appl. Math.* **48**, 377-385.
3. Berkhoff, J.C.W. 1972. Computation of combined refraction-diffraction. *Proc. 13th Int. Conf. Coastal Eng.*, ASCE. Vancouver. 471-490.
4. Berkhoff, J.C.W., Booij, N. & Radder, A.C. 1982. Verification of numerical wave propagation models for simple harmonic linear waves. *Coastal Engng.* **6**, 255-279.
5. Booker, H.G. & Clemmow, P.C. 1950. The concept of an angular spectrum of plane waves, and its relation to that of polar diagram and aperture distribution. *Proc. Inst. Elect. Engrs.*, Part III. **97**, 11-17.
6. Clemmow, P.C. 1966. *The Plane Wave Spectrum Representation of Electromagnetic Fields*. Pergamon Press. 185 pp.
7. Dalrymple, R.A. 1989. Water waves past abrupt channel transitions. *Appl. Ocean Res.* (in press).
8. Dalrymple, R.A. & Kirby, J.T. 1988. Models for very wide-angle water waves and wave diffraction. *J. Fluid Mech.* **192**, 33-50.
9. Dalrymple, R.A., Suh, K.D., Kirby, J.T. & Chae, J.W. 1989. Models for very wide-angle water waves and wave diffraction. Part 2. Irregular bathymetry. *J. Fluid Mech.* **201**, 299-322.
10. Davey, A. & Stewartson, K. 1974. On three-dimensional packets of surface waves. *Proc. Roy. Soc. Lond. A* **338**, 101-110.
11. Djordjević, V.D. & Redekopp, L.G. 1978. On the development of packets of surface gravity wave moving over an uneven bottom. *J. Appl. Math. Phys.* **29**, 950-962.
12. Gabor, D. 1961. Light and information, in E. Wolf (ed.), *Progress in Optics*, vol. I. North-Holland Publishing Company - Amsterdam.
13. Gottlieb, D., Lustman, L. & Orszag, S.A. 1981. Spectral calculations of one-dimensional inviscid compressible flows. *J. Sci. Stat. Comput.*, SIAM. **2**, 296-310.
14. Ito, Y. & Tanimoto, K. 1972. A method of numerical analysis of wave propagation: Application to wave diffraction and refraction. *Proc. 13th Int. Conf. Coastal Engng.*, ASCE. 503-522.

15. Kirby, J.T. 1986. Rational approximations in the parabolic equation method for water waves. *Coastal Engng.*, **10**, 355-378.
16. Kirby, J.T. & Dalrymple, R.A. 1983. A parabolic equation for the combined refraction-diffraction of Stokes waves by mildly varying topography. *J. Fluid Mech.* **136**, 453-466.
17. Kirby, J.T. & Dalrymple, R.A. 1986. An approximate model for nonlinear dispersion in monochromatic wave propagation models. *Coastal Eng.* **9**, 545-561.
18. Longuet-Higgins, M.S. 1962. Resonant interactions between two trains of gravity waves. *J. Fluid Mech.* **12**, 321-332.
19. Majda, A., McDonough, J. & Osher, S. 1978. The Fourier method for nonsmooth initial data. *Math. Comput.* **32**, 1041-1081.
20. Osher, S. 1984. Smoothing for spectral methods, in R.G. Voigt, D. Gottlieb & M.Y. Hussaini (ed.), *Spectral Methods for Partial Differential Equations*, SIAM.
21. Penney, W.G. & Price, A.T. 1952. The diffraction theory of sea waves and the shelter afforded by breakwaters. *Phil. Trans. Roy. Soc. Lond. A* **244**, 236-253.
22. Phillips, O.M. 1960. On the dynamics of unsteady gravity waves of finite amplitude. Part 1. The elementary interactions. *J. Fluid Mech.* **9**, 193-217.
23. Pos, J.D. & Kilner, F.A. 1987. Breakwater gap wave diffraction: An experimental and numerical study. *J. Wtrwy. Port Coast. Oc. Eng.* **113**, 1-21.
24. Ratcliffe, J.A. 1956. Some aspects of diffraction theory and their application to the ionosphere, in A.C. Strickland (ed.), *Reports on Progress in Physics*, vol. XIX. The Physical Society, London.
25. Roskes, G.J. 1976a. Some nonlinear multiphase interactions. *Stud. Appl. Math.* **55**, 231-238.
26. Roskes, G.J. 1976b. Nonlinear multiphase deep-water wavetrains. *The Physics of Fluids*. **19**, 1253-1254.
27. Sharma, J.N. & Dean, R.G. 1979. Development and evaluation of a procedure for simulating a random directional second order sea surface and associated wave forces. *Ocean Eng. Rep.* **20**. University of Delaware.
28. Stamnes, J.J., Løvhaugen, O., Spjelkavik, B., Mei, C.C., Lo, E. & Yue, D.K.P. 1983. Non-linear focusing of surface waves by a lens — theory and experiment. *J. Fluid Mech.* **135**, 71-94.
29. Suh, K.D. 1989. Angular spectrum models for propagation of weakly nonlinear surface gravity waves in water of varying depth. Ph.D. dissertation, University of Delaware.
30. Willmott, C.J. 1981. On the validation of models. *Phys. Geog.* **2**, 184-194.
31. Yue, D.K.-P. & Mei, C.C. 1980. Forward diffraction of Stokes waves by a thin wedge. *J. Fluid Mech.* **99**, 33-52.

Appendix – Summary of the forcing terms

The forcing terms in the boundary value problems (3.14) – (3.17) are summarized as follows:

$$F_1 = 0, \quad (\text{A.1})$$

$$F_2 = -\phi_{1xx_1} - \phi_{1x_1x}, \quad (\text{A.2})$$

$$F_3 = -\phi_{1x_1x_1} - \phi_{1xx_2} - \phi_{1x_2x} - \phi_{2xx_1} - \phi_{2x_1x}, \quad (\text{A.3})$$

$$G_1 = 0, \quad (\text{A.4})$$

$$G_2 = -2\phi_{1xx} - \eta_1\phi_{1xxx} - g\eta_1\phi_{1xx} - 2(\phi_{1x}\phi_{1xt} + \phi_{1y}\phi_{1yt} + \phi_{1z}\phi_{1zt}), \quad (\text{A.5})$$

$$\begin{aligned} G_3 = & -2\phi_{2xx} - 2\phi_{1xx} - \phi_{1x_1x_1} - \eta_1\phi_{2xxx} - 2\eta_1\phi_{1x_1x} - \eta_2\phi_{1xxx} \\ & - g\eta_1\phi_{2xx} - g\eta_2\phi_{1xx} - \frac{1}{2}\eta_1^2\phi_{1xxx} - \frac{g}{2}\eta_1^2\phi_{1xxx} \\ & - \phi_{1x}^2\phi_{1xx} - \phi_{1y}^2\phi_{1yy} - \phi_{1z}^2\phi_{1zz} \\ & - 2(\phi_{1x}\phi_{1y}\phi_{1xy} + \phi_{1x}\phi_{1z}\phi_{1xz} + \phi_{1y}\phi_{1z}\phi_{1yz}) \\ & - 2(\phi_{1x}\phi_{2xt} + \phi_{1x}\phi_{1xt_1} + \phi_{2x}\phi_{1xt} + \phi_{1x_1}\phi_{1xt}) \\ & - 2(\phi_{1y}\phi_{2yt} + \phi_{1y}\phi_{1yt_1} + \phi_{2y}\phi_{1yt}) - 2(\phi_{1z}\phi_{2zt} + \phi_{1z}\phi_{1zt_1} + \phi_{2z}\phi_{1zt}) \\ & - 2\eta_1(\phi_{1xt}\phi_{1xx} + \phi_{1x}\phi_{1x_1x} + \phi_{1yt}\phi_{1yx} + \phi_{1y}\phi_{1y_1x} + \phi_{1xt}\phi_{1xx} + \phi_{1x}\phi_{1x_1x}), \end{aligned} \quad (\text{A.6})$$

$$H_1 = 0, \quad (\text{A.7})$$

$$H_2 = -\phi_{1x_1} - \eta_1\phi_{1xx} - \frac{1}{2}(\phi_{1x}^2 + \phi_{1y}^2 + \phi_{1z}^2), \quad (\text{A.8})$$

$$B_1 = 0, \quad (\text{A.9})$$

$$B_2 = -\bar{h}\mu\phi_{1xx}, \quad (\text{A.10})$$

$$B_3 = -\phi_{1x}h_{x_2} - \phi_{1y}h_{y_2} - \bar{h}\mu\phi_{2xx} - \frac{1}{2}\bar{h}^2\mu^2\phi_{1xxx}. \quad (\text{A.11})$$

Captions of Figures

1. Diagram of the Fourier decomposition of the wave field on a row with an angular spectrum (with lateral wavenumbers, $p\lambda$, $p = 0, \pm 1, \pm 2, \dots$). k_x and k_y are the wavenumbers in the x and y directions, respectively.
2. Definition of depth components.
3. Definition of θ and ϕ .
4. Layout of the wave basin in the experiments of Pos & Kilner (1987).
5. Comparison of the model results against the experimental data of Pos & Kilner (1987) in terms of diffraction coefficient (K_d). \circ = experiment, dotted line = Penney & Price solution, dashed line = linear model, solid line = nonlinear model.
6. Bathymetry of the computational domain for the experiment of Berkhoff *et al.* (1982). Dashed lines indicate the transects of wave measurement.
7. Geometry of the computational domain for the experiment of Ito & Tanimoto (1972).
8. Comparison of the model results against the experimental data by Ito & Tanimoto (1972) in terms of normalized wave amplitude with respect to the incident amplitude: Δ = experiment; solid lines = present nonlinear model; dashed lines = nonlinear parabolic model.
9. Comparison of the model results of $\theta_o = 45^\circ$ and $\theta_o = 60^\circ$ against those of normal incidence in terms of normalized wave amplitude with respect to the incident amplitude at the section 3 indicated in figure 7: (a) present model, (b) parabolic model; solid lines = normal incidence, $\bullet = 45^\circ$, $\circ = 60^\circ$.
10. Same as figure 9 for the results of the test with smaller shoal height.

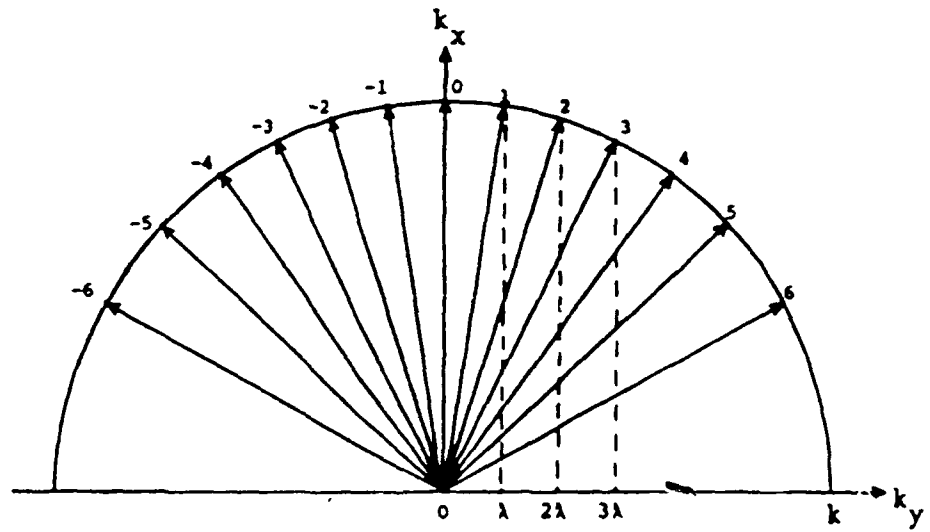


Figure 1

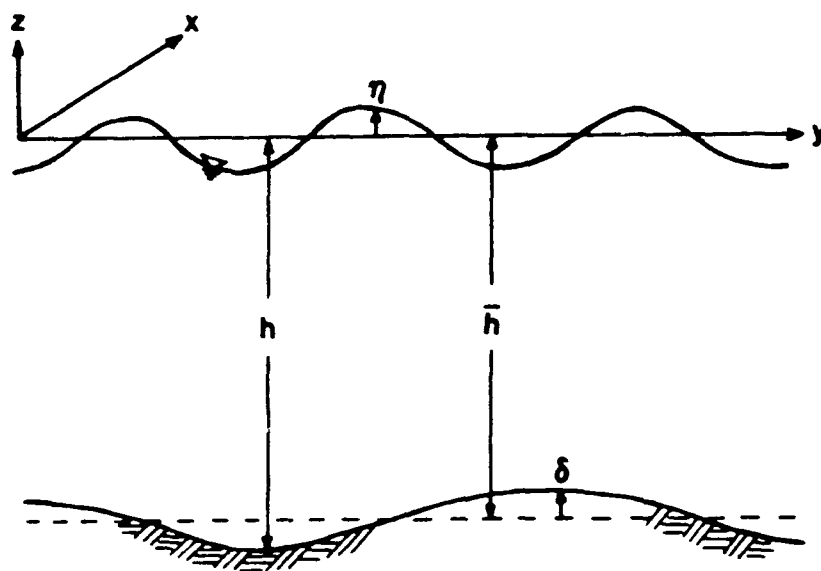


Figure 2

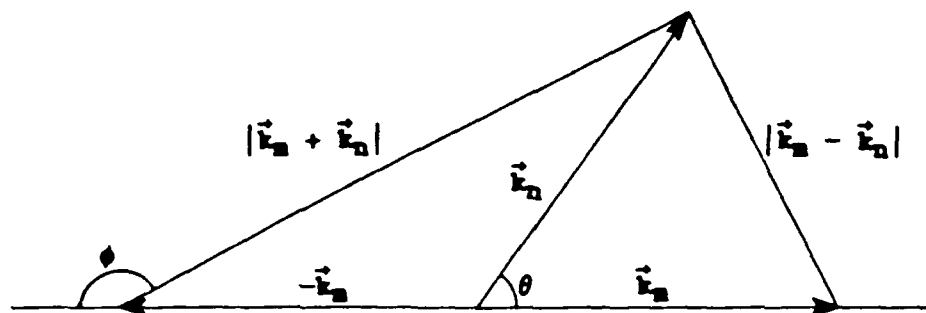


Figure 3

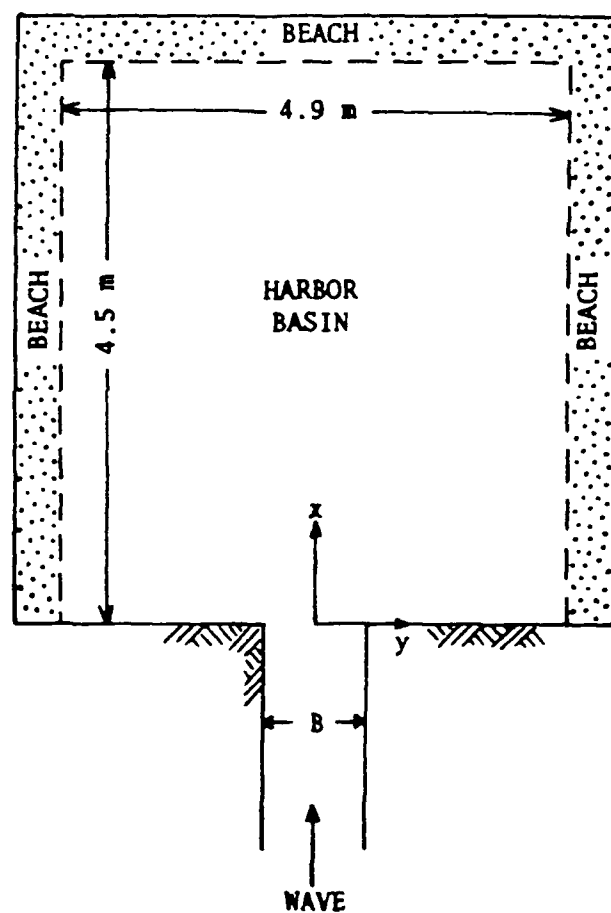


Figure 4

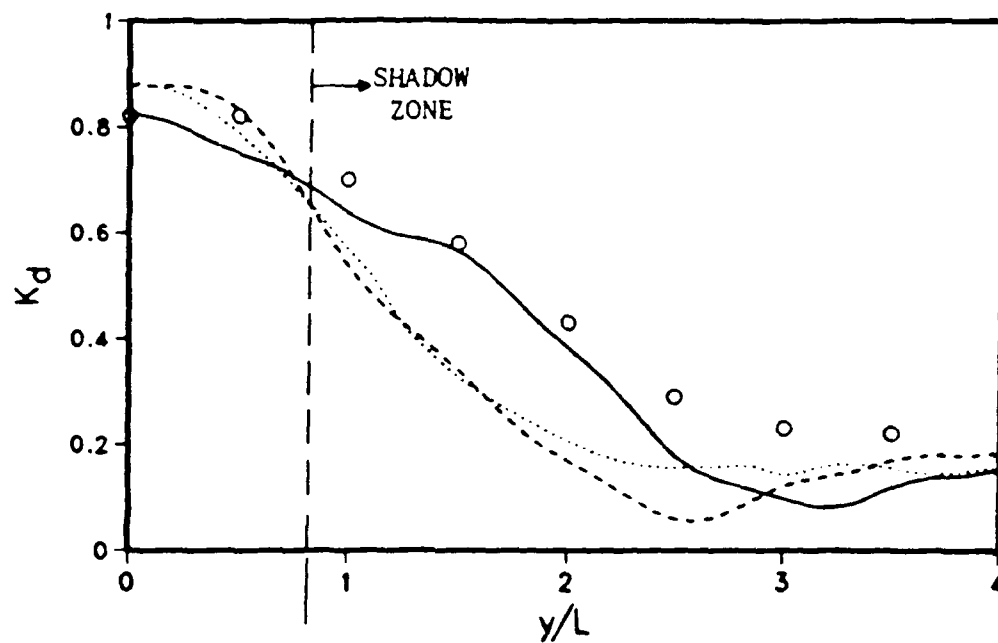


Figure 5

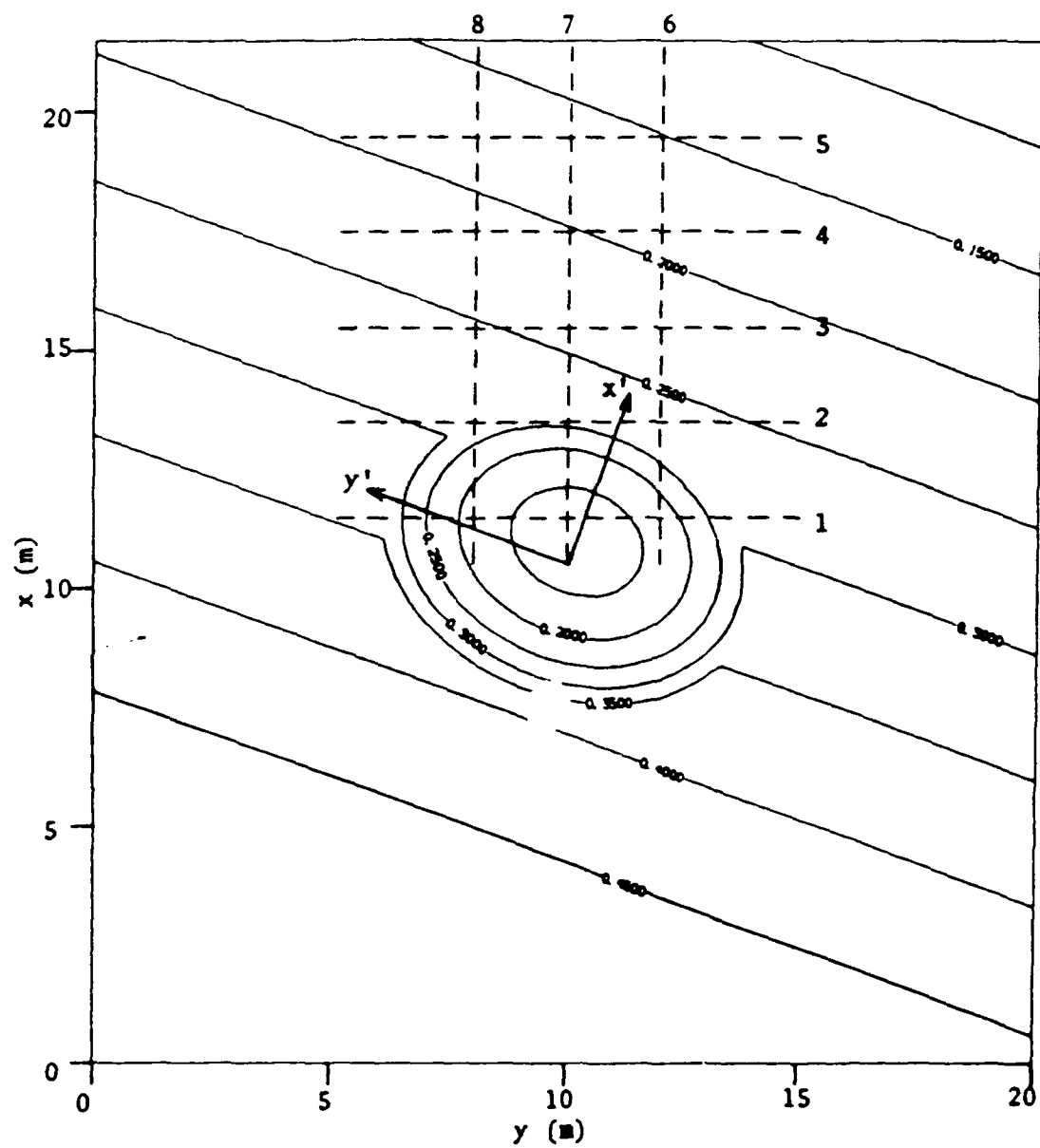


Figure 6

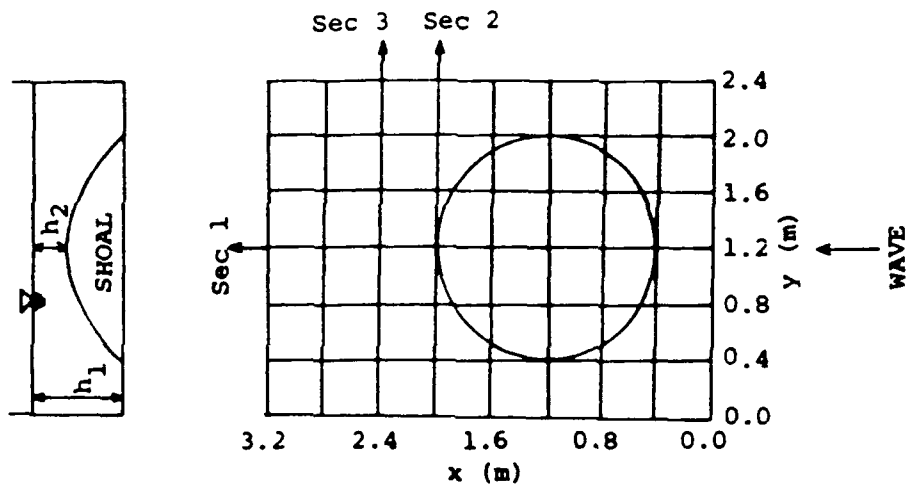


Figure 7

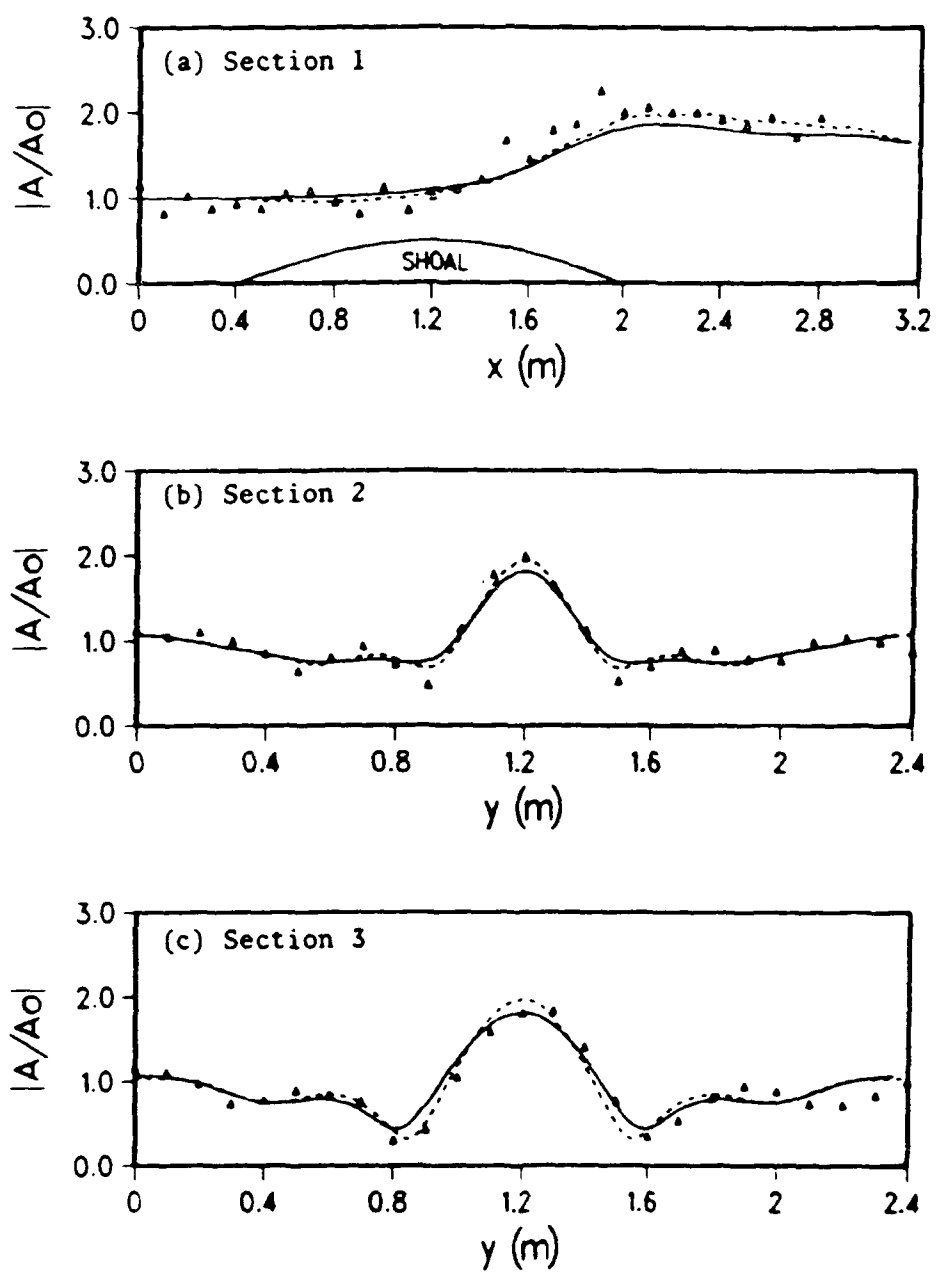


Figure 8

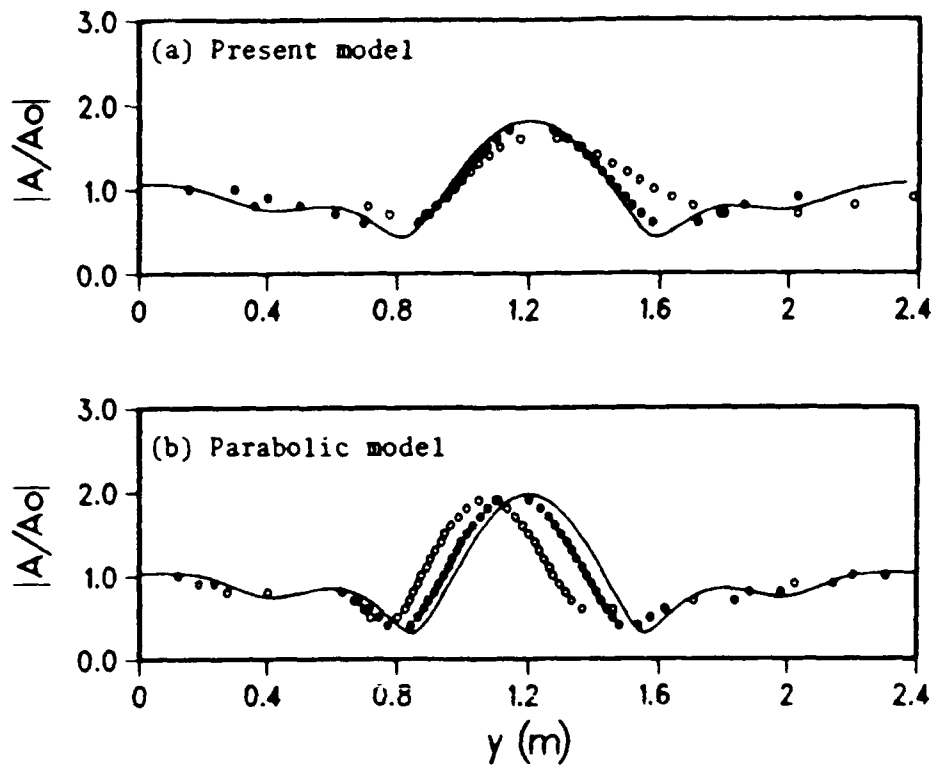


Figure 9

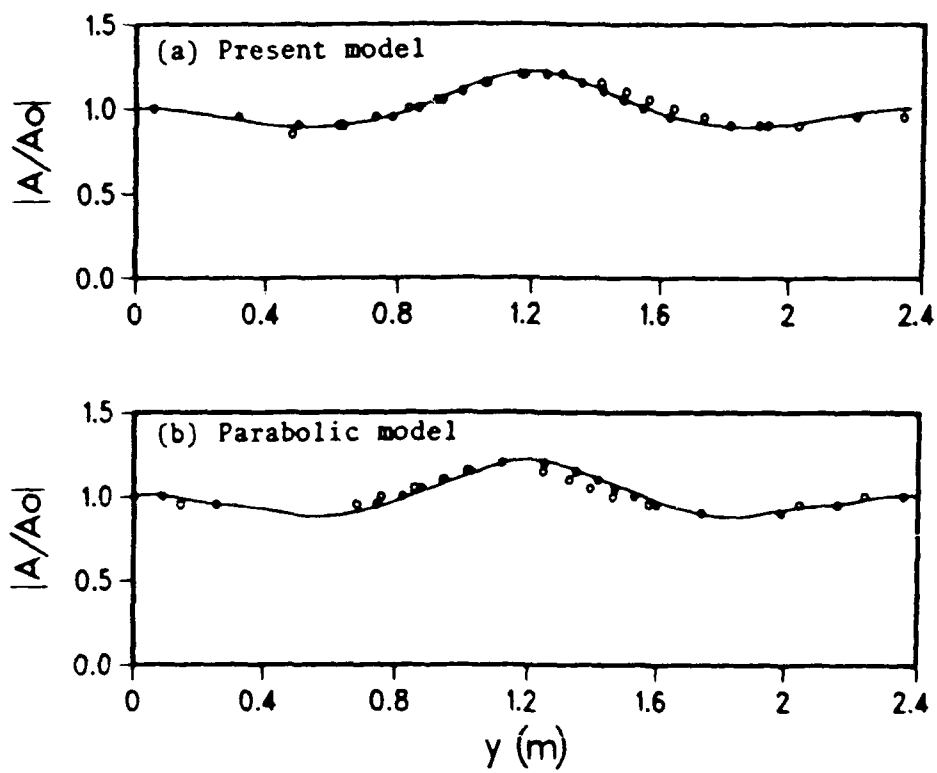


Figure 10

Appendix E: Intercomparison of truncated series solutions for shallow water waves

submitted to *Journal of Waterway, Port, Coastal and Ocean Engineering*, March
1990.

Intercomparison of Truncated Series Solutions for Shallow Water Waves

James T. Kirby

Center for Applied Coastal Research, Department of Civil Engineering
University of Delaware, Newark, DE 19716

Abstract

The relationship between truncated Fourier series solutions of various long wave evolution equations is explored. It is found that the problem of obtaining a steady solution in a coupled-mode model of shallow-water wave evolution is related more to the problem of properly choosing the corresponding time-dependent evolution equation than to the problem of truncating the infinite series representation of the solution to that equation. In the process, existing lowest-order coupled-mode models are related to a particular modified form of the Kortweg-deVries equation.

1 Introduction

There has recently been a great deal of interest in solving the Boussinesq equations for weakly dispersive, weakly nonlinear shallow water waves in the frequency domain, as a means of describing the shoreward evolution of complex nonlinear wave fields. In related studies, Freilich and Guza (1984) modelled the evolution of a broad spectrum of waves with vanishingly small directional distribution using a set of coupled-mode, ODE evolution equations, while Liu et al (1985) used the parabolic approximation to model the two-dimensional spatial evolution of the spectrum over topography. Liu et al's applications were restricted to simple periodic waves with finite resolution of higher harmonics.

When applying models of the form described here to laboratory data, it is desirable to choose initial conditions for the model integration which lead to the maintenance of steady wave forms in regions before the waves interact with topography or obstacles. Yoon and Liu (1989) have discussed this problem in a recent paper describing the Mach reflection of a cnoidal wave at a vertical wall. Yoon and Liu used a truncated spectral model similar to that described in Liu et al (1985). Restricting attention to one-dimensional propagation,

we write a model which is equivalent to the one given by Yoon and Liu, but in dimensional form, as

$$\frac{\partial A_n}{\partial x} - \frac{i}{6} n^3 k^3 h^2 A_n + \frac{3ink}{8h} \left(\sum_{l=1}^{n-1} A_l A_{n-l} + 2 \sum_{l=1}^{N-n} A_l^* A_{n+l} \right) = 0; \quad n = 1, \dots, N, \quad (1)$$

where h is the still water depth, $\omega = 2\pi/T$, T is the wave period, and k is the linear non-dispersive wavenumber given by

$$k = \frac{\omega}{c}; \quad c = \sqrt{gh} \quad (2)$$

The function $A_n(x)$ is the complex Fourier amplitude of the n 'th harmonic, or spectral component of a periodic-in-time wave form, and is related to the physical surface displacement through

$$\eta(x, t) = \frac{1}{2} \sum_n A_n(x) e^{in(kx - \omega t)} \quad (3)$$

Nondimensionalization of time by ω and horizontal distance x by k leads to the dimensionless parameter

$$\mu^2 = \frac{\omega^2 h}{g} = (kh)^2 \ll 1 \quad (4)$$

Further, if a characterizes the maximum surface displacement, then we define $\epsilon = a/h \ll 1$ as the dimensionless parameter expressing the weakness of nonlinearity in the problem. The model being considered is also analogous to the "consistent shoaling model" investigated by Freilich and Guza. A form more in keeping with their formulation would be obtained by allowing complex $A_n(x)$ to be represented by

$$A_n(x) = a_n(x) e^{i\theta_n(x)},$$

where a_n and θ_n are real-valued amplitude and phase. Substituting for A_n in (1) and separating real and imaginary parts would then give coupled evolution equations for a_n and θ_n , as in Freilich and Guza.

Yoon and Liu (1989), in discussing the problem of providing initial conditions for (1), have shown that model results based on a truncation of the Fourier spectrum of the cnoidal

wave solution of the Korteweg-deVries (KdV) equation (Flick et al, 1981; Cayley, 1895) show a degree of unsteadiness when 7 harmonics are retained as input to the numerical model, whereas initial conditions based on direct solutions of (1) with the same number of harmonics as employed in the numerical computation produce a steady solution. (This latter result is, of course, simply a test of the accuracy of the numerical integration scheme for equation (1)). This problem is investigated further in this note, and we show that the problem of obtaining initial conditions for use in the spectral wave model is related more to the choice of the corresponding model equation than to the fact that the infinite series solution must be subsequently truncated. We first show that permanent-form solutions of (1) are related most closely to the modified KdV equation

$$\eta_t + c\eta_x - \frac{3}{2h}\eta\eta_x - \frac{h^2}{6c^2}\eta_{xxx} = 0 \quad (5)$$

rather than the standard KdV model equation

$$\eta_t + c\eta_x + \frac{3c}{2h}\eta\eta_x + \frac{ch^2}{6}\eta_{xxx} = 0 \quad (6)$$

We then compare results for harmonic amplitudes for the extremes of the range of KdV-type equations for several values of relevant parameters. Although the main emphasis in the literature has been on the distinction between members of the KdV-type family caused by variations in linear dispersion effects in the deep-water limit, we see from comparisons here that alteration of the nonlinear term leads to differences in the model results which are most apparent for higher waves in the long wave limit. The implications of both choice of model and truncation of the series solution for input into numerical integration schemes are investigated. Finally, for completeness we give the cnoidal and solitary wave solutions for the family of model equations, and compare results for phase speed and length scales for the solitary wave.

2 Steady Fourier series solutions for the family of KdV equations

We begin here by writing a general KdV-type equation in symbolic form:

$$\eta_t + c\eta_x + \frac{3}{2h}\eta\eta_\zeta + \frac{h^2}{6c^2}\eta\zeta\zeta_\zeta = 0 \quad (7)$$

where

$$\zeta = \frac{x}{c} \quad \text{or} \quad \zeta = -t \quad (8)$$

and where any combination of choices of ζ may be made, leading to eight possible members of the family. This family is described in section 11.5 of Mei (1983), and each member is an equivalently valid asymptotic representation of the physics to $O(\epsilon, \mu^2)$. Aside from the KdV equation (6), the most-studied member of the family is the so-called regularized long wave equation (RLW) or BBM equation, described by Benjamin, Bona and Mahony (1972).

$$\eta_t + c\eta_x + \frac{3c}{2h}\eta\eta_x - \frac{h^2}{6}\eta_{xxt} = 0 \quad (9)$$

For each of the equations described in (7), we write a permanent-form solution in Fourier series form, given by

$$\eta = \frac{1}{2} \sum_{n=1}^{\infty} a_n e^{in(\kappa x - \omega t)} + \text{c.c.} \quad (10)$$

where κ is a wavenumber based on the true wavelength L ; $\kappa = 2\pi/L$. Here, the a_n are real constants due to the assumption of steady form. The wave height of the resulting wave form follows from the sum of the odd components of the series,

$$H = 2 \sum_{i=1}^{\infty} a_{2i-1} \quad (11)$$

The series in (10) is first truncated to a finite number of terms N . Substituting (10) in (7) and grouping the terms at each harmonic n leads to N equations,

$$\left(\omega - \kappa c + \frac{n^2 h}{6g} \alpha^3 \right) a_n - \frac{3\alpha}{8h} \left(\sum_{l=1}^{n-1} a_l a_{n-l} + 2 \sum_{l=1}^{N-n} a_l a_{n+l} \right) = 0; \quad n = 1, \dots, N \quad (12)$$

where

$$\begin{aligned}\alpha &= \kappa c & \text{if } \zeta &= \frac{x}{c} \\ \alpha &= \omega & \text{if } \zeta &= -t\end{aligned}\tag{13}$$

and where, again, any combination of values of α may be chosen depending on the choice of governing equation. An $N + 1$ 'th equation is provided by (11). Then, given h and assuming that the a_n are to be determined, we further require two values of the set H, T or L . In this note, it will be assumed that the wave height and period are known, and thus κ is the $N + 1$ 'th unknown. The resulting set of equations are solved using a standard first-order Newton-Raphson technique, using either a linear nondispersive wave ($a_1 = H/2, \kappa = k$) or a previous nonlinear solution for nearby parameters as the starting guess.

The equivalence of (1) (and thus the models of Liu et al and Yoon and Liu and the "consistent" model of Freilich and Guza) with the modified KdV equation (5) follows by noting that

$$A_n = a_n e^{in(k-\kappa)x}\tag{14}$$

from (3) and (10), and then substituting (14) in (1) to obtain equation (12) with $\alpha = \omega$ in all instances. The correspondence is complete and thus exact solutions of (1) would come from (5) rather than (6).

3 Comparison of Fourier solutions for the family of KdV equations

We consider several examples here in order to investigate the effect of choice of KdV-type model on predicted wave lengths and Fourier spectra. Yoon and Liu considered cases with $H/h = 0.2$ and 0.4 , and chose a uniform depth and wave period such that the parameter $\mu^2 = 0.11$. Results are presented here for the same choices of wave height and for a range $0.0 \leq \mu^2 \leq 0.5$, which covers the reasonable range of validity of the weakly-dispersive theory.

Figures 1 - 3 present results for the smaller amplitude wave $H/h = 0.2$ and show the difference between predictions of the KdV equation and the alternate model (5). Figure

1 presents results for the KdV equation. Figure 1a compares predicted wavelength L/h , and Figure 1b displays predicted harmonic amplitudes a_n/h for Fourier series solutions with $N = 7$ and 20. (In all cases, it was verified that the large N solutions of the KdV equation were accurate in comparison with solutions obtained from the elliptic functions using algorithms presented by Goring (1978). For other members of the family of equations, sufficient convergence with increasing N was investigated.)

Figure 1 demonstrates that for the low-amplitude case considered in Yoon and Liu, there is little effect due to truncation of the series solution in the range of μ^2 of interest. Differences due to truncation do become apparent for longer waves and could be quite severe in the solitary wave limit, as would be expected. Similarly, Figure 2 demonstrates a similar lack of difference between $N = 20$ and $N = 7$ solutions of the model equation (5).

Figure 3 compares $N = 7$ term results for the KdV equation and model equation (5), which corresponds exactly to the numerical propagation model. In this case, differences in predicted wavelength are apparent over the range of higher values of μ^2 , as would be expected due to the different linear dispersion relations for the two models. Figure 2b demonstrates that an additional difference in the predicted Fourier amplitudes exists over the entire range of wavelengths. Given that the $N = 7$ spectra are good representations of the full solutions in the range $\mu^2 \geq 0.1$, it is apparent that the main problem in obtaining steady solutions in the numerical model lies with choosing the KdV equation as an analog for the numerical code. The correct choice is model equation (5).

We illustrate the effect of switching between sets of Fourier solutions as initial conditions for the computational model in Figure 4. For this case, we take KdV and equation (5) solutions for N large and then truncate them to $N = 7$. In either case, we would expect to see some resulting unsteadiness in the highest retained harmonics. The two sets of initial conditions are used to start the integration of equation (1); results are presented for a distance $x/h = 120$, or about 6.1 wavelengths. The figure displays the absolute values of the computed Fourier amplitudes $|A_1| - |A_7|$ on a logarithmic scale, in order to accentuate

unsteady behavior in the higher harmonics. Figure 4a displays the results for the model run started with the KdV solution, while Figure 4b displays results using the truncated solution of equation (5). The effect of initiating the computation with a solution from the wrong evolution equation is clear, as evidenced by the unsteadiness in all Fourier components in Figure 4a. In contrast, unsteadiness in Figure 4b is limited to the highest harmonics, as anticipated.

Turning to the higher of the two wave heights considered, we compare $N = 7$ solutions to high-order converged solutions for the KdV equation (Figure 5a) and equation (5) (Figure 5b). Typically, for this increased wave height it was necessary to retain up to $N = 30$ terms to obtain reasonable convergence. For example, significant divergence between $N = 30$ and $N = 20$ results occurred for $\mu^2 \leq 0.02$. Figure 5 indicates that truncation effects are apparent for both models at $\mu^2 = 0.1$, which is the range of interest, and are somewhat more severe in the KdV results. We would thus expect a truncation of a high-order solution to perform less well than in the example in Figure 4, even if the correct model equation were utilized. The results of a sample numerical integration are shown in Figure 6. Figure 6b displays results using the $N = 30$ equation (5) result truncated to 7 terms, and shows that unsteadiness is still relatively minor and is limited principally to higher modes. In contrast, use of the truncated KdV result (Figure 6a) leads to significant unsteadiness.

4 Solitary and cnoidal wave solutions for the family of model equations

In this section, explicit results are given for the family of solitary and cnoidal wave solutions to the generic model equation (7). Turning first to the case of solitary waves, we assume that solutions may be written in the form

$$\eta(x, t) = H \operatorname{sech}^2 \psi; \quad \psi = \beta(x - c_1 t) \quad (15)$$

where H is the wave height, β is an inverse length scale, and c_1 is the phase speed correct to $O(\epsilon, \mu^2)$. Substituting (15) in (7) gives the generic results

$$(\beta h)^2 = \frac{3H}{4h} \left(\frac{c^2 \gamma_{nl}}{\gamma_1 \gamma_2 \gamma_3} \right) \quad (16)$$

and

$$c_1 - c = \frac{1}{2} \frac{H}{h} \gamma_{nl} \quad (17)$$

where γ takes on a value of c when it corresponds to a space derivative, and c_1 when it corresponds to a time derivative. The subscript nl denotes the derivative appearing in the nonlinear term, and subscripts 1,2,3 denote the three derivatives in the dispersive term. The second relation (17) implies that all models with a space derivative in the nonlinear term lead to a phase speed of

$$c_1 = c \left(1 + \frac{1}{2} \frac{H}{h} \right) \quad (18)$$

while models with a time derivative in the nonlinear term lead to solitary wave phase speeds given by

$$c_1 = \frac{c}{1 - \frac{1}{2} \frac{H}{h}} \quad (19)$$

The two results (18) and (19) are asymptotically equivalent for small ϵ , but differ by large amounts in the range of waveheights close to limiting values, as indicated in Figure 7. Further, the trend of increasing phase speed relative to the KdV result, as seen in the models with a time derivative, is in opposition to the known *decrease* in phase speed relative to (18) as predicted by higher-order theories (see, for example, Fenton (1972)). This feature may render models with a time derivative in the nonlinear term unsuitable as relatively accurate leading-order approximations for steep waves, and we caution that equation (1) falls into this category of models.

The remaining problem for the inverse length scale of the solitary wave depends on the choice of derivatives in the dispersion term, and there are thus 8 distinct solutions, 4 for each choice of nonlinear term. For the choice of an x derivative in the nonlinear term, we

obtain the family of approximations

$$\eta_{xxx} : (\beta h)^2 = \sigma \quad (20)$$

$$\eta_{xxt} : (\beta h)^2 = \frac{\sigma}{(1 + \frac{1}{2} \frac{H}{h})} \quad (21)$$

$$\eta_{xtt} : (\beta h)^2 = \frac{\sigma}{(1 + \frac{1}{2} \frac{H}{h})^2} \quad (22)$$

$$\eta_{ttt} : (\beta h)^2 = \frac{\sigma}{(1 + \frac{1}{2} \frac{H}{h})^3} \quad (23)$$

where

$$\sigma = \frac{3H}{4h} \quad (24)$$

For the case of a t derivative in the nonlinear term, we obtain the family of approximations

$$\eta_{xxx} : (\beta h)^2 = \frac{\sigma}{(1 - \frac{1}{2} \frac{H}{h})} \quad (25)$$

$$\eta_{xxt} : (\beta h)^2 = \sigma \quad (26)$$

$$\eta_{xtt} : (\beta h)^2 = \sigma(1 - \frac{1}{2} \frac{H}{h}) \quad (27)$$

$$\eta_{ttt} : (\beta h)^2 = \sigma(1 - \frac{1}{2} \frac{H}{h})^2 \quad (28)$$

The variations of length scales with wave height in the various solutions are shown in Figure 8 for KdV type nonlinearity and in Figure 9 for time-derivative type nonlinearity.

For the case of cnoidal waves, we obtain the usual solution form

$$\eta(x, t) = \eta_2 + (\eta_3 - \eta_2) \text{cn}^2 \left[\frac{2K(m)}{L} (x - c_1 t) \right] \quad (29)$$

where η_2 is the minimum water level and $\eta_3 - \eta_2$ is the wave height H . $K(m)$ is the complete elliptic integral of first kind with parameter m . The phase speed c_1 for the case of KdV (x -derivative) nonlinearity is given by

$$c_1 = c \left[1 + \frac{H}{2mh} \left(2 - m - \frac{3E(m)}{K(m)} \right) \right] \quad (30)$$

where $E(m)$ is the complete elliptic integral of second kind. For the case of t -derivative nonlinearity, the phase speed is given by

$$c_1 = \frac{c}{\left[1 - \frac{H}{2mh} \left(2 - m - \frac{3E(m)}{K(m)} \right) \right]} \quad (31)$$

The wavelength L depends on the mix of derivatives in the dispersive term, and is given by

$$L = 4hK(m) \left(\frac{m\gamma_1\gamma_2\gamma_3h}{3c^2\gamma_{nl}H} \right)^{1/2} \quad (32)$$

Two parameters (here, H and m or H and period $T = L/c_1$) need to be specified in order to calculate a solution. Goring (1978) has presented efficient algorithms for specifying the cnoidal wave form given any combination of specified independent parameters.

Defining a non-dimensional wavenumber squared in terms of (32), we obtain

$$(\kappa h)^2 = \sigma \frac{\pi^2 c^2 \gamma_{nl}}{mK(m)^2 \gamma_1 \gamma_2 \gamma_3}; \quad \kappa = 2\pi/L \quad (33)$$

where σ is defined above in (24).

5 Conclusions

We have shown here that the solutions for periodic waves produced by the various members of the KdV family of equations are distinctly numerically different in parameter ranges of interest, despite the asymptotic equivalence of the models in a formal sense. These differences lead to anomalous behaviors when the solutions are utilized as initial conditions in numerical computation schemes. We have further shown that the shift from a space derivative to a time derivative in the nonlinear term has effects (in high waves) which overshadow the more typically investigated effects arising when the dispersive term is altered. The effect of changing the nonlinear term is most pronounced in the solitary wave limit. Further, results for the time-derivative form diverge from the KdV results in a sense which is opposite to the divergence between KdV and higher-order solutions at large amplitude. This alone may render the time-derivative model a bad choice as a leading order approximation for numerical studies if high waves are to be considered. Since the fairly common model equation (1) falls into this category, it seems that modelling efforts for spectral wave calculations in shallow water could benefit from further consideration of these points.

The results here present an interesting quandary when the problem of reproducing laboratory data is considered. Each of the theories here contain differences which are

manifested at $O(\epsilon^2, \epsilon\mu^2, \mu^4)$ due to the order of truncation in the theory. It is present practice in laboratory studies of shallow-water waves (Goring, 1976; Hammack et al, 1989) to employ one of the theories (in particular, the KdV equation) as a basis for determining the Lagrangian time-history of paddle stroke. However, it should be recognized that exactly the same level of truncation exists when comparing any of these theories to measured wave fields as exists in comparing the theories to each other. We could thus expect to see as much disagreement between model prediction and experiment as we see here between each model, given the same range of physical scaling parameters. We would also expect to see some degree of higher-harmonic unsteadiness in the wave tank due to this disagreement. It would thus be advantageous to have conclusive knowledge of which of the models here comes closest to predicting physical reality in a numerically accurate sense. Unfortunately, this information is still lacking, as is data with enough resolution to detect fast modulation of the higher harmonics.

Acknowledgements. This work has been supported by the Naval Civil Engineering Laboratory and Office of Naval Research through grant N00014-89-J-1717.

References

- Benjamin, T. B., Bona, J. L. and Mahony, J. J., 1972, "Model equations for long waves in nonlinear dispersive systems", *Phil. Trans. Roy. Soc.* A272, 47-78.
- Cayley A., 1895, *An elementary treatise on elliptic functions*. Reprinted by Dover, N.Y.
- Fenton, J., 1972, "A ninth-order solution for the solitary wave", *J. Fluid Mech.*, 53, 257-271.
- Flick, R. E., Guza, R. T. and Inman, D. L., 1981, "Elevation and velocity measurements of laboratory shoaling waves", *J. Geophys. Res.*, 86, 4149-4160.
- Freilich, M. H. and Guza, R. T., 1984, "Nonlinear effects on shoaling surface gravity waves", *Phil. Trans. Roy. Soc. London*, A 311, 1-41.

- Goring, D., 1978, "Tsunamis - The propagation of long waves onto a shelf", Report KH-R-38, W. M. Keck Laboratory of Hydraulics and Water Resources, California Institute of Technology, Pasadena.
- Hammack, J., Scheffner, N. and Segur, H., 1989, "Two-dimensional periodic waves in shallow water", *J. Fluid Mech.*, 209, 567-589.
- Liu, P.L.-F., Yoon, S. B. and Kirby, J. T., 1985, "Nonlinear refraction-diffraction of waves in shallow water", *J. Fluid Mech.*, 153, 184-201.
- Mei, C. C., 1983. *The applied dynamics of ocean surface waves*, Wiley.
- Yoon, S. B. and Liu, P. L.-F., 1989, "Stem waves along breakwater", *J. Waterway, Port, Coastal and Ocean Engrng.* 115, 635-648.

List of Figures

- 1 Comparison of KdV series solutions with $N = 20$ and $N = 7$. (a) Predicted wave length L/h . (b) Predicted Fourier amplitudes a_n/h . Solid line: $N = 20$; dashed line: $N = 7$ 14
- 2 Comparison of equation (5) series solutions with $N = 20$ and $N = 7$. (a) Predicted wave length L/h . (b) Predicted Fourier amplitudes a_n/h . Solid line: $N = 20$; dashed line: $N = 7$ 14
- 3 Comparison of KdV and equation (5) series solutions with $N = 7$. (a) Predicted wave length L/h . (b) Predicted Fourier amplitudes a_n/h . Solid line: KdV; dashed line: equation (5). 14
- 4 Numerical results computed with equation (1), using $N = 7$ truncated solutions as initial conditions. $H/h = 0.2$. (a) KdV solution. (b) Equation (5) solution. 15
- 5 Comparison of equation (5) and KdV series solutions with $N = 30$ and $N = 7$. (a) KdV results. (b) Equation (5) results. Solid line: $N = 30$; dashed line: $N = 7$ 15
- 6 Numerical results computed with equation (1), using $N = 7$ truncated solutions as initial conditions. $H/h = 0.4$. (a) KdV solution. (b) Equation (5) solution. 15
- 7 Variation of lowest-order solitary wave speed with dimensionless wave height. Solid line: KdV ($\eta\eta_x$) form. Dashed line: equation (5) ($\eta\eta_t$) form. 15
- 8 Length scales for solitary waves for KdV family ($\eta\eta_x$ nonlinearity). 1 - η_{xxx} ; 2 - η_{xxt} ; 3 - η_{xtt} ; 4 - η_{ttt} 15
- 9 Length scales for solitary waves for modified ($\eta\eta_t$) nonlinearity. 1 - η_{xxx} ; 2 - η_{xxt} ; 3 - η_{xtt} ; 4 - η_{ttt} 15

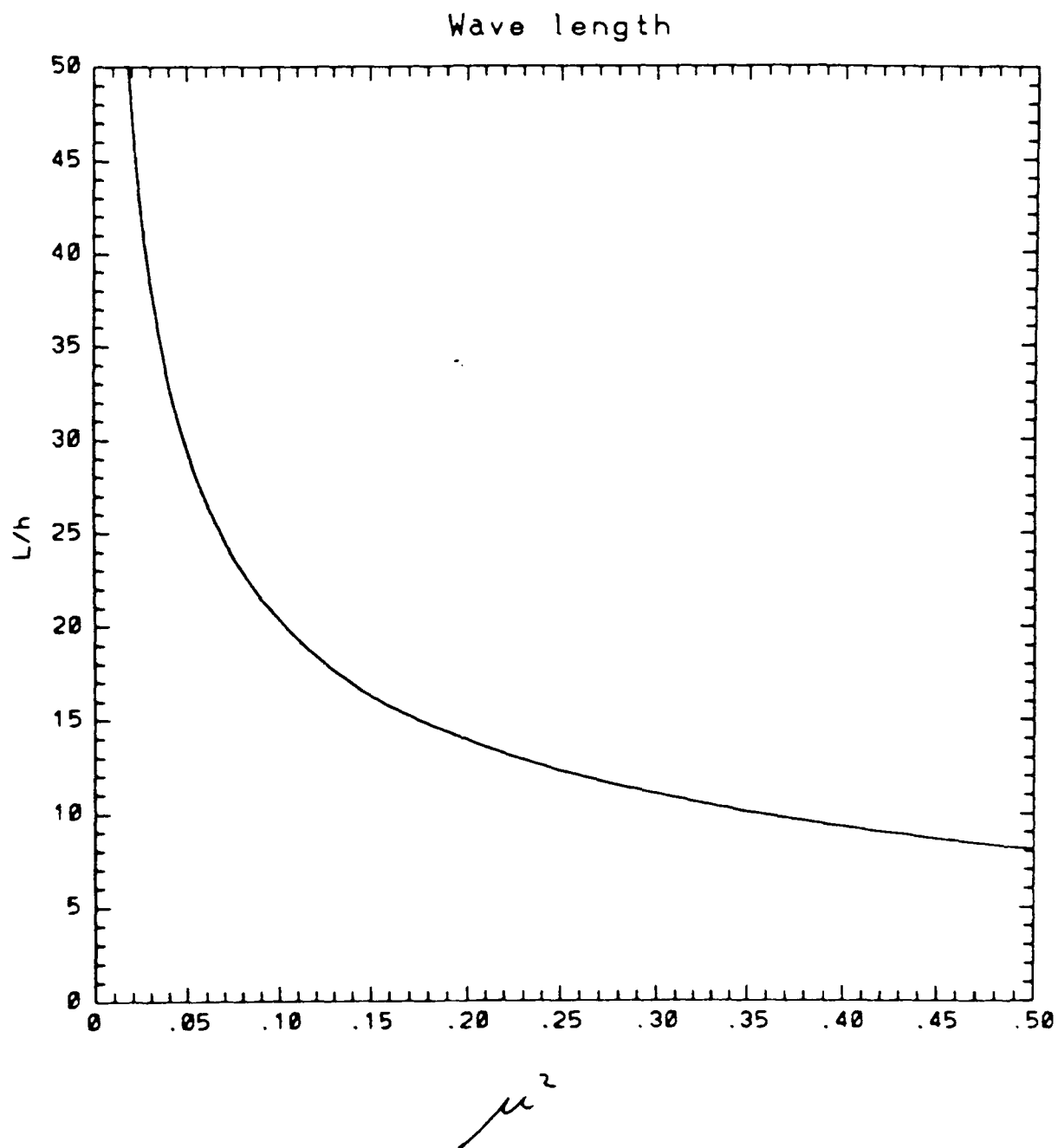


Figure 1a

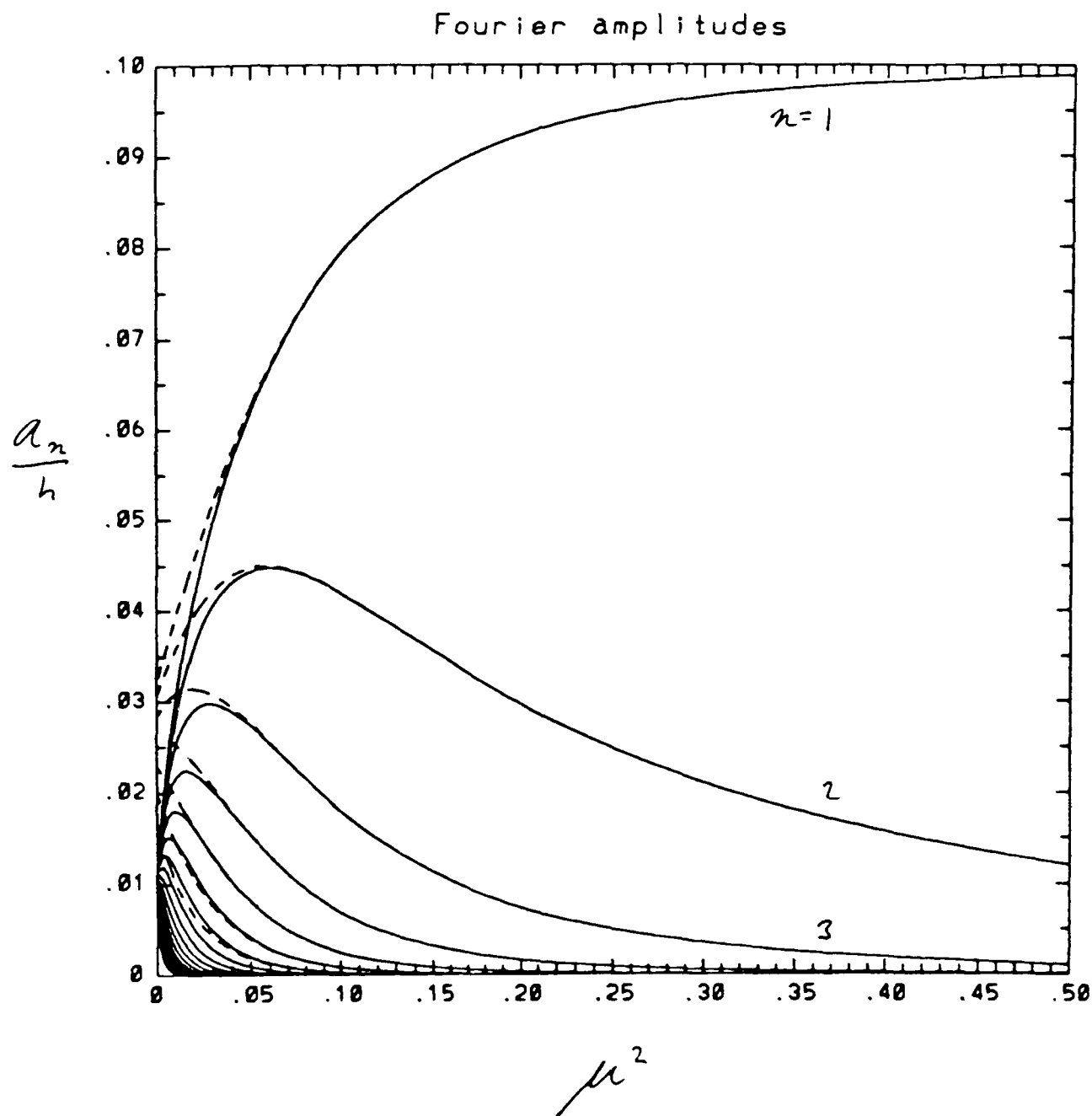


Figure 1b

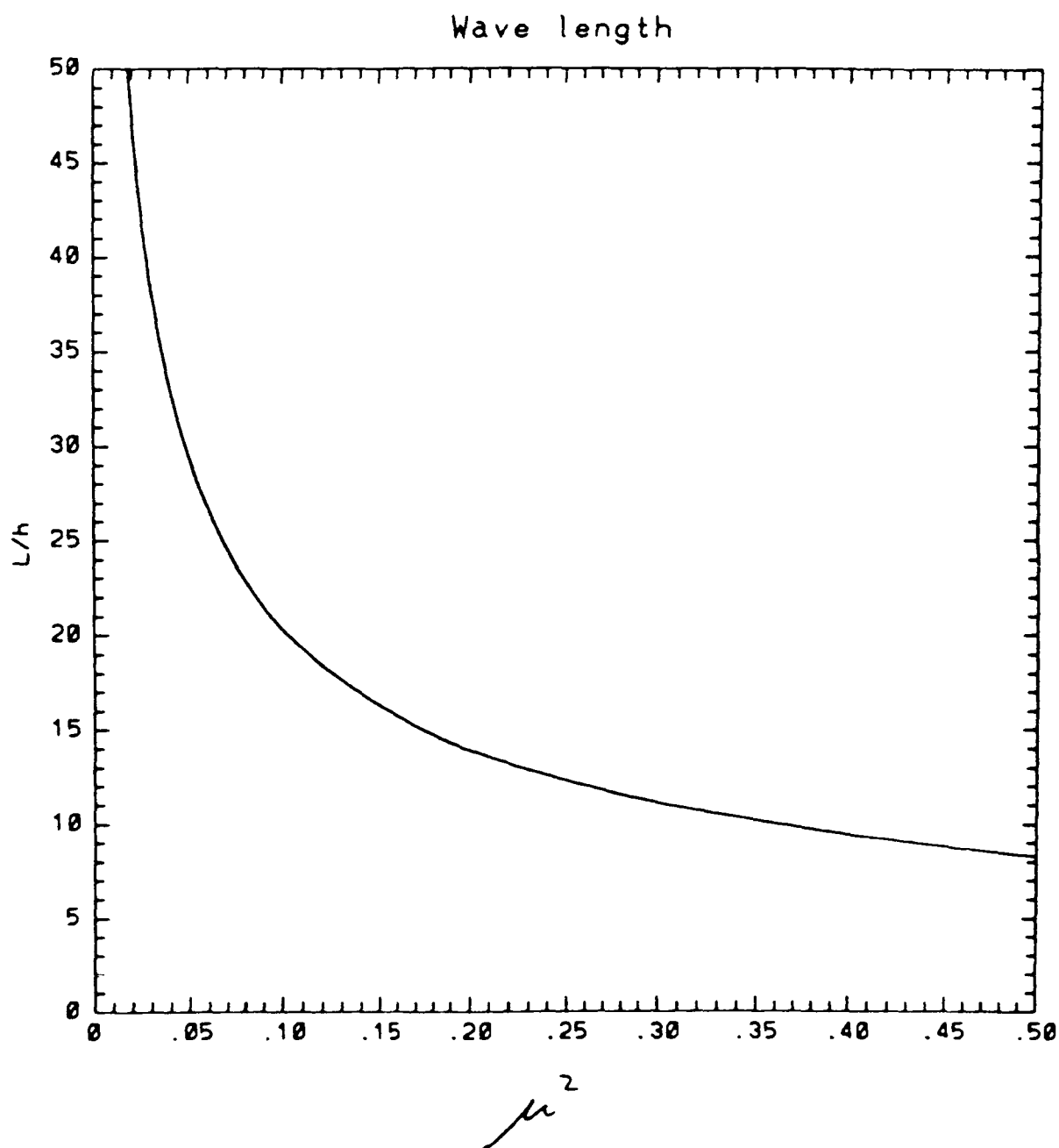


Figure 2a

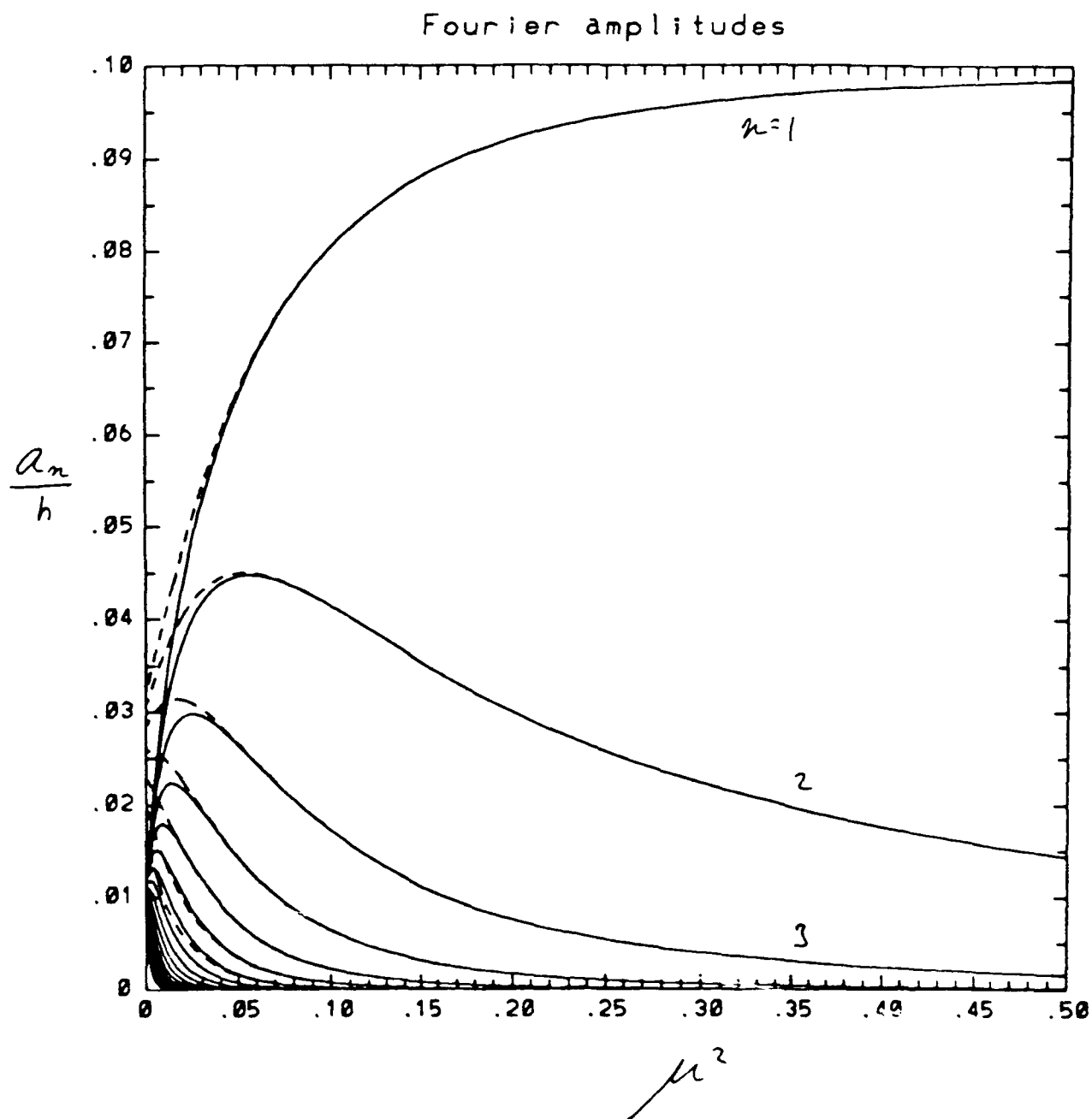


Figure 26

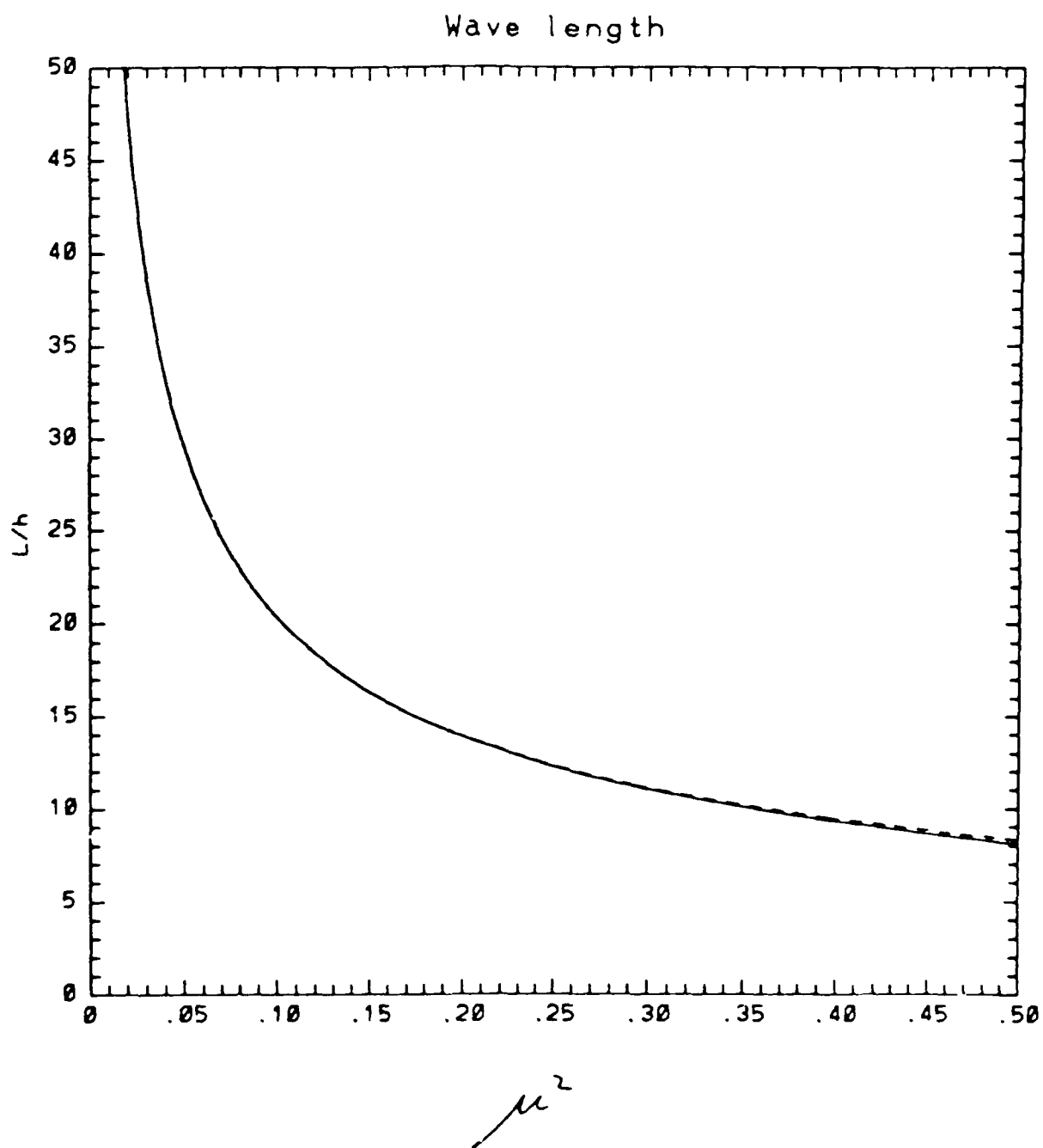


Figure 3a

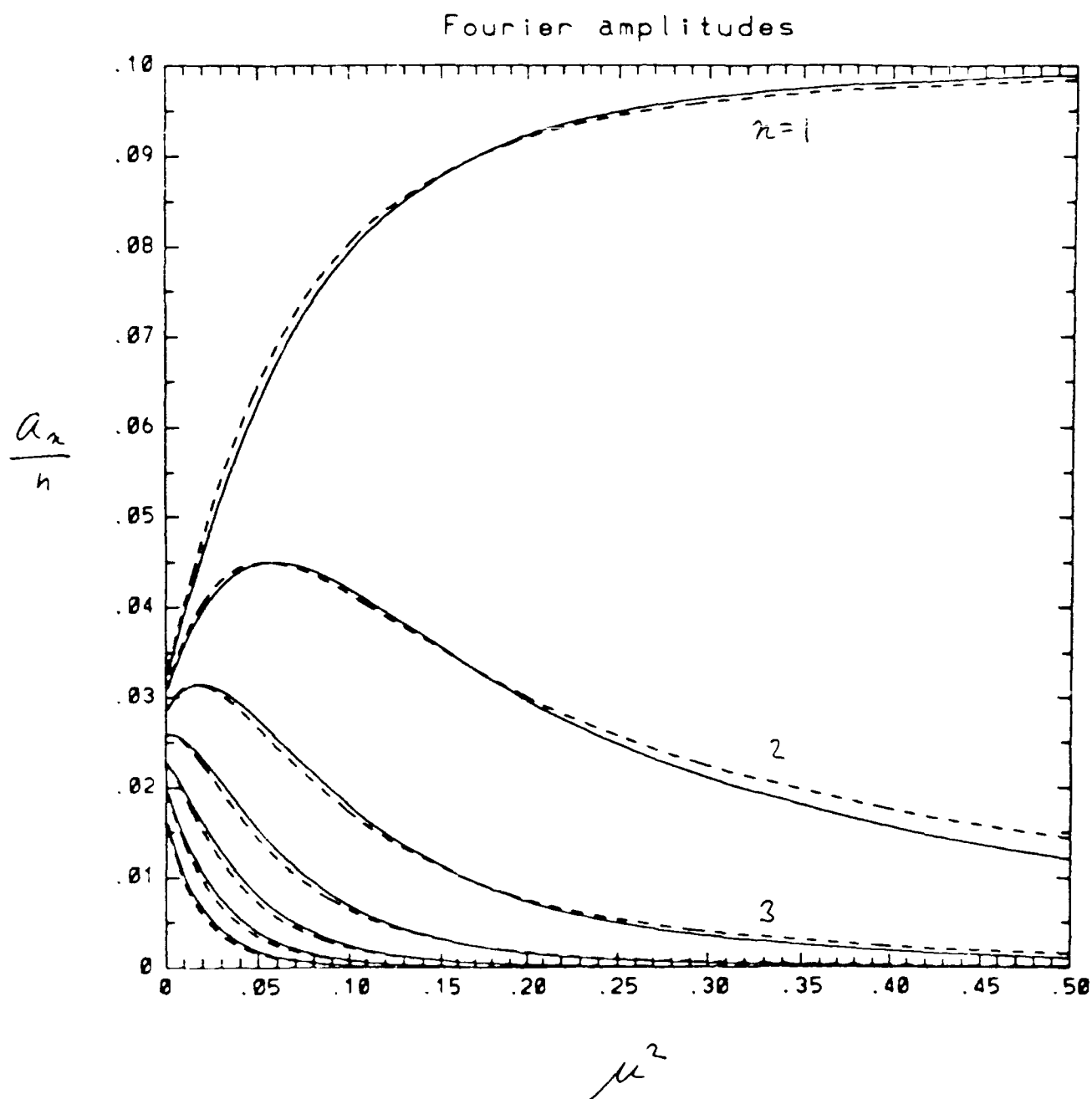


Figure 3b

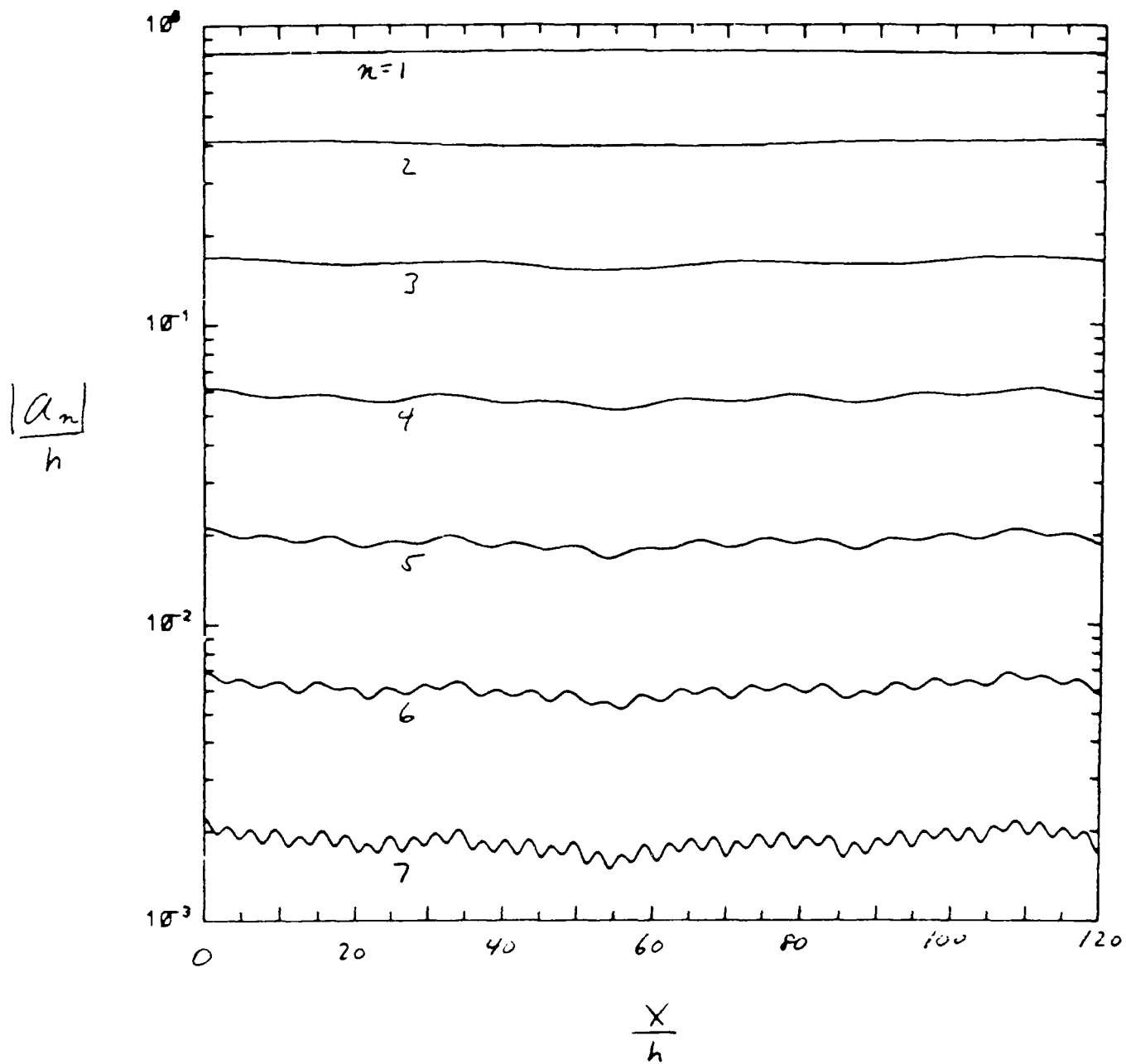


Figure 4a

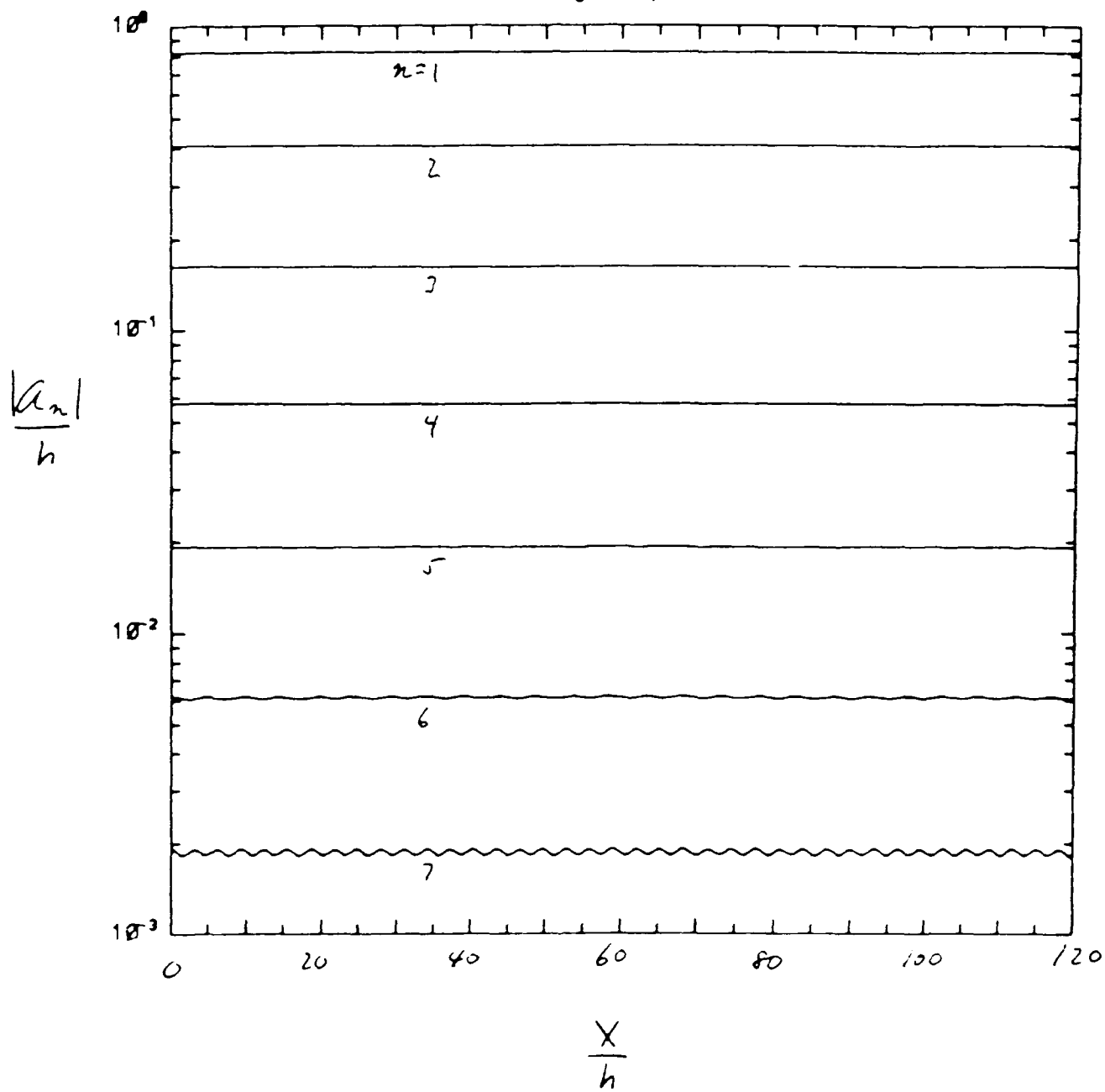


Figure 4b

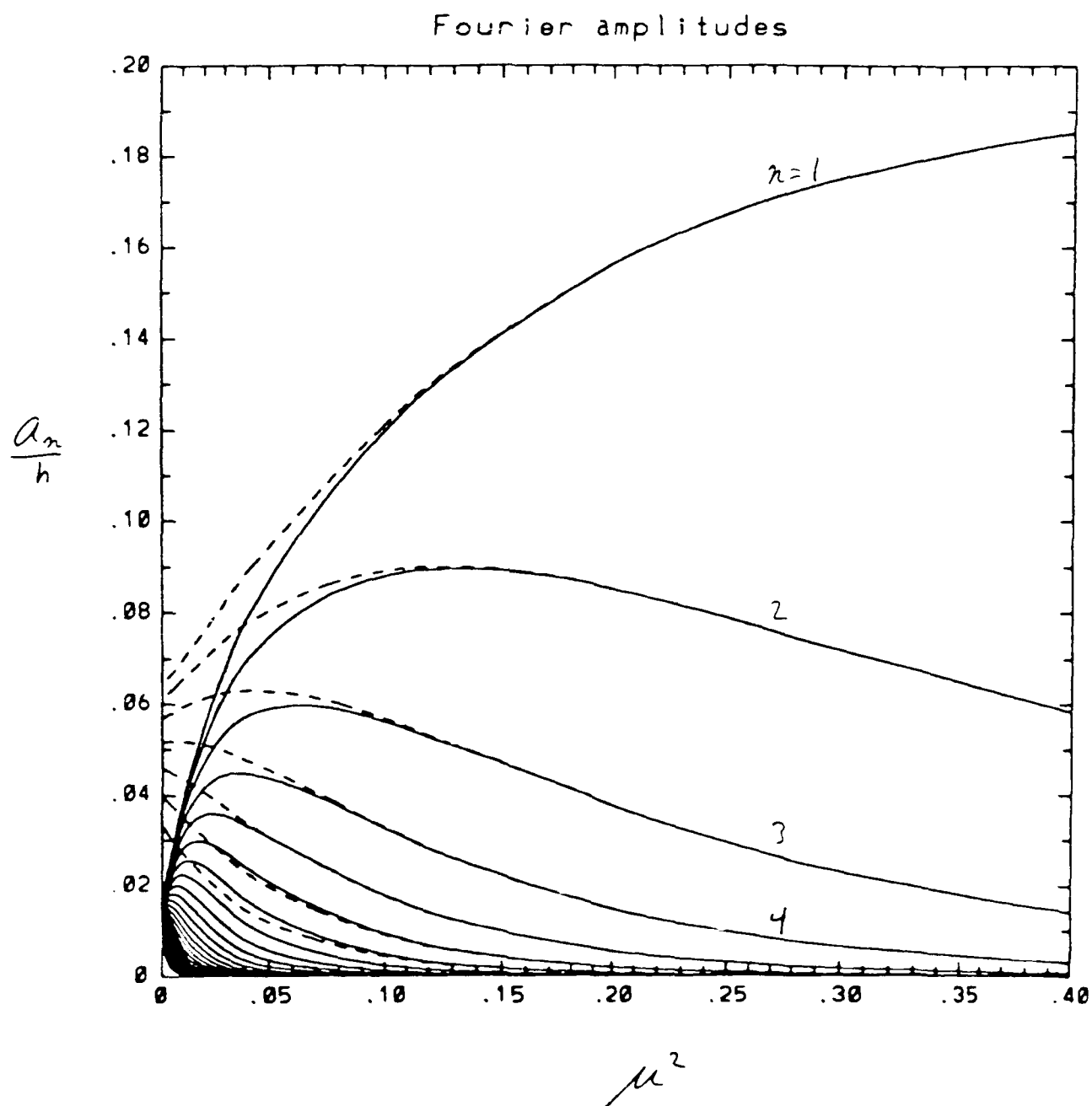


Figure 3h

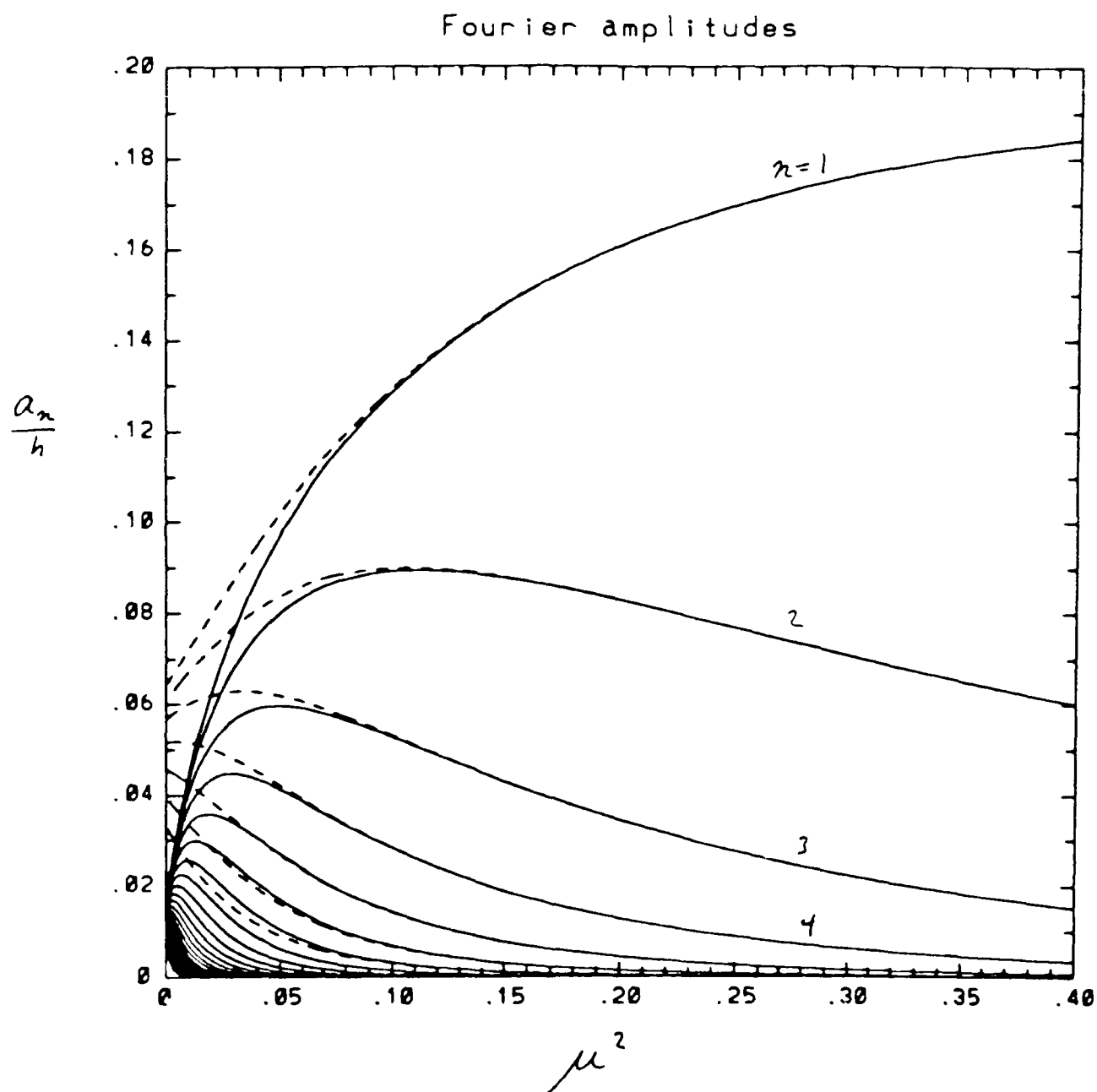


Figure 5b

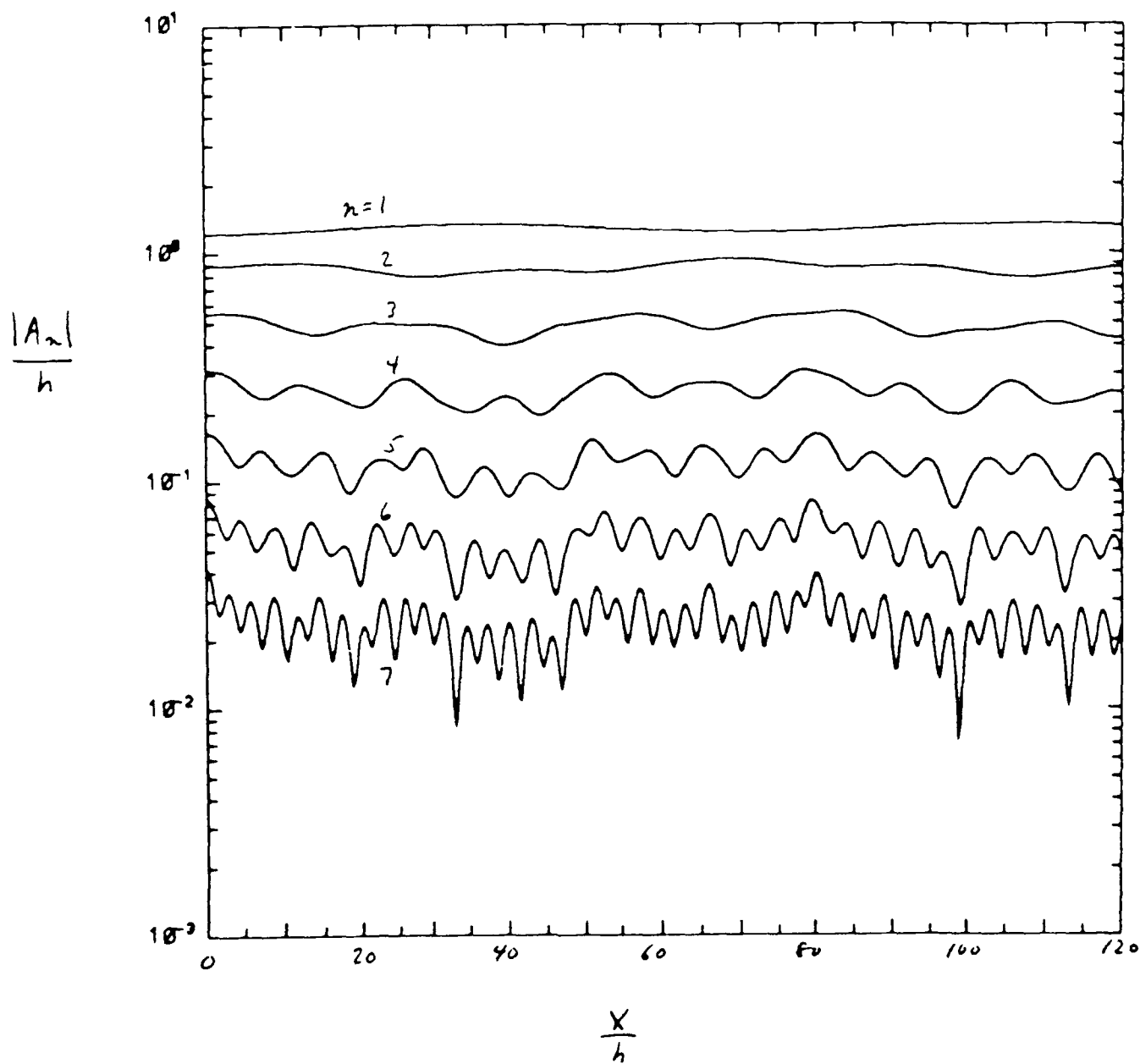


Figure 6a

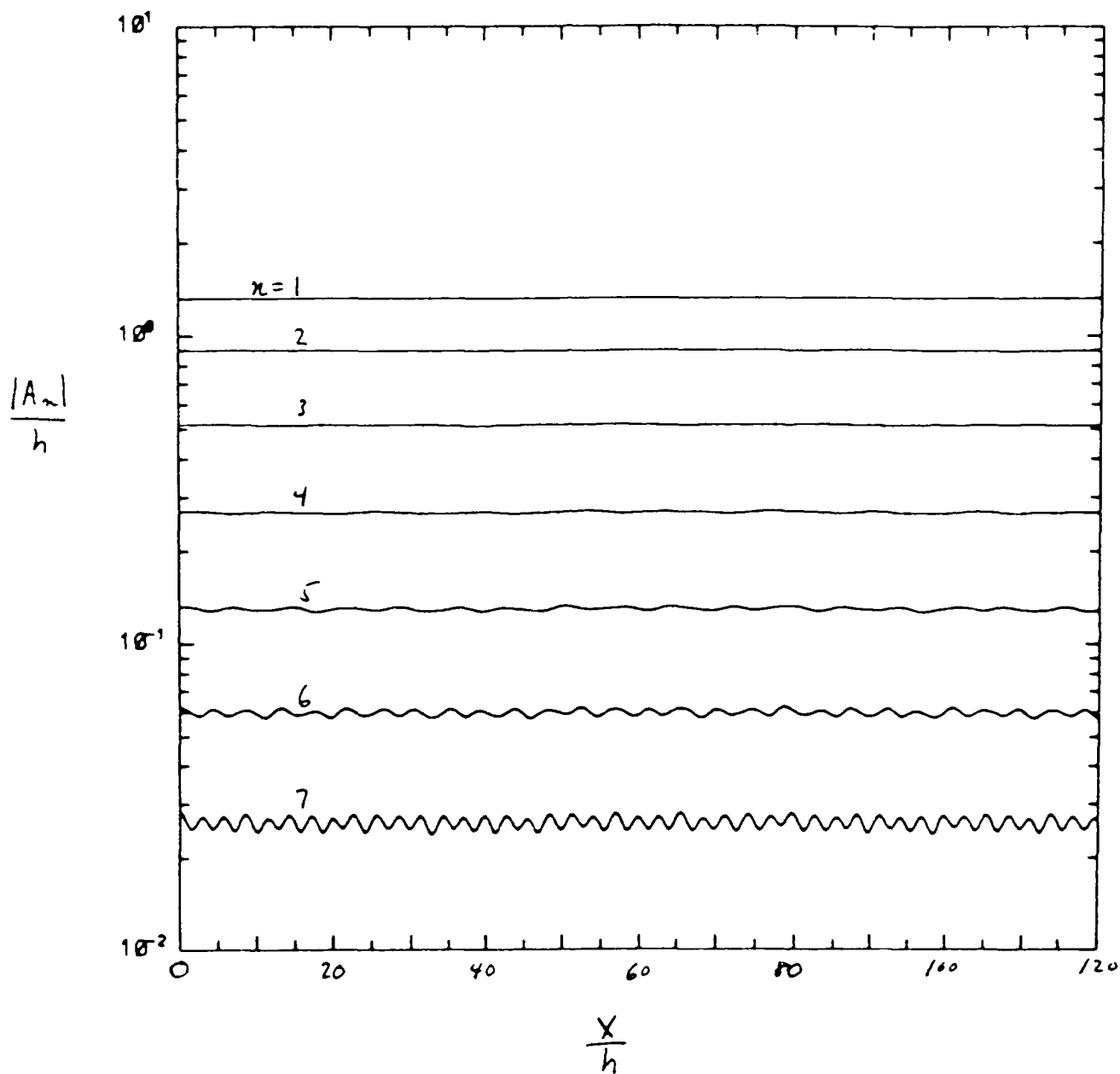


Figure 6b

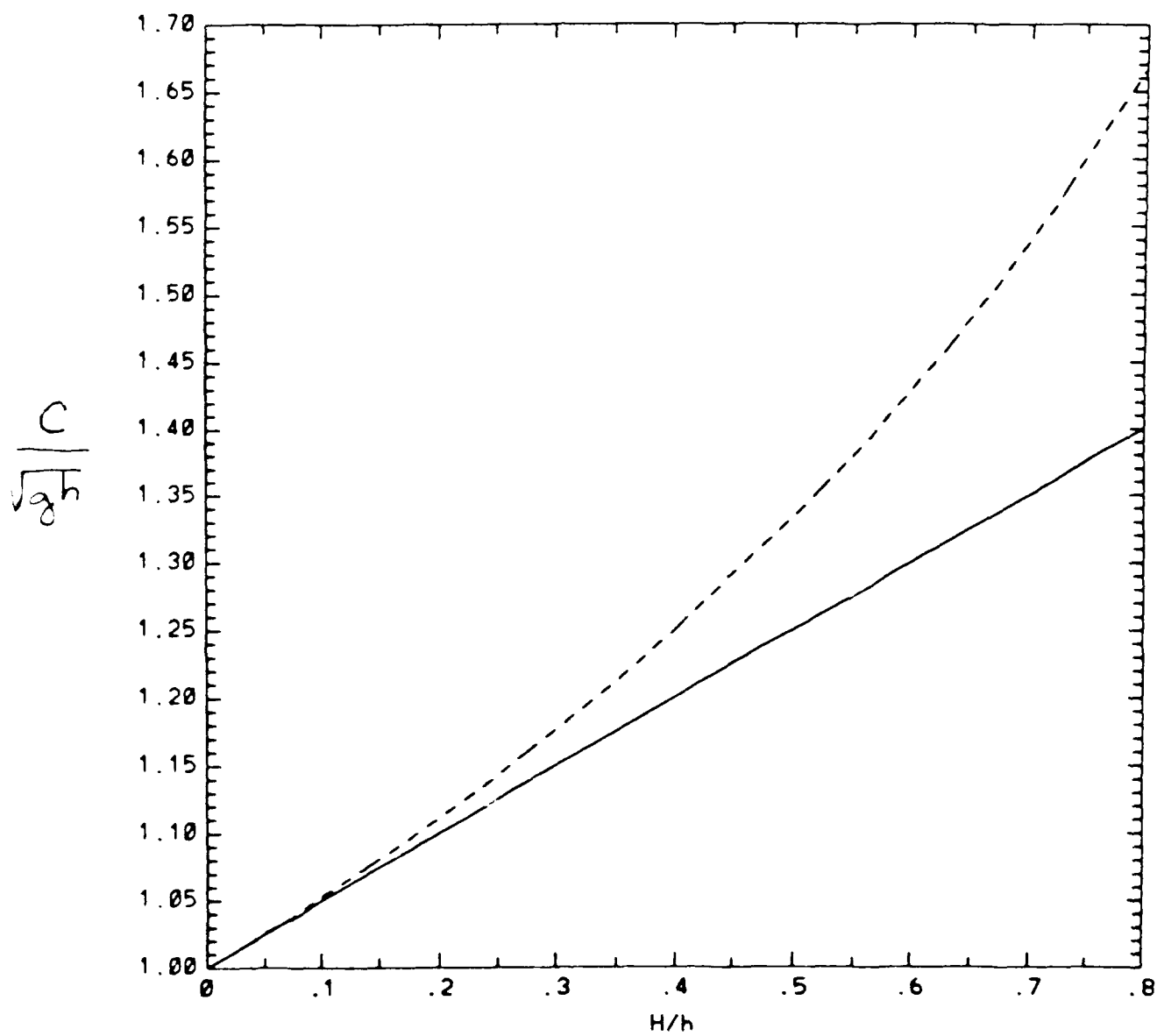


Figure 7

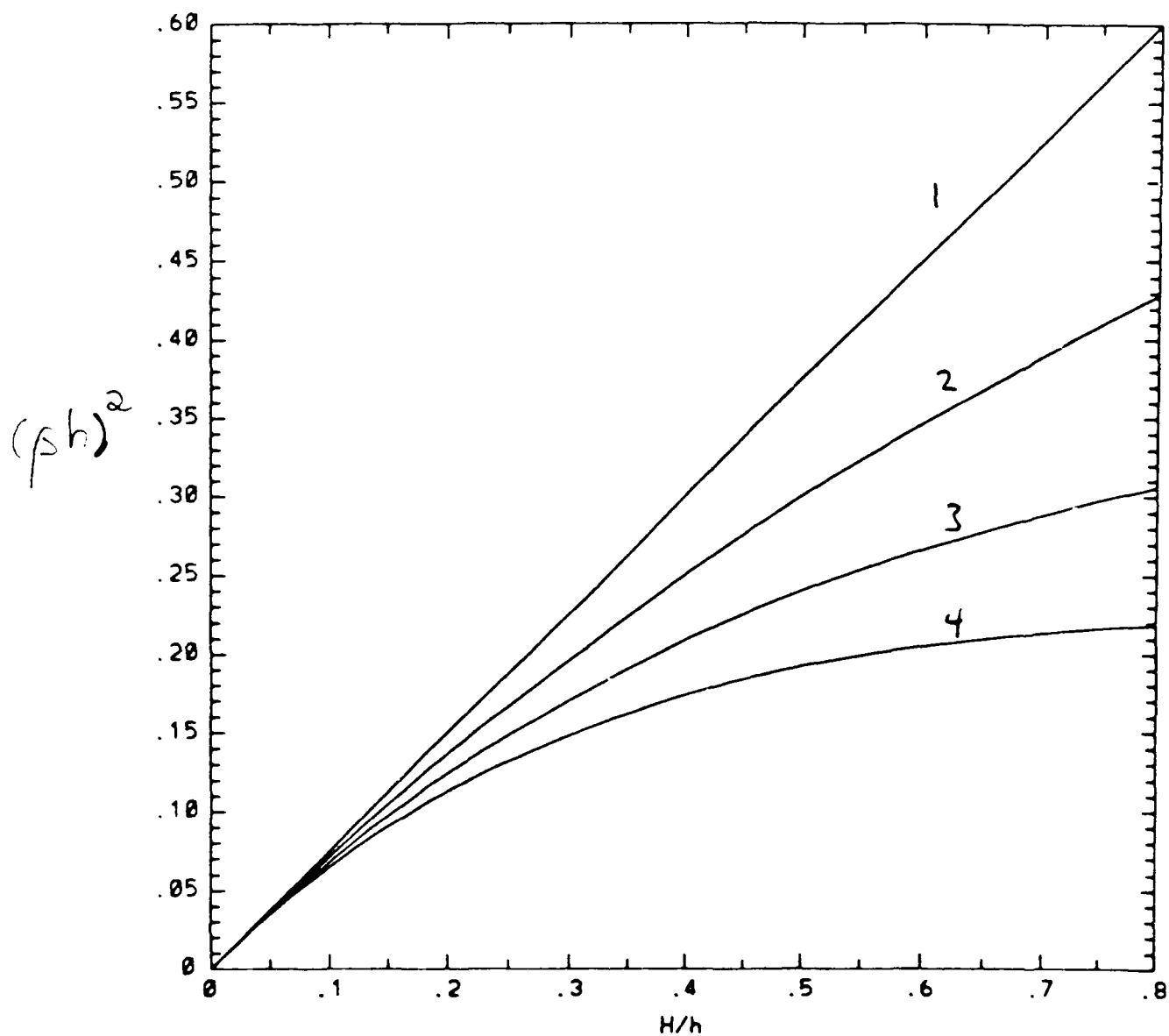


Figure 8

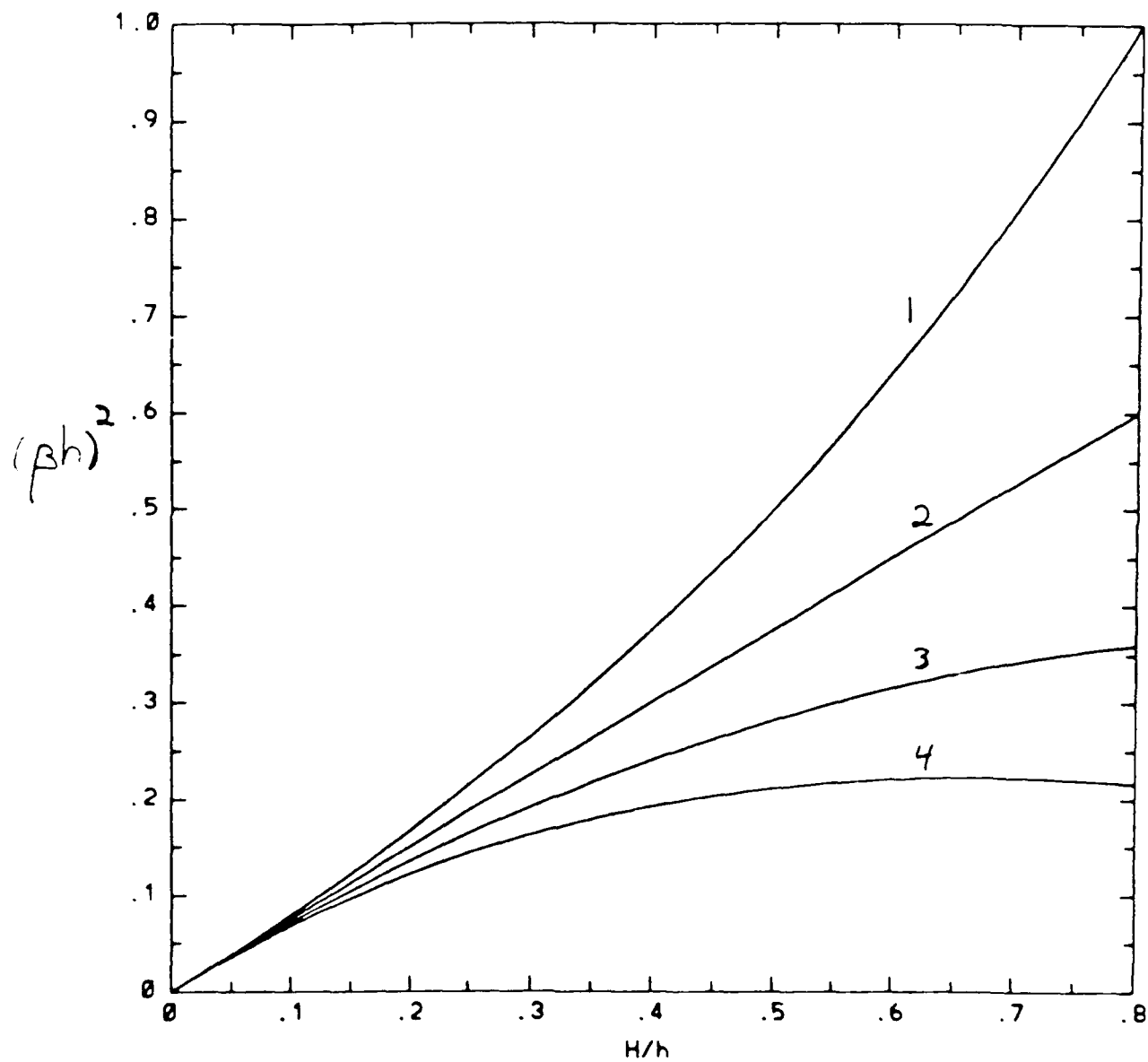


Figure 9